Modeling of mechanisms affecting the growth and breakdown of iron sulfide films

by

Aravind Krishnamoorthy

B.Tech., Metallurgy and Materials Science, Indian Institute of Technology Madras, India

Submitted to the Department of Materials Science and Engineering
in partial fulfillment of the requirements for the degree of

Doctor of Philosophy

at the

MASSACHUSETTS INSTITUTE OF TECHNOLOGY

June 2016

Author .....
Department of Materials Science and Engineering
April 4, 2016

Certified by .....
Bilge Yildiz
Associate Professor of Materials Science and Engineering
Associate Professor of Nuclear Science and Engineering
Thesis Supervisor

Accepted by .....
Donald Sadoway
John F. Elliott Professor of Materials Chemistry
Chair, Departmental Committee on Graduate Students

Modeling of mechanisms affecting the growth and breakdown of iron sulfide films

by

Aravind Krishnamoorthy

Submitted to the Department of Materials Science and Engineering
on April 4, 2016, in partial fulfillment of the
requirements for the degree of
Doctor of Philosophy

Abstract

Modeling the behavior of ionic materials in electrochemical environments is a topic of great scientific interest for important systems like like fuel cells, batteries, and catalysts and corrosion passive films. However, existing analytical and numerical models of such electrochemical systems like passive films are derived from mathematical expressions for the growth and degradation of the ionic material that are not derived from the rates of underlying physical processes and are instead merely benchmarked to experimental data. These models are intrinsically empirical and fall short of providing mechanistic insights into the physical processes occurring in the passive film that are required to design better-performing electrochemical materials. In this thesis, based on our understanding that overall film behavior is a collective outcome of several atomic-scale phenomena like defect formation and ionic diffusion that contribute to the growth and/or breakdown of the passive film, we construct a construct a novel multiscale modeling framework that explicitly models atomic scale phenomena and couples it to higher-length-scale description of the microstructure to estimate passive film behavior in a mechanistic way and we further demonstrate this capability on an ionic system of FeS_x phases on a steel substrate. The primary contributions of the thesis are two-fold:

- We identified the atomistic mechanisms responsible for the growth and breakdown of iron sulfide phases, and also quantified non-empirically the kinetic parameters that govern the rate of these unit processes.
- We constructed a novel multiscale modeling framework that couples accurate modeling of atomic-scale unit processes to efficient modeling of the micron-scale behavior of the passive film that captures phenomena at multiple length scales ranging from point defect dynamics to microstructure formation and evolution.

The thesis is divided into three sections, the first of which is devoted to investigating two unit processes (surface sulfidation and ionic diffusion) that contribute to the growth of iron sulfide phases and is primarily focused on quantifying the kinetic parameters involved in the sulfidation (adsorption energies and dissociation barriers) and ionic diffusion (diffusivities and migration barriers) processes. In this section, we use a combination of *ab initio* density functional theory and kinetic Monte Carlo to quantify the surface-defect-induced changes in the electronic structure (0.4 eV reduction in the band gap and the introduction of mid-gap states) that increase the reactivity of and the rate of sulfidation on FeS_2 (100) surfaces. We also use the d-band theory to explain the effect of surface coverage and surface charge (or electric potential) on the reactivity of the reactivity of the surface, and provide guidelines for more accurate calculation of reactivity metrics in realistic electrochemical conditions. Finally, through the use of high-accuracy hybrid DFT and NEB methods, coupled with kinetic Monte Carlo calculations, we resolve the influence of magnetic and vacancy ordering transitions on ionic migration barriers and diffusivity of pyrrhotite, $Fe_{1-x}S$. Specifically, we identify that the ionic migration barrier is unaffected by the local vacancy configuration in different

pyrrhotite polytypes, but is strongly influenced by the local magnetic order imposed by strong antiferromagnetic superexchange interactions that exist in pyrrhotite, which is a finding that is also important for other scientifically important material systems like NiO.

The next section of the thesis discusses the mechanistic pathways and kinetic parameters of two processes involved in the local degradation of iron sulfide passive films (vacancy agglomeration-induced pit initiation and hydrogen-evolution-assisted debonding). For the first process, we use first-principles modeling to explain experimental observations of non-Arrhenius vacancy concentrations and nanoscale pitting on the FeS_2 surface. We identify a mechanistic pathway comprising of concerted vacancy formation and diffusion unit processes that leads to the formation of vacancy agglomerates that serve as sites for nanopit initiation. We then use the same set of computational tools to identify another mode of failure in the layered iron sulfide phase, mackinawite. We identify through computational stress-strain curves that cathodically generated H_2 molecules are detrimental to the mechanical stability of the mackinawite phase and cause localized degradation of the passive film and act as a precursor to pitting corrosion.

The final section of the thesis describes the formulation of the multiscale modeling framework that incorporates the kinetics of film growth and breakdown mechanisms identified in previous sections. This novel coupled kMC and phase-field model is capable of describing the macroscale morphology, passivity and protectiveness of the passive film while also possessing sufficient resolution to simulate atomic scale dynamics occurring at the film interfaces, and represents a significant improvement in terms of mechanistic detail over existing analytical corrosion models especially for sour systems. We demonstrate the capability of the model in constructing kinetic stability diagrams, which extend the information contained in phase and Pourbaix diagrams by accounting for the relative rates for formation and dissolution of different iron sulfide phases. We also demonstrate the calculation of degradation maps, that help identify the dominant mechanisms behind the localized failure of the passive film at different environmental conditions (temperature, partial pressure of H_2S, electrode potential, pH etc) and thus identify environmental conditions where the passive film is stable against localized degradation. Finally, the direct coupling between atomic scale processes and overall film passivity allows us to identify the impact of different material properties (like vacancy formation energy and diffusivity) on the resistance of the passive film to pitting and localized corrosion.

Thesis Supervisor: Bilge Yildiz
Title: Associate Professor of Materials Science and Engineering
Associate Professor of Nuclear Science and Engineering

Acknowledgments

I am very grateful to my advisor, Prof. Bilge Yildiz for all the guidance, support and encouragement I've received over the course of this project. It has been a privilege to witness her passion for scientific questions and her thorough and meticulous approach to research work and an uncanny instinct for identifying the central scientific point from a jumble of data. I am happy to have been part of the group during a time when she demonstrated the dedication and hard work required to establish oneself as a PI with tenure and create a thriving research group at MIT. It has been an extremely instructive and humbling experience.

I am deeply indebted to William Herbert for all the discussions and experimental input and also for being the driving force behind making this a truly collaborative project and greater than the sum of its parts. His dedication, hard work and scientific rigor continue to be a source of motivation for me and his ever-affable and optimistic nature made day-to-day research work a joyful experience. I cherish working with him and I am grateful to him for giving me my first taste of experimental work at UIUC.

I am very happy to have had a chance to collaborate with Minh Dinh since he was an undergraduate student. Our discussions and his calculations were instrumental in informing large sections of this thesis. His constant enthusiasm and vigor are infectious and made working with him an immense pleasure. Our discussions on topics outside work, ranging from computers to coffee will always remain in my mind.

I also want to thank all the members of the Laboratory of Electrochemical Interfaces at MIT with whom I've had the pleasure of working with for the previous six years. I am especially grateful to Dario M and Mostafa Youssef, who took me under their wing when I had just joined the group. I'm grateful to Yan Chen, Qiyang Lu, Yue Fan, Wen Ma, Lixin Sun, Jing Yang and Jeong-Woo Han for all the feedback and comments that have improved this work immeasurably.

Prof. Krystyn Van Vliet and Prof. Michael Demkowicz were instrumental in keeping the thesis focused and their feedback during the committee meeting greatly improved the quality of this work.

I am grateful beyond words to my mother and father for all the love and support and for always keeping me in their thoughts and prayers. Special thanks also to my little sister Archana for her unconditional kindness and love and for teaching me the meaning of strength in adversity. Her sense of humor is a constant source of joy and never fails to brighten my day. I look forward to her own PhD thesis with pride.

Finally, a shout out to all my friends at MIT (Priyank, Deepak, Ketan, Swarun, Sivaraman and Ashok) who kept me grounded and relaxed and stopped me from getting lost in my work. I'll fondly remember the time spent at the squash courts and movies and TA sessions for years to come.

Contents

Chapter 1

Introduction

1.1 Context: Metals, corrosion and passivity

Modern civilization relies on a wide array of energy, transportation and construction infrastructure containing components made from functional metals and alloys. The importance of these refined metals towards technological progress cannot be overstated when we consider that different eras of human technological development are often denoted by the type of metals or alloys whose refinement enables scientific progress in that era. However, our continued and indeed increasing reliance on these metallic and alloy components for their structural and electronic properties (and more importantly their durability) is in contrast to the thermodynamic tendency of these metals to regress back to their mineral states (usually oxides, sulfides, carbonates etc.) from which they were originally purified. While this unwanted regress to the oxidized state (called corrosion) is thermodynamically guaranteed, it is possible to control and slow down the process responsible for such corrosion thereby ensuring a reasonable long service lifetime for the metal/alloy components in operational environments. One of the most useful tools in our effort at corrosion mitigation is the passivity of the metal, i.e. the ability of metals to self-protect by forming a thin, inert skin of an ionic compound through a partial reaction at the environment interface. The passivity of common metals like iron and copper have attracted attention as early as 1830 when Michael Faraday predicted the existence of an ultra-thin, electronically conducting surface film that protects the underlying metal, i.e. what we would now refer to as a passive film, before the tools required for its characterization were available [1]. Advances in the decades since have given us a better understanding of the nature of passivity, which we can define succinctly as [2]

> A metal is passive if it substantially resists corrosion in a given environment despite a marked thermodynamic tendency to react

This definition clearly indicates the metastable and dynamic nature of the passive film. Specifically, it highlights that the passive film is only kinetically stable and therefore does not provide an infinite barrier against metal dissolution or corrosion in aggressive environments. This assessment is clear when we consider the electrochemical polarization curve (Figure 1-1) for a metal like iron, which plots the corrosion current (i.e. the rate of metal loss due to corrosion) against the electrochemical potential (i.e. the driving force for corrosion). The near-linear dependence of $\log(i)$ on the driving force starting from $E = 0$ is interrupted by the onset of passive film formation at $E = E_{pass}$, which causes the corrosion rate and current to fall sharply to a very low (but finite) value. This very low current, which in the case of more stable films like those on Al, can be up to 6 orders of magnitude lower than the current in the active region, pro-

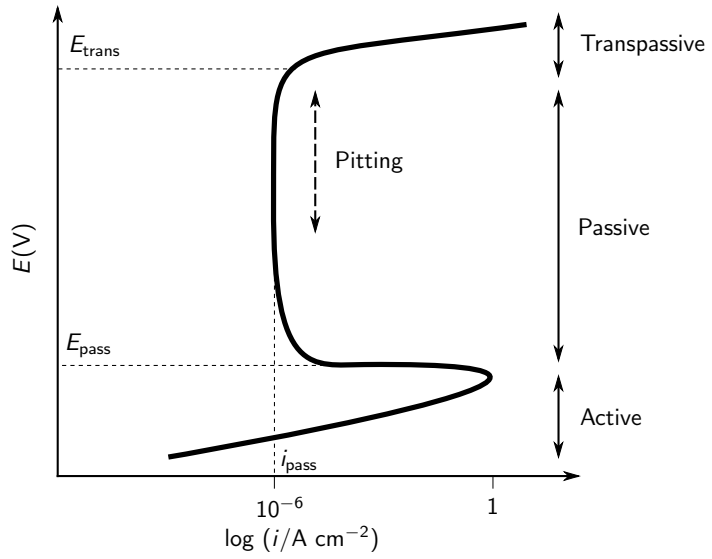

Figure 1-1: Example polarization curve of corrosion current as a function of electrode potential indicating the onset of passivity (i.e. drop in corrosion rate/current) at E_{pass} and a subsequent increase in current at E_{trans}, when the passive film fails due to localized degradation.

vides passivity to the metal until $E = E_{trans}$, when the thermodynamic driving force for corrosion is very large and can overcome the protection offered by the thin passive film.

Even within the region of passivity, the protection offered by the passive film extends only as long as the passive film is stable and does not suffer localized damage due to mechanical or electrochemical processes. Such localized damage, called pitting, can lead to concentrated damage characterized by extremely rapid dissolution of the passive film and the underlying metal.

Over several decades, considerable research and expense [3] has been devoted to corrosion mitigation strategies and a large body of literature has emerged on understanding the kinetics of film formation and propensity for local degradation as a function of macroscopic environmental variables (temperature, concentration of various ionic species and corrosion inhibitors, fluid flow rates etc.). However, for a truly predictive description of the corrosion process, such empirical kinetic data from the field must be paired with details about mechanisms occurring in the bulk and surface of the passive film. Such micro- and nano-scale mechanistic explanations for the growth and breakdown of these films have become more common chiefly due to the increasing resolution and accuracy of characterization and analytical experimental tools for these enormously complicated environmental conditions. This atomic-scale understanding of fundamental mechanism has, in turn, vastly improved the accuracy and applicability of models for predicting corrosion rates and corrosion damage. Continuing in this direction, in this thesis, we investigate the simple hypothesis that we can, through a theoretical understanding of the atomic mechanisms of film growth and breakdown, collectively model the behavior and passivity of the macroscopic passive film. Such a bottom-up approach of modeling kinetically rate-limiting unit reactions such as mass transport by diffusion, surface reactions like oxidation, reduction and dissolution etc. on different length- and time-scales can provide a more universal mechanistically-grounded framework for general passive films that can describe their behavior of films in harsh environments, thus enabling better corrosion prediction and potentially even the design of more robust materials. In the rest of this chapter, as well as in subsequent chapters, we will describe the challenges and unknown metrics involved in such a bottom-up description of passive

film behavior for the case of iron-sulfide passive films formed during the 'sour' corrosion of steel, and highlight the results from the computational investigation into the thermodynamics and kinetics of such unit processes and conclude with a discussion of the multiscale passive film modeling framework that attempts to address the original hypothesis.

1.2 Sour corrosion and iron sulfide passive films – Motivation and challenges

The oxidation (i.e. corrosion) of steel surfaces by H_2S molecules leading to the formation of iron sulfide passive films is a serious concern in the oil and gas industry, where this process detrimentally affects the lifetime of undersea pipelines and through localized pitting increases the potential risk of failure of the pipeline leading to spills and other accidents. The investigation of iron sulfide passive films is important not only because the oil and gas industry constitutes the majority of primary power production now and for the foreseeable future, but also because the remainder of the world's oil reserves are located in fields that contain significantly higher sulfur content. As more easily accessible oil resources are exhausted and fossil fuel extraction moves into more demanding temperature and pressure regimes (the so-called HPHT and Ultra HPHT regimes in Figure 1-2), it becomes increasingly important to understand material behavior and predict material lifetimes in these aggressive conditions.

However, despite seven decades of investigations on iron sulfide corrosion products, several fundamental questions remain unanswered about the mechanism of the sour corrosion process and there is as-yet no consensus on the extent of protectiveness conferred by the passive layer [4]. The iron-sulfur reaction system is of broader interest outside the corrosion community, especially to biologists for its relevance to the origin of life, to geologists for its relevance to the subterranean composition of earth and to astronomers for its relevance to meteorite chemistry. A comprehensive review [5] of information from all these disciplines provides some insight into the solution- and solid-state-chemistry of iron sulfide formation, growth and breakdown. Below, we list the know details of mechanisms involved in the growth of iron-sulfide films during sour corrosion.

1. **Reaction with sulfur and formation of mackinawite**: The very first process that occurs when a steel surface is places in contact with a H_2S-containing environment is the formation of a very thin film of metastable mackinawite on the surface of the steel. This few-nm thick layer is effective in retarding the rate of metal loss primarily by preventing contact between the metal and the sulfidizing environment. In contrast to oxide and carbonate films that form partly by precipitation, mackinawite films are formed by a solid-state reaction between the steel surface and H_2S, and are therefore compact and adherent, offering significantly better corrosion protection than oxide or carbonate scales [4, 6, 7]. While there is significant disagreement on the crystal structure, grain size of this mackinawite layer, it is also known to be highly defective and often contains foreign interstitial atoms and electrolyte molecules in the interlaminar region of the crystal structure.

2. **Mechanical breakdown of the mackinawite layer and initiation of local degradation**: The mackinawite passive layer remains protective as long as it is coherent and does not mechanically degrade [8]. However, at longer exposures (or equivalently at higher corrosion currents), localized regions of the mackinawite film undergo spallation, leading to the formation of discontinuities in the passive film and exposes the metal underneath to the corrosive environment. This exposed

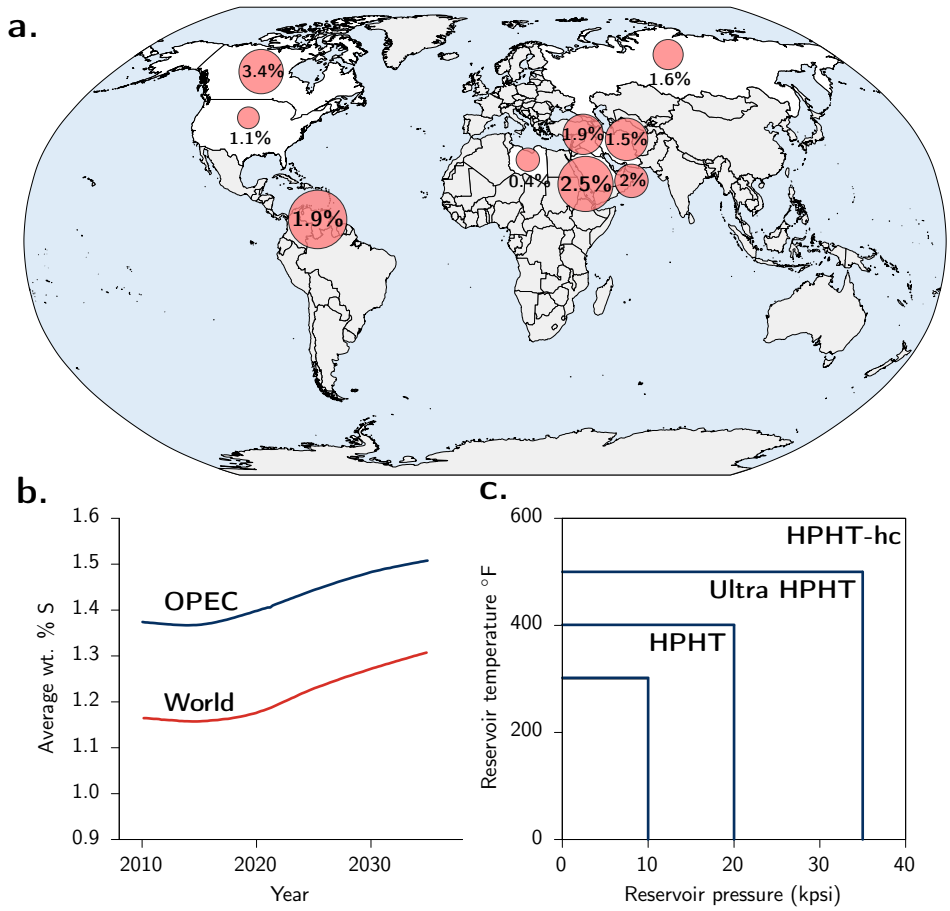

Figure 1-2: (Top) A summary of countries with the largest proven oil reserves as of 2015 along with an estimate of the sulfur content (in wt %) of the fossil fuel. The size of the markers is proportional to the estimated quantity of available reserves. (Left) An estimate of the average sulfur content of oil produced globally and by the Organization of the Petroleum Exporting Countries (OPEC). Both trends point towards an increasing sulfur content in the global supply of oil in the coming decades. (Right) Different temperature and pressure regimes of oil exploration as defined by Schlumberger Ltd.

region can undergo further repassivation due to the formation of another layer of mackinawite. Such a continuous cycle of growth, degradation and repassivation leads to the formation of a bi-layer passive film with a very thin inner (i.e. closer to the meal surface) layer of compact mackinawite and a significantly thicker layer of non-compact exfoliated mackinawite [9]. The passivity of this complex corrosion film is dependent on a variety of factors including the diffusivity of ions through the porous exfoliated layers and other environmental conditions that affect the rate of dissolution of the non-compact passive layer (like pH, fluid flow rate, temperature etc.) [10].

3. **Pit initiation**: Repassivation of the exposed metal surface formed after mackinawite exfoliation is not guaranteed, especially in very aggressive corrosion conditions. The small region of exposed metal is usually more anodic than the surrounding surface of the conducting mackinawite film. This creates a couple between a small anode and a large cathode causing extremely high anodic current densities and very rapid dissolution of the exposed metal. If coupled with the presence of a capping porous layer and other aggressive ions like Cl^- and hydrolysis, this rapid metal dissolution can result in unfavorable geometries for autocatalytic pit growth. It is not surprising that *ex situ* investigation of pitted regions reveals the presence of porous capping FeS layers.

4. **Nucleation of other FeS phases and evolution of film microstructure**: Continued corrosion in more sulfur-rich environments results in the phase transformation of the metastable outer mackinawite layers into more thermodynamically stable phases like pyrrhotite ($Fe_{1+x}S$) and pyrite (FeS_2) [11]. The diffusion of sulfur through the passive film results in a gradient of sulfur chemical potential in the film which leads to a distinct multi-layered microstructure containing the most iron-rich phase, mackinawite closer to the metal surface and the most sulfur rich phase, pyrite closer to the environment. This multiphase corrosion film has a significantly different stability and passivity than the single-phase mackinawite film because pyrrhotite and pyrite are compact (i.e. not layered) phases with greater mechanical stability and slower dissolution rates [12]. Therefore, the passivity controlling rate-limiting processes for these two phases are bulk diffusion of ions through the film and nano-pit initiation due to localized dissolution on the surface of the film.

Phase	Formula	Structure	Space Group	Stability*	Comments
Amorphous Iron sulfide	FeS_m	Amorphous or nanocrystalline	NA	MS	Exact crystal structure unknown
Mackinawite	$Fe_{1+x}S$	Tetragonal/2D	$P4/nmm$	MS	First Fe-S phase to form
Cubic FeS	FeS	Cubic	$F\bar{4}3m$	MS	Metastable to other phases. Not naturally observed.
Troilite	FeS	Hexagonal	$P\bar{6}2c$	TDS	End member of pyrrhotite family
Pyrrhotite	$Fe_{1-x}S$	Hexagonal	$P6/mmc$	TDS	Off-stoichiometry due to Fe vacancies
Greigite	Fe_3S_4	Cubic	$Fd3m$	MS	Fe ions exist both in the +2 and +3 oxidation states
Pyrite	FeS_2	Cubic	$Pa3$	TDS	Semiconducting. Line compound
Marcasite	FeS_2	Orthorhombic	$Pnnm$	MS	Metastable to pyrite. Found in hydrothermal systems

Table 1.1: Stable and metastable iron sulfide phases

* MS = Metastable and TDS = Thermodynamically stable

Despite consensus on this macroscale mechanistic picture, several important questions about the kinetics of film growth and about the mechanism of local damage on multiphase sour films remain to be addressed before a more predictive multiscale model of the sour passive film can be developed. Specifically,

1. Why is local delamination and degradation of mackinawite facile? Understanding the mechanism and kinetics of the exfoliation process can help quantify the passivity of the mackinawite film by understanding the time required for delamination.
2. What governs the kinetics of diffusion-driven film growth in the pyrrhotite phase? How do the numerous phase transformation and varying stoichiometry of the different pyrrhotite polytypes affect the film growth rate?
3. Corrosion films are not monolithic structures with pristine surfaces. How does the presence of surface imperfections like point defects, kinks and ledges as well as other adsorbed reactant and electrolyte molecules affect the rate of the sulfidation reaction and therefore the rate of sulfur uptake?
4. What is the mechanism for the initiation of pitting on the more compact FeS phases like pyrrhotite and pyrite?

Addressing these questions and subsequent quantitative modeling of these atomic-scale mechanisms in the passive film can help answer the most relevant outstanding challenges, specifically, what are the macroscopic environmental conditions at which each of these unit processes dominates the kinetics of growth and breakdown, and ultimately, the passivity of the multiphase FeS_x film (Figure 1-3). We briefly describe the approach taken to addressing these questions in the next section.

1.3 Thesis goals, outline and organization

The questions in the previous section provide the motivation for the work contained in this thesis. In this work, we have attempted to answer these question by quantifying the thermodynamics (formation energies, electronic structure etc.) and kinetics (mostly activation barriers and reaction rates) of fundamental structural units of the passive film (defect-free unit cells, charged and uncharged point defects and surfaces) for the mechanisms described in Section 1.2. We rely on computational methods like Density Functional theory (DFT), Climbing Image Nudged Elastic Band (CI-NEB), Cluster Expansion (CE) and Molecular Dynamics (MD) and kinetic Monte Carlo (kMC) to understand unit processes in such mechanisms in isolation and this provides a significantly better picture of the intrinsic rates of individual unit processes than can be obtained from experimental or field data, where the rates of such unit processes are inextricably tied with others occurring at different length or time scales. In addition, this focused *ab initio* quantification of unit processes kinetics allows us to focus our attention on different unit processes only on the relevant phases in different regions of the composite multiphase passive film. For example, we study the sulfidation unit process only on the pyrite phase, which, as the most sulfur-rich phase, is expect to be in contact with the sulfidizing environment and therefore most relevant for the sulfidation unit process. Similar judgments are made with regard to other unit processes described in this thesis.

In addition to *ab initio* quantification the thermodynamic feasibility and kinetic rates of different unit processes, in the second part of the thesis, we also develop a multiscale modeling framework that incorporates the calculated kinetics of different unit processes and mechanisms, which can help address the original hypothesis – That through an

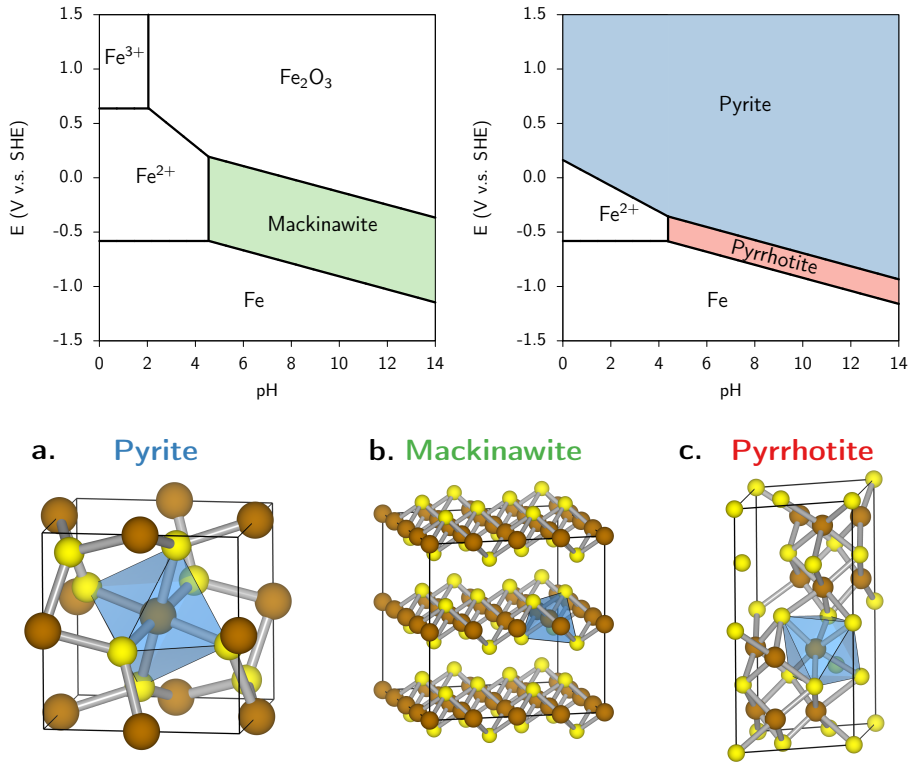

Figure 1-3: (Top left) The Pourbaix diagram for the metastable phases in the iron-sulfur corrosion system and (Top Right) for the stable phases in the iron-sulfur corrosion system determine the three FeS_x phases considered in this thesis. (Bottom) The crystal structure of the pyrite, mackinawite and pyrrhotite phases showing the bonding between the Fe (brown) and S (yellow) atoms along with one representative cation-centered polyhedron describing the ligand structure around the transition metal ion.

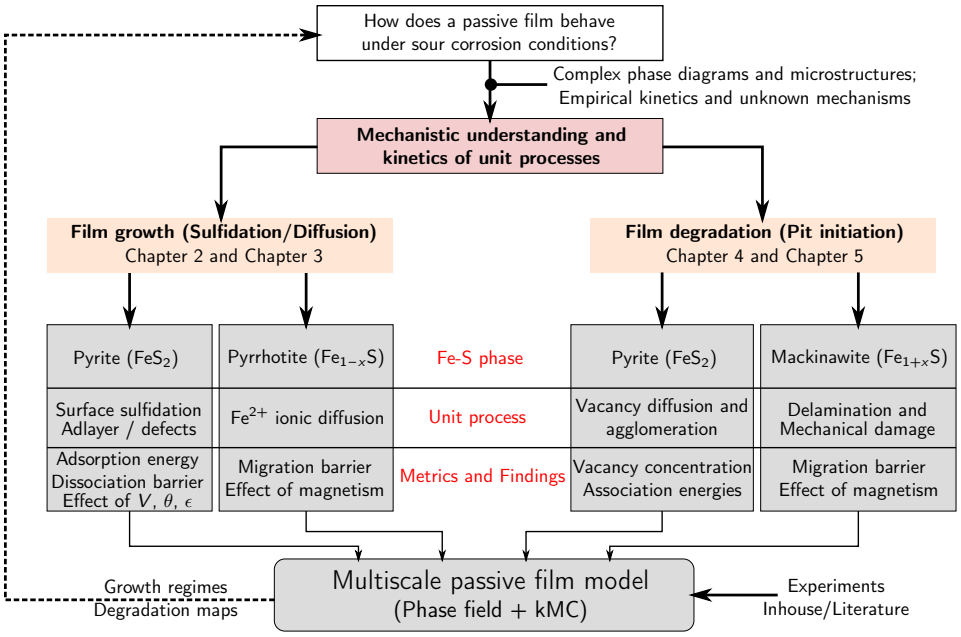

Figure 1-4: Overview of the outline of this thesis describing the relation between individual unit processes and the multiscale model used to address the primary question about the behavior of passive films under sour corrosion conditions. The approach taken in the thesis is identified in red, the organization of the thesis is in orange and the primary scientific contributions are indicated in gray.

accurate characterization of the fundamental unit processes and collective behavior, we can observe emergent phenomena that define the complex growth and passivity of the overall iron sulfide film.

Figure 1-4 shows the interrelations between the individual studies on unit process mechanisms and also shows their relation to the proposed modeling framework which will be used to answer questions about the reactivity, protectiveness and passivity of the FeS_x film.

1.3.1 Thesis organization

The rest of the thesis is dedicated to describing in detail the calculations and results of the different unit processes as well as the multiscale modeling framework. We briefly describe the contents of the subsequent chapters below by way of an outline.

Chapter 2 on the "Reactivity of the FeS_2 (100) surface" deals with the first unit process responsible for iron sulfide film growth – sulfidation by the gaseous or aqueous environment. In this chapter, we attempt to understand the effect of defect, electronic and adlayer structure at the pyrite surface on the rate of the sulfidation reaction (which is rate-limited by adsorption and dissociation of H_2S molecules). In doing so, we also provide an estimate for the correction required to align the results of highly idealized DFT calculations to more realistic experimental or field conditions, where surfaces contain point and extended defects, adlayer interactions and surface charge and strain.

Chapter 3 on "Fe^{2+} diffusion in magnetic pyrrhotite" also addresses the growth of the FeS_x passive film, but deals with the kinetics and mechanisms of diffusion-limited growth of the pyrrhotite phase. The chapter is devoted to one question – What are the ionic (i.e. Fe^{2+}) migration barriers in the pyrrhotite phase at intermediate temperatures ($\approx$ 300 °C). Specifically, we identify how the extremely complicated phase

relations in the pyrrhotite-region of the iron-sulfur phase diagram (See Figure 3-1) and the potential structural and magnetic phase transitions affect the migration barrier for ionic diffusion.

Chapter 4 on "Dynamics of point defect formation, clustering and pit initiation on the pyrite surface" explores the first unit process associated with the degradation of the passive film, namely the initiation of nanopits on the surface of the pyrite phase that can serve as precursors to more macroscale metastable pits. In this chapter, we provide a quantified mechanism for the nucleation of such nano-cavities centered around the collective behavior of surface Fe- and S-vacancies. The observation of such nano-cavity formation supports existing atomistic models like the point defect model for the initiation of local pitting. Further, by quantifying the activation barriers involved in such vacancy dynamics processes, we can estimate a timescale for the initiation of nano-pit sites on the surface and thus provide an understanding of the passivity of the FeS_x film

Chapter 5 on "Hydrogen induced delamination of mackinawite ($Fe_{1+x}S$)" describes with the local degradation of the film induced by debonding at the metal-film interface. Specifically, we focus on the mechanical toughness of the mackinawite phase in contact with the metal and identify hydrogen embrittlement as a mechanism for the facile degradation and poor passivity of the mackinawite corrosion film. The quantification of interlaminar interstitial dynamics also provides suggestions for new exfoliation techniques for the synthesis of monolayer 2D TMDCs.

Chapter 6 on the "Multiscale Passive Film Model (MPFM)" concludes the thesis with a description of the development and use of a multiscale modeling framework using coupled atomistic and mesoscale models to describe the growth and breakdown of sour corrosion passive films. Using results obtained in the previous chapters, we model, at the atomic scale, processes involved in the growth and breakdown of these films and through coupling to a mesoscale model, observe the impact of these processes and mechanisms on the overall passivity and reactivity of the FeS_x film.

Chapter 2

Reactivity of the FeS_2 (100) surface

2.1 Overview

In this chapter, we investigate the reaction energies and activation barriers associates with the adsorption and dissociation of H_2S molecules on the (100) surface of pyrite, FeS_2, a model semiconducting passive film using a combination of Density Functional Theory, Molecular Dynamics and Cluster Expansion. These techniques allow us to model a very accurate representation of the surface of the FeS_2 passive layer in corrosive conditions by including the effect it surface point defects, surface charge state and the presence of adsorbed molecules and thereby helps overcome the so-called 'pressure gap' associated with *ab initio* thermodynamic calculations. The primary results from these studies are threefold. First, these studies demonstrate that surface point defects introduce defect states within the band gap of the surface electronic structure leading to a more facile charge transfer at the film-environment interface. Therefore, reactivity at these defect sites is characterized by a greater H_2S adsorption energy and a significantly reduced barrier for H_2S dissociation leading to a greater effective sulfidation rate and a more reactive passive film surface. Further, through a rigorous statistical analysis of the thermodynamics of the FeS_2 surface at different coverage value we quantify the effective repulsive interaction between adsorbate molecules with the implication that FeS_2 surfaces in real corrosion conditions involve weaker H_2S adsorption energies and greater H_2S dissociation barriers than zero-pressure DFT calculations would suggest. Finally, another important factor for the case of sour corrosion is the impact of surface charge state in the reactivity/passivity of the passive film. Through combined MD, AIMD and DFT calculations, we identify that the electrode potential primarily affects the position of the Fermi level of the pyrite crystal relative the valence and conduction bands. The impact of this change of the electronic structure on the reactivity of the surface is rationalized using the d-band center theory. Other effects related to surface charging, such as the development of an intense electric field in the electrical double layer and the subsequent polarization of the water molecules of the double layer are only secondary effects and do not affect the adsorption energy or dissociation barrier of relatively non-polar H_2S molecules. Taken together, these three inter-related studies quantify corrections required to extend *ab initio* thermodynamics of surfaces from the zero-temperature zero-pressure DFT domain to more realistic representation of surface structures. More specifically, for the case of sour corrosion, it enables us to calculate the reactivity of an iron sulfide surface under realistic corrosion conditions, which is

required for accurately estimating the growth rates and protectiveness of iron sulfides in a multiscale model as discussed in Chapter 6.

2.2 Background and Motivation

As described in Chapter 1 of this thesis, one of the key unit processes in the nucleation and growth of the passive sour-corrosion barrier layer is the incorporation of sulfur into the growing film from the H_2S-rich environment through the cathodic half-reactions $H_2S_{(g)} \rightleftharpoons S^{2-} + 2H^+$ and $2H^+ + 2e^- \rightleftharpoons H_{2(g)}$, where electrons are transferred form the semiconducting FeS_2 layer to reduce the reactant H_2S molecules. Therefore, a predictive model for the growth and breakdown of the iron sulfide film (Chapter 6) must necessarily include an accurate quantification of the sulfidation rates. Specifically, we need to be able to quantify the reaction energies and reaction barriers for the unit processes involved in the sulfidation reaction, namely H_2S adsorption and H_2S dissociation, on realistic iron sulfide surfaces. However, standard DFT calculations of the reaction energies and activation barriers on ionic surfaces impose restrictions on the model system (such as 0 pressure, pristine defect-free surface etc.) that are not representative of a realistic surfaces in corrosion conditions. Therefore, a truly predictive modeling of the passive film behavior requires not only quantification of reaction enthalpies and activation barriers but also an understanding of how factors like defects, surface coverage and charge density (or equivalently surface potential) affect the calculated reaction parameters.

2.3 Chapter goals and layout

In this context, the primary aim of this chapter is to address this fundamental question: "*What is the reactivity of* FeS_2 *surfaces in realistic corrosive conditions?*" which is of broad interest to electrochemists not only in the corrosion community [13], but also in fields such as biogeochemistry [14], battery anodes and photovoltaics. To tackle this broad question, we carry out three individual studies, each dealing with a single aspect (e.g. surface charge, surface coverage) of the passive film surface. This chapter is divided into five sections, as summarized below:

1. **Electronic structure of ionic surface and implications for charge transfer and surface reactivity** describes the fundamental theory of the electronic structure of surfaces and relationships between reactivity metrics and the surface electronic structure. This sections provides context to understand the results from the subsequent studies.

2. **Surface point defects and reactivity of defective surfaces** details the defect chemistry of FeS_2 (100) surface and demonstrates how the presence of defect states in the surface electronic structure correspond to a surface that is more active towards H_2S adsorption and dissociation.

3. **Surface reactivity at finite surface coverage** describes the *ab initio* and statistical methods used to quantify interactions between multiple adsorbates on the FeS_2 (100) surface and thereby extract the effective reactivity of the surface as a function of the surface coverage.

4. **Reactivity of charged semiconductor surfaces** explores the variation of the surface Fermi level (and therefore the electronic state occupancy) on the applied electrode potential and identifies how this variation in the surface electronic structure

affects the important metrics of reactivity, namely H_2S adsorption energy and H_2S dissociation barrier

5. The final section, **Outcomes and Final Work**, summarizes the previous studies to provide a unified picture of the reactivity of realistic FeS_2 surfaces and their impact on the multiscale modeling of sour corrosion passive films and also discusses prospective studies that can extend the methodologies described in this chapter to other material systems.

2.4 Electronic structure of ionic surface and implications for charge transfer and surface reactivity

The kinetics of the sulfidation reaction depends upon the rate of unit processes like H_2S adsorption, charge transfer between FeS_2 and H_2S and H_2S dissociation. In this section, we briefly review existing literature on the thermodynamics of these unit reactions as well as the physics associated with charge transfer and relations between the surface reactivity and electronic structure in an effort to provide required context to interpret the results from this chapter. For a more extensive analysis of these topics, we refer interested readers to the literature cited in this section as well as to the work of Marcus [15], which covers charge transfer between molecular adsorbates and semiconducting surfaces in corrosion conditions.

2.4.1 Adsorption and dissociation of molecular reactants – Sabatier principle and BEP relations

The sulfidation reaction is complex involving several unit processes, notably H_2S adsorption and surface diffusion of H_2S molecules and reaction fragments and the eventual desorption of reaction products. The overall reaction rate of such a surface reaction achieves a maximum when the rate of reactant adsorption and activation equals the rate of desorption of product molecules from the reactive surface. This gives rise to the well-known volcano plot of catalytic reaction rate against energy of adsorption of reactant molecules. A surface reaction with low reactant adsorption rates (indicative of weak adsorption energies) is limited by the surface concentration of activated reactant molecules, while a reaction with low product desorption rates (corresponding to strong adsorption energies) is rate-limited by the low concentration of free active sites on the catalyst surface. This principle, called the Sabatier principle [16], indicates that there is an intermediate value for adsorption energy at which surface activity is maximum, with the surface activity falling off on either side of the adsorption energy. And this opens the door for tailoring surfaces for high reactivity by engineering the adsorption energy of the reactant.

In addition, the harmonic approximation for interfacial charge transfer, coupled with the transition state theory implies the existence of a relation between the activation barriers for dissociation of simple adsorbates like H_2S and their adsorption energy. The existence of such relations, called Brønsted-Evans-Polanyi (BEP) scaling relationships [17, 18], as well as their universal applicability has been verified for a variety of adsorbates on several surfaces [19].

The Sabatier relation and the BEP relations, taken together, imply that the rate of unit processes along a complex surface reaction pathway like sulfidation can be understood through the adsorption energy of reactant molecules on the catalyst surface [20, 21].

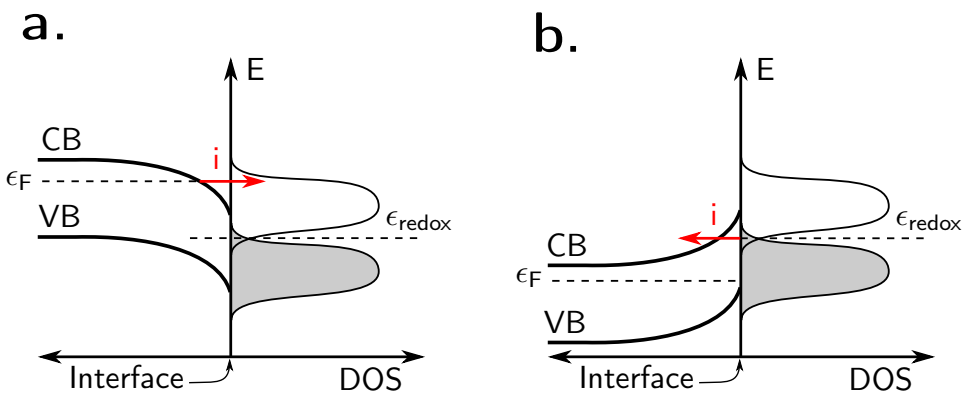

Figure 2-1: Schematics of the interfacial electronic structure during charge transfer via (a) Direct transfer and (b) Tunneling transfer. The two mechanisms differ in the position of the surface Fermi level, ϵ_F, relative to the redox level of the adsorbed molecule, ϵ_{redox}

Therefore, they constitute the theoretical basis for the engineering of surface reactivity based on altering the adsorption energy of reactants through straining/doping etc.

2.4.2 Surface electronic structure and reaction energies and barriers – d-band theory

In addition to semi-empirical relationships between adsorbate energies and reaction rates discussed in the previous section another important class of relationships is the relationship between the electronic structure of the surface and the reactivity of the surface. For electrochemical reactions, the reactivity of such a surface depends on the rate at which charge transfer occurs between the rigid energy levels (specifically the Fermi level) of the passive film and the occupied or unoccupied energy levels of the adsorbed H_2S molecule (which are Gaussian-like due to the continually-reconfiguring solvation shell around the molecule)

Adiabatic charge transfer at the interface is horizontal, i.e. occurs along the same energy level and occurs in both directions, anodic (e^- transfer from the H_2S to the metal) and cathodic (e^- transfer from the metal to H_2S). This type of charge transfer can occur through one of two mechanisms, direct transfer and tunneling transfer.

1. Direct transfer: Direct transfer (see Figure 2-1a) from the semiconductor requires filled states in the CB to be higher in energy, i.e. overlap, than the empty states (oxidized species) of the redox couple. The more negative the electrode potential is in this scenario, the greater the overlap of electronic states and charge transfer can increase exponentially. This is the fundamental explanation behind the well-known linear Tafel slope on a plot of $\ln i$ vs. overpotential, η for corrosion systems.

2. Tunneling transfer: Tunneling transfer (see Figure 2-1b) refers to quantum tunneling of electrons through the space-charge layer. Thus, the narrower the space charge region at the interface, the smaller the tunneling distance d_T and the greater the probability of tunneling T

$$T = \frac{16E(V_0 - E)}{V_0^2} \exp\left[-\frac{2\kappa d_T}{h} \right]$$

where the coefficient κ describes the dependence on barrier height $\kappa = \sqrt{2m^*(V_0 - E)}$,

where V_0 is the total energy barrier, E is the energy level of the tunneling electron and m^* is the reduced electron mass. Charge transfer at the passive layer surface is therefore proportional to the density of occupied states of the redox system ρ_{Red} and that of the empty states within the passive layer CB, ρ_{Ox}. By integrating over all energies above E_F where overlapping occupied and empty states may interfere, the tunneling exchange current i_+ is therefore

$$i_+ = -F \int T \cdot \rho_{\text{Ox}} \cdot \rho_{\text{Red}} \, \mathrm{d}E$$

Several theoretical models have been proposed to explain and predict the activity of catalytic surfaces based on descriptors of electronic structure such as density of states at the Fermi level [22, 23], the 'softness' or mutability of the electronic structure [24] and the number of dangling bonds [25] etc. While an exhaustive discussion of the merits and applicability of each model is infeasible, one particular theory bears mention due to its applicability for the reactivity of transition metals and their compounds: the d-band theory [26].

Within the d-band theory framework, the adsorption energy of a reactant molecule (which is defined as the strength of the bond formed between the d-band of the transition metal surface and the electronic energy levels of the adsorbate) is determined by the relative filling of the bonding and antibonding energy levels formed between the transition metal and the adsorbate. This bond is strongest if all the bonding states and none of the antibonding states are occupied, which is only possible if the d-band is half-filled, with the Fermi-level (of the surface-adsorbate systems) overlapping with the center of mass of the transition metal d-band. If the Fermi-level is below the d-band center, the resulting bonding state is only partially occupied and if the Fermi-level lies above the d-band center, then some of the anti-bonding states are also occupied. In both cases, the resulting bond between the adsorbate and the transition metal surface is weaker than it would be if the d-band was half filled. This dependence gives rise to the characteristic volcano plot of surface activity vs d-band filling, which holds not only for pure transition metals, but also for also for the surfaces of strained transition metals [27, 28], alloys of transition metals [29], as well as compounds of transition metals like oxides [30, 31], sulfides [30, 32] and nitrides [30].

As we show in section 2.6, the adsorption of H_2S molecules on the (100) surface of H_2S also follows this simple DBT model providing a theoretical link between the surface activity and the electronic structure and allows us to relate the H_2S adsorption energy and consequently the surface activity to a metric of the electronic structure of the surface (namely $\epsilon_F - E_{DBC}$; See Figure 2-2)

Given this importance of the Fermi level position relative to the valence and conduction bands on the surface, it is critical to understand the impact of additional energy levels introduced at the surface due to crystal termination or intrinsic point defects or extrinsic dopants on this electronic structure descriptor and the surface reactivity.

1. *Intrinsic surface states:* The abrupt discontinuation of periodic potential at semiconductor surfaces can impose severe perturbations to the crystal's electronic structure. Unless a surface reconstructs to remove dangling bonds and autopassivate, the topmost atoms' crystalline orbitals destabilize in the direction of their free atom orbital character and energy. Binary semiconductors like FeS_2, whose (100) surface does not reconstruct, are predicted from ligand field models [33] and DFT calculations [34–36] to have two associated intrinsic surface states: one for the anion dangling bonds and one for cations.

2. *Extrinsic surface states:* in reality these states are localized at defects such as anion or cation vacancies on the surface steps, kinks, dislocations or impurities [37, 38]. However there is evidence to suggest that these types of defects (as well as step

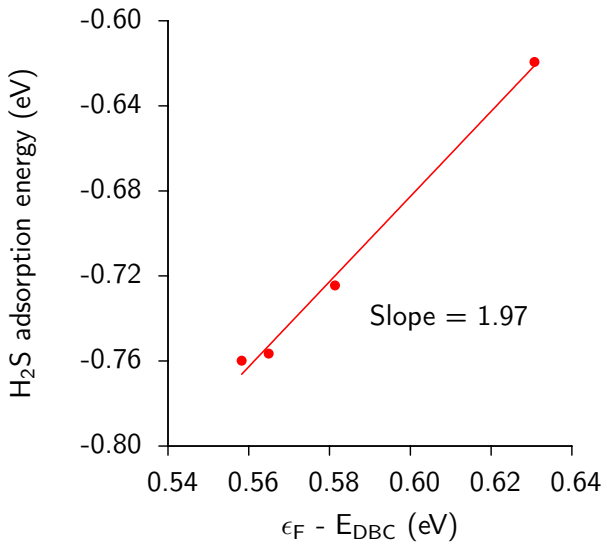

Figure 2-2: The linear variation of the adsorption energy of the H_2S molecule on the metric, $E_{DBC} - \epsilon_F$ of the surface electronic structure indicates that this adsorption system follows the d-band theory model.

edges or intersecting dislocations) can affect the surface electronic structure over nanometer distances.

2.5 Electronic structure and reactivity of defect-free and defective FeS_2 phases

The crystal structure of FeS_2 (space group P*a3*) comprises two interpenetrating cation (Fe^{2+}) and anion ($S_2{}^{2-}$) face centered cubic sublattices, the latter of which is made up of S_2 dimers aligned along the cube diagonal direction <111>. Pyrite is a compound, *d*-band semiconductor with an electronic structure that can be qualitatively understood with the aid of a ligand field model [33]. Each Fe^{2+} ion in the bulk is octahedrally coordinated by $S_2{}^{2-}$ ions (symmetry group O_h), creating a strong ligand field that splits the metal *d* states into non-bonding, triply degenerate Fe 3*d* t_{2g} states (d_{xy}, d_{yz} and d_{x2-y2}) at the top of the valence band (VB). The conduction band (CB) minimum consists of doubly degenerate Fe 3*d* e_g states (d_{z2} and d_{x2-y2}) hybridized with S $pp\sigma^*$ orbitals. An indirect, bulk band gap E_g of 0.83-1.01 eV has been measured in synthetic FeS_2 using various optical [39, 40], photoconductivity [41, 42] and x-ray absorption/emission spectroscopy studies [43].

Before we discuss the energies of adsorption and dissociation of H_2S on defective pyrite surfaces, we identify the type and concentration of intrinsic point defects that are possible in the FeS_2 crystal structure and their effect on the pyrite electronic structure.

2.5.1 Neutral and charged defects in bulk pyrite

The intrinsic point defects that were investigated in this study include both Fe and S vacancies of different charge states, including neutral, singly charged and doubly charged states. In the Kröger-Vink notation, they are denoted as $V_{Fe}^{\times}$, $V_{Fe}^{'}$, $V_{Fe}^{''}$, $V_S^{\times}$, $V_S^{\bullet}$ and $V_S^{\bullet\bullet}$, respectively, for Fe and S. Previous studies indicate relatively higher formation

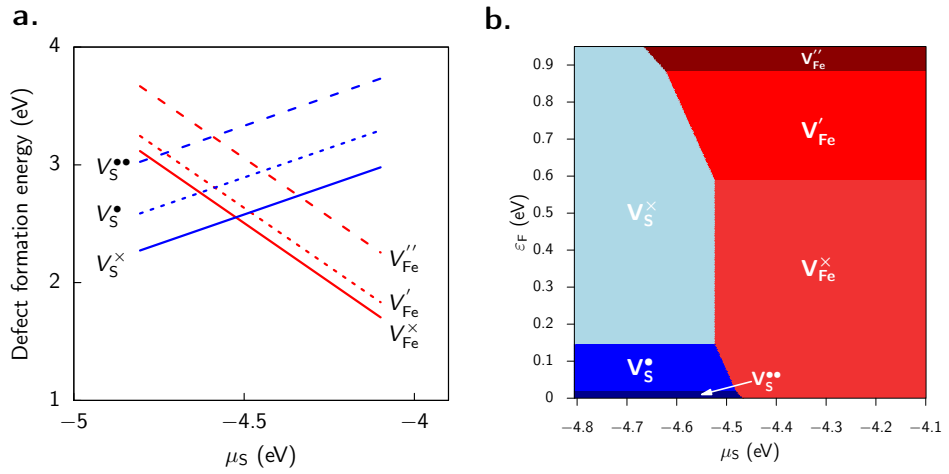

Figure 2-3: (a) Formation energies of differently charged Fe and S vacancies as a function of μ_S at ϵ_F = 0.46 eV. (In our calculations, the Fermi level ϵ_F was found constant at 0.46 eV above the VBM for all allowed values of μ_S.) (b) Predominance map depicting the regions in the $\mu_S - \epsilon_F$ space where the different types of vacancies have the least formation energy, and thus, the highest dominance.

energies for intrinsic interstitial defects in pyrite [44], and hence they were not included in the present study.

As shown in Figure 2-3(a), the formation energies of intrinsic vacancies are too large to induce a large off-stoichiometry at equilibrium, as also indicated computationally in Refs. [44] and [45]. Charge carriers in a semiconductor can be produced either in pairs by excitation of electrons across the band gap, or singly as a co-product during the formation of a charged vacancy. In pyrite, the formation energies of charged vacancies are larger than 1.7 eV (Figure 2-3(a)), while the band gap is only 0.95 eV. Therefore, the number of charge carriers (electrons or holes) created during the formation of charged vacancies is expected to be much smaller than the number of charge carriers created by excitation across the smaller band gap. Hence, a pure pyrite crystal (with no extrinsic defects) is expected to be an intrinsic conductor and does not display any *p*-type or *n*-type conductivity. Among the intrinsic vacancies, the neutral vacancies $V_{Fe}^{\times}$ and $V_S^{\times}$ are the most stable defects for much of the ϵ_F-μ_S space in bulk pyrite (Figure 2-3(b)). This is not the case with point defects in materials with a much larger band gap than that of FeS_2, such as Al_2O_3 (E_g = 8.7eV), for which the highest possible charge state for the given vacancy is the most stable charge state for a wide range of ϵ_F [46].

Note that the Fermi level, ϵ_F, is not an independent variable. Instead, the value of the Fermi level adjusts itself to ensure that the defective crystal is charge neutral. Using the formation energies reported for the entire range of μ_S and ϵ_F for pyrite here, the relative concentration of the different vacancies was calculated while maintaining self-consistency of the Fermi-level, after Sun *et al.* [44], to obtain the Brouwer diagram shown in Figure 2-4. In our calculations, the Fermi level ϵ_F was found constant at 0.46 eV above the VBM for all allowed values of μ_S.

Despite the large formation energies, neutral vacancies are the most abundant point defects of any charge state. Therefore we use these neutral vacancy formation energies to calculate the Schottky defect formation energies. The Schottky defect formation energy compares well with experimental-analytical models which were used to calculate the vacancy formation energy, as shown in Table 2.1.

We also note that the Schottky defect formation energy of 7.66 eV corresponds to the

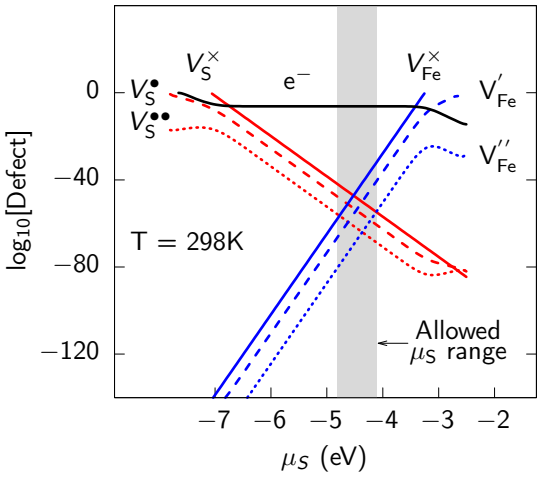

Figure 2-4: Concentration of S and Fe vacancies and electronic charge carriers in pyrite. In the allowed range of sulfur chemical potential, μ_S, pyrite is an intrinsic conductor.

	Fe vacancy (neutral)	**Sulfur vacancy (neutral)**	**Schottky Defect**
This study	1.70 – 3.12 eV	2.97 – 2.27 eV	7.66 eV (non-interacting) 5.07 eV (interacting)
Ref [47] (analytical)	2.54 eV	2.32 eV	7.18 eV
Ref [48] (analytical)	2.18 eV	1.66 eV	5.50 eV
Ref [44] (DFT calculations)	1.8 - 3.3 eV	2.7 - 3.5 eV	8.7 eV

Table 2.1: The large magnitude of vacancy formation energies in bulk pyrite indicate that pyrite is a near-stoichiometric crystal.

creation of 2 S vacancies and 1 Fe vacancy, none of which interact with each other. The energy penalty for the formation of a cluster of 3 neighboring and interacting Fe and S vacancies is found to be lower at 5.07 eV per Schottky defect cluster. This value is more in line with the value predicted by Ref [48], while the non-interacting Schottky defect formation energy is more consistent with the value predicted by Ref [47]. To calculate the vacancy formation energies, Fiechter [47] has used the macroscopic cavity method proposed by Van Vechten [49]. Ellmer *et al.* [48] also have used the general principle outlined by Van Vechten, but have improved the empirical inputs to the macroscopic cavity model to obtain a Schottky defect formation energy of 5.5 eV. These values vary significantly from the value of 0.3 eV per Schottky defect reported by Birkholz *et al.* [50]. The large Schottky defect formation energies reported in this work as well as in Refs. [47, 48], along with the large formation energies for each defect, explain the very small sulfur sub-stoichiometry observed in synthetically prepared pyrite samples [48].

2.5.2 Electronic structure of point defects in bulk pyrite

The electronic properties of pyrite may be strongly influenced by the presence of native defects via a self-doping effect even if present at ppm-concentrations. The location of the defect states due to both the Fe and S neutral vacancies is shown in Figure 2-5.

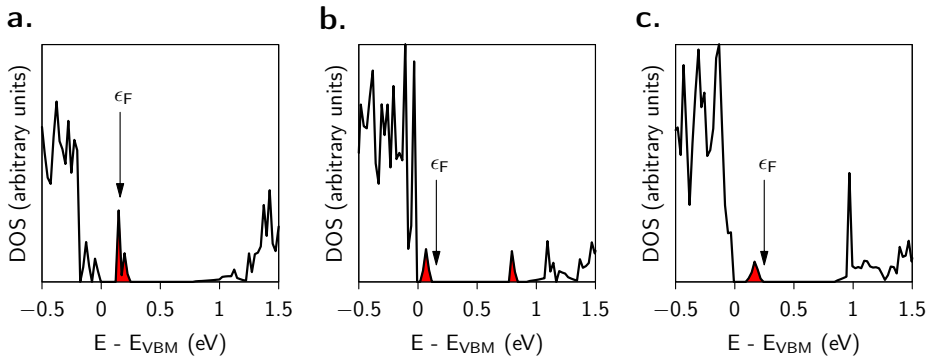

Figure 2-5: Position of neutral defect states (red) in the total density of states (DOS) plots of bulk pyrite due to a) Fe vacancy, b) S vacancy and c) S_2 dimer vacancy.

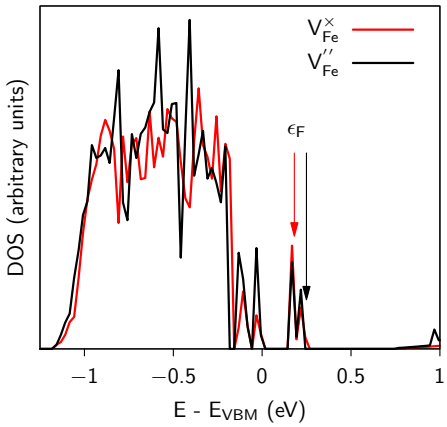

Figure 2-6: Charge state of a given defect changes the Fermi level of the system, but not the total density of states (DOS) – shown here for the neutral and singly charged Fe vacancies.

The defect levels produced by the Fe vacancy in the electronic structure are acceptor-like states in the band gap, created due to the breakage of the Fe-S bond in pyrite. In contrast, a sulfur vacancy creates two distinct defect levels in the band gap. These defect states result from the breakage of two distinct types of bonds: the Fe-S bond, and the S-S dimer bond. If enough of either defect is created, they can cause a change in the position of the Fermi level from near the center of the band gap towards one of the band edges. The Fermi level can also be changed due to the presence of charged defects, some of whose density of states (DOS) does not differ significantly from that of neutral defects except for the location of the Fermi level (See Figure 2-6). This variation of the Fermi level (i.e., state occupancy) can be used as a basis to understand the reactivity of the pyrite crystal using well-established theoretical models like the d-band center theory [51].

2.5.3 Electronic structure of the pyrite (100) surface

Because the pyrite (100) is the surface with the lowest surface energy and is therefore the surface most frequently formed during crystal growth or cleavage, it has been the subject of prior studies related to catalysis [52–54]. As has been found in previous studies [55], the atoms on the (100) surface do not relax appreciably from their bulk-terminated positions. The electronic structure of the (100) surface is expected to be

noticeably different from that of bulk pyrite. Experimental reports that probe the surface band gap on pyrite are scarce, however, they indicate a smaller band gap than 0.95 eV observed in the bulk [56, 57]. Previous first-principles calculations with DFT-GGA without a *U*-correction have shown a surface band gap of 0.16 eV (the corresponding bulk band gap was calculated to be 0.65 eV) [55] and 0.4 eV (vs. 0.87 eV in the bulk) [58]. Recent DFT+*U* calculations with $U = 2$ eV have shown that the direct band gap of the high spin (100) surface is 0.72 eV [36]. We also observe such a band gap reduction at the surface using the Hubbard *U*-corrected DFT model. Using our model, the band gap observed at the surface is 0.55 eV, smaller than our computationally obtained bulk band gap of 0.86 eV. We have validated this theoretically obtained reduction in the band gap on the surface by conducting tunneling spectroscopy measurements on the (100) surface of a synthetically grown sample of pyrite. Our experimentally measured band gap on the surface is 0.34 ± 0.12 eV, as shown on the tunneling spectroscopy plot in Figure 2-7. Both our computational and experimental results consistently demonstrate a significant reduction of the band gap on the (100) surface compared to the pyrite bulk. On the other hand, there are quantitative differences between the measured and computed values of the surface band gap (0.34 eV vs. 0.55 eV, respectively). One possible explanation for this discrepancy may be the fact that it is very challenging to obtain adsorbate- and defect-free pristine pyrite surfaces in experiments. Indeed, for the surface band gap estimate, we modeled the perfect pyrite surfaces without any adsorbed atoms or surface vacancies. As we show from our DFT calculations below, the presence of defects introduces defect states in the surface band gap, and this would lead to an apparent reduction in the observed band gap in the tunneling spectroscopy measurements. Alternatively, the pyrite (100) surface has also been shown to have unit cell-high steps on the surface [57]. These surface steps can lead to a lower surface band gap due to the introduction of defect states at the step edges. Computational uncertainties also contribute to the differences between the experimental and theoretically obtained surface band gap. The *U* parameter used in calculating the surface band gap was benchmarked only using the bulk properties and did not take into account the surface terminations. According to the ligand field model developed by Bronold *et al.* [33], the reduction in the band gap is due to formation of surface states within the bulk band gap that are a result of disturbing the octahedral symmetry around the Fe atom in bulk pyrite. While their model predicts the existence of two discrete surface states inside the bulk band gap, the surface states in the present study are found at the edges of (and remain part of) the valence and the conduction band for all investigated values of the *U* parameter (Figure A-2). This observation of a surface DOS with no discrete surface states (Figure 2-7(b)) inside the band gap is consistent with previous *ab-initio* studies on the (100) surface [59]. This band gap reduction is of interest to corrosion and catalysis studies chiefly because the smaller band gap can aid in electron excitation to the conduction band and its subsequent transfer to an adsorbed reactant on the surface.

2.5.4 Neutral defects on the pyrite (100) surface

The predominance of neutral charge state defects in bulk pyrite provides a motivation for investigating neutral defects on the (100) surface. Another reason for limiting the study to neutral defects is the desire to avoid less accurate DFT calculations involving systems with charged surfaces. The formation energies of both the neutral Fe and S vacancies on the (100) surface are considerably less than in bulk pyrite, as shown in Table 2.2. The lower vacancy formation energy at the surface indicates that the concentration of defects and the corresponding off-stoichiometry at the surface are expected to be higher than in the bulk. However, even these reduced defect formation energies cannot account for the large sulfur sub-stoichiometries observed in previous work [60]. We note that the vacancy formation energies found on pyrite (100) in this work are

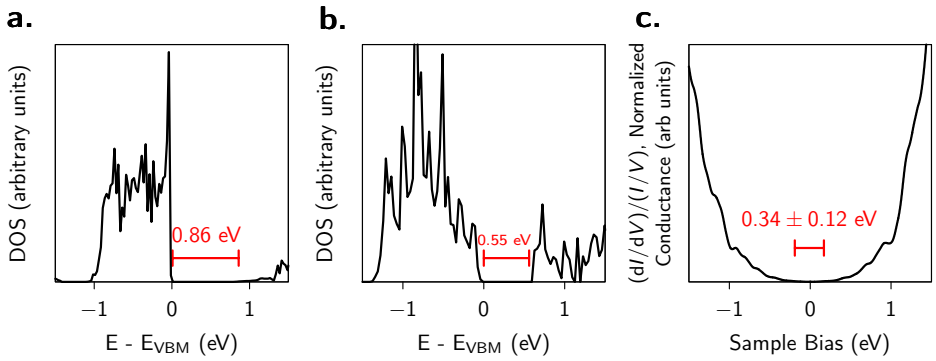

Figure 2-7: Calculated (a,b) and experimental (c) electronic structure (DOS) of the defect-free pyrite bulk (a) and surface (b, c). Both the experiments and calculations show a reduction of the surface band gap compared to the pyrite bulk.

considerably higher than those reported recently by Zhang *et al.* [36]. We think the discrepancy arises because of the different initial spin states of pyrite (100) slab in the two studies. Our relaxed (100) surface is low-spin, in agreement with experiments that report non-magnetism in pyrite nanocrystals [39], and contrary to the net magnetic moment of 4 μ_B on surface Fe ions in ref. [36].

The relatively lower formation energy of Fe vacancies (compared to that of S vacancies) on the surface has been previously reconciled with often-reported sulfur deficiency by demonstrating that most of the experimental observations were conducted on samples prepared in environments that were iron-rich [44]. In our calculations, we found that, in the upper limit of μ_{Fe}, the formation energy of a Fe vacancy was 1.67 eV, which is slightly higher than the calculated formation energy of a S vacancy (1.42 eV) under the same conditions. This difference in formation energies may explain, in part, the often observed S-deficiency rather than Fe-deficiency. Alternatively, naturally observed sulfur deficiency in pyrite may be due to the presence of small amounts of sulfur deficient iron sulfide phases such as pyrrhotites [35]. Substitutional defects, such as oxygen, on sulfur sites in pyrite have previously been shown to have smaller formation energies than native sulfur vacancies [44]. If such substitutional defects have sufficiently low formation free energies under driving chemical potential conditions, they may also contribute to an apparent sulfur deficiency.

Fe vacancy (neutral)	**S vacancy (neutral)**	**Schottky defect**
0.26 – 1.67 eV	1.42 – 2.13 eV	4.51 eV

Table 2.2: The relatively lower formation energy of neutral Fe and S vacancies on the pyrite (100) surface support the presence of a defective surface

The vacancy-induced defect states on the (100) surface of pyrite are similar to those observed in the bulk. However, the twin-defect-state structure observed in Figure 2-5(b) due to the sulfur mono-vacancies in the bulk is replaced by a single defect state on the surface (Figure 2-8). The single defect state that was observed for a Fe vacancy in bulk FeS_2 splits and broadens into multiple states in the surface band gap and results in the formation of a pseudo-metallic surface. This is because the Fe atom 'exposed at the surface' is actually located lower than a layer of surface S atoms and the removal of such a subsurface Fe atom results in large relaxations of the neighboring atoms. The root-mean-squared displacement of atoms during such a relaxation is nearly three times as much as the displacements due to removal of a surface S atom. These large

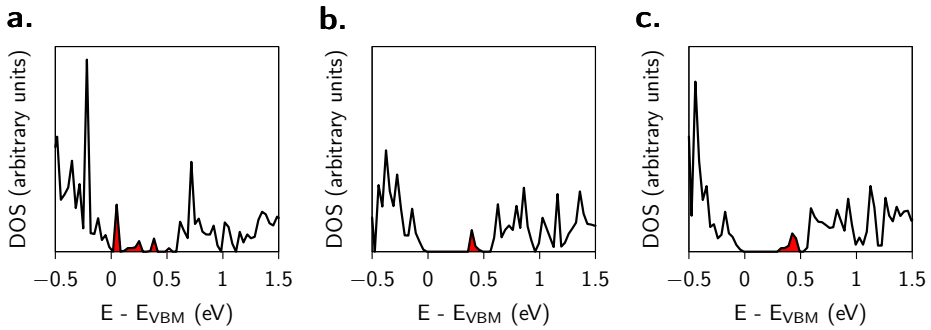

Figure 2-8: Position of neutral defect states (red) in the total density of states plots of the pyrite (100) surface due to a) Fe vacancy, b) S vacancy and c) S_2 dimer vacancy.

relaxations result in a less localized defect state for the Fe vacancy compared to that for the S vacancy.

2.5.5 Reaction energies and surface reactivity

The above findings offer several important implications for the reactivity of pyrite in the context of geochemical reactions, catalysis, corrosion and photoelectrochemistry. Similar to the case of other defective ionic surfaces like CeO_2 [61], the individual vacant sulfur sites are highly reactive, especially towards the chemisorptive dissociation of H_2S during redox reactions. We calculated the energy barriers for the dissociation of a H_2S molecule adsorbed on the pyrite (100) surface using NEB. As shown in Figure 2-9, we find that this reaction is endothermic and has an activation barrier of 0.85 eV for a defect-free surface. By contrast, at a sulfur vacancy site the dissociation of H_2S is barrier-less and leads to an exothermic reaction liberating 2.85 eV per dissociation. For an H_2S molecule adsorbed at the step edge (e.g., of a pit created upon agglomeration of point vacancies), we find the dissociation process has a barrier of 1.28 eV. As a result, this reaction is less favorable, with a high energy barrier, than the reaction at an isolated sulfur vacancy site.

This relatively high barrier at the step-edge site (compared to the defect-free surface) is contrary to the expectation that under-coordinated surface sites such as atomic steps and kinks are more active than flat surfaces. We propose a simple bond-counting argument to explain these results. In the pyrite crystal, all sulfur atoms are sp^3 hybridized leading to a tetrahedral coordination with four bonds per sulfur atom. Any reaction that, as a result, replenishes this ideal number of (four) bonds for the adsorbed sulfur atom from H_2S will be favorable, with reduced energy barriers. An H_2S molecule adsorbed on a defect free surface initially has three bonds around the central S atom (two S-H bonds and one S-Fe bond). After dissociation, the S atom is bonded only to two atoms (one S-H bond and one S-Fe bond). On the other hand, an H_2S molecule adsorbed on a surface vacancy has five bonds around the central S atom (two S-H, two S-Fe and one S-S bond), while after dissociation, it is bonded to four other atoms (one S-H, two S-Fe and one S-S bond). Given the four bonds here resemble the bulk ideal tetrahedral coordination, this results in a strongly exothermic dissociation reaction, effectively with no energy barrier. On the other hand, before dissociation at a step-edge vacancy, the sulfur atom of the H_2S molecule is bonded ideally to four other atoms (one S-Fe, one S-S and two S-H bonds), while after dissociation, it is left with only three bonds (one S-Fe, one S-S and one S-H bond). As a result, dissociation of H_2S from an edge site has a high energy barrier, and is less favorable than the dissociation reaction at a V_S site.

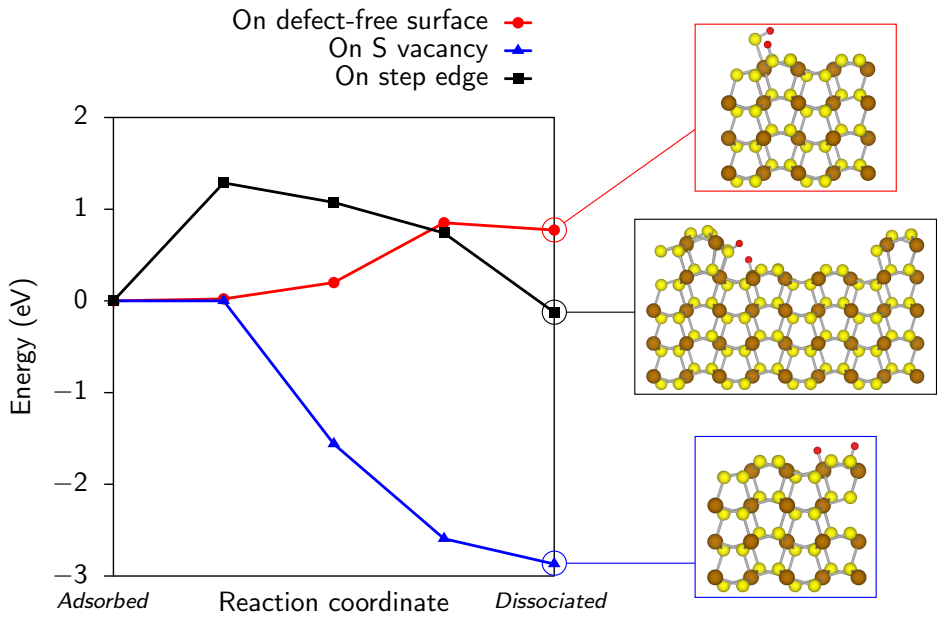

Figure 2-9: (a) Energy landscape of the dissociation of H_2S molecules at different sites on the pyrite surface, as listed in the legend. Inset (b) shows a (010)-oriented FeS_2 slab, where an H_2S molecule is adsorbed on the (100) surface at an Fe site. (c) dissociated H_2S molecule at a defect-free surface site. (d) dissociated H_2S molecule at a vacant sulfur site.

2.5.6 Summary

The formation energy for all bulk vacancies was found to be too high to induce any off-stoichiometry in bulk pyrite, and the concentration of intrinsic charge carriers was estimated to be several orders of magnitude greater than the concentration of bulk charged and uncharged vacancies. While the calculated vacancy formation energies at the (100) surface are lower than those in the bulk, no significant deviation from the ideal stoichiometry is predicted at ambient temperatures. Intrinsic bulk vacancies induce the formation of defect states in the band gap, where anion vacancies form donor-like defect states while cation vacancy states are more acceptor-like. A reduction in symmetry at the (100) surface caused the formation of surface states connected to the edges of the valence and conduction bands. The presence of these surface states is responsible for the marked reduction in the band gap of the pyrite from 0.86 eV in the bulk to 0.55 eV on the (100) surface. The reduction of the band gap at the pyrite surface and the presence of defect states in the gap have important implications for electronic processes such as charge transfer reactions at the surface as in catalysis and corrosion. Specifically, H_2S adsorption becomes extremely exothermic by $\approx$ 4eV and H_2S dissociation becomes a barrier-less process on the reactive point defect sites.

2.6 Quantifying the origin of inter-adsorbate interactions on reactive surfaces for catalyst screening and design

As described in Section 2.2, the adsorption energy of reactant molecules and reaction intermediates is one of the key descriptors of catalytic activity of surfaces. These adsorption energies can depend strongly on interactions between adsorbed molecules in the adlayer, which are typically not accounted for in standard DFT-based calculation of zero-coverage adsorption energies. Usually, these adsorption energies are calculated *ab initio* in simulation cells that contain a single reactant molecule on a surface that is laterally large enough to eliminate adsorbate-adsorbate interactions. This simplistic 'zero-coverage' picture of the reacting surface differs greatly from real catalyst surfaces that contain a finite surface coverage of reactant molecules in that it does not include interactions between adsorbed species in the adlayer.

Strong inter-adsorbate interactions have been observed on a variety of reaction systems, such as $H_2O/TiO_2(110)$[62], CO/Ru(0001) [63], and O on the (111) surface of several transition metals[64]. These interactions result in effective adsorption energies that are significantly different from values at zero-coverage and are, in some cases, strong enough to cause surface restructuring and roughening [65]. These modified adsorption energies can not only alter the activity of surfaces along the Sabatier 'volcano curve' [66], but can also alter the shape of the curve itself leading to a pronounced flattening near the peak activity[67]. Previous studies into the effect of inter-adsorbate interactions have been mostly limited to quantification of the total magnitude of these interactions [68, 69]. While such studies lead to a better representation of the catalytic activity, the physical basis of these interactions is under-investigated, without a quantitative understanding of their dependence on variables like surface strain and composition.

Ab initio calculations can help isolate the mechanism behind inter-adsorbate interactions, but a very large configurational sample space of adsorbed surface sites must be sampled to identify ground-state configurations. Since a brute-force sampling of the entire configurational space is computationally intractable for all but the smallest supercells, past studies for quantifying the magnitude of these interactions have typically resorted to a random sampling of the configurational space [68] or using a more rigorous statistical sampling method like cluster expansion [69]. In both cases, efforts have focused on quantifying the total magnitude of inter-adsorbate interactions rather than on uncovering the dominant mechanism behind these interactions, which is more useful in providing design rules for catalyst surfaces.

Here, we report investigations into the nature and strength of inter-adsorbate interactions, demonstrated on a model system of H_2S adsorbates on the pyrite FeS_2 (100) surface. We use Density Functional Theory (DFT) and cluster expansion methods to calculate adsorption energies as a function of surface coverage. We find that the adsorption energy of H_2S molecules can be affected by over 0.55 eV by the repulsive inter-adsorbate interactions caused primarily by the adsorbate-induced changes to the electronic structure of the FeS_2 surface. These interactions also show a strong monotonic dependence on surface strain, being three times stronger on compressively strained surfaces than on surfaces under tensile strain. The large magnitude of inter-adsorbate interactions as well as their strong dependence on lattice strain demonstrate the need for using coverage-dependent adsorption energies for more accurate screening, for example for strained catalytic systems like core-shell and overlayer structures.

The rest of this section is structured as follows. In Section 2.6.1 and 2.6.2, the method-

ology used to calculate adsorption and interaction energies is briefly described followed by the computational details. Section 2.6.3 is devoted to quantifying the contribution of different types of forces, i.e. Coulombic and Pauli repulsion, and different mechanisms, i.e. adsorbate-induced surface relaxation and adsorption-induced change of surface electronic structure, to the overall inter-adsorbate interaction. In the final section, the framework is applied to the study of adsorption on biaxially strained FeS_2 (100) surfaces to extract adsorption energies under conditions of finite coverage and finite surface strain. We conclude by listing briefly some implications of the current work for the selection and design of strained and unstrained catalyst surfaces.

2.6.1 Methodology

We briefly describe below the framework adopted [70, 71] to quantify inter-adsorbate interactions from a calculation of adsorption energies at different coverage values, and introduce some terms that are used frequently in the rest of the article. This is followed by a discussion about the need for cluster expansion sampling in obtaining these adsorption energies. We then apply this framework to carefully chosen adsorbate/surface systems, closely related to the H_2S/FeS_2 (100) system, in order to isolate the influence of individual mechanisms on the overall interaction. The considered mechanisms include both direct adsorbate-adsorbate and surface-mediated interactions.

On a catalyst surface containing M adsorption sites, the cumulative adsorption energy of n adsorbates (defined as the sum of adsorption energies of n adsorbates) of species X, corresponding to a surface coverage of $\theta = \frac{n}{M}$ monolayer, is given by

$$E_{\text{ads}}^{\text{sum}}\left(\theta = \frac{n}{M}\right) = E_{S-nX} - E_S - (n \cdot E_X) \tag{2.1}$$

where E_{S-nX} is the DFT-calculated energy of the system containing n molecules of species X that are adsorbed to the catalyst surface, E_S is the energy of the bare catalyst surface, and E_X is the energy of an isolated molecule of species X. In the absence of any interactions between adsorbates (direct or surface-mediated), the cumulative adsorption energy will be a linear function of the surface coverage. Therefore, one simple way to measure the magnitude of inter-adsorbate interactions is to subtract zero-coverage contributions from $E_{\text{ads}}^{\text{sum}}(\theta)$ to obtain the cumulative inter-adsorbate interaction, $E_{\text{inter}}^{\text{sum}}(\theta)$ (Equation 2.2).

$$E_{\text{inter}}^{\text{sum}}(\theta) = E_{\text{ads}}^{\text{sum}}(\theta) - (\theta \cdot E_{\text{ads}}(0)) \tag{2.2}$$

For direct comparison with experiments, a more useful quantity is the binding energy or the effective adsorption energy at a given coverage, $E_{\text{ads}}\left(\theta = \frac{n}{M}\right)$, which can be derived from Equation 2.1 using

$$E_{\text{ads}}\left(\theta = \frac{n}{M}\right) = \frac{\mathrm{d}\left[E_{\text{ads}}^{\text{sum}}(\theta)\right]}{\mathrm{d}\theta} \tag{2.3}$$

Calculating the adsorption energy using Equation 2.1 and Equation 2.3 is not straightforward because E_{S-nX} is not unique for a given value of n $(n \neq 0, M)$, since there are several configurational arrangements of adsorbates on the available adsorption sites each resulting in a different value of E_{S-nX}. Since adsorbates are highly mobile at operating temperatures, of most interest to this study is the configuration which results in the lowest E_{S-nX} for a given surface coverage. Identification of these *a priori* unknown

ground states is a challenging problem since a brute-force sampling of the entire adsorbate configurational space is computationally intractable for all but the smallest simulation cells, and a random sampling of the configurations [68] is not guaranteed to identify all ground states. Instead, we implement the cluster expansion method [69, 72], as applied previously to other adsorbate systems like NO/Pt(111) [73] and H/graphene [74], to construct a Ising-like Hamiltonian of the adlayer using DFT-calculated energies of a subset of adsorbate configurations. This Hamiltonian is then used to predict ground state configurations at different coverages, whose energies are explicitly calculated using DFT.

To measure the contribution of individual forces and mechanisms to the overall inter-adsorbate interaction in the H_2S/FeS_2 system, $E_{\text{ads}}(\theta)$ and $E_{\text{inter}}^{\text{sum}}(\theta)$ are compared among closely related adsorbate/surface systems. These related systems are created by altering one aspect of the original H_2S/FeS_2 system at a time, such as the rigidity or strain state of the surface or replacing the H_2S adsorbates by H atoms. The different mechanisms investigated in this work and the corresponding adsorbate/surface systems are discussed in more detail in the Results and discussion section.

2.6.2 Computational details

All DFT calculations [75] in this study were performed with the Vienna *Ab initio* Simulation Package [76, 77] using the spin-polarized PBE functional [78] and atomic potentials generated by the projector augmented wave method [79]. To correct for electronic self-correlation effects commonly found in 3d transition metal compounds, we adopt the DFT+U method [80], with a U-J value of 1.6 eV for the Fe 3d electrons, determined to be appropriate for iron sulfide phases [34]. Cluster expansion calculations were carried out using the MIT *Ab initio* Phase Stability [81] code included as part of the Alloy Theoretic Automated Toolkit [82]. Adsorbate configurations were sampled with 1, 2 and 3 points per cluster and the one-removed cross-validation score is less than 0.03 eV in the case of H_2S adsorbates and 0.01 eV in the case of H adsorbates, indicating good predictive power of the cluster expansion to generate thermodynamically accurate ground state adsorbate configurations.

All adsorption energies are calculated on 4 layer pyrite FeS_2 slabs of 2x2 unit-cell lateral size, separated by 10 Å of vacuum in a periodic simulation cell. Each simulation cell contains 32 formula units of pyrite. Wave functions are expanded in plane waves with kinetic energies up to 350 eV and the reciprocal space was sampled using 3x3x1 Monkhorst-Pack grids [83]. This choice of plane-wave energies and Brillouin-zone sampling grids leads to well-converged adsorption energies over the entire range of surface coverage, $\theta \in [0, 1]$ (Figures S4 and S5). Total energies are converged to within $5\text{x}10^{-5}$ eV in each self-consistency cycle and the forces on ions were converged to within 0.05 eV/Å.

We confirm the accuracy of the calculated adsorption energies by using a program [84] to perform a simulation of temperature programmed desorption of H_2S from the FeS_2(100) surface. The program generates the TPD spectrum by numerically solving the differential equation describing the dependence of surface coverage on temperature in the first-order desorption process:

$$\frac{\mathrm{d}\theta}{\mathrm{d}T} = -\frac{A}{\beta}\exp\left(\frac{E_{\text{ads}}(\theta)}{k_B T}\right)\theta$$

where A is the Arrhenius pre-exponential factor (assumed to be 10^{13} s^{-1}, in the limit of an immobile transition state during desorption [85]), β is the experimental heating rate[86], k_B is the Boltzmann constant and T is the absolute temperature.

All images of crystal structures used in this article were generated using the VESTA structural visualization program [87].

2.6.3 Results and discussion

The non-dissociative adsorption of the weakly nucleophilic H_2S molecules occurs on the eight Fe ions exposed at the 2x2 FeS_2 (100) surface, where the LUMO of the pyrite surface is localized [55, 88]. The resulting Fe-SH_2 bond has a bond length of 2.30 Å (at all coverage values), which is similar to the Fe-S bond lengths in the bulk of the FeS_2 crystal (2.25 Å). H_2S adsorption saturates the dangling bond on the Fe ion by completing the Fe-S_6 octahedron, leading to a change of the electronic structure of the FeS_2 surface.

While the adsorbed H_2S molecule is free to rotate about the rigid Fe-SH_2 bond, the inter-adsorbate separation is determined by the distance between the adsorption sites and is independent of surface coverage (Figure 2-10). On the FeS_2 (100) surface, this results in a nearest-neighbor S-S distance of just 3.4 Å, which is close to twice the van der Waals radius of sulfur (1.8 Å [89]), indicating the presence of direct non-bonding interactions between adsorbates.

In the following sections, we quantify the overall strength of inter-adsorbate interactions between H_2S molecules (Section 2.6.3) and identify both direct adsorbate-adsorbate as well as surface-mediated mechanisms that contribute to the overall interaction (Section 2.6.3).

Coverage-dependent adsorption energy on FeS_2 (100)

The cumulative adsorption energy, $E_{\text{ads}}^{\text{sum}}(\theta)$ for the H_2S adsorbate ground-state structures (Figure 2-10) predicted by cluster expansion can be well-fitted by the quadratic expression in Figure 2-11a, where a negative energy indicates exothermic adsorption and the deviation towards positive energies indicates the presence of repulsive interactions that lead to weaker binding at higher surface coverages.

The dashed straight-line in Figure 2-11a describes the expected behavior of a system with no inter-adsorbate interactions, as represented by the second term in RHS of Equation 2.2. Subtracting this from the DFT-calculated energy, we get a measure of the total inter-adsorbate interaction energy, $E_{\text{inter}}^{\text{sum}}(\theta)$ in Figure 2-11b. For comparison with experiments, the corresponding binding energy or the effective adsorption energy per molecule, $E_{\text{ads}}(\theta)$ is calculated by taking the derivative of $E_{\text{ads}}^{\text{sum}}(\theta)$.

$$E_{\text{ads}}(\theta) = \frac{\partial \left[E_{\text{ads}}^{\text{sum}}(\theta)\right]}{\partial \theta} = -0.76 + 0.56\ \theta \text{ eV} \tag{2.4}$$

To validate the adsorption energy calculated in Equation 2.4 we simulated the outcome of a temperature programmed desorption (TPD) experiment for H_2S adsorption on the defect-free pyrite (100) surface. We choose simulation parameters like the initial dosing temperature (79 K) and the heating rate (8 Ks^{-1}) to be the same as the experimental conditions used by Guevremont *et al.* for the TPD of H_2S from the (100) surface of pyrite [86]. In comparing the simulated TPD results with experimental data of Guevremont *et al.*, we find that the adsorption energies derived from the cluster-expansion approach generates a desorption spectrum is well-matched with the experimental one, in terms of reproducing the broad width of the peak. In contrast, if a single value of adsorp-

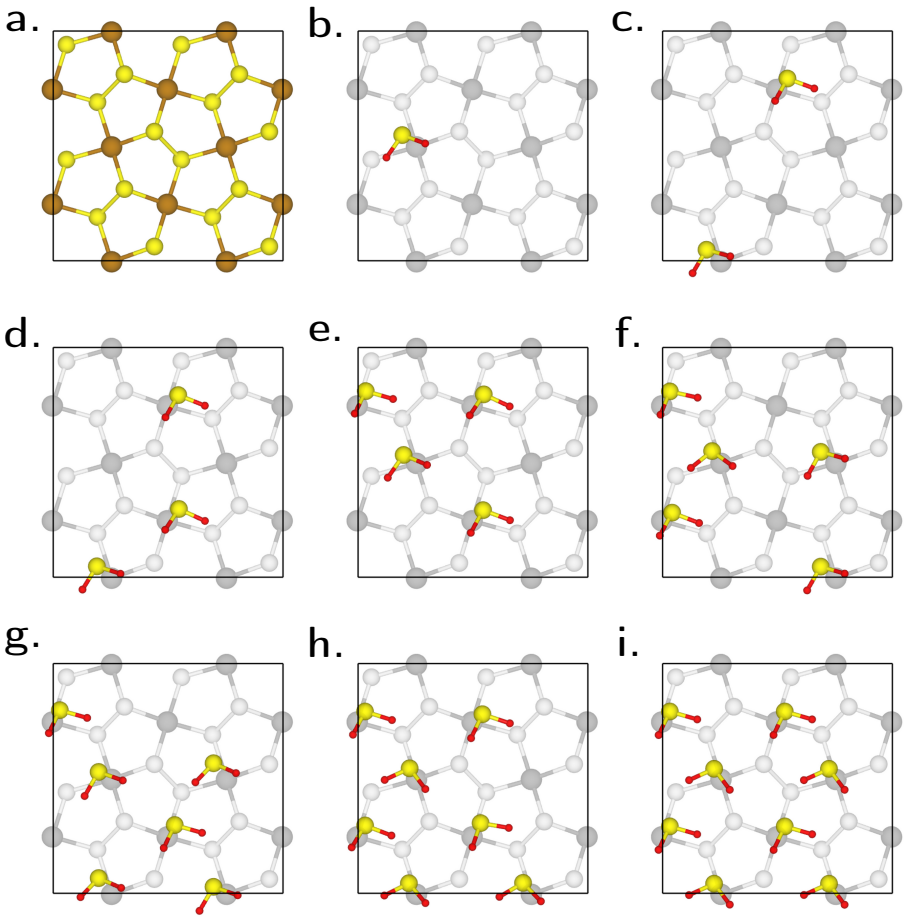

Figure 2-10: (a) Atomic structure of the FeS_2 (100) surface showing 8 non-equivalent adsorption sites, Fe^{2+} ions (brown) and 16 S^{-} ions (yellow). (b-i) Adsorption configurations at increasing surface coverage values in steps of 12.5% predicted by cluster expansion.

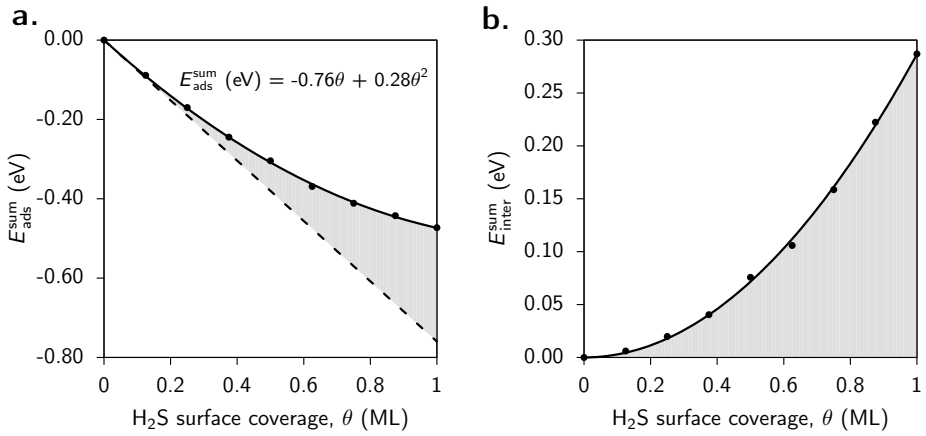

Figure 2-11: (a) The sum of adsorption energy deviates from ideal linear behavior at higher coverage values, indicating the presence of repulsive inter-adsorbate interactions (Shaded region). (b) Removing the linear component from (a) reveals the quadratic form of the inter-adsorbate interaction energy, E_{inter}^{sum}.

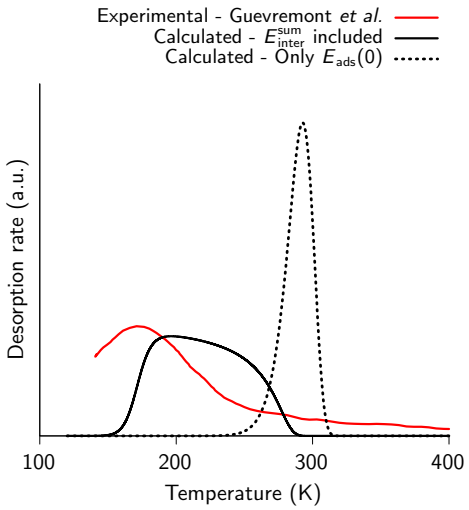

Figure 2-12: The calculated TPD spectrum based on coverage dependent adsorption energies deduced by the cluster expansion method has a much closer fit to the experimental spectrum compared to the calculated TPD spectrum based on adsorption energies that do not consider inter-adsorbate interactions. The comparison is made both in terms of the onset temperature for desorption and the temperature range for the desorption process. The curves are normalized by the area under the curve.

tion energy (obtained for zero-coverage) is used throughout the TPD, a very different, narrow peak shape is predicted (Figure 2-12).

Simulated TPD using adsorption energies from the cluster-expansion method is also in better agreement with the experiment than the TPD calculated using adsorption energies derived from a random sampling of the adsorbate configurational space (Figure S3). This result demonstrates the importance of identifying finite-coverage ground state configurations rigorously using cluster expansion, and the reliability of the cluster-expansion procedure for calculating coverage-dependent adsorption energies.

Mechanisms responsible for inter-adsorbate interactions

It can be seen that the cumulative adsorption energy in Figure 2-11 increases, i.e. becomes less negative and exothermic, with increasing surface coverage, indicating a repulsive effective interaction between H_2S adsorbates. More significantly, the cumulative adsorption energy depends quadratically on the surface coverage. This quadratic dependence has previously been observed in lattice gas model Hamiltonians that include pair-wise interactions between adsorbed species [90]. Depending upon the adsorbate/surface pair, several physical mechanisms have been shown in literature to be responsible for pairwise inter-adsorbate interactions. We consider four mechanisms here.

1. Coulombic repulsion between charged adsorbates, as seen in O/Pd(111),[91]
2. Through-space steric interactions between adsorbates, as observed in the NO/Pd(111) system, [92]
3. Adsorbate-induced surface-stresses resulting in surface-mediated elastic interaction between adsorbates, as seen in Cl/Au(111), [93] and
4. Adsorbate-induced altering of the electronic structure of neighboring adsorption sites, such as in S/Rh(001).[22]

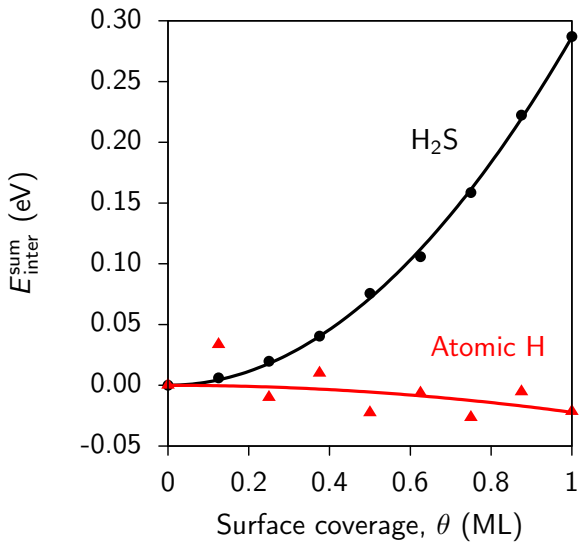

Figure 2-13: H_2S and atomic H adsorbates that have the same charge around 0.1 e^-, show very different interaction strengths within their corresponding adlayers. This indicates that Coulombic interactions (which scale with adsorbate charge) are only minor contributors to the inter-adsorbate interaction in the H_2S adlayer.

It is likely that a combination of the above mechanisms is responsible for the observed inter-adsorbate interactions on the FeS_2 (100) surface. In the following sections, the magnitude of each contribution is quantified by calculating $E^{sum}_{ads}(\theta)$ and $E^{sum}_{inter}(\theta)$ for different adsorbate-surface systems that allow us to isolate the effect of each mechanism.

1. *Coulombic repulsion*

Chemisorption of H_2S on FeS_2 (100) is accompanied by charge transfer between the adsorbed molecule and the surface, which may result in Coulombic interactions between the adsorbates. To quantify this interaction, the partial charge present on adsorbates was identified by performing a Bader charge analysis [94] on adsorbed and isolated H_2S molecules. We found that the adsorbed H_2S molecules are nearly electrically neutral with residual charge of $0.06 \pm 0.02\ e^-$ compared to isolated molecules (Figure S1). To identify if Coulombic interactions are a source of significant inter-adsorbate interactions in the H_2S/FeS_2 (100) system, we compare it to interactions in the atomic H/FeS_2 (100) system. This is useful because atomic H adsorbates have a Bader charge of $-0.13 \pm 0.01\ e^-$, and are therefore expected to exhibit Coulombic interactions of similar magnitude to H_2S molecules. Unlike the H_2S adsorbates, atomic H adsorbates show no observable inter-adsorbate interaction (Figure 2-13). Therefore, the contribution of Coulombic repulsion to the overall interactions among H_2S adsorbates is expected to be negligible.

1. *Through-space steric interactions*

   Spatially large molecules also sterically block the adsorption of other molecules on neighboring adsorption sites by penalizing the non-bonding overlap of the electron clouds of nearby adsorbates. This mechanism is also operative in the H_2S/FeS_2 system, where it is observed that the electronic charge in the adlayer is redistributed away from an incoming H_2S adsorbate (Figure 2-14a).

   To quantify the effect of Pauli repulsion, $E^{sum}_{inter}(\theta)$ was calculated for systems in the absence of the FeS_2 (100) surface. Since this eliminates the possibility of any surface-mediated effects, the only interactions captured in these calculations are

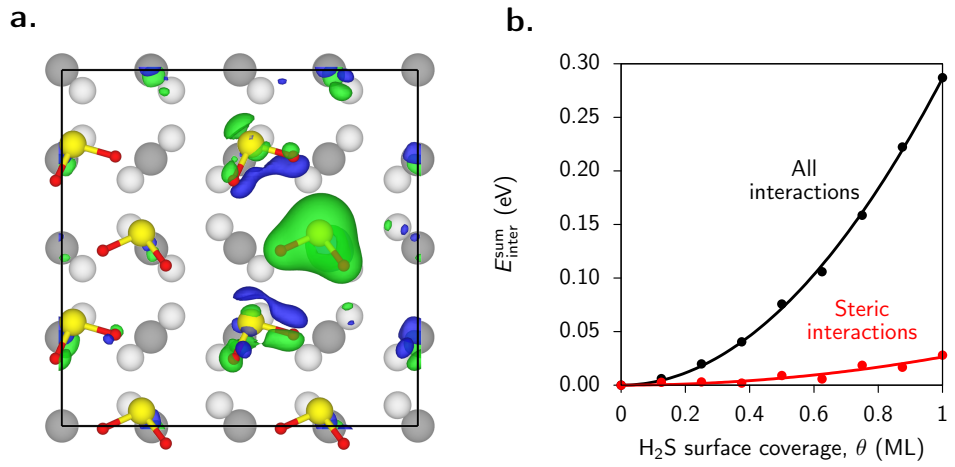

Figure 2-14: (a) Electron density isosurfaces indicate that Pauli repulsion is responsible for redistributing electrons (green) away from the newly adsorbed H_2S molecule creating a region of depleted electron density (blue). (b) Pauli repulsion contributes to only about 10% of the overall inter-adsorbate interaction seen in the H_2S/FeS_2 (100) system.

through-space steric effects (Coulombic effects do not come into play because the molecules are identically uncharged). It was found that steric effects account for a measurable, but still a minor part (≈10%) of the overall inter-adsorbate interactions between adsorbed H_2S molecules (Figure 2-14b).

2. *Adsorbate-induced surface stresses*

   Adsorbates can also induce local surface stresses that lead to relaxation of neighboring adsorption sites, potentially affecting the adsorption energy of subsequent adsorbates. To understand this effect, inter-adsorbate interaction energies, $E_{\text{inter}}^{\text{sum}}(\theta)$, are compared for two related systems; one where the Fe and S atoms in the surface are allowed to relax in response to H_2S adsorption and another one where they are held in fixed positions. The latter system does not contain any adsorbate-induced surface stress within the FeS_2. Therefore, a difference in the $E_{\text{inter}}^{\text{sum}}(\theta)$ between these two systems gives us a measure of the contribution of elastic interactions on the catalyst surface towards the overall inter-adsorbate interaction. Although H_2S adsorption causes noticeable relaxation of the FeS_2 (100) surface, the observed interaction energies are very similar for both the rigid and relaxed surfaces, indicating that the contribution of surface-mediated elastic interactions within FeS_2 is not significant in this system (Figure 2-15).

3. *Adsorbate-induced change of surface electronic structure*

   In addition to charge transfer, formation of the adsorbate-surface bond alters the electronic structure of the surface, which, in turn, affects the adsorption energy of the subsequent adsorbates. To quantitatively capture this influence on the effective inter-adsorbate interaction, two pieces of information are required.

   (a) A metric that measures the change in electronic structure due to increasing H_2S coverage, and

   (b) A dependence of the H_2S adsorption energy on this surface electronic structure metric.

   We perform a two-part calculation to obtain these pieces of information. Since H_2S molecules adsorb on the Fe^{2+} sites on the pyrite surface, we use the distance between the Fe 3d band and the Fermi level calculated from the Density of States

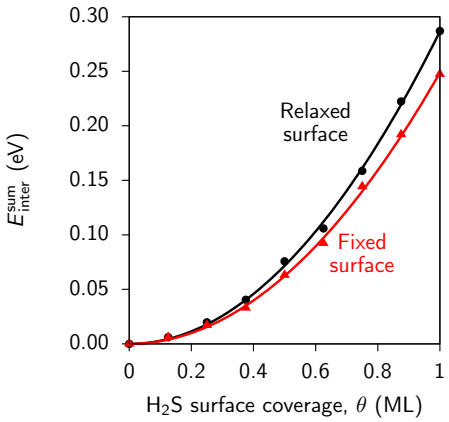

Figure 2-15: The magnitude of inter-adsorbate interaction remains largely unchanged regardless of the relaxation of the surface, indicating that the surface-mediated elastic effects contribute only marginally to the overall inter-adsorbate interaction for the H_2S/FeS_2 (100) system.

as a metric to represent the electronic structure of the surface, as prescribed by the widely adopted d-band theory[26]. In the first step, we calculate the Density of States at different H_2S coverages and observe the dependence of this metric on surface coverage. In the second step, to understand how the surface electronic structure affects H_2S adsorption, the surface electronic structure metric is systematically and controllably varied by imposing lateral strain on the FeS_2 (100) surface and the corresponding zero-coverage adsorption energy is calculated. A product of these two dependencies (Figure S2) quantifies the contribution of adsorbate-induced electric structure change on the overall inter-adsorbate interaction (Equation 2.5).

$$\frac{dE_{ads}}{d\theta} = \frac{dE_{ads}}{dE_{DBC}} \times \frac{dE_{DBC}}{d\theta} \tag{2.5}$$

where E_{DBC} is the electronic structure metric derived from the d-band theory and E_{ads} and θ have their usual meanings as previously described.

A summary of contributions from all the individual forces and mechanisms considered in this study (Figure 2-16) clearly demonstrates that the altered surface electronic structure is the largest factor to the observed dependence of adsorption energy on surface coverage. Since the independently computed contributions very nearly sum up to the overall observed interaction (denoted by the thick line in Figure 2-16), any forces not considered in this study (i.e. van der Waals) are expected to be relatively minor contributions.

Inter-adsorbate interaction on biaxially strained surfaces

The dependence of the 'zero-coverage' adsorption energy on the strain state of the catalyst surface is well-established, and elastic strain is understood to be an important variable in several catalytic systems [95–97] . However, the impact of lattice strain on the interactions within the adlayer has not been explored so far, to our knowledge. Quantifying the role of strain on inter-adsorption interactions and understanding its impact on the different interaction mechanism that were presented above can allow us to exploit lattice strain accurately as an important parameter in catalyst selection.

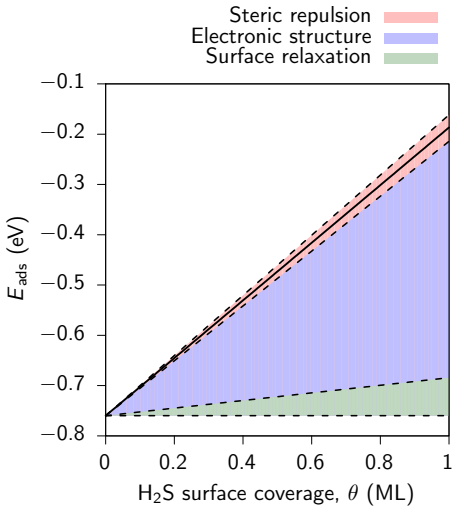

Figure 2-16: Adsorbate-induced changes to surface electronic structure are largely responsible for the coverage dependence of adsorption energy in the H_2S/FeS_2 (100) system. Both the surface elastic relaxation and Pauli repulsion are minor contributions to the overall inter-adsorbate interaction.

To elucidate the role of strain, the cumulative inter-adsorbate energy, $E_{\text{inter}}^{\text{sum}}(\theta)$ is calculated as described in the Methodology section for H_2S adsorbates on FeS_2 (100) surfaces under biaxial strains, ε ($= \varepsilon_{xx} = \varepsilon_{yy}$) ranging from -0.05 to 0.05 in steps of 0.025. Figure 2-17a shows that inter-adsorbate interactions strengthen monotonically with closer packing of adsorption sites as the lattice strain is varied from 0.05 (tensile) to -0.05 (compressive). Quantitatively, interactions on the most compressively strained surface are three times stronger than on the most tensile strained surface. This increasing interaction translates to a greater dependence of adsorption energy on surface coverage with increasing compressive strain. The most immediate implication of this interplay is that the variation of adsorbate binding energy with elastic surface strain is significantly different at finite coverage values than at zero coverage. For instance, the difference in adsorption energies of a H_2S molecule on the unstrained and 5% tensile strained FeS_2 surface is less than 0.05 eV at zero coverage but expands to over 0.30 eV at 1 monolayer coverage (Figure 2-17b).

We further describe a method to resolve these interactions into contributions from direct steric and Coulombic repulsion among the adsorbates, as well as indirect interactions due to adsorbate-induced change of electronic structure and surface relaxation and demonstrate the same for H_2S molecules on the FeS_2 (100) surface.

On the FeS_2 surface, repulsive interactions between H_2S molecules due to changes in the surface electronic structure were found to affect the H_2S adsorption energy by over 0.55 eV. Inter-adsorbate interactions also show a strong dependence on the biaxial strain on the surface, with compressively strained surfaces exhibiting the strongest inter-adsorbate interactions. The large magnitude of these inter-adsorbate interactions as well as their strong dependence on experimental parameters like surface strain highlight the need for moving beyond 'zero-coverage' adsorption energies in the material screening process, especially for strained catalyst systems. Towards this end, the identification and quantification of individual contributions to the inter-adsorbate interactions described in this work can help understand how adsorption energies on realistic surfaces vary with experimental conditions and enables better-informed screening of materials for heterogeneous catalysis applications.

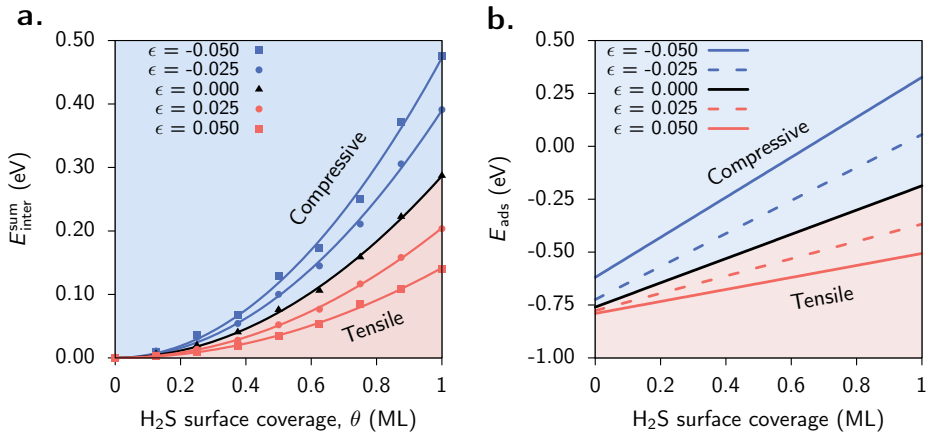

Figure 2-17: (a) Inter-adsorbate interactions among H_2S adsorbates are stronger on the compressively strained FeS_2 (100) surface compared to the unstrained surface or the tensile strained surface. (b) Increased inter-adsorbate interactions on the compressively strained surface are reflected as a stronger dependence (larger slope) of adsorption energy on surface coverage.

2.6.4 Summary

In this section, we quantified the magnitude of inter-adsorbate interactions by using DFT and cluster expansion method, and by selected modifications of the surface to allow for isolating the magnitude of each interaction mechanism. The coverage-dependent adsorption energies and the contributing mechanisms were demonstrated for H_2S molecules on the FeS_2 (100) surface. We further resolved these interactions into contributions from direct steric and Coulombic repulsion among the adsorbates, as well as indirect interactions due to adsorbate-induced change of electronic structure and surface relaxation.

On the FeS_2 surface, repulsive interactions between H_2S molecules, arising mainly from changes in the surface electronic structure were found to affect the H_2S adsorption energy by over 0.55 eV. Inter-adsorbate interactions also show a strong dependence on the biaxial strain on the surface, with compressively strained surfaces exhibiting the strongest inter-adsorbate interactions. The large magnitude of these inter-adsorbate interactions as well as their strong dependence on experimental parameters like surface strain highlight the need for moving beyond 'zero-coverage' adsorption energies in the material screening process, especially for strained catalyst systems. Towards this end, the identification and quantification of individual contributions to the inter-adsorbate interactions described in this work can help understand how adsorption energies on realistic surfaces vary with experimental conditions, enables more accurate surface reaction kinetic models, and provides for better-informed screening of materials for heterogeneous catalysis applications.

2.7 Reactivity of charged semiconductor surfaces

Another vital consideration in modeling the sour corrosion process is the accurate modeling of unit processes, namely adsorption and dissociation, at the interface between the charged passive film and the aqueous environment. Electrochemical reactions at the semiconductor-water interface underpin some of the most critical existing and upcoming technologies in fields like photocatalytic water splitting [98], electrolytic hydrogen evolution [99], electrochemical energy storage [100], corrosion[13] etc. and are widely

recognized as being central to addressing some of the most important materials challenges. Fundamental information about overall reaction rates and energy efficiencies and even reaction mechanisms of such electrochemical reactions depend not only on Faradaic charge transfer, but also on non-Faradaic behavior of nominally uncharged reaction intermediates [101]. While the thermodynamics of Faradaic unit processes are reliably estimated using a zeroth-order correction to reaction free energies [102, 103], characterization of non-Faradaic steps is considerably more complex because they depend closely on atomic-scale features like interfacial charge separation, polarization of water molecules, adsorbate solvation and intense electric fields, which must be understood for informed design of better electrocatalysts and corrosion-resistant materials. However, such chemical and structural properties at the interface remain largely unexplored due to difficulties in employing ambient-condition experimental probes based on diffraction and scattering techniques [104]. Therefore, the identification and design of electrochemically active surfaces remains grounded in vacuum-based surface science techniques and vacuum-based *ab initio* modeling, which ignore the influence of the aqueous environment. This gap between model systems and real-life catalyst surfaces is increasingly being bridged by an increasing number of theoretical models of aqueous electrode surfaces, which use Density Functional Theory (DFT) to provide an accurate description of bonding and structures at the electrode-water interface. While such models have been successfully demonstrated on model catalyst surfaces like Pt(111) [105] and Ti(001) [106], challenges relating to creating a statistically accurate representation of interfacial and bulk water and estimating reaction free energies in an ensemble of constant electrode potential (in contrast to the constant charge ensemble, commonly employed in DFT calculations) remain. Additionally, aqueous-semiconductor surfaces involve greater complexity in the form of charge localization on surface and/or defect states and presence of non-equivalent surface sites, the effects of which have not been investigated so far.

In this study, we use a combination of classical molecular dynamics and *ab initio* DFT to study the charged interface between water and a model semiconductor surface of FeS_2 (100). Specifically, we aim to understand the role of phenomena such as strong interfacial electric field, polarization of water molecules in the electrical double layer and partial charge transfer during electrosorption in affecting energies of adsorption of H_2S and H and dissociation of H_2S. This reaction system is of immediate interest for sour corrosion in oil fields [13], and it also allows us to quantify trends about the behavior of adsorbates of different sizes and polarizabilities on two distinct adsorption sites (Fe and S) on the electrode surface. Such trends are helpful in understanding the initial stages of electrochemical processes and for defining design rules to screen for electrochemically active surfaces. We find that the variation of adsorption and dissociation energies on electrode potential is determined by the relative filling of the bonding and antibonding states of the adsorbate-electrode bond, as described by the "*d*-band model" of surface activity and that the trends in adsorption energy can be estimated by the extent of partial charge transfer between the reactant species and the electrode surface. Other factors such as the strong double-layer electric field (up to 25 MV/cm) and the polarization of water molecules in the double layer do not affect the adsorption or dissociation energies of small reactants like H_2S and H with compact charge distributions and negligible dipole moments.

2.7.1 Methodology and Computational Details

It is well known that the work function and surface potential and, therefore, the surface charge state of electrode depend on the atomic structure of the dipole configuration of water molecules near the electrode surface [107, 108]. Therefore, an analysis of

electrochemical reaction energies on charged surfaces must necessarily begin with an accurate representation of molecular configuration of interfacial water. While a truly representative picture can be obtained only by calculating reaction energies averaged over an ensemble of all possible configurations of H_2O molecules, such a treatment is computationally intractable for all but the smallest supercells. Most previous studies circumvent this difficulty by assuming a predetermined configuration of water molecules (usually that of ice) at the electrode surface. Instead, we perform a two-step calculation to ascertain the structure of water molecules near the surface.

In the first step, we perform a 1 nanosecond simulation of a pyrite slab of (001) orientation immersed in an aqueous environment modeled as 123 water molecules using classical molecular dynamics. This results in a realistic distribution of bulk-like water molecules far from the interface. To accurately resolve interfacial adsorption and bonding, we perform a shorter 1 picosecond first principles molecular dynamics using the atomic configuration generated by the classical MD simulation. By capturing the short-range interfacial order as well as long-range bulk-like order away from the interface, the two-step calculation provides a reasonable description of the Electrical Double Layer (EDL). Reaction free energies are then calculated using high-accuracy static DFT calculations and correlated to the corresponding potential of the FeS_2 surface using the double reference method of Taylor *et al.* [109]. Briefly, the double reference method computes the absolute of the charged electrode (whose charge density is controlled by the number of electrons added or removed from the supercell) from the Fermi level and the Hartree potential of two reference points, a region of vacuum and another aqueous region far away from the interface. This absolute potential can easily be related to the standard hydrogen potential by subtracting the absolute potential of the standard hydrogen electrode, estimated to be in the range of 4.4 to 4.8 eV [110] (Taken to be 4.8 eV in the current study). Readers are referred to the study by Taylor *et al.* [109] for further details regarding the implementation of the double reference method.

Initial classical molecular dynamics calculations were performed using the LAMMPS simulation program [111] on a four-layer pyrite slab in a 10.8 Å × 10.8 Å × 43.8 Å simulation cell filled with 123 water molecules equilibrated at 300 K at ambient pressure (i.e. in the NPT ensemble), while the equations of motion were integrated with a time step of 1 fs. During the course of this calculation, the Nosé Hoover thermostat with a damping time of 100 fs. Interaction between water molecules were modeled using the TIP3P potential [112], while interactions between the pyrite surface and the liquid environment was modeled using a previously described Lennard-Jones potential [113]. Long-range Coulombic interaction were also included using a particle-particle/particle-mesh Ewald algorithm.

Subsequent first-principles MD and DFT calculations [75] are performed using the Vienna *ab initio* simulation program [76, 77]. We use the Projector Augmented Wave form [79] of the PBE functional [78] with wavefunctions expanded in plane waves with components up to 500 eV. Long-range interactions between water molecules are accounted for by including dispersion forces using the DFT-D2 formulation [114]. In order to correct for spurious electron delocalization on Fe^{2+} ions, we adopt the Hubbard DFT+U model with an effective Coulombic potential ($U_{\text{eff}} = U - J$) of 1.6 eV added to the 3d orbital of Fe ions, previously determined to be accurate for iron sulfides [34]. The Brillouin zone of the large 460-atom supercell is sampled at the Γ point. Calculations are performed till energies in the electronic self-consistent field cycles are converged to within 10^{-4} eV and the absolute residual forces on all atoms are below 10^{-1} eV/Å.

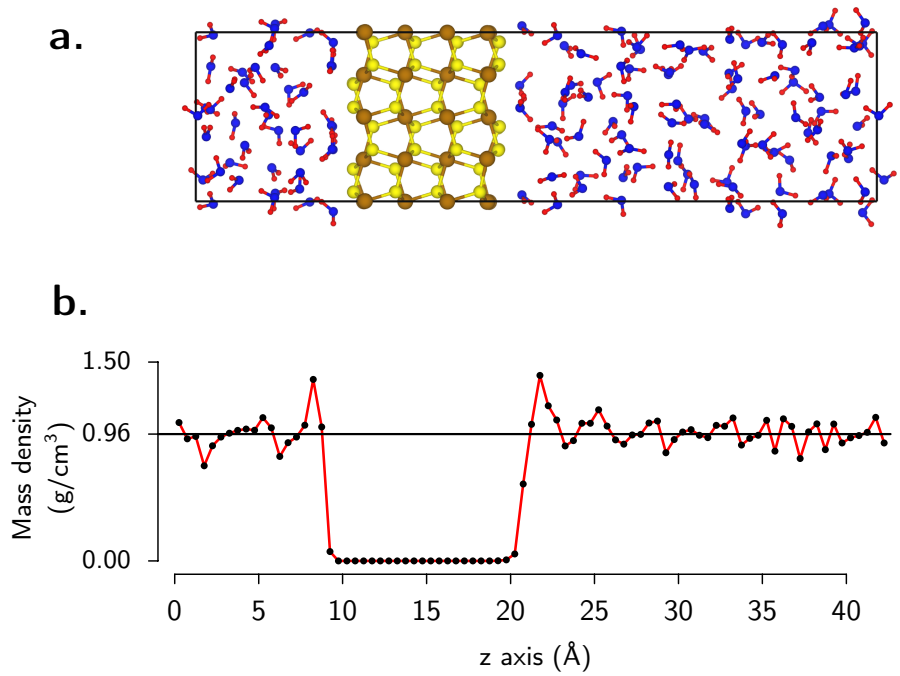

Figure 2-18: (a) Snapshot of the pyrite-water interface during an ab initio MD simulation showing the (b) dense adlayer of water molecules and the bulk-like density profile away from the interface. The density profile was obtained from an average of 10 ab-initio MD runs, each lasting 1 ps.

2.7.2 Results and discussion

The two-step classical and *ab initio* MD simulation leads to the formation of a bilayer structure of water molecules near the semiconductor surface. There is a single dense ($\rho \approx 1.4$ g cm^{-3} monolayer of water molecules adsorbed on Fe^{2+} ions at the pyrite surface (Figure 2-18). Immediately outside this adlayer, the remaining water molecules of the EDL are more bulk-like ($\rho \approx 0.96$ g cm^{-3}). This bilayer structure with increased density at the interface is also consistent with previous models of water on metallic surfaces [115] and with previous studies of water on the pyrite surface [116].

This adsorbed monolayer serves to passivate dangling bonds on Fe^{2+} sites at the surface and exposes the S^{-} sites on the surface to nucleophilic attack by localizing the pyrite conduction band on the S^{-} ions. By contrast, in vacuum environments, both the valence and conduction band edges are localized on Fe^{2+} sites, which are known to be active sites for redox reactions (Figure 2-19). This distinction represents a significant difference between the reactivity of pyrite in vacuum and aqueous environments and demonstrates that modeling the water layer using explicit water molecules leads to a more realistic representation of the electronic structure of the electrode than using a continuum effective medium for modeling the aqueous region [117].

The addition (removal) of electrons from the simulation cell causes the Fermi level to shift towards the LUMO (HOMO) states of the system, which are the valence (conduction) bands edges of the FeS_2 slab. Since the valence and conduction band edges are localized on high-density surface states, the Fermi level is pinned at the valence/conduction band edge during charging, leading to the formation of a flat potential profile inside the pyrite slab, characteristic of metallic electrodes (Figure 2-20). By calculating the energies of adsorption and dissociation of H_2S and atomic H on surfaces of different charge

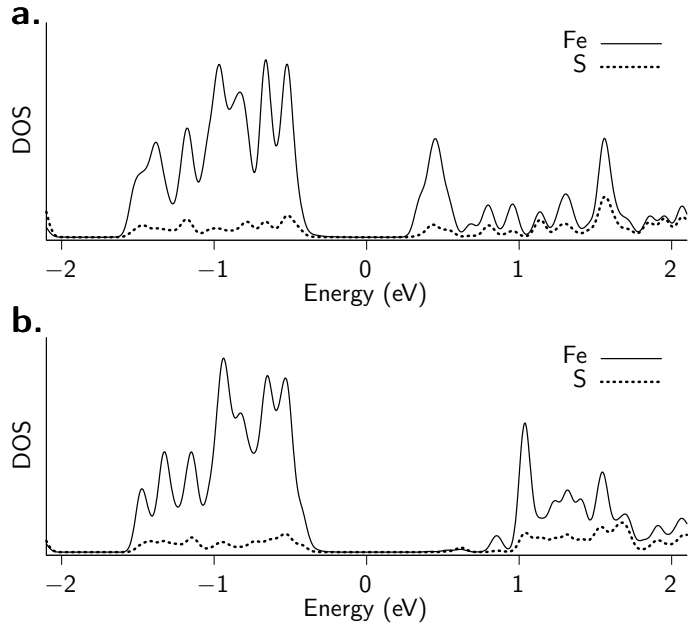

Figure 2-19: Density of states of the pyrite surface in (a) vacuum and (b) aqueous environments shows that the adsorption of water molecules and the formation of the water adlayer passivates the Fe^{2+} dangling bonds that make up the conduction band states.

states, we can quantify the variation of reaction energies as a function of potential of the FeS_2 electrode (Figure 2-22). In order to understand the difference between the reactions, we explore the effect of three mechanisms operative at the electrochemical interface.

1. Strong electric field – In electrochemical systems, the surface charge of the electrode is shielded by the mobile counter charges in water within 5-50 Å of the interface, leading to the formation of very intense interfacial electric fields with strengths of 1-5 MV/cm, which can substantially affect energies of reactions involving polar molecules [118].

2. Polarization in the electrical double layer [119, 120] – The strong electric field in the EDL leads to reorientation of dipoles in water molecules, thus affecting hydrogen bond networks and solvation shells of charged or polar adsorbates and consequently the free energies of reactions involving such adsorbates.

3. Partial charge transfer – Unit processes like adsorption and dissociation, which involve forming or breaking of bonds are accompanied by partial redistribution of electrons from or to the electrode surface. Therefore, any changes in the Fermi level of the electrode are reflected as variations in binding and reaction energies.

Figure 2-22a shows the variation of adsorption and dissociation energies as a function of potential of the FeS_2 (100) surface. In order to assess the effect of the double layer electric field, we compare these reaction energies (and corresponding electric fields calculates from potential profiles similar to that in Figure 2-20b) to those from simulations performed in the absence of water (i.e. with FeS_2 (100) in contact with vacuum) but with an externally-applied electric field of constant strength. In vacuum, there is a noticeable change of reaction energies with the applied electric field, but this weak dependence is insufficient to explain the large changes in reaction energies observed at the aqueous interface for relatively modest electric fields. Therefore, the effect of the interfacial electric field is negligible for small non-polar molecules like H_2S and H

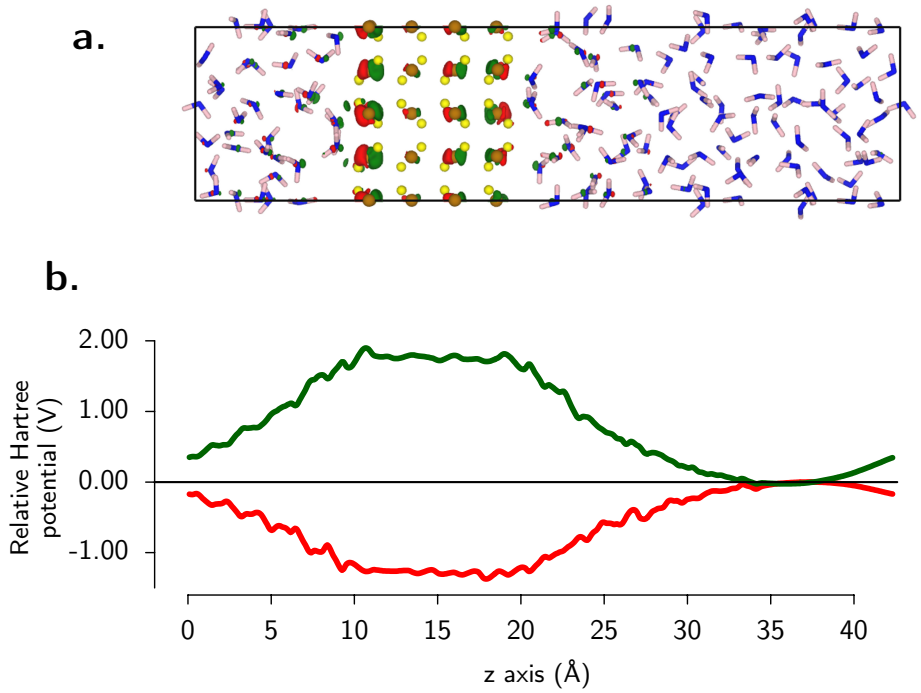

Figure 2-20: (a) Charge redistribution due to the addition of an electron is localized on the surface states, where the Fermi level is pinned. (b) This form of charge localization leads to a flat potential profile within the slab.

(Figure 2-21).

In addition to the adsorbed monolayer, there is an extended region (up to ≈ 15 Å from the interface in the supercells considered) where the electric field of the charged surface causes polarization of water molecules. In order to quantify this effect, we compare reaction energies from two simulations, one where the molecules in the double layer are allowed to relax and polarize in response to the electrode charge (solid lines in Figure 2-22a) and another where the water molecules are held fixed (dashed line in Figure 2-22a). This similarity between the two sets of curves over a wide range of electrode potentials indicates that the polarization of EDL molecules plays only a minor role in reaction thermodynamics. This is not surprising since the small H_2S and H adsorbate species interact only with the immediate water adlayer, which does not polarize significantly under the interfacial electric field.

Figure 2-22b shows that the electrode response towards various reactions is strongly correlated with the extent of charge transfer to the electrode, as calculated by Bader charge calculations [94]. This indicates that the response of different reactions to electrode bias can be explained by understanding bonding configurations between reactant molecules and the FeS_2 surface. To explore this further, we compare and contrast the trends in adsorption energies of H_2S and H species on the Fe^{2+} sites on the pyrite surface as an example. In both cases, chemisorption is a product of interaction between the HOMO states of the adsorbate ($1s$ for H and $1b_1$ (mostly $2p_z$ like) for H_2S) with the conduction band edge states on the surface Fe^{2+} ion (mostly $3d_z{}^2$ states) (Figure 2-23 and Figure 2-24). Since the adsorbate orbitals interact primarily with the localized $3d$ orbitals during adsorption, we adopt the "d-band model" formalism that explains the strength of the 'strong' chemisorption reaction as an outcome of the relative filling of the bonding and anti-bonding states that result from the interaction of adsorbate and

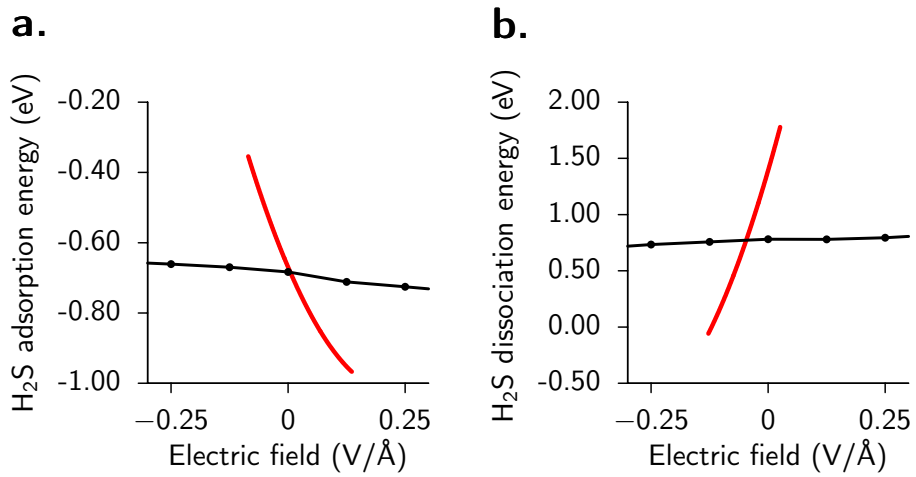

Figure 2-21: For comparable electric field strengths, reaction energies calculated at the aqueous interface show a steeper variation than those calculated at vacuum surfaces, indicating that the interfacial electric field does not affect energies of reactions like (a) H_2S adsorption or (b) H_2S dissociation

surface orbitals. Trends in adsorption energy against electrode potential can be rationalized by relating the varying electrode potentials to varying Fermi levels (and correspondingly different filling of the a1 surface state) within the rigid band formalism (See Figure S1)

Figure 2-23 shows that the interaction of the $1b_1$ HOMO state of H_2S with the conduction band edge of the uncharged surface leads to the formation of a completely filled bonding state and any subsequent increase in the Fermi level (corresponding to more negative potentials) only results in the filling of antibonding states that would lead to the weakening of the adsorption bond.

In contrast, interaction of the a_1 conduction band state with the 1*s* state of the H atom leads only to a partially filed bonding state (Figure 2-24). Therefore, increasing the Fermi level of the surface (more negative potentials) leads only to subsequent filling of the bonding state, further strengthening the FeS_2-H bond.

2.7.3 Conclusions

We performed a two-step classical MD and *ab initio* DFT simulation of the charged interface between the FeS_2 (100) surface and water molecules to understand the effect of electrode potential on energies of adsorption and dissociation of H_2S and atomic H species. We shows that the bilayer structure of the EDL, especially the dense water adlayer adjacent to the surface is critical in reproducing the expected electronic structure and reactivity in aqueous environments. The intense electric field due to the charged electrode surface and the resulting polarization of molecules in the EDL do not significantly affect reaction energies for small, non-polar adsorbates like H_2S and atomic H. Instead, most of the variation in adsorption and dissociation energies with electrode potential can be explained on the basis of varying Fermi level of the electrode and the relative filling of the bonding and anti-bonding states of the electrode-adsorbate bond, as described in the *d*-bond model of surface activity of transition metals and their compounds.

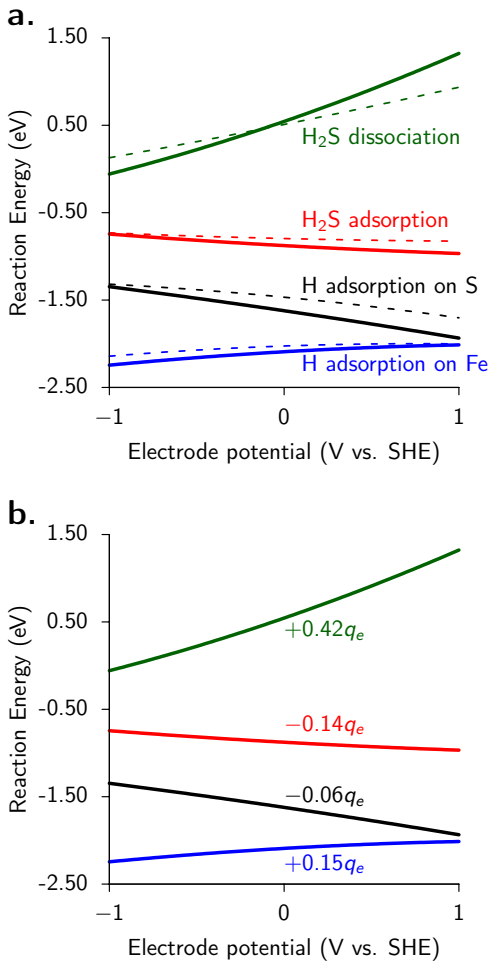

Figure 2-22: (a) Reaction energies calculated using simulations containing polarizable water molecules in the EDL (solid lines) are similar to those calculated using fixed water molecules (dashed lines), showing that EDL polarization is not a significant factor affecting reaction energies. (b) The variation of reaction energies with electrode potential closely mirrors the magnitude of charge transfer to the Fermi level. The color scheme is identical to (a).

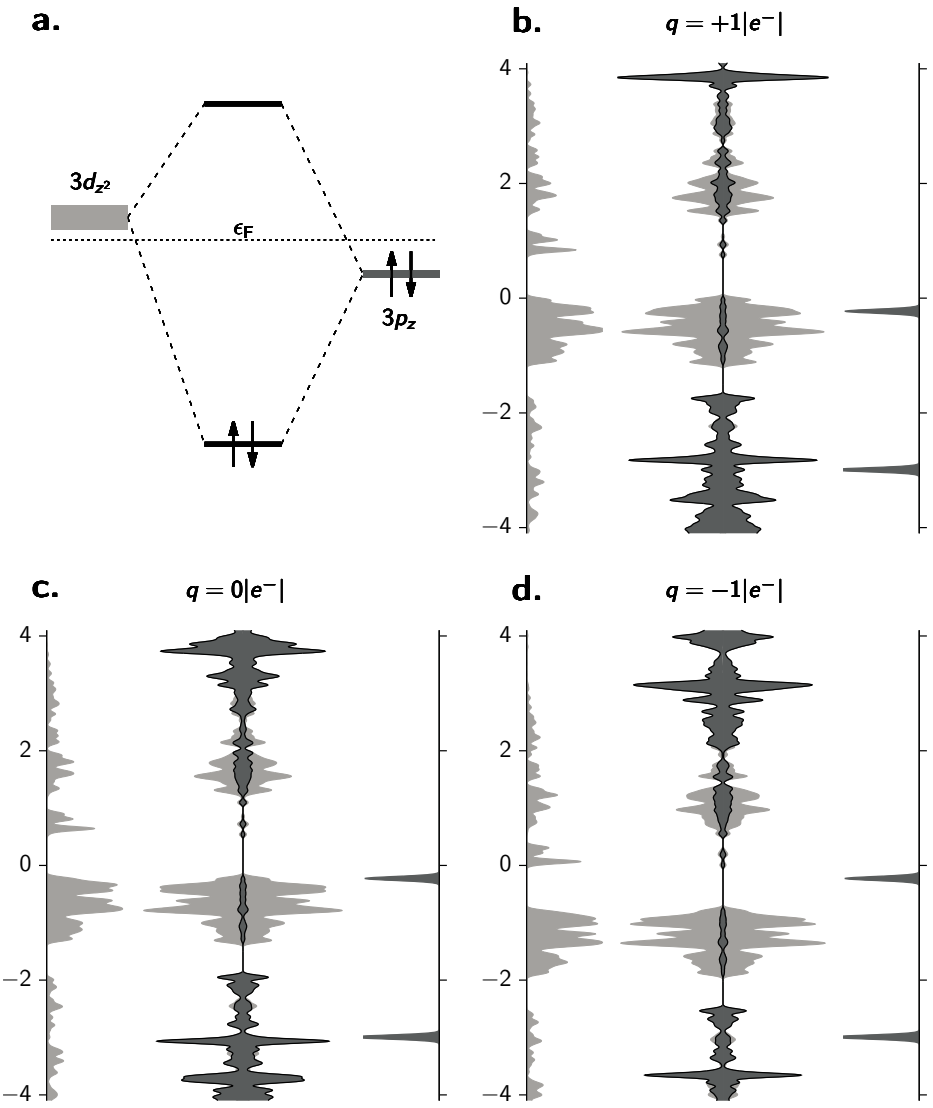

Figure 2-23: (a) The molecular orbital diagram of the H_2S-FeS_2 bond shows that a higher Fermi-level leads to increased filling of the antibonding state, leading to a weaker bond, as demonstrated by the Density of States of (b) positively-charged (c) neutral and (d) negatively-charged FeS_2 surfaces. The adsorbate density of states are amplified 4X for clarity.

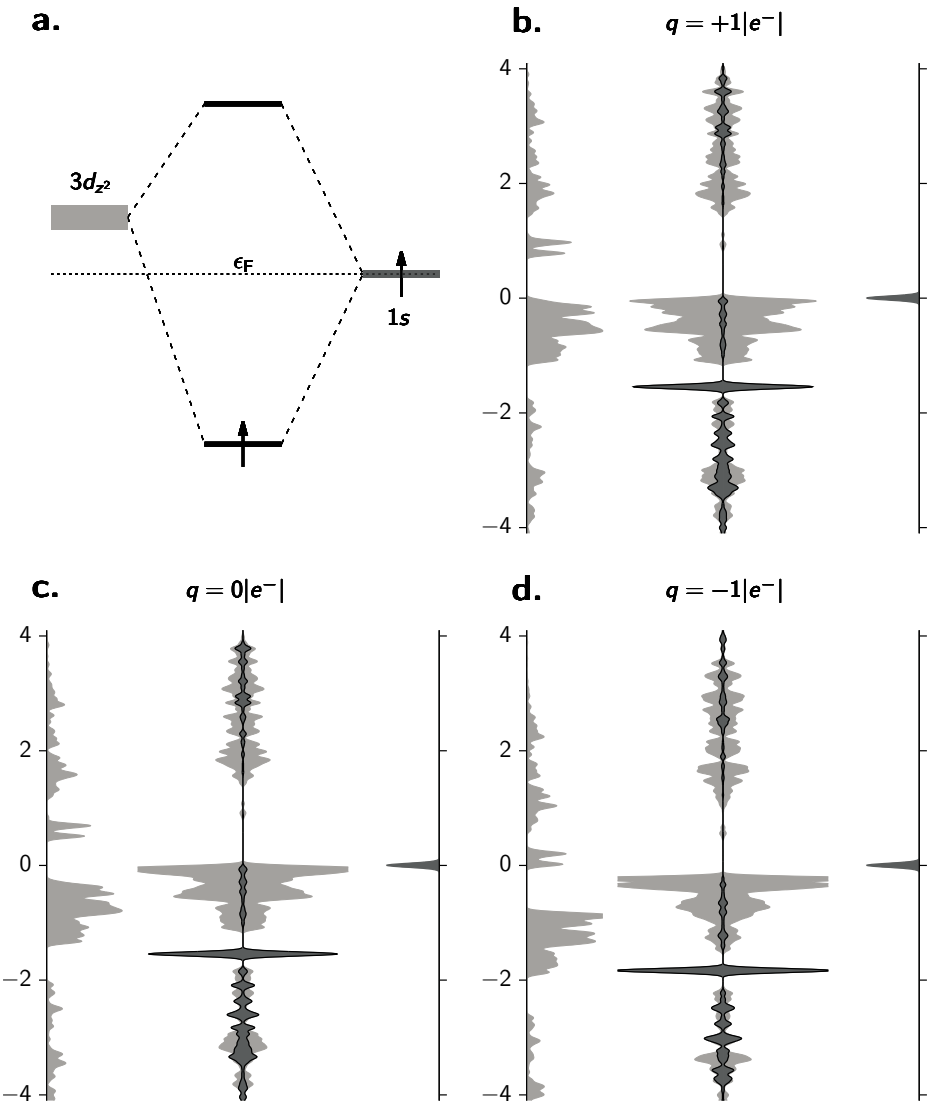

Figure 2-24: (a) The molecular orbital diagram of the H-FeS_2 bond that a higher Fermi-level leads to increased filling of the partially-occupied bonding state, leading to a stronger bond, as demonstrated by the Density of States of (b) positively-charged (c) neutral and (d) negatively-charged FeS_2 surfaces. The adsorbate density of states are amplified 6X for clarity.

2.8 Outcomes and Future Work

The primary aim of this chapter is to provide a quantitative understanding of the effect of surface defects, charge state and adsorbate coverage on the reactivity of the pyrite, FeS_2 (100) surface in an effort to estimate the behavior of passive film surfaces in realistic corrosion conditions. Below, we summarize the results from the previous three sections and propose an outline for extending the work in this thesis.

2.8.1 Outcomes

Surface defects: Intrinsic vacancies induce the formation of defect states in the band gap, where anion vacancies form donor-like defect states while cation vacancy states are more acceptor-like. A reduction in symmetry at the (100) surface caused the formation of surface states connected to the edges of the valence and conduction bands. The presence of these surface states is responsible for the marked reduction in the band gap of the pyrite from 0.86 eV in the bulk to 0.55 eV on the (100) surface. The reduction of the band gap at the pyrite surface and the presence of defect states in the gap lead to the formation of a more reactive surface, and has important implications for charge transfer reactions at the surface as in catalysis and corrosion. Specifically, H_2S adsorption becomes extremely exothermic by $\approx$ 4eV and H_2S dissociation becomes a barrier-less process on the reactive point defect sites.

Surface coverage: On the FeS_2 surface, repulsive interactions between H_2S molecules, arising mainly from changes in the surface electronic structure were found to affect the H_2S adsorption energy by over 0.55 eV. Inter-adsorbate interactions also show a strong dependence on the biaxial strain on the surface, with compressively strained surfaces exhibiting the strongest inter-adsorbate interactions. The large magnitude of these inter-adsorbate interactions as well as their strong dependence on experimental parameters like surface strain highlight the need for moving beyond 'zero-coverage' adsorption energies in the material screening process, especially for strained catalyst systems. Towards this end, the identification and quantification of individual contributions to the inter-adsorbate interactions described in this work can help understand how adsorption energies on realistic surfaces vary with experimental conditions, enables more accurate surface reaction kinetic models, and provides for better-informed screening of materials for heterogeneous catalysis applications.

Surface charge/potential: The intense electric field due to the charged electrode surface and the resulting polarization of molecules in the EDL do not significantly affect reaction energies for small, non-polar adsorbates like H_2S and atomic H. Instead, most of the variation in adsorption and dissociation energies with electrode potential can be explained on the basis of varying Fermi level of the electrode and the relative filling of the bonding and anti-bonding states of the electrode-adsorbate bond, as described in the *d*-bond model of surface activity of transition metals and their compounds.

2.8.2 Future Work

The work described in section 2.6 quantifies the interactions between adsorbed H_2S molecules on a defect-free FeS_2 (100) surface. This is a marked improvement over the zero-coverage DFT-calculated adsorption energies used to estimate surface reactivity. A natural extension of this approach with respect to sour corrosion is to investigate FeS_2 surfaces with adsorbed H_2S and H_2O molecules. This will enable us to quantify H_2S-H_2S, H_2S-H_2O and H_2O-H_2O inter-adsorbate interactions and enable modeling of the sulfidation process at the FeS_2-H_2O interface, which is of immediate relevance to

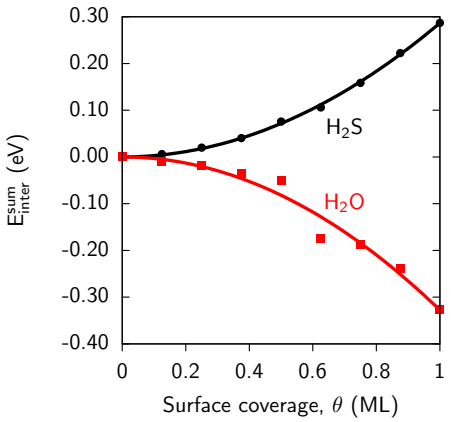

Figure 2-25: Interactions within the H_2O adlayer on the FeS_2 (100) surface are attractive in contrast to interactions within the H_2S adlayer

the sour corrosion process. This is especially interesting because as preliminary data in Figure 2-25 shows, the more compact charge distributions and the more polar bonds of water molecules lead to a negative inter-adsorbate interaction energy for the water adlayer, indicating an effective attraction between water molecules, in contrast to the case for H_2S molecules.

Section 2.7 demonstrates how the surface charge state impacts the electronic structure and therefore the thermodynamics of adsorption and dissociation reactions on a defect-free FeS_2 surface and is an important step in modeling reactivity of surfaces under a constant electric potential, as encountered in electrochemical systems. A reasonable next step would involve the quantification of adsorption and dissociation thermodynamics on the surface of FeS_2 containing point defects. This is of both practical and scientific interest because localized defect states associated with these surface vacancies are known to cause Fermi level pinning, leading to new behavior that is not observable in the defect-free calculations described above.

Another potentially interesting study be to identify the difference between the reactive properties of charged surfaces of semiconducting pyrite, semi-metallic pyrrhotite and metallic mackinawite. Such a study would provide insights about how charge transfer is affected by Fermi-level variations in materials with different band-gaps.

Chapter 3

Fe^{2+} diffusion in magnetic pyrrhotite

3.1 Abstract

In this chapter, we report on the growth of off-stoichiometric pyrrhotite ($Fe_{1-x}S$) phases, a process which is kinetically-limited by the diffusion of cations through the bulk of the pyrrhotite phase. Specifically, we performed DFT and kMC modeling to quantify the role of various structural and magnetic phase transformations in the pyrrhotite crystal on the self-diffusivity of Fe^{2+} cations, in order to explain the significantly suppressed diffusivities observed in natural and synthetic pyrrhotite crystals in tracer and magnetokinetic experiments.

We identify, using on-lattice kinetic Monte Carlo simulations of the anti-Curie λ-transition, that a single value of cation migration barrier is sufficient to capture the complex (i.e. not simple-exponential) kinetics of this phase transformation across a range of pyrrhotite vacancy superstructures and polytypes. This implies that stoichiometry - dependent vacancy ordering transformations do not significantly impact the diffusivity of Fe through pyrrhotite.

On the other hand, non-collinear hybrid Density Functional Theory calculations of cation migration barriers and cation vacancy formation in pyrrhotite crystals indicates that both defect formation and migration are significantly more difficult in the low-temperature AFM phase than in high-temperature magnetic phases. Specifically, cation migration in the AFM magnetic phase has a barrier of 1.3 eV, which is 0.8 eV greater than the value than in the FM phase (which is representative of the behavior of high-temperature PM phase, which is difficult to simulate). This agrees both qualitatively and quantitatively with recent low-temperature radiotracer measurements of cation diffusivity in pyrrhotite.

Both these results indicate that while the different vacancy configurations and polytypes of pyrrhotite have negligible impact on Fe diffusivity, the intermediate-temperature magnetic phase transition leads to an increase in the migration barrier of Fe^{2+} ions, and a concomitant decrease in Fe self-diffusivity at lower temperatures. This can result in a difference of over two orders of magnitude between the low-temperature diffusivity and the extrapolated high-temperature diffusivity at operating sour corrosion conditions around 180 °C. These two studies together provide the physical basis for the role of second order vacancy and magnetic ordering transformations on the cation migration barrier in pyrrhotite and provide a complete picture of diffusivity of iron in pyrrhotite

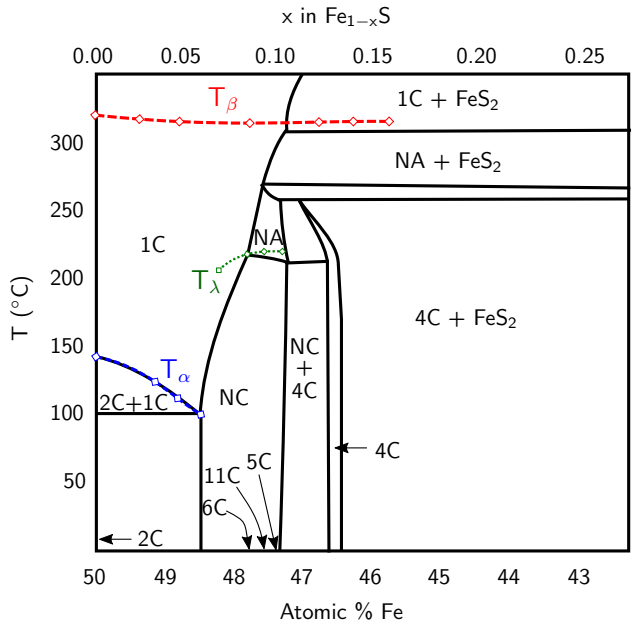

Figure 3-1: Iron-sulfur phase diagram near the region-of-stability of the pyrrhotite phases

as a function of temperature and stoichiometry, which is an important parameter for calculating the growth-rate, thickness and protectiveness of pyrrhotite scales for higher scale corrosion models like the one discussed in Chapter 6.

3.2 Motivation

Pyrrhotites are a family of thermodynamically stable off-stoichiometric iron sulfides ($Fe_{1-x}S$; $0 \leq x \leq 0.125$) commonly found in sour corrosion passive films formed under high-temperature highly sulfidizing environments [12] (See Figure 3-1). Under these conditions, the behavior of pyrrhotite is defined by its role as a diffusion barrier, thus necessitating a fundamental understanding of ionic diffusivity in this material. While it is rate-limiting, pyrrhotites have relatively high diffusivities due to a large degree of off-stoichiometry leading to a diffusion-limited growth rate of the form $X = \sqrt{4Dt}$ [11, 13]. Thus, while the high-temperature diffusivity in pyrrhotite has been consistently measured by several authors using thermogravimetric [121–123] and radiotracer methods [124, 125], the precise value of cation self-diffusivity D^*_{Fe} at low temperatures is difficult to obtain due to the widely-varied stoichiometry, multitude of polytypes and numerous structural and magnetic phase transformations. Among these factors, the role of pyrrhotite off-stoichiometry on mass transport in pyrrhotite is known to affect D^*_{Fe} by one order of magnitude [121], but the impact of phase transformations is less well understood.

This is especially important in light of recent radiotracer measurements [126, 127] which indicate a markedly reduced diffusivity of intermediate temperatures highlighting a phase transformation at 315 °C. Therefore, for a truly predictive model of pyrrhotite diffusivity, we must quantify the $V_{Fe}{}^{\times}$ migration barriers as well as the impact any structural and magnetic phase transformation on these barriers.

This is especially important in light of recent radiotracer measurements [126, 127] which indicate a markedly reduced diffusivity of intermediate temperatures highlight-

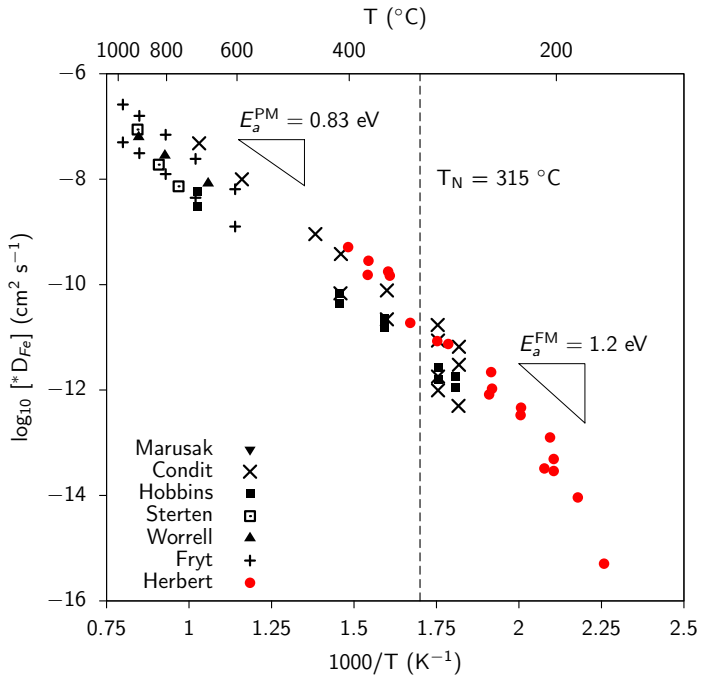

Figure 3-2: Figure 2: Collected literature values of Fe self-diffusivity. Data from Marusak [128], Condit [125], Hobbins [124], Sterten [123], Worrell [122], Fryt [121] and Herbert [129]. Red points indicate data that show different slopes at low and high-temperature regions.

ing a phase transformation at 315 °C. Therefore, for a truly predictive model of pyrrhotite diffusivity, we must quantify the V_{Fe} migration barriers as well as the impact any structural and magnetic phase transformation on these barriers.

3.3 Chapter goals and layout

The primary goal of this chapter is to quantify the migration barrier and therefore the self-diffusivity of V_{Fe} in pyrrhotites of different vacancy and magnetic configurations. The chapter is divided into four sections, as summarized below.

a. **Structural and magnetic phase transformations in non-stoichiometric $Fe_{1-x}S$ phases** describes the various first and second order phase transformations that can occur in pyrrhotite at intermediate temperatures

b. **Diffusion in pyrrhotite polytypes and effect of vacancy ordering** explores the effective diffusivity of Fe ions over the course of a vacancy rearrangement transformation from one pyrrhotite polytypes to another

c. **Diffusion in magnetic pyrrhotite phases discusses the impact of local magnetic order** (ferromagnetic, antiferromagnetic and paramagnetic) on the barrier of migration of an Fe ion

d. The final section, **Outcomes and Future Work**, discusses the effective diffusivity for pyrrhotite of different stoichiometries, polytypes and temperatures and its impact on the modeling

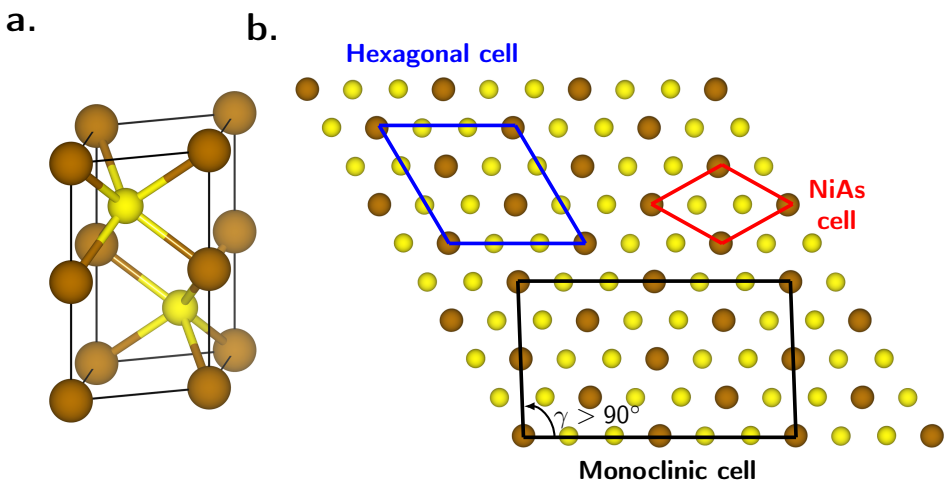

Figure 3-3: Pyrrhotite crystal structures. (a) The hexagonal NiAs unit cell that serves a basis cell for all pyrrhotite crystal structures. (b) Relations between the NiAs- hexagonal- and monoclinic-cells along the ab plane of the crystal

3.4 Structural and magnetic phase transformations in non-stoichiometric $Fe_{1-x}S$ phases

In this section we will describe the underlying crystallographic and magnetic properties common to pyrrhotite family of phases and identify phase boundaries that separate pyrrhotite phases of different atomic and magnetic structure

3.4.1 Crystal and defect structure and magnetism in pyrrhotite

The term pyrrhotite refers to a family of off-stoichiometric $Fe_{1-x}S$ phases in the stoichiometry range of $0 \leq x \leq 0.125$, which constitute the most complex region in the Fe-S phase diagram [130]. The crystal structure of all members of this family is derived from a hexagonal basis cell containing two formula units of FeS arranged according to the Nickeline (NiAs) crystal structure with basis vectors a and c and space group $P6_3/mmc$ [131–135]. The most obvious example of this underlying structure is found in the case of Troilite, the stoichiometric end-member of the pyrrhotite family, which adopts a hexagonal unit cell with lattice parameters $A = B = 3a$ and $C = 2c$

Other off-stoichiometric pyrrhotites are derived from this hexagonal structure by introducing neutral cation vacancies, V_{Fe}. At low and intermediate temperatures below 250 °C, these cation vacancies, which can number up to 12.5% of cation sites, rearrange themselves to minimize inter-vacancy interactions into stoichiometry-dependent superstructures known as Kagome nets: an array of tetrahedral that share apexes in all three dimensions [136]. The multitude of pyrrhotite polytypes thus formed are characterized based on the periodicity of the vacancy superstructure along the z-axis into $2C, 4C, 5C$ or more generally, NC, where C refers to the z-axis dimension of the underlying NiAs hexagonal cell. The formation of such ordered vacancy superstructures also slightly deforms the unit cell causing $4C$ and other pyrrhotites to adopt a monoclinic, rather than a hexagonal unit cell. At higher temperatures, (specifically above the $NC - 1C$ solvus line in Figure 3-1 the cation vacancies entropically disorder leading to a breakdown of ordered Kagome structures and a uniform distribution of vacancies leading to the formation of the so-called $1C$ superstructure.

In addition to these structural phase transformations, pyrrhotite phases of all compositions exhibit a second-order magnetic phase transformation, also called the β-transition, at the Néel temperature, $T_N = 315°C$ [137]. Above this Néel temperature, the localized moment on the Fe^{2+} ions (which adopt a valence shell electronic structure of $\left(t_{2g}\right)^4\left(e_g\right)^2$ with a net magnetic moment of $4\mu_B$) are randomized spatially and temporally leading to a paramagnetic crystal with zero net magnetism. Below this Néel transition temperature, the spins on the Fe ions align such that they are ferromagnetically coupled in each $a-b$ plane and are AFM-coupled between adjacent $a-b$ planes in the c direction, giving rise to an AFM crystal.

Considering the low temperature distribution of vacancies in Kagome nets as well as the low-temperature antiferromagnetic arrangement of magnetic moments, it is easy to generalize that most pyrrhotite phases are AFM at room temperature. The exception to this generalization is the $4C$ pyrrhotite, which, due to its unique vacancy arrangement, retains an uncompensated net magnetic moment as shown in Figure 3-4 [138, 139].

3.4.2 Common pyrrhotite polytypes

Troilite

Troilite (FeS) adopts a $2C$ hexagonal unit cell with dimensions $A = B = 3a$ and $C = 2c$. In the absence of cation vacancies, phase transitions in this crystal are defined purely in terms of changes in the magnetic order on the Fe^{2+} ions. At temperatures below 140 °C, magnetic moments on the cations are arranged antiferromagnetically with spins aligned parallel to the c-axis. Above this temperature, the crystal undergoes a spin-flip transition, with local spins are pointed along the a-axis, but the spins continue to remain antiferromagnetically coupled between adjacent $a-b$ planes. This spin-flip transition is related to structural parameters, especially the Fe-Fe inter-ionic distances and is therefore accompanied by minor changes in the lattice parameters and volume of the unit cell [140]. The second magnetic phase transformation occurs at the Néel transition temperature of 315 °C, when these in-plane spins completely disorder to form a paramagnetic crystal, in common with other pyrrhotite phases.

$4C$ pyrrhotite

The most Fe-deficient pyrrhotite has a stoichiometry of $Fe_{1-x}S$; $0.120 \leq x \leq 0.125$ and it adopts a monoclinic structure where the Fe cation sublattice is arranged in alternating fully-filled and partially-vacant layers with a stacking sequence along the c-axis of the form $\cdots FAFBFCFD\cdots$, where F represents a fully filled layer of Fe^{2+} ions and A, B, C and D represent 25% vacant layers containing vacancies in four different in-plane configurations [141]. This ordered arrangement deforms the underlying hexagonal lattice into a monoclinic structure with a periodicity along the c-axis of four-times that of the NiAs unit cell.

The uncompensated magnetic moment due to the alternating filled and partially-vacancy ionic layers is lost when these vacancies disorder at the $4C-1C$ solvus line. This loss of net magnetic moment is complete when the individual spins themselves disorder causing paramagnetism in the crystal. Previous neutron diffraction experiments [137] indicate that both the magnetic and vacancy ordering phase transitions occur within a very narrow window of temperatures and may even overlap with each other.

NC pyrrhotite

Between the two extremes of pyrrhotite composition, there exist a wide variety of monoclinic pyrrhotite polytypes, whose stoichiometry-dependent vacancy superstructures have periodicities along the c-axis ranging from 5-11 times that of the NiAs unit cell. A major difference between the $4C$ and NC pyrrhotites is that in the NC pyrrhotites, the position of vacancies in the crystal are not deterministically known and are best described probabilistically [133, 142]. However, like $4C$ pyrrhotite, these phases also undergo magnetic ordering at the Néel temperature, while the vacancy disordering temperature (coincident with the $NC-1C$ solvus line) is very dependent on the stoichiometry.

3.4.3 Diffusion in pyrrhotite polytypes and effect of vacancy ordering

As described previously, the primary aim of this project is to quantify the effect of vacancy configuration on diffusivity and therefore measure the relative values of D^*_{Fe} in different pyrrhotite polytypes. An ideal system to investigate this property is the λ-transition that is characteristic of NC pyrrhotite phases, which is exemplified by the appearance of a peak in the magnetization vs temperature profile as a NC pyrrhotite is heated. This unusual anti-Curie transition (where the net magnetization σ increases as T increases) is present in all natural, geological, single crystal and nanowire samples. This transition is thought to occur by diffusive rearrangements of $\mathrm{V_{Fe}}$ from a NC to a $NC+4C$ structure followed by a complete disordering of vacancies to form the $1C$ phase [128, 143]. This initial rise in the net magnetization due to the formation of $4C$ and subsequent decay leads to the characteristic peak-like pattern in the $\sigma-T$ graph.

Therefore, to understand the mechanism and kinetics of this diffusion-driven phase transformation, we perform a kMC simulation of the temperature-dependent and time-dependent evolution of the net magnetic moment of the $11C$ pyrrhotite sample as it undergoes the λ-phase transition to a $4C$ sample, assuming only diffusion unit processes. In contrast to previous studies of Marusak *et al.* [128], we find that the kinetics of the λ-transition follows the general form of a stretched exponential function

$$\alpha(t) = 1 - \exp\left(-\left(\frac{t}{\tau}\right)^n\right) \tag{3.1}$$

where τ is the temperature-dependent relaxation time and, n is the stretching exponent and $\alpha(t)$ is the extent of the phase transformation at time t. In the following sections, we describe the setup of the kMC calculation and discuss the mechanism of the lambda transition along with the physical basis for the stretched exponential form of reactions as well as a derivation of the diffusion migration barrier.

Methods

Kinetic Monte Carlo (kMC) simulations were performed on a model block of cation deficient pyrrhotite to test the mechanistic hypothesis that mass transport of vacancies between AB-planes at elevated temperatures can gradually convert an antiferromagnetic lattice to a ferrimagnetic one. The model aimed to simulate the time-dependent magnetization of a superstructure containing randomly-dispersed vacancies as it evolves towards a more $4C$-like, layer-by-layer alternating occupancy structure. We defined an

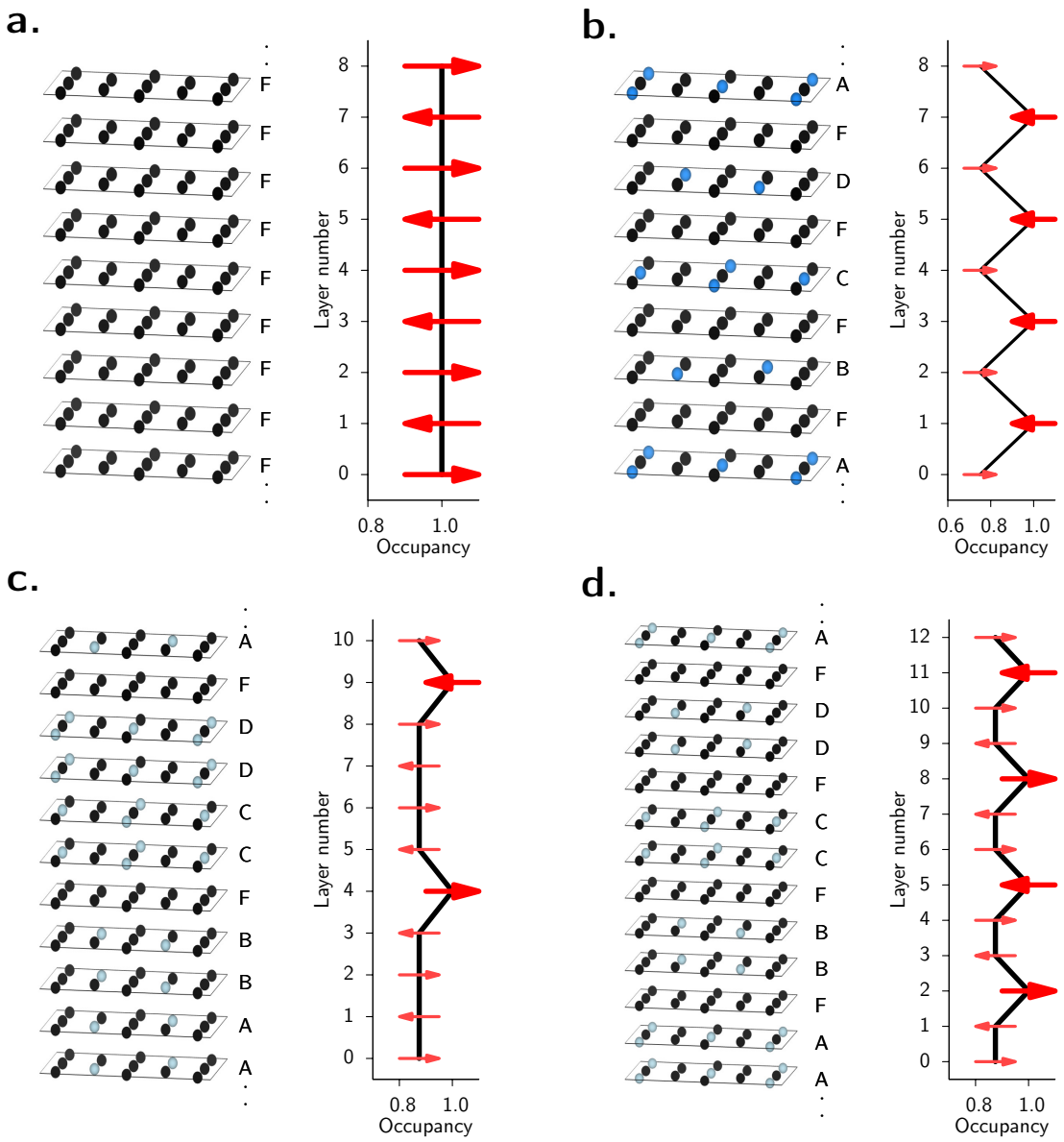

Figure 3-4: Pyrrhotite polytypes. The distribution of Fe atoms (black), Fe vacancies (blue) and partial vacancies (light-blue) in one unit cell of the (a) Troilite, (b) 4C, (c) 5C (d) 6C pyrrhotite crystal structures. Each structure is accompanied by a graph of the atomic occupancy in each layer. The size and direction of arrows indicate the magnitude of overall magnetic moment in the layer.

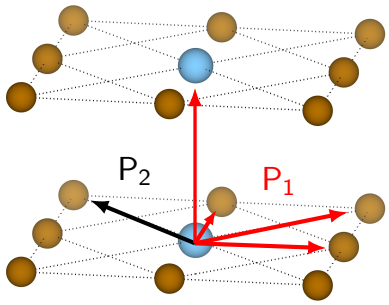

Figure 3-5: Schematic of the diffusion unit processes modeled in the pyrrhotite kMC calculation. Diffusive hops indicated in red occur with a probability P_1 while those in black occur with a probability $P_2 = \sqrt{3}P_1$

order parameter based on the ideal $4C$ pyrrhotite vacancy distribution shown in Figure1b of the main text to continually assess the magnetism of the structure as it evolved in time through diffusive jumps of V_{Fe} alone.

These kMC simulations are defined by the probability P of a diffusive vacancy jump, given by: (i) the intrinsic activation barrier to migration E_m ; (ii) an energy bias, E_{therm}, due to a thermodynamic driving force towards ordering; and (iii) a bias due to the magnetic energy, E_{mag}

$$P = \nu \exp\left(-\frac{E_m}{k_B T}\right) \exp\left(-\frac{E_{\text{therm}}}{k_B T}\right) \exp\left(-\frac{E_{\text{mag}}}{k_B T}\right) \tag{3.2}$$

where k_B is Boltzmann's constant. The energy barrier E_m was taken to be 1.2 eV, as calculated from Density Functional Theory. The energy term E_{therm} was based on thermodynamic data for pyrrhotite polytypes. Subsequent to each diffusive jump, an order parameter Θ was assigned to the updated structure, based on the root mean squared (RMS) difference from the periodically alternating occupancy of a perfectly vacancy-segregated superstructure. Net magnetization σ was evaluated by summing over all individual magnetic moments on lattice sites.

A detailed list of simulation parameters are provided below:

1. A three-dimensional, cubic Ising model block consisting of $20 \times 20 \times 44$ unit cells was set up. Only iron sites were considered, under the assumption that the sulfur sublattice is saturated and therefore does not contribute to mass transport. Individual lattice points can be full (1) or vacant (0) only. The hexagonal symmetry of the NC-type pyrrhotite lattice was imposed by biasing the diffusion paths such that a hop in one of the diagonals was $\sqrt{3}$ times as unlikely (Figure 3-5).

2. One in every eleven sites was selected to be 0 at random to simulate an antiferromagnetic, $11C$ lattice. The start point for the lattice is not ordered; however, there is no unique 11C structure established in the literature. Moreover, we found that imposing a rigid initial structure only added to computation time without affecting the time-evolution results

3. A vacant site in the structure was selected at random and its nearest neighbor (NN) sites are evaluated as potential jump destinations. The only atomic process modeled by the kMC code was the diffusion of V_{Fe} in the a-, b-, c- directions. Occupied NN's populated a list of diffusive jump locations; specifically, five nonequivalent diffusion paths with different jump probabilities were considered

(Figure 3-5). The probability P for a jump to any of these sites is calculated in a subroutine using equation described above, based on:

(a) the self-diffusivity or intrinsic activation barrier to migration E_m, in the absence of an imposed driving force;

(b) an energy bias due to a thermodynamic driving force towards ordering, E_{therm}, as described below in step (4);

(c) a bias due to the magnetic energy in the applied field of 10 kOe, E_{mag};

4. Subsequent to each diffusive jump, the occupancy of the seven adjacent supercell planes above and seven below the elected vacant site was assessed. The closeness of the layer-by-layer occupancy of this volume was compared to the idealized ferrimagnetic 4C-type lattice occupancy (...full, 1/4 vacant, full, 1/4 vacant ...) and was quantified by taking the root mean square (RMS) difference from the ideal 4C structure occupancy

5. The energy landscape of the simulation was biased such that the structure is thermodynamically driven to evolve towards a more 4C-like structure. A linear bias of the form $E_{\text{therm}} = A\Theta + B$ was used, where the parameters A and B provide the difference in Gibbs free energy, ΔG between a disordered vacancy structure and the 4C structure at a given temperature of interest, and Θ is the order parameter we assign to the system, with 0 assigned to a randomly-ordered antiferromagnetic lattice and 1 representing the full 4C structure. The free energy, G of each phase at a given temperature was approximated via the relation:

$$G = \Delta H_{f,298K} + \int_{298K}^{T} C_p \mathrm{d}T - T\left[S_{298K} - \int_{298K}^{T} \frac{C_p}{T}\mathrm{d}T\right] \tag{3.3}$$

where $\Delta H_{f,298K}$ is the formation enthalpy at 298 K, S_{298} K is the entropy at 298 K and C_p the heat capacity. Values for these thermodynamic parameters, as listed in Table 3.1, were obtained from Waldner and Pelton [144].

Pyrrhotite polytype	$\Delta H_{f,298K}$ **(kJ/mol)**	S_{298K} **(J/mol-K)**	C_p **(J/mol-K)**
FeS (2C)	-100.1	60.3	$2437.1 - 9.9T + 0.01T^2 - (41.1 \times 10^6)T^{-2}$
$Fe_{11}S_{12}$ (6C)	-1148.1	755.2	—
$Fe_{10}S_{11}$ (11C)	-1048.5	693.0	—
Fe_9S_{10} (5C)	-950.8	623.5	$170.6 - 0.5T + 0.0005T^2 - (3.0 \times 10^6)T^{-2}$
Fe_7S_8 (4C)	-755.4	486.3	$140.5 - 0.7T + (3.1 \times 10^{-7})T^2 - (3.9 \times 10^6)T^{-2}$

Table 3.1: Thermodynamic properties of different pyrrhotite polytypes as used in the diffusion kMC model

Results - Magnetokinetics and continuous ordering of the vacancy superlattice

We performed a time-dependent isothermal measurement of magnetic moment on simulated pyrrhotite crystals with an initial 11C configuration of vacancies at temperatures between 180-210 °C for up to 100000 seconds.

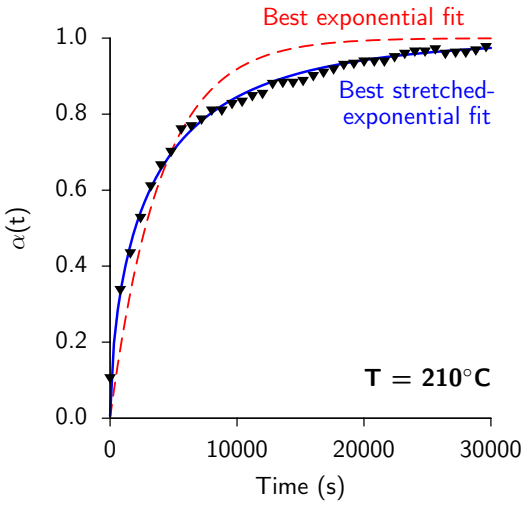

Figure 3-6: The magnetokinetic data from the kMC calculation is much better described using a stretched exponential kinetics than using simple exponential kinetics

Temperature (°C)	n	τ
180	0.70	737 ± 38
190	0.73	651 ± 40
200	0.66	275 ± 19
210	0.62	150 ± 8

Table 3.2: Best fit parameters for the stretched exponential expression

The time-dependent magnetic moments at each temperature were converted to an effective phase fraction of the ferrimagnetic (FIM) phase to represent the extent of the reaction, $\alpha_{FIM}(t)$ is given by

$$\alpha_{FIM}(t) = \frac{\sigma(t) - \sigma(0)}{\sigma(t_{end}) - \sigma(0)} \tag{3.4}$$

where $\sigma(t)$ is the measured net magnetization at time t and t_{end} is the time elapsed at the end of the kMC calculation. Figure 3-7 shows the results for the kMC-simulated magnetokinetic curves for the λ-transition indicating that the V_{Fe} diffusion is the rate-limiting process in the transformation. Another feature of note is that the magnetokinetics of the transformation is well described by a stretched-exponential function rather than a simple exponential one employed in the earlier studies of Marusak *et al.* [128]. This is in very good agreement with recent magnetokinetic experiments on 11*C* pyrrhotite [126].

The stretched exponential parameters provide a quantification of the reaction kinetics but not of the atomic mechanism underlying the transformation. Generally τ represents the temperature-dependent relaxation time and n is the deceleration in reaction kinetics with increasing phase fraction. In order to understand the physical basis for the stretched exponential form, we consider other examples of phase transformation and dynamics that express these kinetics.

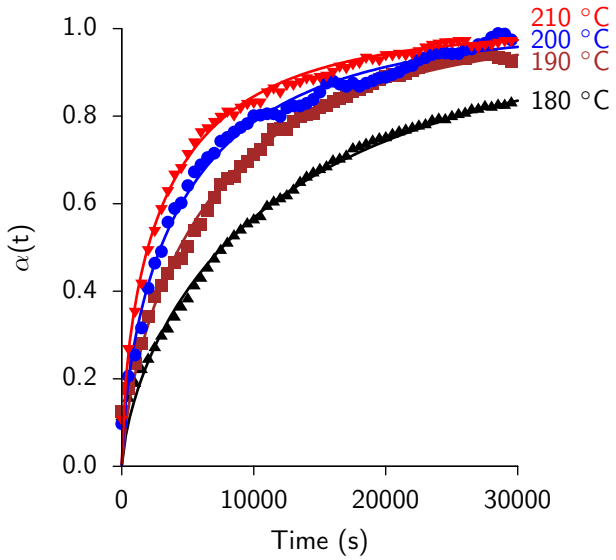

Figure 3-7: Stretched exponential fits for magnetokinetic kMC data at different temperatures along the λ-transition will help extract the effective diffusion barrier in different pyrrhotite polytypes

While less common than simple exponential kinetic forms, stretched exponential kinetics have been previously observed for magnetic and diffusion systems such as

a. Magnetic relaxation in $Li_2(Li_{1-x}Fe_x)N$

b. Nucleation and growth in reduced dimensions

c. Non-equilibrium dynamics described by the Kohlrausch equation

To identify the physical basis for the stretched exponential kinetics in the $Fe_{1-x}S$ system, we compare it to the three mechanisms described above. The magnetic relaxation encountered in $Li_2(Li_{1-x}Fe_x)N$ is observed only at cryogenic temperatures below 20 K [145] and a similar relaxation of spin states is expected to be extremely rapid at the temperatures encountered in the $Fe_{1-x}S$ system. Therefore, this mechanism is unlikely to be responsible for the stretched exponential magnetokinetics in $11C$ pyrrhotite.

Similarly, if we consider the lambda transition to be a classical nucleation and growth process, as described by the semi-empirical JMAK equation, as is the case for the AFM-FM transition in FeRh (which was described using a growth exponent $n = 0.86$ [146])

$$\alpha(t) = 1 - \exp[-Kt^n] \tag{3.5}$$

Within the scope of the Johnson-Mehl-Avrami-Kolmogorov (JMAK) theory, an exponent of value 0.5 describes the formation of the FM phase out of the homogeneous AFM lattice via 1-D growth and zero-nucleation rate. This corresponds to a presence of minute FM nuclei at time $t = 0$ and subsequent growth of magnetic order along one dimension (i.e. in this case, along the c-direction). To verify if this zero-nucleation one-dimensional growth occurs, we look at the spatial distribution of the $4C$ phase in the simulation cell over the course of the λ-transition. Figure 3-8 shows the evolution of the magneto-structural order parameter Θ at different points along the kMC lattice at various times along the lambda transition. Instead of observing the formation of FIM nuclei and their subsequent growth (as would be consistent with the JMAK theory), we observe the emergence of regions of intermediate Θ followed by a diffusion-limited continuous reordering process akin to spinodal decomposition. Evidence for such a second-order

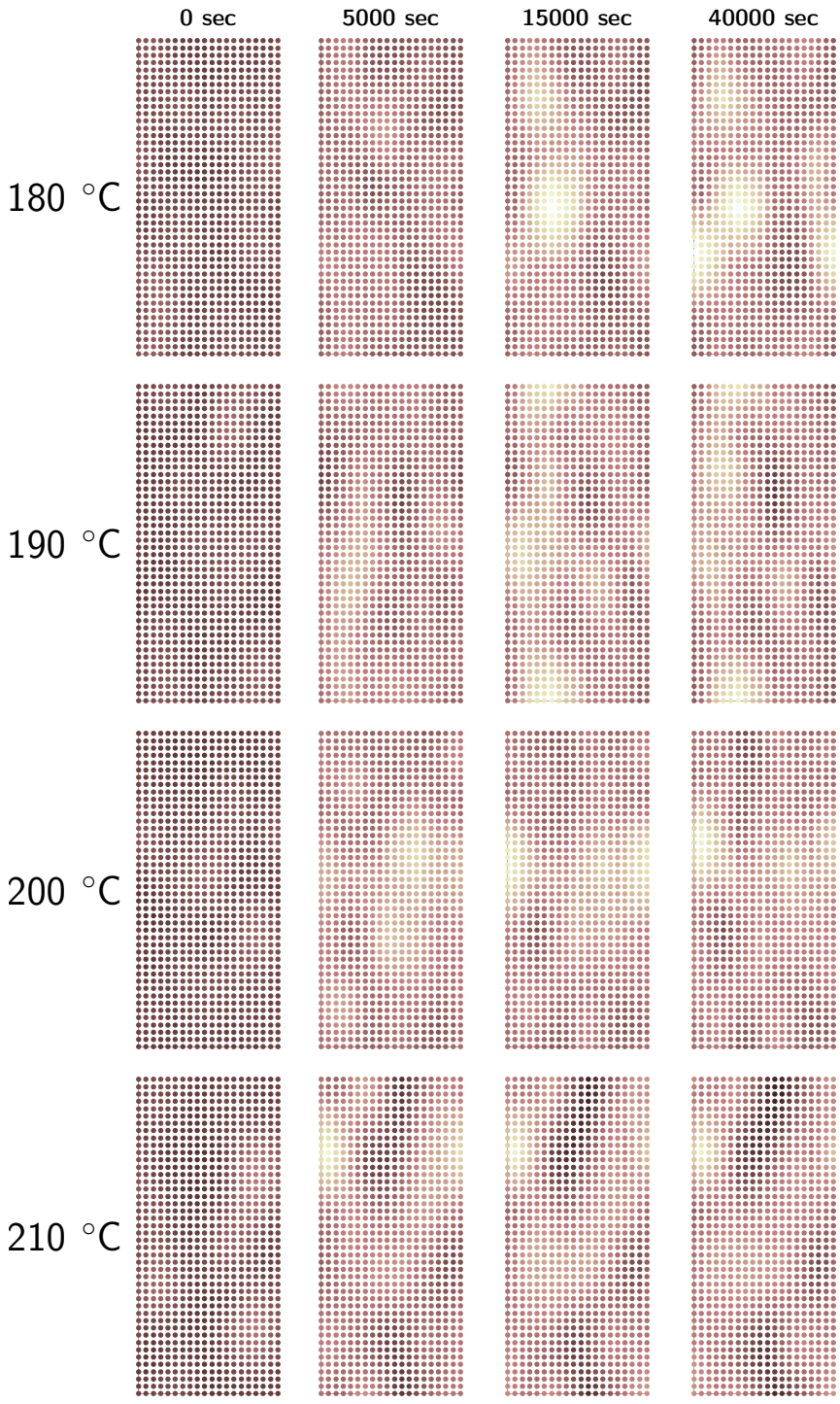

Figure 3-8: Evolution of pyrrhotite order parameter at all temperatures indicates that the λ-transition proceeds via a continuous rearrangement of vacancies rather than by a nucleation-and-growth process.

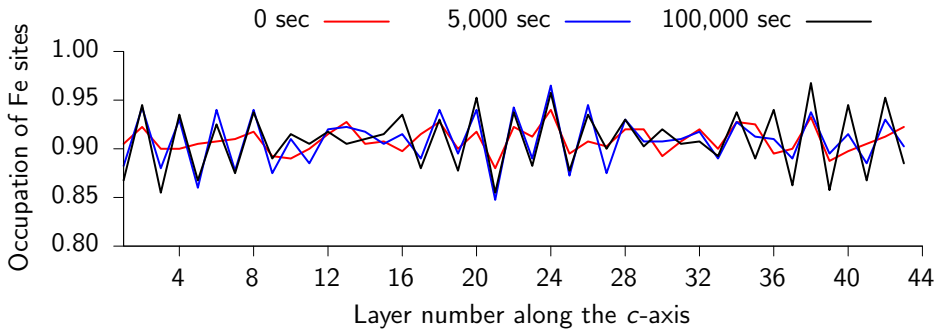

Figure 3-9: Average occupancy of Fe sites in each of the 44 $a-b$-planes in the simulation cell at different times along the λ-transition show a gradual evolution of a $4C$-like structure supporting the hypothesis of continuous rearrangement of vacancies

phase transition is obtained from previous differential scanning calorimetry (DSC) that demonstrate the continuity of enthalpy H, and a discontinuous variation of the instantaneous heat capacity $\frac{\partial H}{\partial T}$, at the λ-transition temperature (at 210 °C) [129]. These observations indicate that a classical nucleation and growth process is not responsible for the observed kinetics of the system.

Therefore, we believe that the stretched exponential kinetics of the transformation as well as the continuous variation fluctuation in the layer by layer vacancy concentrations is best described by the magnetokinetics of the transformation conforming to the Kohlrausch-Williams-Watts law [147] used to describe non-equilibrium dynamics in disordered condensed matter systems such as H migration in amorphous Si and diffusion in glassy systems [148]. This is similar to the present case of $Fe_{1-x}S$, where V_{Fe} diffusion occurs in a continually varying free-energy landscape.

These systems suggest parallels to the existing FeS systems where magnetization evolution may be explained as a combination of short-timescale diffusion processes coupled with longer-timescale evolution of long-range order. Specifically, at temperatures around 200 °C, there is sufficient thermal energy for vacancies to break the AFM ordering found at $t = 0$ and migrating rapidly to adjacent (i.e. along the c-direction) Fe planes due to the thermal driving force over a period of hundreds of seconds, a process that corresponds to a rapid increase in the net magnetization of the pyrrhotite sample.

Further increase in $\sigma(t)$ depends on the much slower evolution of long-range order leading to the observed deceleration of growth in $\sigma(t)$ with increasing time and FIM phase fractions.

Further evidence of this slowdown can be obtained by comparing the number of inter-layer hopes (i.e. Fe diffusive hops between adjacent $a-b$ planes) to the number of intralayer hops (Fe diffusion hops within the same $a-b$ plane). We observe a gradual decrease in the number of inter-layer hops, as a fraction of the total hops over the course of the λ-transformation Since only the interlayer hops contribute to change in $\sigma(t)$, we observe a concomitant decrease in the rate of change of $\sigma(t)$.

In conclusion, the magnetokinetics of the anti-Curie λ-transition in NC pyrrhotites was modeled using an on-lattice kMC model, which identified that this transition proceeds as a nucleation-free continuous ordering transformation mediated by the diffusion of vacancies in the cation sublattice. The kinetics of the transformation was found to be of the stretched-exponential type which is consistent with diffusion dynamics in a continually varying free-energy landscape, as described by the Kohlrausch-Williams-Watts function.

3.5 Ionic diffusion in different magnetic environments

The previous sections demonstrated a quantification of V_{Fe} diffusion through different polytypes across multiple structural phase boundaries. Therefore, the next step in complete quantification of D^*_{Fe} is the identification of the impact of the magnetic phase transformation at the Néel temperature on cation migration. This is especially important because recent radiotracer measurements that show significantly lower mobilities for Fe ions at low temperatures around 150 °C than at temperatures above 320 °C attribute it to the different magnetic states of the pyrrhotite crystal at these temperatures.

In this article, we corroborate this 'magnetic diffusion anomaly' based on the first reported direct quantification of migration barriers and defect formation energies in different magnetic phases of pyrrhotite using hybrid Hartree-Fock/Density Functional Theory calculations. Specifically, ionic diffusion in antiferromagnetically-ordered pyrrhotite is found to be slower, with an activation barrier of 1.35 eV, compared to 0.56 eV for pyrrhotite crystals where local magnetic moments on Fe ions are ferromagnetically coupled. Fe vacancy formation enthalpies follow an identical trend with values for the antiferromagnetic crystals being 1.59 eV higher than that for ferromagnetic ones. We further show that a simple Heisenberg Hamiltonian model of the dominant magnetic interaction, the Fe-S-Fe superexchange can explain the difference in ionic migration barriers and vacancy formation energies between the magnetic phases of pyrrhotite. This mechanistic description of magnetic contributions to ionic transport will not only enable more accurate characterization of pyrrhotite performance in corrosion barriers and future memory devices, but is also broadly applicable to the study of ionic mobilities in other related superexchange-driven antiferromagnetic materials like NiO and MnO.

3.5.1 Methodology

For an accurate characterization of ionic diffusion across the Néel transition temperature, it is necessary to be able to model defect formation and migration in both antiferromagnetic (AFM) and paramagnetic (PM) local order reflecting the magnetic structure of the low and high temperature pyrrhotite respectively. While the properties of the ground state antiferromagnetic configuration are readily accessible within the zero-Kelvin Density Functional Theory (DFT) framework, calculating paramagnetic properties is considerably more challenging using a ground-state method like DFT.

In this regard, there has been considerable progress in modeling paramagnetism in metals like BCC Fe [149–151] and Co [149], but such methods remain to be demonstrated for ionic systems like pyrrhotite. Therefore, in order to capture the effect of local magnetic order, we compare vacancy formation energies and migration barriers from the ground-state antiferromagnetic configuration with another magnetic phase where the local moments on all Fe ions are identical to moments in the AFM phase, but are ferromagnetically aligned to each other (Figure 3-10). This ferromagnetic (FM) state is an acceptable substitute for the PM state in these calculations because, as we describe in Section 3.5.2, both the FM and PM phases lack the extensive Fe-S-Fe superexchange interactions found in the AFM phase which are responsible for affecting the ionic migration barrier. This approach has previously been adopted for the study of the paramagnetic phase of oxides like $LaXO_3$ (X = Sc - Ni), which are similarly intractable using traditional DFT methods [152].

The FM phase is metastable relative to the AFM phase at 0 K. Therefore, we stabilize the FM phase by imposing an energy penalty for magnetic moments that deviate from

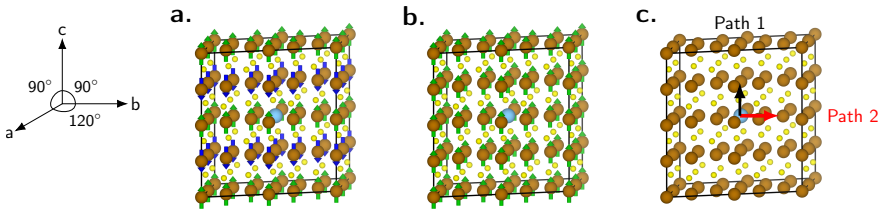

Figure 3-10: (a,b) Two magnetic phases of pyrrhotite considered in this study. Green and blue arrows represent the magnetic moments localized on the Fe ions (brown), while the sulfur atoms (yellow) are nonmagnetic. The Fe vacancy is represented as the light blue sphere at the center of the supercell (c) Ionic migration along the c-axis (black arrow; Path 1) and in-plane migration (red arrow; Path 2) are assumed to proceed through direct ionic hopping. Images rendered using the VESTA program

the FM structure. Specifically, the penalty function applied to the DFT energy is of the form

$$E_{\text{penalty}} = \sum_i \lambda (\mu_i - \mu_{FM})^2 \tag{3.6}$$

where μ_i is the magnetic moment on each Fe site and μ_{FM} is the desired ferromagnetic moment and λ is a scaling parameter that is modified till the energy penalty is less than 5 meV/atom. Our attempts to stabilize a random configuration of magnetic moments (which is more representative of the high-temperature paramagnetic crystal) using this method were unsuccessful.

In order to accurately describe the stability of different magnetic phases, we use the range-separated hybrid functional HSE06 [153], which includes a component of screened Hartree-Fock exchange that offsets the spurious self-interaction error present in semi-local functionals like PBE. This parameter-free hybrid functional has been shown to provide an accurate description of magnetic interaction and electronic structure in transition metal compounds like NiO [154], MnO [155], $EuTiO_3$ [156] and $SrTiO_3$ [157]. First principles calculations were performed in the Kohn-Sham Density Functional Theory framework [75] using the Projector Augmented Wave method [79] implemented in the Vienna Ab-initio Simulation Package [76, 77]. All calculations are performed on a $2 \times 2 \times 2$ supercell of hexagonal pyrrhotite crystal containing 48 formula units of FeS. One-electron wavefunctions were expanded in plane-wave components up to 320 eV and integration in the reciprocal space was done by sampling the Brillouin zone at the gamma point. All calculations were done until supercell energies were converged to within 5×10^{-4} eV and the force on each ion was converged to within 0.1 eV/Å. Ionic migration calculations were performed using the Climbing-Image Nudged Elastic Band to ensure that the saddle point at the transition state is correctly identified [158].

3.5.2 Results and Discussion

Before we discuss the calculated value of vacancy formation energies and migration barrier, and magnetic interactions, we briefly outline the applicability of the HSE06 functional in calculating the properties of ground state antiferromagnetic phase of pyrrhotite. The lattice parameters of the relaxed stoichiometric pyrrhotite supercell are $a = b = 6.73$ and $c = 11.31$ and within 2% of values from experimental [159] and natural samples [160] of pyrrhotite. Another structural parameter of interest in the bonding arrangement around the S^{2-} anion specifically the Fe-S-Fe bond angles, which are vi-

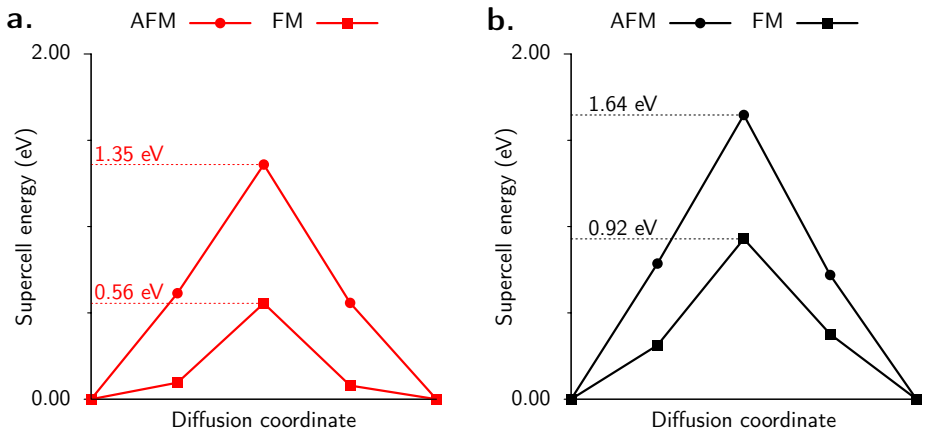

Figure 3-11: Fe migration barriers in the AFM phase of pyrrhotite are approximately 0.8 eV higher than in the FM phase for diffusion along both (a) Path 1 and (b) Path 2.

tal in determining the magnitude of superexchange interaction. Further the magnetic moment inside the PAW spheres of each Fe^{2+} ion is 3.49 μ_B and 0.00 μ_B inside each S^{2-} ion is in good agreement with previous X-ray magnetic circular dichroism measurements [161] and within the range estimated from powder neutron scattering techniques [162].

Ionic migration barriers and vacancy formation energies

A Monte Carlo analysis of diffusion pathways in pyrrhotite by Murch *et. al.* indicated that Fe migration in this phase is dominated by direct ionic hopping between lattice sites [163]. Therefore, we consider only nearest-neighbor jumps between Fe sites and disregard any interstitialcy transport mechanisms in our analysis. Since pyrrhotite is a hexagonal crystal, we model ionic diffusion in two representative directions (Figure 3-10b), i.e. along the c-axis (Path 1) and along the $a-b$ plane (Path 2). We find that ion migration is easiest along the c-axis, occurring with a migration barrier of 1.35 eV, in very good agreement with experimental tracer diffusivities in the low temperature AFM phase of pyrrhotite11. Diffusion along the basal plane (Path 2) in slower with a migration barrier of 1.64 eV because the ionic jump distance is noticeably larger for basal jump (3.4 Å) than for diffusion along the c-axis (2.83 Å).

The migration barriers are significantly lower in the FM phase for both paths 1 and 2 at 0.55 eV and 0.92 eV respectively (Figure 3-11). These lower barriers are consistent with the experimental 'magnetic diffusion anomaly' that leads to faster ion transport at temperatures above the magnetic ordering temperature [121, 125]. These barriers indicate that magnetic interactions lead to an effective strong binding of Fe^{2+} ions to their lattice positions in the AFM crystal. This is supported by a calculation of the vacancy formation energies (Figure 3-12), where ΔH_f^v for AFM phase is significantly larger at 2.44 eV and the corresponding value for the FM crystal is only 0.85 eV. In the following section, we characterize the nature and strength of the magnetic interactions responsible for the difference in ΔH_f^v and E_s^{migr}.

Exchange interactions in the pyrrhotite crystal

Unlike metallic Fe, there is no significant overlap between the Fe 3d orbitals inplane due to the large Fe-Fe interionic distances involved ($\approx$ 3.4 Å). Therefore the dominant

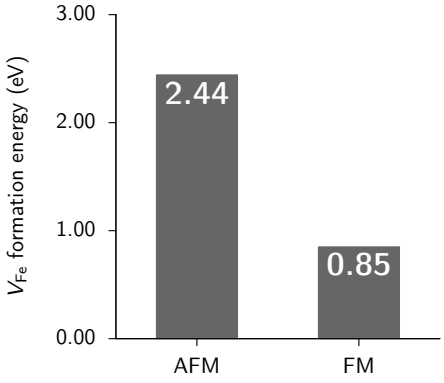

Figure 3-12: Vacancy formation energies are 1.59 eV higher in the AFM phase of pyrrhotite because magnetic interactions stabilize the Fe^{2+} ions at their lattice sites

magnetic interaction in the pyrrhotite system is not direct exchange, but superexchange (SE) where moments on two Fe ions are coupled to one another through an intervening nonmagnetic S^{2-} ion. In a previous study, Lyubutin et. al. applied the Goodenough-Kanamori rules of superexchange [164, 165] to identify that the antiferromagnetic interplanar Fe-S-Fe exchange (black lines in Figure 3-14) is the dominant magnetic interaction in the pyrrhotite crystal [166]. These high-angle AFM interactions are expected to be significantly stronger than the low-angle FM and AFM interactions (red and blue lines respectively in Figure 3-14).

Considering only the strong 120° interplane AFM SE interactions allows us to express the magnetic energy of the system using a simple Heisenberg Hamiltonian of the form

$$H = \sum_{i<j} J\left(\sigma_i \cdot \sigma_j\right) \tag{3.7}$$

where and are Fe lattice sites connected by a SE interaction shown in Figure 3-14, is the superexchange parameter and and are the unit vectors representing the direction of moments on the corresponding lattice sites such that for the AFM crystal and for the FM phase.

The magnitude of the superexchange parameter can be easily extracted from the difference in vacancy formation energies in the AFM and FM phases. Since the formation of a Fe vacancy involves the breaking of 12 SE interactions, we can estimate as follows.

$$\Delta H_f^{\mathrm{v,AFM}} - \Delta H_f^{\mathrm{v,FM}} = 1.59\mathrm{eV} \tag{3.8}$$

$$= 12\,J\left(\sigma_i^{\mathrm{AFM}}\sigma_j^{\mathrm{AFM}}\right) - 12\,J\left(\sigma_i^{\mathrm{FM}}\sigma_j^{\mathrm{FM}}\right) \tag{3.9}$$

$$\implies J = 66.25\mathrm{meV} \tag{3.10}$$

which is similar to superexchange parameters for other ionic compounds like NiO [167] ($J = 38$meV) and MnO [168] ($J = 28$meV). Surprisingly, this simple Hamiltonian model of magnetic interaction can also explain the large difference in migration barriers between the FM and AFM phases. To understand this, we begin by calculating the magnetic contributions to system energy at the transition state along the ion migration path.

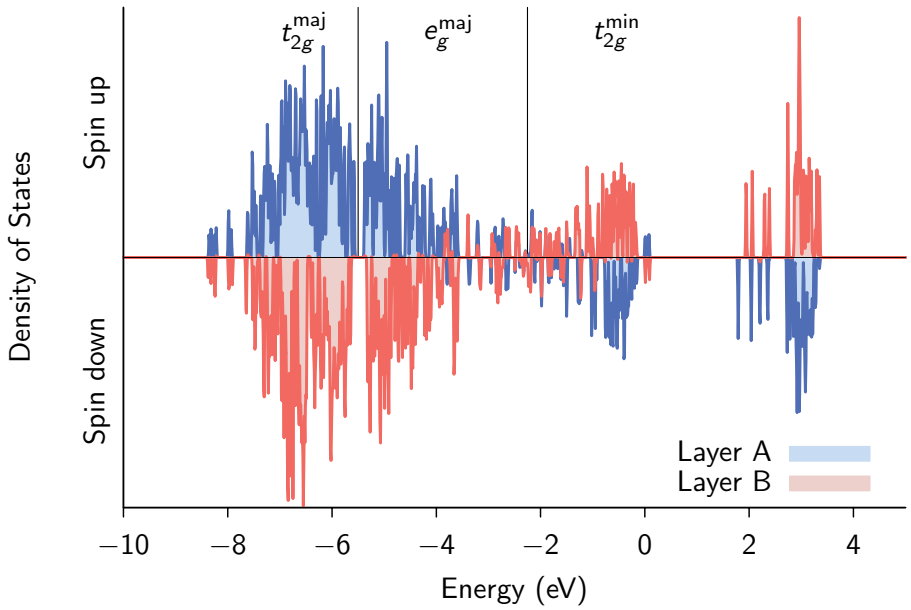

Figure 3-13: Unsmoothed local density of states of Fe^{2+} $3d$ orbitals showing the t_{2g} and e_g orbitals with the majority and minority spin carriers

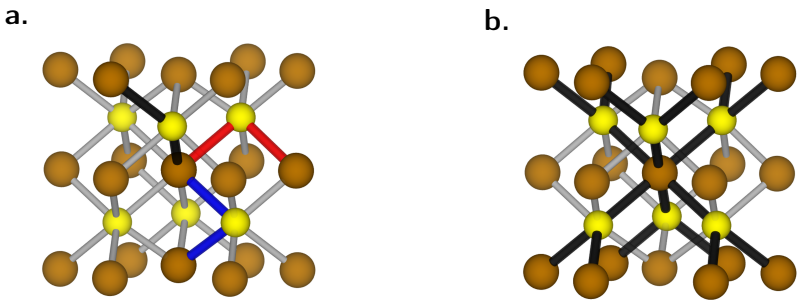

Figure 3-14: (a) The high-angle interplanar AFM-SE interactions (black) are significantly stronger than the low-angle interplanar AFM-SE interactions (blue) or intraplanar FM-SE interactions (red). (b) Each lattice site in the pyrrhotite crystal is stabilized by 12 strong high-angle AFM-SE interactions

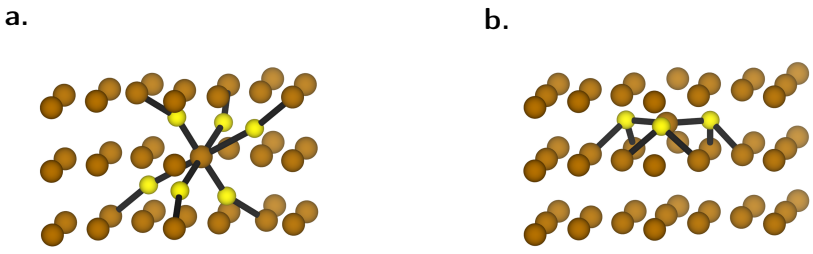

Figure 3-15: The migrating Fe ion is stabilized by 6 AFM-SE interactions at the transition state of the diffusion process for diffusion along (a) Path 1 and (b) Path 2. Only the S atoms involved in the SE interaction are shown for clarity

It is clear from Figure 3-15 that the transition state for diffusion along both paths 1 and 2 are stabilized by six superexchange interactions, one-half the number for a lattice site. Therefore the difference between the activation energy for migration between the two magnetic phases can be expressed as the difference in the magnetic energies between the transition state and initial state.

$$\begin{aligned}
\Delta E_a^{\text{migr}} &= \Delta\left(H_{TS} - H_{IS}\right) && (3.11)\\
&= \Delta H_{TS} - \Delta H_{IS} && (3.12)\\
&= 6\,J\left(\sigma_i^{\text{AFM}}\sigma_j^{\text{AFM}} - \sigma_i^{\text{FM}}\sigma_j^{\text{FM}}\right) - 12\,J\left(\sigma_i^{\text{AFM}}\sigma_j^{\text{AFM}} - \sigma_i^{\text{FM}}\sigma_j^{\text{FM}}\right) && (3.13)\\
&= -6\,J\left(\sigma_i^{\text{AFM}}\sigma_j^{\text{AFM}} - \sigma_i^{\text{FM}}\sigma_j^{\text{FM}}\right) && (3.14)\\
&= 0.795\text{eV} && (3.15)
\end{aligned}$$

In brief, since the transition state during ionic migration between two identical lattice sites in pyrrhotite involves breaking one-half of the magnetic interaction present in the bulk, the difference in migration barriers between two magnetic phases in approximately one-half of the difference between vacancy formation energies. Such a magnetic configuration at the diffusion transition state is not unique to pyrrhotite and therefore a similar relation between migration barriers and vacancy formation energies is also found in different magnetic phases of Fe and Co.

3.5.3 Summary

We calculated activation barriers for ionic migration and formation enthalpies for Fe vacancies in two different magnetic phases of pyrrhotite ($Fe_{1-x}S$). Cation migration in the antiferromagnetic phase is more difficult, with an activation barrier that is 0.8 eV greater than in the ferromagnetic phase, thus confirming the existence of the magnetic diffusion anomaly. We also calculate that the formation enthalpy of a Fe vacancy is 1.59 eV more energetically expensive in the antiferromagnetic phase. Both observations are attributed to the magnetic Fe-S-Fe superexchange interactions that stabilize the Fe^{2+} lattice site in the antiferromagnetic phase. This mechanistic description of the influence of local magnetic structure on ionic mobilities in ionic systems is relevant to pyrrhotite and other functional magnetic compounds like NiO and MnO, whose transport properties are critical to technologies like fuel cells and battery electrodes.

3.6 Outcomes and Future Work

The primary aim of the chapter is to provide a fundamental understanding of the impact of structural and magnetic phase transitions on the mass transport in pyrrhotites. The previous two sections investigated the effect of each individual type of phase transition alone. Here, we summarize the results and also provide a suggestion on extending the work done in this thesis to provide a fuller picture of cation diffusion in pyrrhotite.

3.6.1 Outcomes

The anti-Curie order-disorder transition was successfully modeled using an on-lattice kMC model and by assuming that the diffusion of V_{Fe} is the rate-limiting unit process. More importantly, the stretched exponential form of the transformation kinetics as well

as the spatially continuous ordering transformation were successfully modeled using a single value for the migration barrier of the Fe^{2+} ion across all the different pyrrhotite polytypes and vacancy configurations. On the other hand, cation migration barriers are very strongly dependent on the local magnetic order (AFM or PM). These two observations have the following important implications for the modeling of iron-sulfide passive films:

a. Pyrrhotite phases of different vacancy configurations and polytypes are functionally equivalent as a diffusion barrier. This obviates the need for explicitly modeling a passive film with individual pyrrhotite phase distributions.

b. Diffusion through the pyrrhotite film should account for the change in migration barrier between the low-temperature AFM phase and the high-temperature PM phase.

3.6.2 Future Work

The on-lattice kMC calculations described above provide strong, but indirect evidence for the independence of ionic migration barrier on the local vacancy distribution. More direct evidence for this effect can be obtained by performing an explicit ab-initio simulations of the ionic migration process using the climbing-image nudged elastic band calculations.

Extension of spin-dynamics calculations, already demonstrated in metallic systems, can be extended to the pyrrhotite structure to enable direction calculation of ionic migration barriers in a paramagnetic environment. This would provide an unambiguous quantification between diffusivity of iron in the known high-temperature and low-temperature magnetic phases of pyrrhotite.

Chapter 4

Dynamics of point defect formation, clustering and pit initiation on the pyrite surface

4.1 Overview

The stability of ionic surfaces under redox conditions is defined by the dynamics of point defects on the surface, whose collective behavior can lead to local breakdown by pitting. Here, we explore the degradation mechanism using experimentally-informed lattice kinetic Monte Carlo to simulate unit processes on the FeS_2 (100) surface including formation and annihilation of Fe and S vacancies, surface migration and vacancy association and condensation. This simple kinetic Monte Carlo model can probe realistic experimental length scales ($\approx$ 100 nm) and time scales ($\approx$ 1-10 hours) and quantitatively demonstrates the non-Arrhenius growth of surface vacancy concentration and the agglomeration of isolated vacancies into nano-scale defect clusters, which can act as pit initiation sites. These results about surface chemistry and morphology are confirmed by synchrotron X-ray photoelectron spectroscopy (XPS) and scanning tunneling microscopy (STM) measurements of the pyrite (100) surface annealed at high temperatures in vacuum. This mechanistic and quantitative detail about atom-scale behavior on the model ionic surface of pyrite under redox conditions and is technologically important for processes like corrosion and catalysis, where surface structure and activity determine performance. Portions of this chapter were published in Electrochimica Acta [169] and the XPS and STM measurements reported here were performed by William Herbert.

4.2 Background and Motivation

The primary mechanism by which a passive film protects the base metal from corrosion is by retarding or preventing the transfer of ions and/or charge from the metal surface to the reactive environment. Therefore, a large degree of the protectiveness of passive films depends on the stability of the film as a physicochemical barrier in reaction conditions.

One of the major mechanisms that compromises the stability of these passive films is the rapid localized dissolution of the film leading to pitting corrosion. Such localized

degradation and pitting has previously been observed in several other passive film systems [170–172], where breakdown originates at defect sites on the film surface. While an empirical measurement of overall corrosion rates is sufficient to design materials against the predictable and slow general corrosion process, localized damage occurs very rapidly and unpredictably, necessitating a thorough understanding of the atomic mechanisms and rates involved in the pitting process [173]. Specifically, it is important to characterize the unit processes involved in the initiation of nanoscale pitting and quantify their rates because the rate of pit growth is very rapid [174]. Therefore, in the context of sour corrosion, we are interested in understanding the dynamics of point defects on the surface of iron sulfides with a focus on quantifying collective behavior that can lead to nucleation of potential pit sites.

4.3 Chapter Goals and Layout

The primary motivation of this study is to uncover the dynamics of isolated point defects on the surface of a model iron sulfide, FeS_2 (100) surface to identify the mechanism behind the nucleation of pitting sites on passive films in sour corrosion. We address this question in the following three sections of this chapter.

1. The next section, **passivity breakdown due to pitting**, describes some existing literature on pitting corrosion in iron sulfides and other passive films including details about proposed mechanisms for pit initiation and efforts to model pit initiation processes. This provides important context to interpret results from the subsequent sections.
2. **Modeling point defect dynamics on pyrite FeS_2(100)** discusses the unit processes associated with point defects on the pyrite surface along with a description of the kMC model used to simulate these dynamics. We then discuss results from the kMC model about surface chemistry and morphology and support it using XPS and STM measurements.
3. In the final section, **Outcomes and Future Work**, we summarize our results from the kMC model and discuss the implications of our observations for modeling pitting behavior in multiscale passive film models.

4.4 Passivity breakdown due to pitting

The breakdown of passive films by pitting and local degradation is an extremely common mechanism of corrosion film failure and is therefore widely studied in a range of corrosion systems [173, 175, 176], including sour corrosion [8, 177]. While correlations between global corrosion variables like temperature, pressure and pH and the local corrosion rates and currents are known and broadly understood, the mechanisms behind pit initiation and growth are less thoroughly investigated due to difficulties in the experimental analysis of the solid-liquid interface. Therefore, pit initiation and growth is often considered, for both analytical and modeling purposes, to be a stochastic process, occurring with empirically-determined reaction rates [178, 179]. While such approximations are made in the interest of simplicity of analysis, the fact remains that such local degradation processes are deterministic in nature, occurring due to a combination of simpler unit processes that can be better characterized. For instance, association and condensation of vacancies is known to occur both at the metal-passive film interface and at the passive film-environment interface and either process can lead

to localized breakdown [180]. At this point it is important to note that such surface imperfections (mainly microstructural and/or microchemical inhomogeneities) can affect the rate of these unit processes and are therefore prime candidates for initiation sites for such localized degradation, even in the absence of preferential dissolution due to the presence of aggressive anions in the electrolytic environment [181].

Various mechanistic theories and models have been proposed to describe this process [182], the most comprehensive of which is the Point Defect Model (PDM) which serves as the framework guiding the development of a multiscale model in this project. The PDM also provides a mechanistically-based explanation of the role of alloying elements, pH and other critical breakdown parameters (critical breakdown voltage, V_c, and induction time, t_{ind}) in the inhibition of passivity breakdown and hence localized corrosion. Clustering of vacancies is thought to be necessary for pit initiation, the rate-controlling step in overall pitting corrosion [183] and this process has been observed on metals [184] and alloys [185] as well as a limited number of ionic systems like Ni-O, Ni-OH and Cr_2O_3, [186, 187]. However, in all such cases, there is a lack of concerted modeling and experimental demonstration at the atomic scale, due to difficulties in Matching simulated time scales to experimental ones [176, 188]. Therefore, even in simpler systems such as pure metals and semiconductors, where surface pitting is relatively better understood, modeling of surface degradation is generally limited to the use of empirical kinetic parameters.

4.4.1 FeS_2 surface chemistry and morphology

Native point defect concentrations in bulk FeS_2 are low (O(10^6) cm^{-3}) at room temperature [44]. On the other hand, anionic vacancies, specifically sulfur vacancies denoted as V_S, are expected to be far more prevalent at free surfaces, with calculated formation enthalpies as low as 0.4 eV [35, 189]. The (100) surface of FeS_2 is unreconstructed and is the most stable surface, as shown by low energy electron diffraction (LEED) [57, 190] and scanning tunneling microscopy (STM) [191, 192]. Recently, Herbert *et al.* [169] examined the formation of individual and clustered point defect on the (100) surface of pyrite under successive reduction at increasing temperatures in UHV environments. Using high-intensity synchrotron X-ray Photoelectron Spectroscopy (XPS), they were able to extract element-specific signals from the pyrite surface annealed at different temperatures through deconvolution and peak fitting, we can extract quantitatively, the relative magnitudes of three types of sulfur sites – defect free sulfur sites, bulk sulfur vacancies and sulfur vacancies at the surface. The plot of the measured surface vacancy concentration as a function of annealing temperature describes an unusual non-Arrhenius behavior Figure 4-1, which indicates that the point defect dynamics on the surface of the pyrite crystal are more complicated and include more unit processes than just vacancy formation and annihilation.

Further, Scanning Tunneling Microscopy (STM) images of single crystal pyrite (100) surfaces both at room temperature and after *in situ* annealing to 220 °C and to 300 °C for >150 min. Figure 4-2 provides further details on the behavior of defects underlying the results in Figure 4-1. After annealing at 220 °C in UHV, we observed the appearance of multiple small, irregularly-shaped vacancy clusters or pits on the surface of flat terraces (Figure 4-2), with a dispersion of cluster sizes (widths) from smaller than 1 nm to $\sim$ 10 nm (Fig. 6e). Following annealing at 300 °C, these grew to form a more homogeneous spread of clusters with lateral dimensions consistently between 5-10 nm (Fig. 6 g, 6 h, 6i). The pits exhibited a curved, non-faceted morphology that can be rationalized by comparison to the curved terrace steps observed by Rosso *et al.* on conchoidal fracture surfaces of FeS_2 [57]. Normal to the free surface of the crystal, the depth of the defect clusters also changed between 220-300 °C: at 220 °C the surface pits were consistently

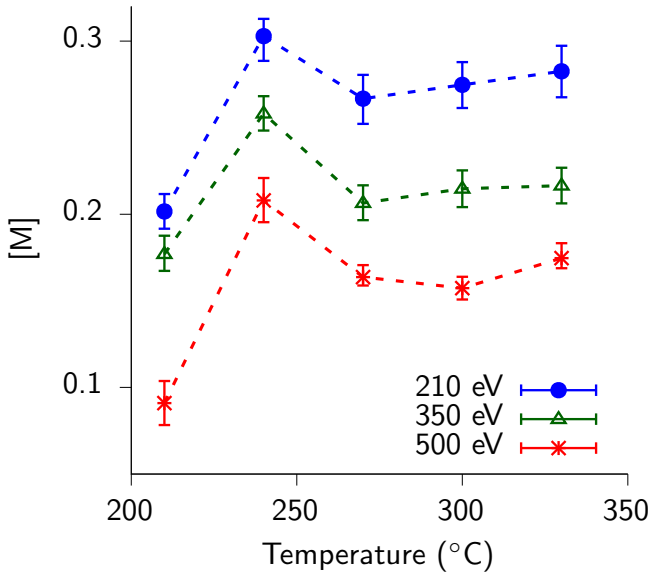

Figure 4-1: Proportion of the V_S component of the S 2p photoelectron spectra on FeS_2(100) at 200-330 °C, measured using three different excitation energies: 210, 350 and 500 eV. The fraction of the total signal represented by M increased up to 270 °C then dropped and stayed approximately constant

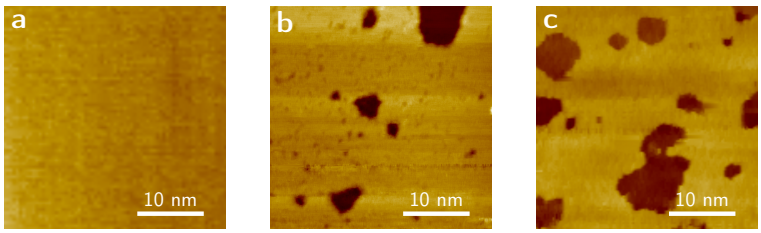

Figure 4-2: **Scanning tunneling microscopy (STM) images of single crystal FeS_2(100) surfaces** (a) prior to any in situ annealing in ultra high vacuum, (b) after three hours of in situ annealing at 220 °C, and (c) after three hours at 300 °C. The surface morphology of atomically-flat terraces at room temperature changes under annealing due to the formation of vacancy clusters

2.7 ± 0.1 Å deep whereas at 300 °C the majority of pits have a depth of 5.4 ± 0.1 Å. Given the lattice parameter of pyrite of 5.41 Å [193], these pit depths correspond to one half and one full lattice parameter, respectively.

4.5 Modeling point defect dynamics on pyrite FeS_2 (100)

Based on the XPS and STM results described above, we propose a mechanism involving three distinct unit processes occurring in tandem during the *in situ* reduction of the FeS_2 (100) surface, as described in Figure 4-3.

1. The formation of isolated sulfur mono-vacancies (V_S) and outward migration of Fe vacancies from the bulk of the pyrite crystal leading to an increase in the number of measured surface vacancies.

2. Surface diffusion of Fe and S vacancies followed by a clustering of small number of adjacent vacancies.

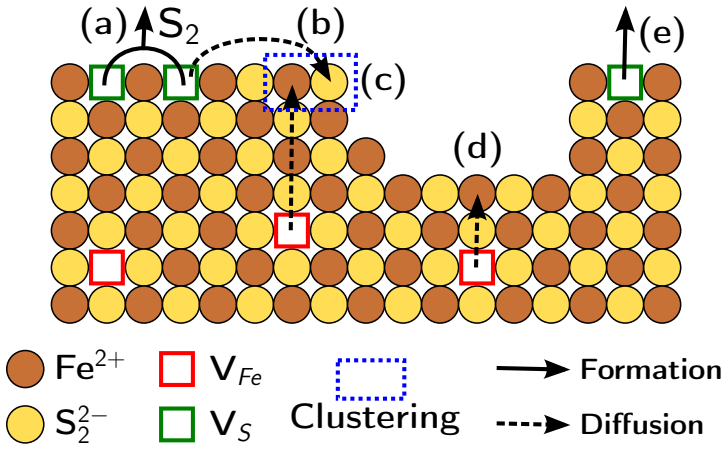

Figure 4-3: Illustration of atomic processes involved in the proposed mechanism of pit formation and growth on pyrite (100). (a) Formation of surface sulfur monovacancies, V_S through evaporation into vacuum. (b) Diffusion of V_S to a pit site. (c) Agglomeration of vacancies on the iron and sulfur sublattices by diffusion, leading to the initiation and growth of the pit. Presence of an initiated pit (as depicted in this figure) is not a necessary precursor to the process in (c). (d) Iron vacancies, denoted as V_{Fe}, that are already present in the bulk migrate to the surface during annealing.(e) V_S formation at under-coordinated sites surrounding pits has lower formation enthalpy as compared to isolated vacancy formation process in (a).

3. Growth of such vacancy clusters due to minimization of system energy. These vacancy clusters are more stable features due to the fewer number of broken bonds per vacancy and correspondingly lower vacancy formation energies relative to isolated vacancies

This mechanism was cast into a kMC model described below to identify if these unit processes can explain the unusual non-Arrhenius growth of the surface vacancy concentration observed from XPS measurements and morphology of the defect clusters formed at higher temperatures, as seen in STM images.

4.5.1 Methodology – DFT Calculations and kMC simulations

Density Functional Theory (DFT) calculations were conducted to quantify energy barriers for the formation, diffusion and agglomeration of surface point defects at the atomic level. All DFT calculations [75] were carried out with projector augmented wave method [79] using the Vienna Ab-initio Simulation Package (VASP) [76, 77] using the Perdew-Burke-Ernzerhof (PBE) form of the GGA functional [78] with spin polarization included. Activation barriers for the surface diffusion process were calculated using the Climbing Image Nudged Elastic Band (CINEB) method [158] with five images on 2x2x2 unit cell slabs of the pyrite (100) surface separated by 10 Å of vacuum. The thickness of the slab and the vacuum condition were chosen such that the surface energy of the (100) surface converged to within 0.03 J/m^2. In all slab calculations, the topmost two surface layers of S-Fe-S were allowed to relax while the other layers remained fixed at positions consistent with bulk pyrite. The reciprocal space was sampled with a 4x4x1 Monkhorst-Pack grid [83] and integrated over with a Gaussian smearing ($\sigma = 0.1$ eV). DFT+U corrections were applied using the previously calculated value of U-J = 1.6 eV [34]. All calculations were performed with a plane-wave cut-off energy of 350 eV. Total energies for each image were converged to within 10^{-5} eV in each self-consistency cycle. The forces on ions were converged to within 0.01 eV/Å for each image. All crystal structures shown were generated using the VESTA visualization program [87].

Kinetic Monte Carlo (kMC) simulations [194] were performed on a model of the pyrite

(100) surface to understand the processes responsible for the experimentally observed defect structure and concentrations. The kMC method permits us to describe the time-evolution of the system structure under non-equilibrium conditions or towards an equilibrium state. Towards this end, we attempt to identify a kMC model made up of a small set of elementary processes that can reproduce the experimentally observed phenomena. In particular, our aim is to elucidate the mechanisms of both surface pit initiation and the non-Arrhenius variation of the vacancy concentration at elevated temperatures.

The simulated model system consisted of a FeS_2 slab containing $110 \times 110 \times 2$ lattice sites under periodic boundary conditions in the lateral direction. This corresponds to a real-life sample of lateral size 30 nm × 30 nm and a height of 1 unit cell, appropriate for modeling surface processes. Each lattice site was initially occupied by either a Fe^{2+} of ${S_2}^{2-}$ ion organized in a checkerboard pattern to reproduce the NaCl-type crystal structure. In this model, Fe^{2+} sites can exist in one of two states (vacant or occupied by a Fe^{2+} ion) and ${S_2}^{2-}$ sites can exist in one of three possible states (occupied by a ${S_2}^{2-}$ dimer ion, occupied by a single S^{2-} ion indicating the presence of a monomer vacancy, V_S, or fully vacant with a dimer vacancy).

The effective time for system evolution depends on the activation energy barriers of the elementary processes included in the kMC model. Here, we modeled two elementary processes occurring in tandem: surface vacancy formation and surface vacancy diffusion. The probability of occurrence of each process, j, at a temperature T is given by the Arrhenius equation, $j = \nu \exp\left(-\frac{E_b}{k_B T}\right)$ where ν is the attempt frequency, E_b the activation barrier, and k_B is the Boltzmann's constant. For surface vacancy diffusion, only the jumps between nearest neighbors of the same species were considered. For example, V_{Fe} was allowed to move only to the nearest-neighbor site containing a Fe^{2+} ion, and V_S only to a nearest-neighbor site containing a monomer vacancy or ${S_2}^{2-}$ ion. Vacancy formation processes were allowed to occur on any site that is not already completely vacant. To satisfy detailed balance requirements, each vacancy formation process also included a corresponding vacancy annihilation process, which was allowed to occur on any site that is not completely occupied (i.e. it was allowed on Fe^{2+} vacancies, S^{2-} monomer vacancies and ${S_2}^{2-}$ dimer vacancies). The barriers for the different elementary processes described in our kMC model were obtained in part by our DFT calculations, in part from our experiments, and in part by fitting to reproduce experimental observations. Activation energy barriers for the surface diffusion process were obtained from DFT and CINEB, as this process is well-defined at the atomic level, down to atomic trajectories. Activation barriers for Fe and S vacancy formation and annihilation processes were obtained via empirical fitting to reproduce experimental time-scales and experimentally observed vacancy concentrations; these barriers are rather intractable using ab initio calculations, due to both a multiplicity of pathways that must be sampled and the contributions of gaseous species' entropic contributions that are not captured via DFT. Finally, difference between the activation barriers of vacancy formation and annihilation were constrained by the formation enthalpy determined by our XPS experiments. It is important to note that the strength of the kMC models rests not on the exact values used for the activation energy barriers but on its ability to explain emergence of complex phenomena mechanistically as an interaction among a small number of elementary unit processes.

Since all the elementary processes described so far involve the formation or breaking of bonds around a lattice site, we make the reasonable assumption that the activation energy barriers for the processes depend upon the coordination number of the site under consideration. More specifically, we implement a bond-counting model where the activation barrier for each elementary process depended linearly on the number of bonds broken during the process, an approach that has been applied in previous kMC studies [195, 196]. In our model, local site coordination was sampled using the parameter N_{bb}

given by

$$N_{bb} = \frac{\text{Number of neighboring defects} - \text{ free sites}}{4} \tag{4.1}$$

Here, the denominator of 4 is equal to the theoretical maximum number of defects around a lattice site in our checkerboard model. Using this parameter, vacancy formation processes were modeled to have an energy barrier, $E_{i,vf}$, of the form

$$E_{i,vf} = E_i^0 + (\alpha \times N_{bb}) \tag{4.2}$$

where E_i^0 is a neighborhood-independent constant barrier for the process, and α is a scaling parameter that represents the dependence of activation barriers on site coordination. According to Equation 4.2, the value of α is the change in the barrier for vacancy formation between a site where $N_{bb} = 1$ (a fully coordinated site) and $N_{bb} = 0$ (a hypothetical, fully uncoordinated site). This is equivalent to the energy required to break all nearest-neighbor bonds, i.e. to create a vacancy in a full-coordinated site. Therefore, the value of α is chosen to be of the same order as the experimentally measured surface vacancy formation enthalpy of 0.10 eV.

Conversely, vacancy annihilation processes (which can be thought of as processes leading to the filling-in of an existing vacancy by formation of bonds with occupied nearest-neighbor sites) are expected to become easier (i.e. have a lower activation energy barrier) with increased site coordination. Therefore, vacancy annihilation processes are modeled to have an energy barrier, $E_{i,va}$ of the form

$$E_{i,va} = E_i^0 - (\alpha \times N_{bb})$$

The activation barriers for the surface vacancy diffusion process have a similar form, given by

$$E_{i,diff} = E_{i,diff}^0 + \left(\alpha \times \left(N_{bb}^f - N_{bb}^i\right)\right)$$

Here, N_{bb}^i is the neighborhood sampling parameter at the site from which the vacancy initially diffuses and N_{bb}^f is the neighborhood sampling parameter at the final site to which the vacancy moves. If the selected vacancy diffusion process breaks more bonds than it re-forms, the activation barrier for the process is higher; if the selected vacancy diffusion process breaks fewer bonds than it re-forms, the activation barrier for the process is lower.

Due to the partial empiricism in the identification of the activation barriers, in particular E_i^0 and α, additional kMC calculations were conducted to assess model sensitivity to these parameters Figure 4-5. The range of values for each process explored in this study is given in Table 4.1. In addition, the value of alpha was also sampled from 0.05 eV to 0.1 eV. For the reminder of the paper, we will refer to calculations conducted using activation barriers equal to the mean of the range given in Table 4.1: $V_{S,form} = 1.62$ eV, $V_{S,anni} = 1.62$ eV, $V_{Fe,form} = 1.54$ eV, $V_{Fe,anni} = 1.64$ eV, $V_{diff} = 1.45$ eV.

The kMC simulation is performed by holding an initially perfect defect-free simulation cell at the annealing temperature for 3×10^7 kMC steps. At lower temperatures around 210 °C, this corresponds to an experimental time of close to 10^7 seconds, while at higher annealing temperatures around 330 °C, the same number of simulation steps corresponds to only 10^4 seconds of experimental time. To compare the monomer concentrations in the simulation to experiments, we take a snapshot of the system 14440 seconds after the initialization at different temperatures. This is quantitatively equal to the 4 hour annealing performed in experiments.

Elementary unit process	Range of activation barriers simulated (eV)
E_i^0 for V_{Fe} formation	1.49 - 1.59
E_i^0 for V_S formation	1.57 - 1.67
E_i^0 for V_{Fe} annihilation	1.49 - 1.59
E_i^0 for V_S annihilation	1.57 - 1.67
E_i^0 for surface diffusion	1.40 - 1.50

Table 4.1: Activation barriers for elementary processes in the kMC model

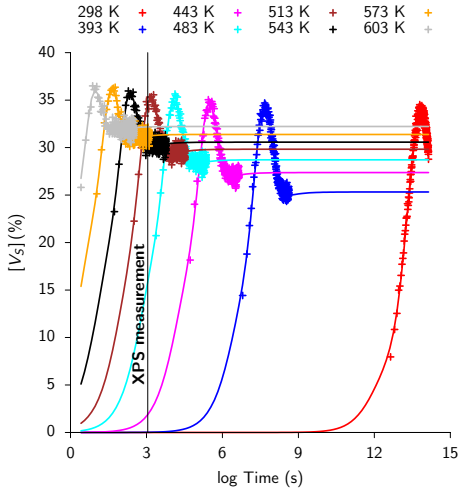

Figure 4-4: Evolution of calculated monomer concentration with time at different temperatures. The vertical line indicates the time at which the system in the kMC model is expected to represent the experimental XPS setup.

4.5.2 Non-Arrhenius surface vacancy concentrations and pit initiation

The most important quantitative outcome of the kMC model is the time variation of surface sulfur vacancy concentration at different temperatures. Figure 4-4 demonstrates three distinct regimes of surface degradation occurring at different time scales (or equivalently, at different temperatures for a given simulation time). Initially, there is stochastic formation of isolated vacancies on the defect-free surface. Elemental sulfur is highly volatile in comparison to iron, with a melting temperature of 115 °C at 1 atm pressure. We therefore assume sulfur sublimes from pyrite and is dynamically removed from the sample surface until the pyrite crystal surface equilibrates with the ambient sulfur chemical potential in the UHV environment (chamber pressure of $10^{-9} - 10^{-10}$ mbar in the experiment of Herbert *et al.*) We also note the importance of iron vacancies in our model. Since Fe loss through evaporation into vacuum is unlikely at the relatively low annealing temperatures compared to the melting point T_m of iron (300 °C $< 0.2\ T_m$), the increase of V_{Fe} requires an alternative explanation. It is known that the formation enthalpy of the V_{Fe} in pyrite increases by up to 1.42 eV as the environment changes from sulfur-rich to one deficient in sulfur [34]. This large change implies that the sizable number of V_{Fe} defects originally present in the pyrite crystal during synthe-

sis in sulfur-rich conditions are not stable in the sulfur-deficient conditions encountered during the annealing process. In order to equilibrate the bulk under these experimental conditions, the oversaturated V_{Fe} point defects migrate from bulk towards the free surface at high temperatures to annihilate. In providing iron vacancies to the surface, coincidentally in this work, the situation is analogous to the dissolution of metal cations from the passive film in liquid electrolytes [197]. These processes lead to a steady and rapid increase of the monomer concentration with time, which defines the first regime of surface vacancy concentration growth.

In the second regime, beyond a critical vacancy concentration (corresponding to the peak of the curves in Figure 4-4), surface diffusion of vacancies becomes a dominant unit process. In addition, vacancy formation near existing defects becomes more facile, thereby promoting vacancy clustering. This phenomenon, combined with rapid diffusion, leads to agglomeration of surface vacancies into nano-scale pits seen in Figure 4-6 b and c. Within the kMC model, when two or more vacancies encounter each other stochastically, a small cluster is formed which is more stable relative to the dispersed individual vacancies. STM imaging by Rosso *et al.* has recorded surface diffusion of iron vacancies on natural single crystals of FeS_2 at room temperature over time scales of minutes, so diffusive processes are expected to occur with low energy barriers [191]. In the kMC model in this work, a higher barrier was taken for diffusion of vacant surface sites away from the pits compared to diffusion of vacancies towards the pits, simulating the trapping of vacant sites by the initiated pits. Since these agglomerated vacancies no longer contribute to the monomer signal in the XPS, we see a drop in the concentration of monomer defects corresponding with the onset of large-scale pitting.

The third stage of surface chemistry evolution proceeds with the growth of existing nanopits on the surface. Once a stable pit nucleates, the reduced coordination of sulfur atoms at the newly-created step edges of pits reduces the formation energy for vacancies at these sites, and accelerates the growth of pits. Indeed, our DFT calculations showed that ΔH_f for individual V_S at a step edge of a pit could be up to $\approx$ 40% lower than that on an atomically-flat surface. This type of dependence of defect formation on the local atomic configuration has also been observed in sulfide inclusions in pitting corrosion [198]. The formation and expansion of surface vacancy clusters in this manner provides an explanation for the surprisingly low ΔH_f for sulfur vacancies of around 0.1 eV that we measured using XPS below 240 °C (Fig. 4-6), as compared to recent theoretical predictions in the range of 0.4-1.44 eV [34, 35, 189]. Upon raising the temperature to greater than 240 °C, the majority of sulfur vacancy formation occurs at the pit step edges. This process results in the growth of existing pits, but does not introduce additional monomer vacancies and therefore does not contribute to the measured vacancy concentration in XPS measurements.

effect of growing the vacancy clusters is to maintain the XPS signal intensity from M at a roughly constant value. This is because the removal of a sulfur atom from the step edge of a vacancy cluster, while growing the cluster, does not result in the creation of an adjacent monomer M site on the surface structure; therefore the M signal intensity does not increase in the S 2p spectrum

This combined, multi-stage behavior can be used to explain the variation of the experimentally observed monomer concentration in Figure 4-1(a). As Figure 4-5 shows, at low temperatures like 210 °C, the system is continuing to evolve after 10^4 seconds of annealing and has not yet reached equilibrium. Therefore the observed monomer concentration is low. At 300 °C and higher temperatures, by 10^4 seconds, the system has undergone not only stochastic vacancy formation (which increases monomer concentration), but also large-scale agglomeration and pit formation (which decreases monomer concentration). As a result, the observed monomer concentration is still low. At 240 °C, 10^4 seconds is sufficient time for the system to reach the critical concentration re-

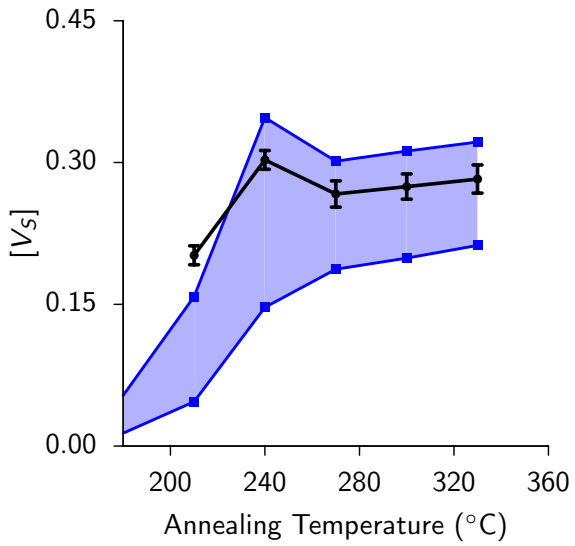

Figure 4-5: kinetic Monte Carlo simulation results. Simulated values of the sulfur monomer vacancy concentration [V_S] on the pyrite surface as a function of annealing temperature, obtained by kinetic Monte Carlo simulations (kMC) and indicated by the blue zone. The width of predicted [V_S] indicated by this blue band is given by variation in kMC energy barrier values over the range described in Table 1. Values of [V_S] experimentally determined from our XPS measurements are shown for comparison

quired for pit formation, but still insufficient for substantial pit formation to actually take place. The result is an observed monomer concentration that is higher than those observed at higher or lower temperatures.

4.6 Outcomes and Future Work

The primary aim of the chapter is to elucidate the mechanism behind the initiation of nanoscale pit sites on the surface of pyrite, FeS_2 (100) and to quantify the rates of unit processes involved using kinetic Monte Carlo to explain observations about surface structure and chemistry from XPS and STM measurements. Here, we summarize the results from the kMC modeling study of defect dynamics, discuss some important implications for the surface activity of other defective surfaces and also outline some suggestions about extending the results in this chapter to other ionic surfaces.

4.6.1 Outcomes

We investigate the evolution of surface morphology and chemistry of the pyrite (100) surface as a function of annealing temperature in order to capture the mechanism behind the nucleation of nanoscale pits observed in previous experiments. To explain this behavior, we propose a minimal set of unit processes involving vacancy formation, annihilation and diffusion that can adequately explain the observed changes to the surface structure. Specifically, the interplay between vacancy formation, association and diffusion was found to be responsible for both the observed surface structures and the observed non-Arrhenius growth of surface vacancy concentration.

This quantitative kMC study provides a mechanistic understanding of the evolution of the reactive surface under redox conditions and has implications for ionic surface activity under reactive conditions, where the number of active sites like surface vacancies

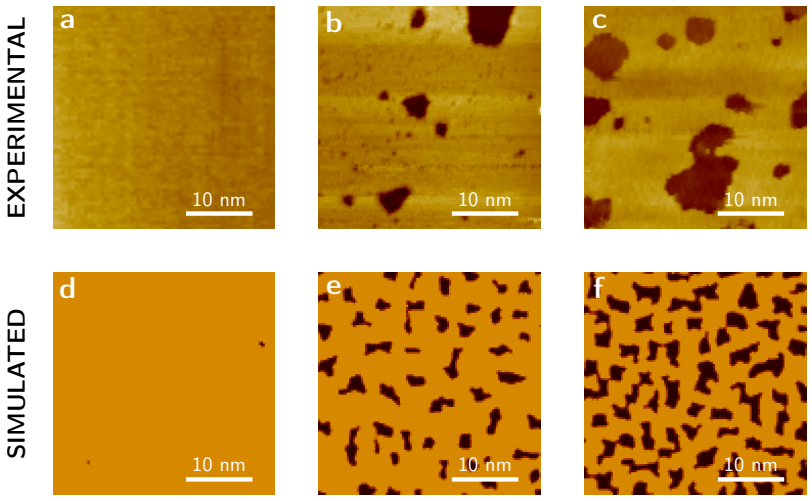

Figure 4-6: **Scanning tunneling microscopy (STM) images of single crystal FeS_2(100) surfaces** (a) prior to any in situ annealing in ultra high vacuum, (b) after three hours of in situ annealing at 220 °C, and (c) after three hours at 300 °C. The surface morphology of atomically-flat terraces at room temperature changes under annealing due to the formation of vacancy clusters. All STM data were collected at room temperature using tunneling conditions in the range ± (1-2) V and 200-1000 nA. The bottom row of images (d, e, f) display the results of kinetic Monte Carlo (kMC) simulations performed at the same temperatures of (d) 25 °C, (e) 220 °C and (f) 300 °C for comparison with the experimental images.

and pit edges are important metric for the overall activity of the surface. In the context of sour corrosion, the dynamics of surface point defects observed under controlled reducing environments offer an atomistic level description of the incipient stages of pit formation in passive films, as postulated in models of surface degradation such as the Point Defect Model

4.6.2 Future Work

There are several interesting directions in which the work presented in this thesis can be extended. Two interesting extensions are outlined below.

1. One potentially useful extension would involve the modeling of these unit processes in more realistic electrode conditions with the inclusion of the effects of an aqueous interface and electrode bias and interfacial electric fields.

2. Another interesting study would involve the quantification of surface reactivity on similar defective surfaces in redox conditions. Most common metrics of reactivity of ionic surfaces, including iron sulfides [199], correlate a higher activity for surfaces with higher defect concentrations, implicitly assuming the existence of only isolated vacancies, without accounting for the possibility of vacancy association and diffusion leading to the formation of potentially less reactive ledge and step edges. On the other hand, defect clusters are understood to the more active sites for reactions like dissociative hydrogen adsorption on the surfaces of catalysts like Pd(111) [200]. In both cases, a thorough understanding of atomic surface structure, as performed in this work, is crucial to understanding surface activity.

Chapter 5

Hydrogen induced delamination of mackinawite ($Fe_{1+x}S$)

5.1 Overview

Hydrogen point defects degrade the mechanical properties of passive corrosion films, whose protectiveness depends, to a large extent, on their physical integrity. This mechanical stability is particularly important for layered surface films like mackinawite ($Fe_{1+x}S$), which are held together mainly by weak van der Waals forces along one crystal axis. The embrittling effect of hydrogen is well understood in metals and some compact oxides, the impact of hydrogen defects on the mechanical behavior of layered chalcogenides like mackinawite is unknown. In the first part of the study, we detail density functional calculations on the influence of different hydrogen point defects on important mechanical metrics like binding energies, elastic moduli and tensile and shear strengths of $Fe_{1+x}S$. When present as H_2 interstitials in the interlaminar space, hydrogen severely degrades the strength of inter-layer van der Waals interactions.

Once we calculate the thermodynamics of the different laminar (directly bonded to the FeS layer) and interlaminar (H defect is attached to the FeS layer by weak dipolar or dispersion interactions) hydrogen defect configurations, we focus on quantifying the kinetics of hydrogen interstitial dynamics including hydrogen diffusion as well as any association or dissociation reactions. Using a combination of DFT, NEB and kMC calculations, we quantify the activation barriers for hydrogen diffusion and the Tafel reaction ($2\,H \longrightarrow H_{2(g)}$), paying special attention to reactive sites inside the mackinawite crystal such as Fe vacancies. We identify that the already favorable H_2 evolution reaction is catalyzed by over 300% by the presence of small fraction (<1%) of Fe vacancies in the mackinawite lattice. These calculations provide a coherent mechanistic explanation for the presence of H_2 molecular interstitials in the mackinawite bulk in contact with acidic environments.

Taken together, these studies provide a mechanistic explanation for the poor protectiveness of layered passive films like mackinawite that undergo failure by spalling or delamination. Implications of these results for cathodic electrochemical exfoliation of other layered crystals as well as defect-engineering of layered materials for catalytic hydrogen evolution are also discussed.

5.2 Background and Motivation

As described in Chapter 1 of this thesis, one of the primary determinants of the protectiveness of the passive film is its resistance to localized damage. Unlike the slower and more predictable rate of damage resulting from general corrosion, localized corrosion occurs very rapidly and unpredictably. Therefore, the first step in estimating the protectiveness of the passive film against localized damage must be a thorough understanding and kinetic quantification of the mechanisms responsible for the onset of localized damage.

Specifically, in the context of sour corrosion, one long-standing question which can benefit from an elucidation of such atomic-scale mechanistic details is the question about the poor passivity of the nominally protective mackinawite corrosion film due to localized degradation. Therefore, in order to provide mechanistic input to higher-level predictive models (like in Chapter 6), we hypothesize a plausible mechanism for the localized mechanical breakdown of the mackinawite crystal aided by hydrogen interstitial defect. Over the course of this chapter, we use a variety of computational methods to

1. Characterize defect chemistry and identify the configuration of the most stable defects based on the thermodynamics and quantify their impact on the mechanical properties of mackinawite.

2. Measure the kinetics of reactions between H interstitials to identify plausible pathways for H-induced breakdown of mackinawite crystal

5.3 Chapter goals and layout

The primary aim of this chapter is to mechanistically explain the formation of different hydrogen interstitials in the mackinawite crystal and understand the impact of these interstitials on the mechanical properties of the crystal. We address these two topics in the rest of this chapter, which is divided into four sections.

1. The first section, **Behavior of mackinawite passive films**, introduces collected evidence from literature for the poor mechanical stability of and ease of exfoliation of mackinawite in sour corrosion.

2. In the second section, **Hydrogen induced delamination of mackinawite**, we present computational evidence, using virtual tensile and shear stress-strain tests, for the poor interlaminar bonding in mackinawite in the presence of interlaminar H_2 interstitials

3. We rationalize the presence of these mechanically detrimental H_2 interstitials, by mechanically tracing the behavior of cathodically discharged protons in the next section, **H_2 evolution in layered mackinawite**.

4. Finally, we summarize our proposed mechanism for the H-induced mechanical degradation of mackinawite in the next section, **Outcomes and Future Work**, and extend these concepts to other related areas like catalytic HER and exfoliation of other layered systems.

Anodic reaction	$Fe \longrightarrow Fe^{2+} + 2e^{-}$
Surface adsorption reaction	$HS^{-}_{m,ad} \longrightarrow H^{+}_{m,ad} + S^{2-}$
Cathodic reaction	$H^{+}_{m,ad} + e^{-} \longrightarrow H^{0}_{m,ad}$
Surface chemical reaction	$H^{0}_{m,ad} + H^{0}_{m,ad} \longrightarrow H_{2(g)}$
	$H^{0}_{m,ad} \longrightarrow H^{0}_{m,abs}$
Film formation reaction	$xFe^{2+} + yHS^{-} \longrightarrow Fe_xS_y + yH^{+}$

Table 5.1: Chemical reactions involved in the sour corrosion process

5.4 Behavior of mackinawite passive films

The first steps in the sour corrosion of iron involve the reaction of the Fe surface with sulfur, which exists as HS^{-} ions. The HS^{-} ion, the hydrolysate of H_2S, has greater chemisorptivity than $HCO_3{}^{-}$ or OH^{-} ions on the surface of iron [201] and reacts with iron in mildly acidic conditions (pH 3-5) to form a thin featureless, coherent layer of mackinawite through a solid state reaction as described by the mechanism below [202–205]

This thin film of metastable mackinawite [205] is the first sulfide phase to form in the Fe-H_2S system [202, 206–209], and offers some protection against further corrosion [209–211] primarily by acting as a diffusion barrier against the penetration of H_2S to the bare metal surface, as deduced by hydrogen permeation experiments in a H_2S-saturated NACE solutions [211]. However, unlike other compact iron sulfide phases like pyrrhotite and pyrite that are formed at more sulfur-rich environments, mackinawite is not very protective [206] because the coherent mackinawite layer is electronically conductive and nobler than the base metal leading to pitting corrosion and severe localized degradation and cracking of the passive film. The extensive cracking of the mackinawite layer is [211] followed by localized dissolution of metal and subsequent precipitation of mackinawite at the cracks where the high concentration of Fe^{2+} ions exceeds the solubility product of mackinawite. This precipitated layer is extremely porous and highly non-protective against further corrosion [203]

Mackinawite crystallizes in a tetragonal unit cell [212] with slightly distorted edge-sharing tetrahedra [213] and lattice constants of $a = b = 3.67$ Å and $c = 5.03$ Å [214]. Iron atoms occupy the Wyckoff position 2a (0,0,0) and sulfur occupies the position 2b (0,1/2,1/4) [214]. Bonding in the a-b plane is covalent with Fe-Fe distances in mackinawite (2.65 Å) being comparable to those in BCC iron (2.8 Å) [213, 215]. Fe-S bond lengths in plane are approximately 2.25 Å and are also indicative of strong bonding in-plane [214]. However, the a-b planes are bound along the *c*-direction only by relatively weak van der Waals forces [5, 216, 217], which suggests that exfoliation is a facile failure mode.

Like other layered materials, there is little direct information about the shear and tensile strength of mackinawite along the weakly-bonded direction, but recent determinations of the bulk modulus of mackinawite (27 GPa) [214] are close to tensile modulus of other layered materials like graphite (29 GPa) [218], indicating that the van der Waals forces in these crystals are similar in magnitude. In these studies, the bulk modulus is a good representative for the Young's modulus along the weakly bonded direction be-

cause compressibility of mackinawite in the 'c' direction is 5-7 times that in the strongly-bonded a-b plane [214]. Another important implication of the weak interlaminar bonding and the larger interlaminar void is the possibility of intercalation by other atoms and molecules. This can be observed experimentally in the case of nanocrystalline mackinawite, which has larger lattice constants and significant lattice expansion mainly due to the intercalation by H_2O or OH- species [216, 217, 219]. Similar mechanical failure and interlaminar fracture was observed in mackinawite crystals during the intercalation of lithium ions [220].

The stoichiometry of the mackinawite crystal is uncertain, with early studies indicating that synthetic mackinawite crystals are near-stoichiometric ($Fe_{0.98\pm0.02}S$), with any off-stoichiometry explained as resulting from inclusions resulting from the synthesis [213, 217, 219, 221], however, more recent studies have identified that most naturally occurring mackinawite is actually measurably iron-rich ($Fe_{1+x}S$; $0 < x < 0.15$) due to the presence of Fe interstitials in the tetrahedral inter-laminar interstitial site for excess iron compositions in the range of $0 < x < 0.3$ [222].

Mackinawite is a metallic crystal within the a-b plane because of the very close Fe-Fe distance (2.6 Å), which compares favorably with the distance in BCC Fe (2.48 Å) [223]. But unlike metallic Fe, the mackinawite crystal is not ferromagnetic because the DOS at the Fermi level is not high enough to ensure that the Stoner criterion is satisfied at a values of less than 3.8 Å [223]. The magnetic properties of mackinawite are not very well understood, with Mössbauer spectroscopy indicating that mackinawite is paramagnetic crystal, while DFT calculations show an antiferromagnetic ground state structure. More recent studies suggest that mackinawite might exhibit itinerant spin fluctuations, which can explain both the DFT-calculated AFM ground state as well as the paramagnetic moment over the course of a relatively long (about 0.1 μs) Mössbauer spectroscopy measurement [223]. To account for this fact, we use a non-magnetic mode of the mackinawite crystal for the remainder of the study.

5.5 Hydrogen induced delamination of mackinawite

The behavior of hydrogen point defects in layered, van der Waals-bonded crystals is of central importance to several applications like electrochemical hydrogen generation [224], hydrogen storage [225], and two-dimensional crystal synthesis by exfoliation [226]. In most of these studies, the problem of interest is the effect of such point defects on the mechanical properties of the host crystal. A specific example is found in the industrially important case of 'sour' corrosion of steels, where surface passive films containing layered iron sulfides like mackinawite act as the primary barrier layer protecting the underlying steel surface against further corrosion and hydrogen embrittlement [202, 208]. This nominally passive layer helps measurably reduce the overall corrosion rate and remains protective as long as it retains its physical integrity [211]. Under continued corrosion, this passive film undergoes spallation leading to exposure of the bare metal and subsequent catastrophic localized corrosion [202, 211]. Therefore, understanding the mechanisms behind mechanical failure of these layered systems in electrochemical environments is critical to improving the service lifetime of steels under sour corrosive conditions.

Towards this end, there are several studies, both experimental and computational, that explain the embrittling role of hydrogen in compromising the mechanical properties on compact (i.e. not van der Waals bonded) crystals like metals [227], semiconductors [228] and oxides [229, 230]. While there are investigations into the role of intercalating ions and molecules on the mechanical properties of layered systems [231–233],

primarily in the context of electrochemical exfoliation of two-dimensional crystals, a similarly rigorous analysis of the role of different hydrogen defects is lacking.

To address this problem, we use density functional theory calculations (details in Section 5.5.1) to identify dominant hydrogen defects in mackinawite based on their formation energies and quantify their effect on the mechanical properties of mackinawite by mapping stress-strain behavior. Section 5.5.2 describes how molecular H_2 interstitials in low concentrations can significantly degrade the inter-layer van der Waals bonding and enable easy interlayer sliding and exfoliation of mackinawite crystals and explains this behavior in analogy to interstitials and intercalants in other layered systems. The implications of this loss of mechanical stability for protectiveness of mackinawite films and for exfoliation strategies for other layered compounds are also discussed.

5.5.1 Methodology and computational details

The first step in understanding the role of hydrogen defects on the mechanical properties of mackinawite is to identify thermodynamically stable hydrogen defects. We calculate formation energies of different hydrogen defect configurations to identify the most stable defect structures expected to exist at moderate temperatures around 200 °C encountered in sour corrosion conditions.

We then compare the mechanical properties of hydrogen-containing mackinawite crystals to those of hydrogen-free mackinawite crystals by computing virtual stress-strain diagrams for two modes of displacement chosen to reflect the strength of the interlayer bond, namely strains along the z-direction, ε_{zz} (simulating an uniaxial tensile test along the z-direction) and shear strain along a plane perpendicular to the z-direction, γ_{xz} and γ_{yz}. These virtual stress-strain diagrams give us two important metrics, namely the elastic modulus and the stress to failure, which are then compared among calculations of different hydrogen defect structures.

All DFT calculations [75] were carried out with the projector augmented wave method [79] using the Perdew-Burke-Ernzerhof (PBE) form of GGA functional [78] implemented in the Vienna Ab-initio Simulation Package (VASP) [76, 77]. For accurate reproduction of the mackinawite electronic structure, the DFT+U method was used with the previously determined value of $U - J = 1.6$ eV that was found to be suitable for iron chalcogenide phases [34]. Plane wave components up to 350 eV were included to avoid wrap-around errors and integrations in the reciprocal space were performed on a $6 \times 6 \times 6$ Monkhorst Pack grid that includes 27 non-equivalent points in the Brillouin zone [83]. For defect formation energy calculations, computations were performed on a $2\sqrt{2} \times 2\sqrt{2} \times 2$ unit cell containing 32 formula units and total energies were converged to within 10^{-5} eV in each self-consistency cycle. The forces on ions were converged to within 0.01 eV/Å.

Stress-strain curves are plotted by calculating the internal stresses in the crystal as strains are increased in uniform increments of 0.04. For these high-accuracy calculations, atoms in the crystal were relaxed till forces on each atom are less than 10^{-3} eV/Å and all other stress components are less than 5 MPa. In keeping with previous studies, we use internal stress tensor computed directly by VASP because it avoids the numerical errors associated with the manual calculation of the derivative of the system energy. Previous calculations have shown these two approaches to be identical in the case of another layered system, graphite [234].

There are conflicting reports on the ground state magnetic configuration of mackinawite, with prior studies that support both antiferromagnetic [223] and non-magnetic [213] configurations. In this work, the non-magnetic configuration was found to have

the lower system energy, consistent with previous simulations as well as experiments [212]. Therefore, in this work, we use the non-magnetic form of the crystal for all calculations.

Accurately modeling van der Waals forces is essential to modeling the mechanical properties of layered systems. Since semilocal functionals like PBE do not include long-range electronic correlation effects, we use Grimme's DFT-D2 formulation of dispersion interactions to explicitly account for them [114]. While semi-empirical in nature, this approach has previously demonstrated good accuracy in calculating elastic constants in graphite and MoS_2 [235]. Where possible, we have also calculated stress-strain behavior using the optB86b-vdW functional, one of a class of parameter-free formulations of van der Waals-functionals [236]. Since the results from the optB86b-vdW functional are qualitatively similar to that of the DFT-D2 method (See Section B.1), we will restrict our discussion in Section 5.5.2 to DFT-D2 results.

5.5.2 Results and discussion

Prior studies have established that the mechanical response of the hydrogen-doped crystal depends strongly on the specific nature of the hydrogen defect, so the next section on hydrogen defect chemistry describes the identification of sulfur-bonded monoatomic hydrogen interstitial and the interlayer H_2 interstitial as the most stable hydrogen defects in mackinawite. Consequently, only these two defects are analyzed for their impact on mackinawite's mechanical properties. Sections on tensile and shear testing show how one of these defect structures, the H_2 interstitial, is responsible for a 90% decrease in the van der Waals bonding strength between mackinawite sheets. We conclude with a discussion on the implication of this observation for the performance of mackinawite as a passive film as well as prospects for intentional functionalization of this phenomenon.

Hydrogen defect chemistry in mackinawite: We calculate defect formation energies for two classes of hydrogen point defects, H atoms substituting the Fe^{2+} or S^{2-} lattice sites and interstitial H atoms at three crystallographically non-equivalent sites as shown in Figure 5-1. We limit our calculations to neutral H defects in all cases because the metallic mackinawite films [237] do not admit the presence of charged point defects unlike semiconducting oxides [230]. In addition to these point defects, layered compounds also admit another type of point defect, namely the molecular hydrogen interstitial in the interlayer space. Specifically, the H_2 molecule in mackinawite occupies the large tetrahedral void formed between the S^{2-} ions from adjacent layers (Figure 5-1f).

Defect formation energies are calculated using the formula

$$\Delta G_f^i = E\left(\mathrm{FeS}\cdot \mathrm{H}_i\right) - E\left(\mathrm{FeS}\right) + eU + 2.3\ k_B T\ \mathrm{pH}$$

where ΔG_f^i is the free energy of formation of the hydrogen defect, $E\left(\mathrm{FeS}\cdot \mathrm{H}_i\right)$ and $E\left(\mathrm{FeS}\right)$ are DFT-calculated energies of the hydrogen-containing and hydrogen-free mackinawite crystal, e is the magnitude of electronic charge, U is the electrostatic potential of the mackinawite crystal relative to the standard hydrogen electrode, T is the temperature and k_B and pH have their usual meanings. For all formation energies, we use U = -0.5 V SHE, pH = 2, and T = 200 °C to reflect conditions that are encountered in sour corrosion. The formation energies for substitutional defects is calculated in the 'iron-rich' chemical potential regime as defined in [34]. This is appropriate for mackinawite in sour corrosion conditions, where mackinawite films are in thermodynamic equilibrium with iron.

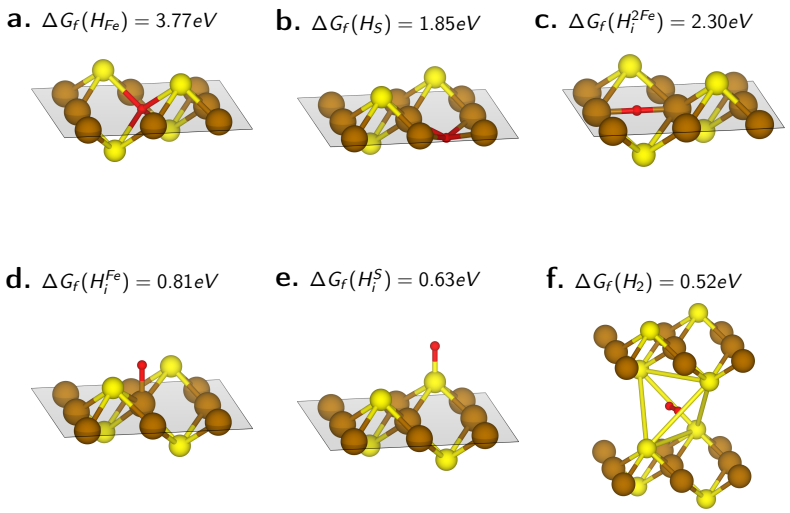

Figure 5-1: Hydrogen point defect structures considered in this study along with formation energies. Brown, yellow and red spheres represent iron, sulfur and hydrogen atoms respectively. Dashed lines are guides for the eye that shows the S-Fe-S basal layer. (a-b) are substitutional defects. (c-e) are monoatomic interstitial defects and (f) is the molecular H_2 interstitial inside the interlayer tetrahedral void (yellow lines). Crystal structure images were rendered using the VESTA visualization program - [87].

The S-bonded monoatomic hydrogen interstitial and the interlayer H_2 interstitial have the lowest formation energies of all the defects considered and are therefore expected to dominate the hydrogen defect chemistry in mackinawite at low temperatures. Therefore, we will only consider the effect of these two defects on the mechanical properties in subsequent sections.

Mechanical response to uniaxial strain, ε_{zz}: The simulated uniaxial tensile test of the H-free mackinawite crystal yields a tensile strength of 1772 MPa and an elastic modulus of 26 GPa (Figure 5-2), which is very similar to experimental and calculated values for out-of-plane elastic modulus for graphite [238, 239] and bilayer graphene [240], indicating that the main forces operative in this simulation are van der Waals in the z-direction.

Repeating the simulation on a mackinawite crystal with S-bonded H interstitials, we find that both the ultimate strength and elastic modulus improve marginally to 2137 MPa and 29 GPa respectively. This strengthening effect has been previously observed for other interstitial atoms K, Li and Cl in graphite [234, 238].

To understand the mechanism behind the strengthening, we plot the charge redistribution due to hydrogen defect formation. Similar to the case of K/Cl in graphite, there is moderate charge transfer between the monoatomic interstitial and the mackinawite layers (Figure 5-3a). This introduces new dipolar and hydrogen-bonding interactions between layers that complements the weak van der Waals interactions leading to strengthened interlayer bonds and better mechanical properties.

The mackinawite crystal weakens significantly in the presence of H_2 interstitials with both the yield stress and elastic modulus decreasing by over 90% to 173 MPa and 1.7 GPa respectively. This is also similar to other molecular interstitials and intercalants in other layered systems like KCl and C_6H_6 in graphite [233] . In the absence of any charge transfer to the layered crystal (Figure 5-3b), the closed-shell interstitial species introduces repulsive steric interactions between the host crystal sheets that undermines the attractive van der Waals interactions. This steric behavior of H_2 molecules has

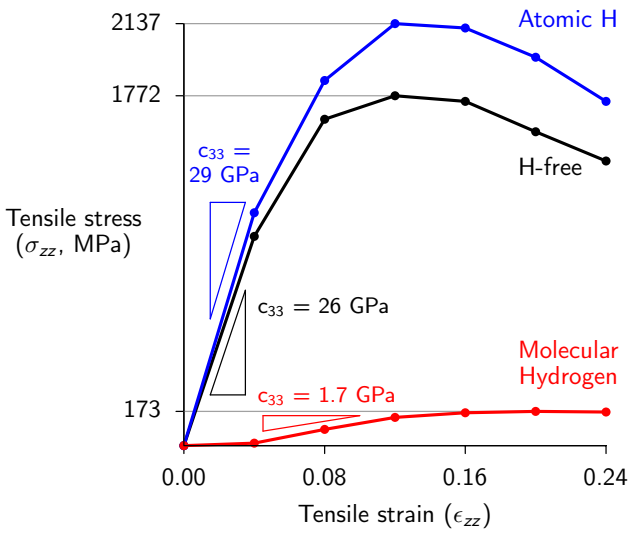

Figure 5-2: The presence of molecular hydrogen interstitials reduces both the ultimate strength and elastic modulus by more than 90% over hydrogen-free mackinawite.

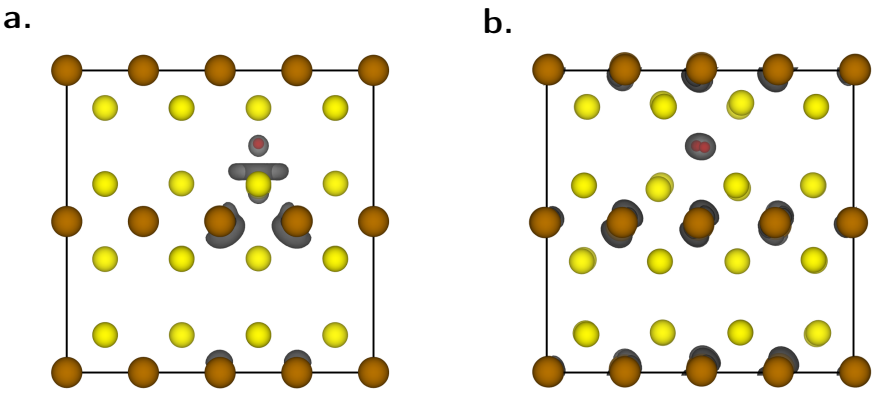

Figure 5-3: Atomic H interstitials induce charge transfer to the mackinawite layers and create dipolar attractive interactions among layers leading to strengthening, whereas molecular H_2 interstitials induce only steric repulsion that weakens existing attractive van der Waals bonding.

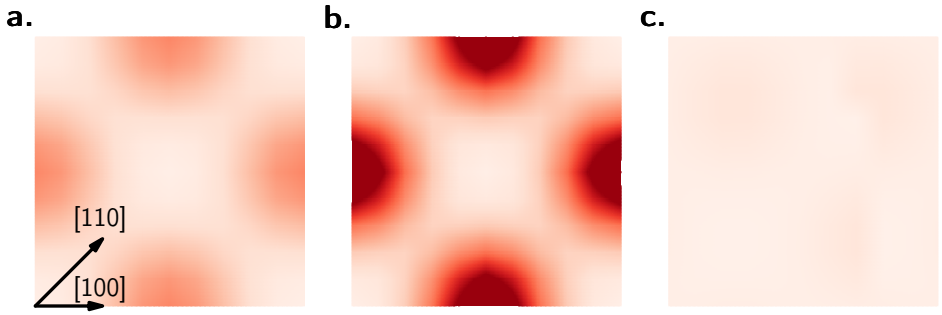

Figure 5-4: Atomic H interstitials (b.) strengthen inter-layer interactions leading to a sharper potential energy surface compared to that of hydrogen-free mackinawite (a.). Molecular interstitials (c.) weaker inter-layer attractive interactions leading to a very flat potential energy surface that enables easy inter-layer sliding and exfoliation. Each PES shown here spans 1 unit cell in the x- and y-directions.

previously been observed on graphene monolayers, where the most stable physisorption site for H_2 molecules is the hollow of the hexagonal graphene ring, away from the electron densities of the C-C σ bonds [241].

Mechanical response to shear strain, τ_{xz} and τ_{yz}: Sliding between layers is an inevitable and required mechanism during exfoliation of layered systems [242]. Therefore, resistance to interlayer sliding is an important part of overall resistance to mechanical damage. However, this resistance depends strongly on the specific direction of sliding. This dependence is described by potential energy surface (PES) maps that show the variation of potential energy of the layered system as one crystal sheet slides over another one. The complete PES maps for hydrogen-free and hydrogen-containing mackinawite crystals in Figure 5-4 shows that [110] is the easy sliding direction with the lowest energy barriers while sliding along the [100] direction involves the largest activation barrier.

These PES descriptions can be directly related to the shear stress-strain behavior by observing that the resistance to sliding (i.e. the calculated shear stress for a given shear strain) is equal to the gradient of the change in potential energy in the given direction. To capture the role of H-defects on the inter-layer binding, we plot stress-strain diagrams for shear strain along two representative directions, [100] and [110] that span the entire range of potential energy gradients.

In the easy-glide [110] direction, the hydrogen-free mackinawite crystal shows maximum stress of 1279 MPa and shear modulus of 11 GPa (Figure 5-5), values that are similar to those observed for MoS_2 [235, 243]. Similar to the case of tensile strain, atomic H interstitials strengthen interlaminar bonding, making it difficult to shear the sheets relative to one another while H_2 interstitials degrade interlaminar bonding to such an extent that sliding becomes facile.

Hydrogen-induced exfoliation and impact on protectiveness of mackinawite passive films: The poor mechanical properties of mackinawite crystals containing H_2 interstitials suggests a plausible mechanistic explanation for easy spallation and concomitant poor protectiveness of mackinawite passive films. It is well known that epitaxially-grown passive films on metal surfaces undergo cracking and mechanical damage upon reaching a certain critical thickness in order to release epitaxial strain energy [244]. However, this mechanism is not operative in layered films like mackinawite, which are capable of accommodating all the epitaxial strain within the inter-layer van der Waals

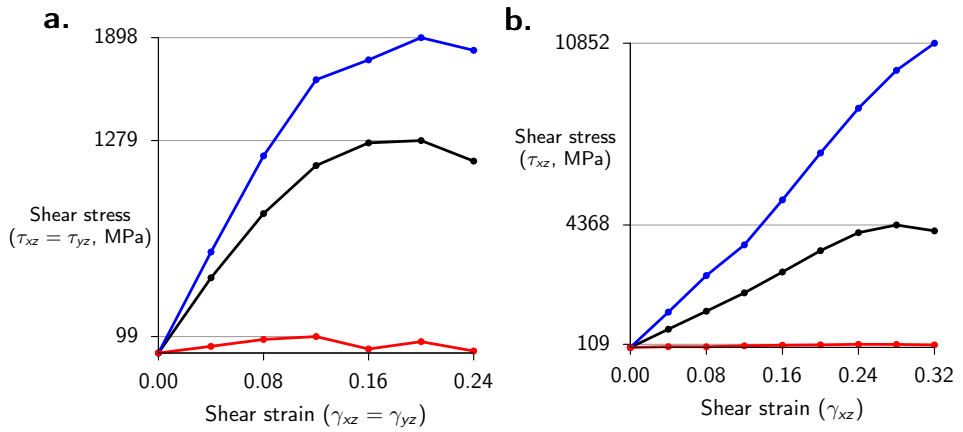

Figure 5-5: Molecular H_2 interstitials weaken inter-layer binding and enable facile sliding along both the (a.) [110] and (b.) [100] directions. This reduced resistance to inter-layer sliding implies easier multi-layer exfoliation and consequently poorly protective mackinawite.

regions [245]. In this context, H-mediated exfoliation emerges as an important mechanism to explain the observed exfoliation and rupture of mackinawite films.

The effective degradation of interlayer bonds in mackinawite by hydrogen point defects suggest interlayer H_2 evolution as an effective exfoliation technique. Specifically, in conducting films like mackinawite that admit easy intercalation of water and protons [246], simple cathodic polarization can lead to proton discharge and hydrogen evolution leading to exfoliation, a fact that can be exploited in other layered systems like 1T-MoS_2.

5.5.3 Summary

In order to understand the role of hydrogen defects on the mechanical properties of layered systems, we performed *in silico* stress-strain tests on mackinawite crystals with monoatomic hydrogen interstitials as well as interlayer molecular H_2 interstitials. Steric interactions due to molecular H_2 interstitials was found to severely degrade the attractive van der Waals interactions enabling facile inter-layer sliding and exfoliation.

This observation provides a plausible explanation for the spontaneous cracking and spalling observed in these layered passive films. The difference in the mechanical behavior due to H and H_2 interstitials also suggests an effective non-destructive exfoliation technique involving electrochemical generation of H_2 molecules in the bulk of layered compounds like $Fe_{1+x}S$. Elucidation of this mechanism involves calculation of energy barriers involved in atomic H intercalation and subsequent H_2 evolution which will be the focus of our future work.

5.6 H_2 evolution in layered mackinawite

The primary method for modulating the mechanical and electronic properties of functional layered materials is by controlling the behavior of interstitials, both laminar (where interstitials are bonded to the layered structure using strong chemical bonds) and interlaminar (where interstitials are bound to the layered crystal only through weak dipolar or dispersion interactions). The dynamics of these interstitials (such as atomic migration and chemical reactions) are key to understanding the behavior of several

functional material systems like battery electrodes [247], supercapacitors and cement as well as addressing fundamental scientific questions about the origin of life [248]. More recent studies on interstitial behavior in layered systems are focused on applications for energy storage and in the synthesis of mono-layer two-dimensional through chemical and electrochemical [249].

In spite of this importance, information about the structure and kinetics of such interstitials, especially those relate to interstitial transport and migration and reactions between interstitials in the confined interlaminar space remains unknown. One prototypical of interstitial dynamics in confined regions is the case of hydrogen blistering of passive corrosion films, a process where atomic hydrogen interstitials aggregate to form H_2 molecules leading to the formation of telltale blisters and subsequent mechanical damage to the passive film and embrittlement and loss of passivity for the underlying metal. Similar mechanisms are also theorized to occur in non-compact layered passive films like mackinawite, which can explain their poor passivity. However, a mechanistic description of the interstitial processes leading up to the formation of H_2 molecules and further embrittlement does not yet exist.

To address these questions we quantify the kinetics of mass transfer and chemical reactions involving hydrogen interstitials in the layered transition metal chalcogenide (TMC), mackinawite, FeS. This model system helps answer outstanding questions related to the poor protection of mackinawite films due to suspected hydrogen-induced embrittlement and delamination and also provides mechanistic insights into hydrogen evolution reaction, which is the prototypical reaction for electrochemical energy generation and storage, and whose kinetics on layered TMCs like MoS_2 are a topic of intense interest. In quantifying the kinetics of the hydrogen evolution reaction (HER), we pay special attention to the reactivity of point defect sites in the 2D crystalline lattice, since previous studies have established both experimentally and theoretically that point defects and associated undersaturated sites are catalytic in nature [250–252].

In Section 5.6.1, we discuss the density functional theory and nudged elastic band calculations used to quantify energy barriers for unit processes, like diffusion and association, of hydrogen interstitials in mackinawite. In the same section, we also investigate the impact of intrinsic point defects in mackinawite on these unit process and formulate a kinetic Monte Carlo model to capture hydrogen dynamics. We quantify the rate of the hydrogen evolution reaction and the impact of intrinsic point defect concentration on this rate in Section 5.6.2 along with an implication for the sour corrosion system as well as for electrochemical exfoliation synthesis methods for other layered crystals.

5.6.1 Methodology

The first step in quantifying the dynamics of hydrogen interstitials in to measure the energy barriers for the migration/diffusion of hydrogen point defects as well as reactions between hydrogen interstitials. As a starting point, we consider only the most thermodynamically stable laminar and interlaminar hydrogen defects as deduced in Section 5.5.1. We perform climbing-image nudged elastic band (CINEB) calculations to identify energy barriers for migration of these point defects as well as the barriers for the Tafel reaction ($2\,H_{ad} \longrightarrow H_{2(g)}$) in the interlaminar region of the mackinawite crystal. We focus on the Tafel reaction because it is shown to be the rate limiting process for the overall hydrogen evolution reaction for both metallic surfaces [253] as well as for transition metal chalcogenide surfaces [254].

Details about the DFT calculations including unit cell parameters, pseudopotentials, energy cutoffs, Brillouin zone sampling and convergence criteria are identical to those

described in Section 5.5.1. Reaction pathways and barriers are derived from the three images between the initial and final state in the NEB calculation

To model HER on a longer timescale, we use on-lattice kinetic Monte Carlo (kMC) to simulate the interstitial migration and Tafel reaction with the NEB-calculated barriers. The kMC calculation is performed in a tetragonal lattice of $50 \times 50 \times 20$ grid points representing 20 mackinawite layers of 50×50 grid points each. Each of these grid points represents a checkerboard pattern of Fe and S lattice sites to reflect the bonding topology in the mackinawite basal plane. Each Fe site in the kMC model is Ising-like, where a value of 1 indicating a defect-free Fe lattice site and a value of 0 indicates a Fe vacancy. The sulfur sites are similarly Ising-like with a 1 indicating a sulfur site with an adsorbed H atom and a 0 indicating a sulfur site without any adsorbed interstitials

The two main processes that are simulated are the migration of the atomic hydrogen interstitial and the Tafel reaction between two atomic hydrogen interstitials. Interstitial migration occurs between nearest-neighbor sulfur sites in the kMC grid with a probability of $P = \nu \exp\left(-\frac{E_a + 0.5\Delta E}{k_B T}\right)$, where ν is the exponential prefactor, taken to be equal to $10^{13} s^{-1}$ and E_a is the activation barrier for the process and ΔE is the change in system energy due to migration between two non-equivalent sulfur sites and k_B and T are the Boltzmann constant and absolute temperature respectively. The Tafel reaction is modeled as the process leading to the formation of an interlaminar H_2 molecule due to a reaction between hydrogen atomic interstitials on two adjacent sulfur sites in the crystal. This process also occurs with a probability of $P = \nu \exp\left(-\frac{E_a^{\text{Tafel}}}{k_B T}\right)$, where E_a^{Tafel} is the barrier for the Tafel process and all other terms are identical to those described before. In order to satisfy the principle of detailed balance for the Tafel association reaction, we also explicitly model the dissociation reaction, where a H_2 molecular interstitial dissociates into two H atomic interstitials on adjacent, vacant sulfur sites. This process is modeled to occur with a probability of $P = \nu \exp\left(-\frac{E_a^{\text{Tafel}} + \Delta E}{k_B T}\right)$, where ΔE is the difference in formation energies of the H_2 molecular interstitial and two atomic H interstitials.

A schematic of these different unit processes along with the activation barriers for each is shown in Figure 5-7 and a copy of the code used to perform the kMC calculations can be accessed at `www.github.com/arvk`.

5.6.2 Results and Discussion

Defect Thermodynamics As a first step towards understanding dynamic processes in the mackinawite-hydrogen system, we characterize the defect chemistry of point defects in the mackinawite crystal. Since the thermodynamics of the hydrogen point defects in mackinawite was established in Section 5.5.2, we focus here on the intrinsic point defects and lattice imperfections. Specifically, we calculate the formation energies of V_{Fe}, V_S and Fe_i defects in bulk mackinawite. In addition to the iron and sulfur vacancies, which are common and widely studied on other compact iron sulfide phases [34, 44], we also consider the presence of Fe interstitial atoms, which are hypothesized to exist in significant concentrations in natural mackinawite crystals. Figure 5-6 shows the DFT-calculated defect formation energies for the three point defects considered in this study. As described in [34, 44], the formation energy of such intrinsic defects assumes a range of values corresponding to the range of values of μ_S, the chemical potential of sulfur, within which mackinawite is thermodynamically stable relative to the parent elemental phases. Within this wide range of μ_S, we focus on defect formation energies in the region of lowest μ_S (i.e. the most Fe-rich region) for two reasons – Mackinawite crystals formed during synthesis and in sour corrosion conditions are commonly found

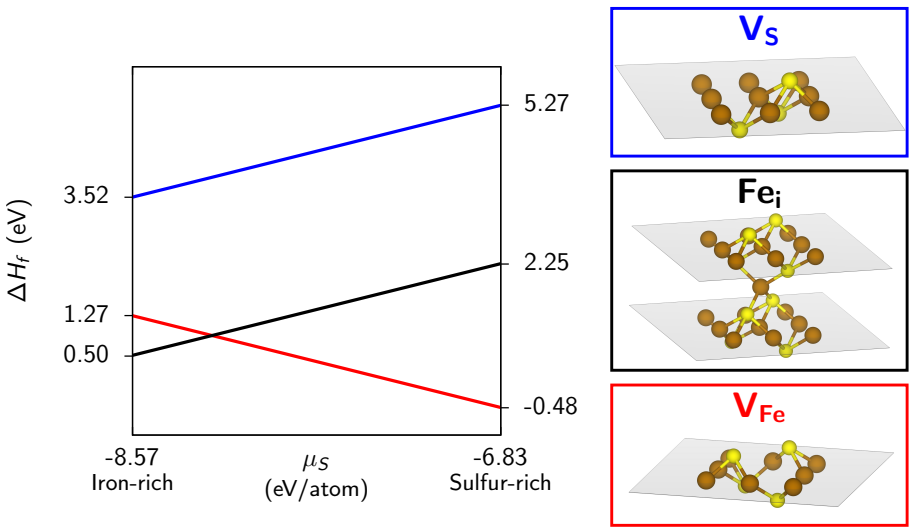

Figure 5-6: Formation energies for intrinsic defects in the mackinawite crystal

in contact with metallic iron and mackinawite is metastable relative to other sulfur-rich iron sulfide phases like pyrrhotite (FeS_{1+x}) and pyrite (FeS_2) ate higher values of μ_S.

In the limit of low μ_S, the formation energy of the Fe vacancy ($\Delta H_f\,(V_{\mathrm{Fe}}) = 1.27$ eV) is significantly lower than that for the S vacancy ($\Delta H_f\,(V_{\mathrm{S}}) = 3.52$ eV), implying a greater concentration of Fe vacancies. This quantification is in contrast to the defect chemistry of other layered TMCs like MoS_2 [255, 256], where S vacancies are the dominant intrinsic point defects. Therefore, for the remainder of this study, we consider the presence of Fe vacancies (and associated dangling bonds and under-saturated atoms) as potential catalytic sites in mackinawite. In addition, we also find that the Fe interstitial has a formation energy of only 0.5 eV, which is markedly lower than that of either vacancy. This finding, which is supported by other DFT calculations of interstitial formation in mackinawite [222, 257], suggests that even though the Fe vacancies outnumber S vacancies, the mackinawite crystal has Fe-rich off-stoichiometry, consistent with experimental observations [258, 259].

Energy barriers for hydrogen point defect dynamics We characterize the dynamics of hydrogen interstitials in this system by calculating the activation barriers for two unit processes, namely hydrogen migration and hydrogen association, using the CINEB method for DFT. The former quantifies the kinetics of hydrogen transport through the crystal and the latter represents the rate of the Tafel reaction. The calculated barriers for these two processes are summarized in Figure 5-7 and Figure 5-8 for processes occurring in a defect-free mackinawite region and near a Fe vacancy respectively. The primary migration pathways for atomic hydrogen in the bulk mackinawite crystal (Processes a and b in Figure 5-7 and Figure 5-8) involve hopping of hydrogen atoms between sulfur ions in adjacent mackinawite basal planes.

In order to quantify the effect of point defects on hydrogen dynamics, we first compare the activation barriers for processes a and b in a defect-free and defective crystal. In a defect-free crystal, these two processes represent identical hydrogen diffusing steps and therefore have the same activation barrier of 0.46 eV. Near a Fe vacancy, processes a and b are qualitatively different, with process a representing ionic hopping from a defect-free region of the crystal to near an Fe vacancy and process b represents hy-

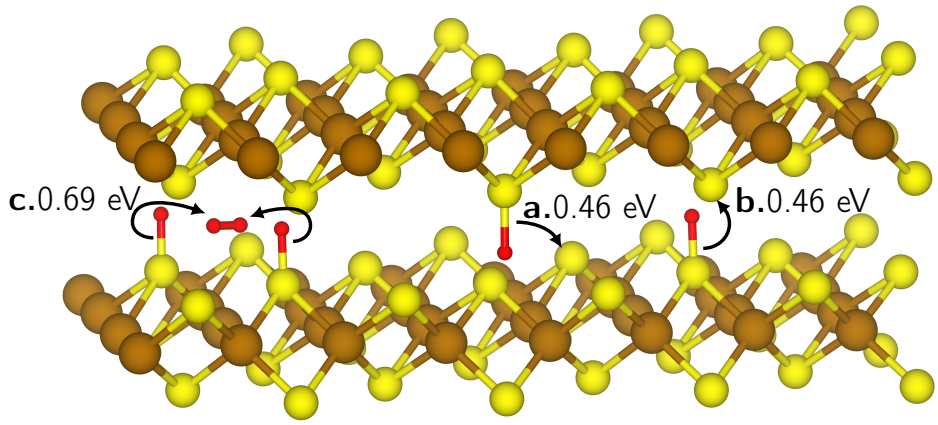

Figure 5-7: Defect dynamics in a defect-free mackinawite crystal. Processes (a) and (b) are diffusion processes and process (c) is the hydrogen association process leading to H_2 formation

drogen migration away from the defect site. Further, the difference between diffusion barriers into and away from the vacancy indicates that the undersaturated sulfur ions next to the vacancy bind an interstitial hydrogen atom more strongly than a defect-free sulfur site. In contrast, the barriers for the other dynamic unit process, Tafel hydrogen evolution reaction, are only marginally lower near the V_{Fe} ($E_a^{\text{Tafel}} = 0.68$ eV) compared to a defect-free site ($E_a^{\text{Tafel}} = 0.69$ eV). The significantly stronger bonding of the H atom and the moderate values of the Tafel barrier indicate that the Fe point defect sites may be catalytically active towards the hydrogen evolution reaction. At this point, it is important to note that while point-defect-induced catalysis has been described in other material systems, this mechanism of catalytic activation is qualitatively different from catalytically active point defect in other materials like layered $K_4Nb_6O_{17}$ [260] and carbon-nitride [261, 262] and nanostructures like CeO_2 nanorods [263], where defect-induced changes to the electronic structure of the semiconducting/insulating crystal affects the proton discharge reaction, $H^+ \longrightarrow H_{ad}$, i.e. the Volmer reaction. Instead, this form of catalysis by point defects has a lot more in common with HER catalysis by sulfur atoms at the edge of MoS_2 single crystals [100, 264], oxygen vacancies in NiO [265], and other synthetic catalytic sites that mimic the behavior of enzymes [266].

To explain this catalytic behavior, we focus on the electronic structure of the reaction sites. More fundamentally, the stronger S-H bonding that forms the basis for the increased catalytic activity can be understood by plotting the local density of states (LDOS) of the adsorption sites near the Fe vacancy. Figure 5-9 shows the orbital-projected LDOS for the orbitals involved in the adsorption of H ($2p$ for S and $1s$ for H) before and after H adsorption on a defect-free and defective region in the mackinawite crystal. The closer alignment of the hydrogen $1s$ and sulfur $2p$ energy levels near the Fe vacancy implies a greater overlap of the hydrogen and sulfur orbitals leading to a stronger H-S bond at the undersaturated defect site.

kinetic Monte Carlo modeling The combined impact on the effective hydrogen evolution rate of the different migration and Tafel barriers and adsorption energy at the defect site is difficult to estimate analytically. Therefore, in this section, we describe results from the on-lattice kMC model developed based on the barriers identified in the previous section to quantify any catalytic effects of the Fe vacancies in the crystal. Figure 5-10 shows the number of H_2 molecules evolved in the kMC simulation cell in

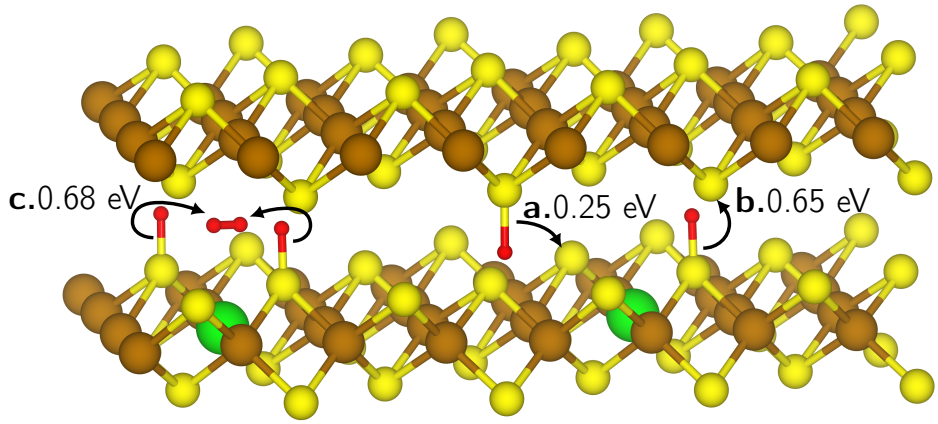

Figure 5-8: Defect dynamics in a mackinawite crystal with intrinsic Fe vacancies. Processes (a) and (b) are diffusion processes, with the former representing the barrier to move next to the Fe vacancy and the latter describing the barrier for moving away from the Fe vacancy. Process (c) is the hydrogen association process at the Fe vacancy leading to H_2 formation

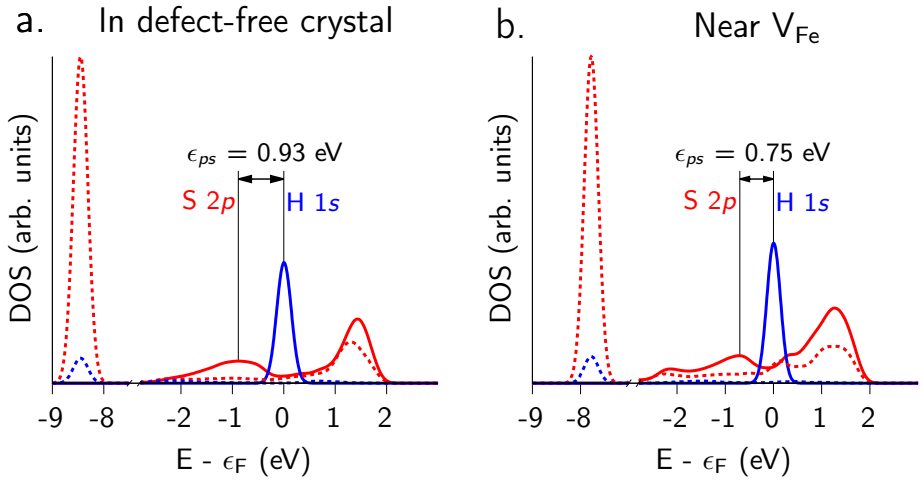

Figure 5-9: The overlap between the sulfur and hydrogen orbitals is weaker in the defect-free crystal (a) than near the Fe vacancy (b) leading to a stronger adsorption and bonding in the defective crystal.

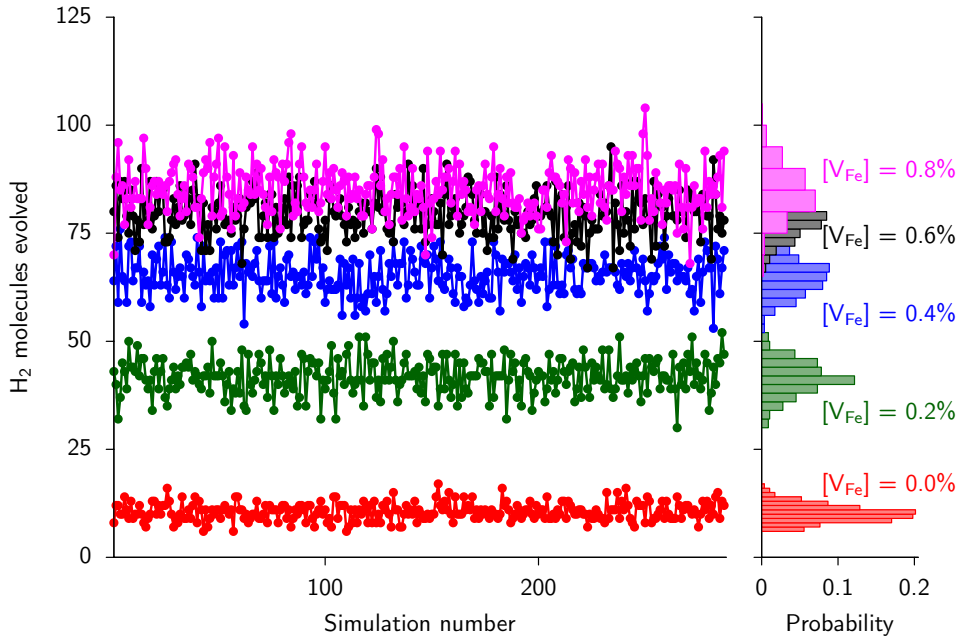

Figure 5-10: Number of H_2 molecules evolved in the kMC simulation cell as a function of the intrinsic defect concentration

a period of 1 μs for systems where 0, 0.2, 0.4, 0.6 and 0.8 % of the Fe sites are vacant. For consistency of comparison, we perform these calculations on a system with an initial concentration of atomic hydrogen interstitials of 0.02, which corresponds to experimental conditions of pH = 0, U = -0.76 V SHE at a temperature of T = 200 °C. Additionally, instead of relying on a single kMC calculation to estimate the hydrogen evolution reaction rate, we take the average of H_2 molecules evolved from an ensemble of 288 identically initialized calculations. Specifically, we recognize that the number of H_2 molecules evolved at the end of the 1 μs of simulations is a Poisson random variable and therefore calculate the average by fitting a Poisson distribution and extracting the value of λ, the HER rate, from the best fit.

Based on the barriers for the unit processes in the previous section, we see that H_2 evolution proceeds at a surprisingly high rate of 10.6 H_2 molecules per simulation cell, which corresponds to a H_2 evolution rate of 3.152 moles/s per gram of mackinawite at U = -0.76 V SHE, which compares favorably with hydrogen evolution from the defect-free basal planes of other layered catalysts like MoS_2 [267]. This relatively high rate of HER can partially be explained by the high electronic conductivity of the mackinawite basal plane. A similar trend was observed for semiconducting catalysts like MoS_2, where increasing basal plane conductivity through phase transformations, addition of a conductive matrix like CNTs or by increasing the fraction of more conductive edge sites correlated to an increase in the effective HER rate [100, 268].

Figure 5-10 also indicates that a small increase in the number of Fe vacancies from 0% to 0.8% increases the effective number of hydrogen molecules evolved over 7-fold to 85.1 H_2 molecules per simulation cell. However, the catalytic activity of the Fe vacancies does not increase linearly with the Fe vacancy concentration, with the majority of the HER catalysis occurring at low V_{Fe} concentrations and higher V_{Fe} concentrations providing only marginal increases in catalytic activity. Similarly, if the kMC calculation is repeated for a simulation cell containing a greater initial concentration of hydrogen atomic interstitials (8% instead of 2% as in Figure 5-10), the catalytic efficiency of the

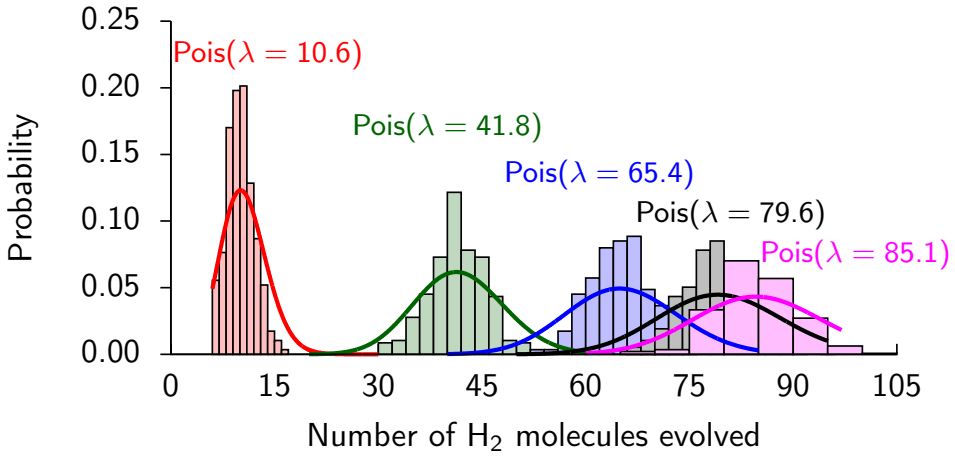

Figure 5-11: The number of H_2 molecules evolved in the kMC simulation is a Poisson random variable, whose parameter, λ, is a measure of the average number of H_2 molecules evolved in the ensemble of calculations. The color key is identical to the one used for Figure 5-10

Fe vacancies over a defect-free crystal is less pronounced, even though the number of evolved H_2 molecules is higher (Figure 5-12).

These two observations can be rationalized by observing that the V_{Fe} sites catalyze H_2 evolution primarily by increasing the effective number of neighboring reactant hydrogen atoms at the reaction site. Therefore, while a small concentration of Fe vacancies will increase the local concentration of atomic hydrogen interstitials due to stronger bonding, a larger concentration of Fe vacancies will be less effective because it introduces the possibility of isolated, single hydrogen atoms pinned at separate V_{Fe} sites. Similarly, the catalytic efficiency of V_{Fe} is stronger in the limit of low hydrogen concentrations, because at higher hydrogen concentration, even defect-free reaction sites have sufficient concentration of adjacent hydrogen atoms leading to a comparable hydrogen evolution rate.

Defect-engineering the hydrogen evolution reaction The modulation of hydrogen adsorption energy due to undersaturated defect sites presents an opportunity for controlling the hydrogen evolution activity through defect engineering. Based on the ubiquitous Sabatier principle [16], and the free-energy landscape of the hydrogen evolution reaction, Norskøv *et. al.* theorized that the optimal (i.e. most rapid) hydrogen evolution reaction rate occurs when the free energy of adsorption of hydrogen at the reactive site (relative to the energy of a free H_2 molecule) is 0 eV, effectively placing the peak of the Sabatier volcano at the point where the hydrogen evolution reaction is isergonic, i.e. when the $\Delta G = 0$ [269]. This insight has been used to explain increased catalytic activity in systems like defect-engineered MoS_2 [270] and $CoSe_2/MoS_2$ ($\Delta G = 0.10$ eV) [254], where hydrogen evolution reaction activity compares favorably with more expensive, traditional catalysts like Pt.

In a defect-free crystal, the ΔH_f for two atomic hydrogen interstitials is 1.847 eV and that for the interlaminar H_2 interstitials is 1.643 eV giving is a net reaction enthalpy of -0.203 eV. Similarly, the energy of atomic interstitials near the Fe vacancy is 1.016 eV and the energy of the H_2 molecule near the Fe vacancy is 0.95 eV giving a net reaction enthalpy of -0.065 eV, which is closer to 0 eV and indicates a more rapid H_2 evolution reaction.

In order to investigate the possibility of further improving the hydrogen evolution ac-

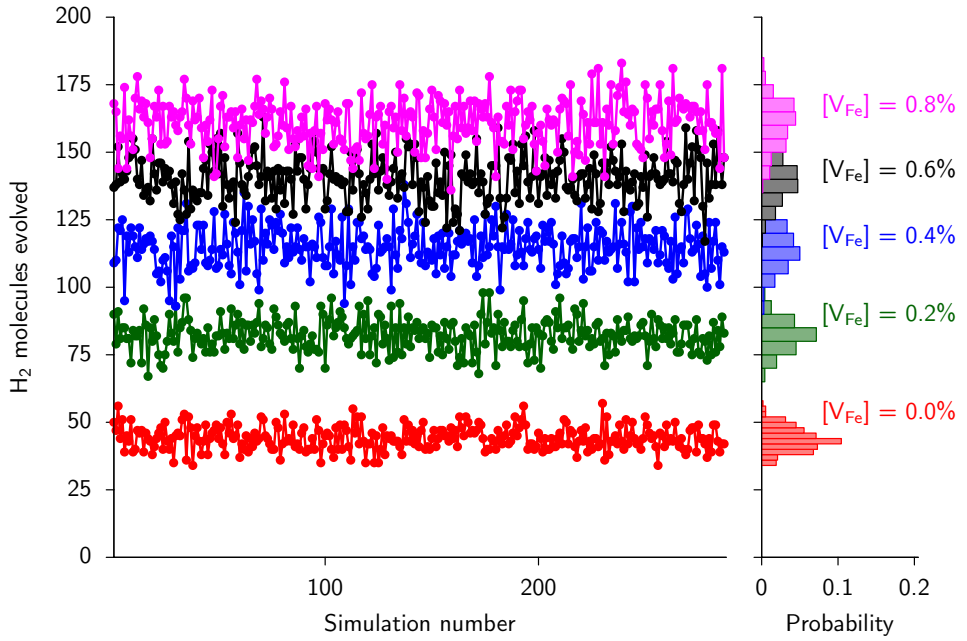

Figure 5-12: The catalytic efficiency of the Fe vacancies is reduced at higher interstitial concentrations even though the number of evolved molecules is greater

tivity, we perform a series of kMC calculations, identical to those described in Section 5.6.2, on bulk mackinawite supercells containing 0.2% Fe vacancies. The calculations differ only in the adsorption energy of the hydrogen atoms at the Fe vacancy site. The adsorption energy is varied from -0.5 eV to 0.2 eV relative to an interstitial H_2 molecule, allowing us to probe scenarios, where hydrogen binding to the mackinawite crystal is both stronger and weaker than the binding energy calculated by DFT (-0.31 eV). Figure 13 shows the variation in the number of hydrogen molecules evolved in the kMC simulation as a function of the adsorption energy at the defect site, clearly reproducing the Sabatier volcano curve for hydrogen evolution activity. Interestingly, the curve indicates that the Fe vacancy in mackinawite binds the hydrogen atoms too strongly allowing for a greater concentration of hydrogen at the reaction site, but a lower rate of Tafel (hydrogen recombination) reaction, leading to an overall low rate of H_2 evolution. The calculations indicate that weaker adsorption at the vacancy (i.e. with a 0.2 eV increase in adsorption energy to -0.10 eV) increases the number of evolved H_2 molecules from 45 to 141, suggesting that engineering the adsorption energies through doping, lattice strain and substrate interactions can improve the hydrogen evolution activity of defective mackinawite by over 200%. Similar schemes have recently been proposed for improved hydrogen evolution on nanostructured metal [271] and semiconductor [272] catalyst particles.

5.6.3 Conclusions

We used DFT and NEB to understand migration and association reactions of hydrogen interstitials in the interlaminar space of the layered transition metal sulfide, mackinawite (FeS). We identified, using CINEB-informed kinetic Monte Carlo calculations, that conductive mackinawite layer leads to a moderately high HER rate in defect free mackinawite, which increases by over 7-fold due to the introduction of less than 1% Fe vacancies. Electronic structure measurements of the catalytic site near the Fe vacancy

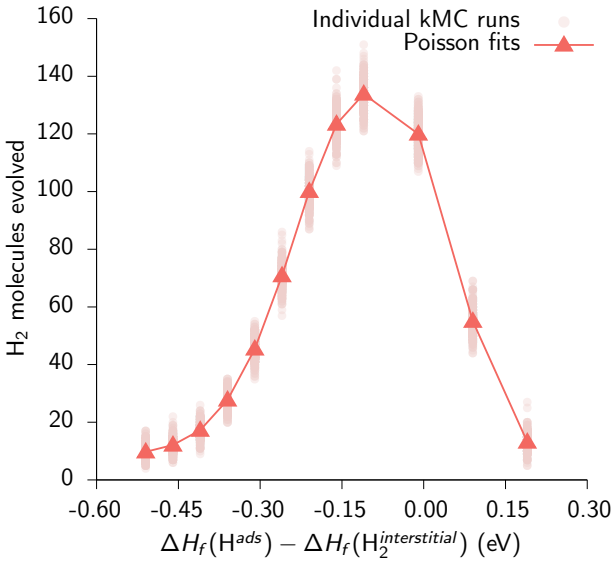

Figure 5-13: Variation of hydrogen evolution activity as a function of hydrogen binding energy indicates that the hydrogen binding at the mackinawite Fe vacancy ($'H_f = -0.31\ eV$) is too strong and a slightly weaker binding energy can lead to a 200% improvement in hydrogen evolution activity. This highlights the potential for designing better hydrogen evolution activity by modifying adsorption energy through doping and lattice strain.

indicate that the hydrogen adsorption at the defect site is stronger than in a defect-free site due to a greater overlap between the S 1*p* and H 1*s* orbitals. This stronger bonding leads to an increased concentration of reactant species for the Tafel reaction and effectively a greater H_2 evolution rate. These calculations quantify a mechanistic pathway for interlaminar evolution of hydrogen gas in acidic environments and has implications for non-destructive electrochemical exfoliation of layered materials as well as interlaminar strength and stability of mackinawite.

5.7 Outcomes and Future Work

The primary aim of this chapter is to mechanistically explain the formation of different hydrogen interstitials in the mackinawite crystal and understand the impact of these interstitials on the mechanical properties of the crystal in an effort to identify if hydrogen-induced mechanical degradation can explain the observed poor passivity of mackinawite films. Below, we summarize the results from the previous sections and propose and outline for extending the work in this thesis to the analysis of other catalytic reactions and the behavior of other material systems.

5.7.1 Outcomes

Hydrogen defects: In contrast to compact iron sulfide phases, layered mackinawite can accommodate both laminar and interlaminar interstitials. The two most stable hydrogen defects are the sulfur-bonded monoatomic hydrogen interstitial and the interlaminar H_2 molecular interstitial, with formation energies of 0.92 eV and 0.81 eV respectively, relative to a free H_2 molecule.

Point defect dynamics

The electronic structure of the undersaturated sulfur ions near the Fe vacancy leads to stronger bonding of the hydrogen atom and an effective increase in the concentration of neighboring hydrogen atoms participating in the Tafel hydrogen evolution reaction and subsequently a greater rate of H_2 evolution. This mechanism leads to a seven-fold increase in the number of H_2 molecules evolved at low concentrations of hydrogen interstitials and indicates that H_2 interstitials occur in considerable concentrations under electrochemical conditions.

H-induced exfoliation

Tensile and shear stress-strain tests indicate that the presence of H_2 interstitials in the interlaminar region significantly reduces the strength of attractive van der Waals binding forces between the mackinawite basal planes leading to easy exfoliation and poor mechanical stability.

These three results, taken together, outline a mechanistic description of the role of hydrogen interstitials in causing mechanical degradation of mackinawite films in sour corrosive conditions.

5.7.2 Future Work

The work in Section 5.5.2 quantifies the interlaminar binding forces in the presence of hydrogen interstitials in the interlaminar spacing using dispersion-corrected DFT. However, the study is restricted to relatively large hydrogen defect concentrations ($H : Fe \approx 25\%$) due to limitations on the lateral size of the simulation cell. A useful extension of this work would involve quantifying the weakening of the interlaminar binding interactions at lower hydrogen concentrations ($H : Fe \approx 1\%$) that are more realistic in corrosion conditions.

The results from this chapter provide mechanistic detail into the mechanical degradation and eventual exfoliation of mackinawite due to hydrogen interstitials. A similar approach can be applied to identify other interstitials like O_2, Br_2 etc. suitable for non-destructive exfoliation of interesting 2D crystals like MoS_2 and graphene.

The kinetic Monte Carlo calculations described in Section 5.6.2 also quantify precisely the hydrogen evolution rate at the point defect sites in the layered structure and thus provide a metric that is more accurate at estimating the effective catalytic efficiency of point defects than the LDOS or the adsorption energy at the defect site. This method can supplement existing screening procedures for defective or doped materials by providing a more accurate picture of realistic catalytic activity.

Chapter 6

Multiscale Passive Film Model (MPFM)

In light of the importance of corrosion prevention and prediction, several analytical and numerical corrosion models of varying degrees of sophistication have been devised to evaluate corrosion rates and estimate material lifetimes. Dedicated models for iron sulfide passive films and sour corrosion processes are a recent addition reflecting the relative paucity of sour-field corrosion data used to benchmark such models. Such models are typically benchmarked to or even exclusively derived from existing field data resulting in a degree of empiricism that renders it non-predictive and applicable only to a selective set of corrosion environments

In contrast, recent efforts in quantifying the thermodynamics and kinetics of unit processes occurring in iron sulfide passive films (Chapters 2-5) provides a novel opportunity to model film passivity as a result of the collective behavior of such unit processes. However, such 'bottom up' modeling of atomic scale phenomena and processes throughout the macroscale passive film is prohibitively expensive therefore such an approach must necessarily involve multiscale modeling of the passive film with judicious use of coarse graining in regions of the passive film where atomic resolution is not required.

In this chapter, we describe the development of one implementation of a multiscale passive film model using meso-scale phase field method coupled with atomic-scale kinetic Monte Carlo and contextualize this new modeling framework with a review of existing public models for passive films in both sour and non-sour corrosion systems. Further, we describe details about the formulation and numerical implementation of the multiscale passive film model along as well as the utility of the model in constructing kinetic stability diagrams and degradation maps that can provide design rules for improving corrosion performance in sour conditions. We then conclude the chapter with a summary of the capabilities and shortcomings of the existing model with suggestions about extending the framework to address these concerns.

6.1 Background and Motivation

The overarching motivation for this thesis is to understand the collective behavior of unit processes and work towards the construction of a more deterministic model for electrochemical passive films that is capable of predicting *a priori* degradation rates and trends under realistic pipeline corrosion conditions, using parameters that can be

measured and compared through experiment, with the aim of using the predictive capabilities of the model to identify safe operating conditions and to design more protective materials and inhibitors for corrosive environments. Desirable characteristics of such a model are:

1. Non-empirical: able to calculate passive layer growth rates $L(t)$, transient and steady state corrosion currents $i(t)$ and passivity breakdown (e.g. pitting probability $P(t)$ and stable pit growth rate $\frac{dL}{dt}$) using a "bottom-up" approach, i.e. by simulating unit steps such as atomic diffusion and charge transfer reactions. The model should have as few empirical (fitted) parameters as possible.

2. Predictive: able to make accurate predictions that can be related to corrosion tests and cover a range of environmental conditions such as temperature, pressure, sulfur concentration and applied potential.

3. Modular: complexity can be added or removed by considering unit processes as separate elements of the model.

4. Bridges length- and timescales: can make predictions from the atomic- and nanometer scale in fractions of a second, to the macroscopic level over timescales of hours and years that can be compared to laboratory experiments and industry tests.

6.2 Chapter goals and layout

The primary aim of this chapter is to describe the development of a multiscale model for passive films in sour environments that incorporates results about atomic scale phenomena like sulfidation (Chapter 2), diffusion (Chapter 3), pit initiation (Chapter 4) and hydrogen-induced film embrittlement and debonding (Chapter 5) into a macroscopic model of a multiphase (mackinawite, pyrrhotite, and pyrite) passive film.

The primary objective of such a multiscale model is two-fold

1. Identify the impact of the considered unit processes towards the growth (phase stability, growth kinetics and regimes) and breakdown (film dissolution and susceptibility to pitting) of these passive films.

2. Establish a framework of universal atomic processes common to all electrochemical passive films and, thus, enable an extension of the existing model to other systems beyond iron sulfides.

The rest of the chapter is divided into four main sections. In the first section, we provide a **review of existing corrosion models** for electrochemical passive films. We then open the next section on the **formulation of the multiscale passive film model** by describing the coupling of length scale between the atomic-scale kinetic Monte Carlo (kMC) and mesoscale phase-field (PF) frameworks before describing the general features of kMC and PF modeling methods as well as their numerical implementation. In the next section, we describe the **results** of the application of the PFM framework to the sour corrosion system and demonstrate its utility by constructing kinetic stability diagrams and degradation maps at different environmental conditions. We conclude the chapter with a brief discussion on the **model outcomes and proposed future work** to extend the results of the model to other corrosion systems.

6.3 Review of existing models

Research work on analytical and computational modeling of passive film behavior dates back at least 70 years. In the interest of providing some context to subsequent sections on the multiscale passive film model, we provide here a brief discussion on the merits and shortcomings of the a few important existing corrosion models for passive film growth and breakdown, although we do not attempt an exhaustive review of corrosion models.

6.3.1 Film growth models

High field models have often been used for describing the incipient stage of film formation on metals [273–275] In such nanometer-thick passive films, film growth kinetics is governed by the rate of electromigration (i.e. the diffusion of cations and/or anions under the influence of an extremely strong electric field. In this regime, the oxidation rate is inversely proportional to time t, yielding a logarithmic law:

$$L(t) = k_e \log(\alpha t + 1)$$

where k_e and α are temperature- and field- dependent constants and $L(t)$ is film thickness at time t.

The Wagner theory describes the growth of passive films in conditions where diffusion of ions through the film is the rate-limiting unit process [276]. This leads to a parabolic film growth law of the form:

$$L(t) = \sqrt{k_p t}$$

where k_p is the parabolic rate constant, a function of the ionic diffusivity D of the mobile species. High-temperature sulfidation of iron at temperatures greater than 500 ^{o}C is well described by Wagner theory [121, 277].

In conditions where surface sulfidation (or oxidation) is comparable to the ionic flux through the growing film, the growth profile including a linear (at shorted timescales) as well as a parabolic (at longer timescales) growth profile and is best described the well-known Deal-Grove equation of film growth [278]

$$L(t)^2 + A \cdot L(t) = B(t + \tau)$$

where $L(t)$ is the film thickness at any given time, t, and A and B are material-dependent constants and τ is a time-offset factor to account for presence of an initial passive film (i.e. at time $t = 0$)

Continuum-scale models generally lack the resolution to describe atomistic mechanisms, because the experimental capabilities required to image and characterize physical phenomena at interface at the atomic scale are only just being developed [279] and we are only just beginning to understand the impact of phenomena like interfacial water structures on reactivity [280]. Therefore, these continuum models are limited to simulating more well-known unit processes such as diffusive transport of ions (or ionic clusters [281]) through the microscopically homogeneous passive film [282]. To overcome the problems associated with a continuum description of passive films, several atomistic models have been proposed [283], but the development of such atomistic models are limited by the complexity involved in considering multiple phases (metal, different sulfides, electrolyte), their interfaces, the electric field, the temperature, its nanostructural defects and the surface defects. In addition, it is worth mentioning that while atomistic models better handle the mechanisms involved in oxidation reactions

occur at the film-electrolyte interface [284], such processes are also handled in some continuum scale analytical models [285, 286].

6.3.2 Models for film dissolution and degradation

While film growth kinetics provide useful data, it is also desirable to model the breakdown or loss of passivity in aqueous conditions. Mackinawite formation models that describe iron sulfide scale formation have been proposed by Nesic *et al.* [177, 287, 288]. The model assumes a bi-layered mackinawite film comprised of a thin (10 nm), compact inner layer and porous outer scale, 100s of microns thick. The corrosion rate is limited by mass transport (diffusion) through the mass transfer boundary layer at the scale-electrolyte interface, through the liquid in the porous outer scale and finally through the compact inner sulfide. In addition, general corrosion scale damage by hydrodynamic stresses is considered. However, the model is inherently empirical, requiring several parameters to be fitted using experimental data. Moreover, the evolution of the scale to form stable sulfides at longer times is not considered. A significantly more relevant and difficult topic is to model localized film degradation by pitting, which requires simulation of atomic processes involved in pit initiation and pit nucleation as well as processes involved in extremely rapid film dissolution leading to pit growth. While it is understood that metastable pitting is an essential step towards the formation of longer lasting stable pits, the mechanism for the nucleation and evolution of these pits is still not well-understood [173], with several competing theories for the origin of localized pits [172].

This is also reflected in the paucity of atomic deterministic models for pit nucleation [284] and also the fact that all continuum-scale models use parameterized stochastic models to predict the formation of these metastable pits [179]. In the absence of robust atomistic explanations, empirical simulation methods like deterministic Cellular Automata (CA) and stochastic Monte Carlo (MC) have been used to explain pit morphology [289–292]. Such models are usually used to reproduce experimental observables like pit onset potentials, pit morphology and pit growth rates. A large majority of such pit growth models are concerned with the growth of an existing metastable pit and often model this pit in isolation [293], but fewer stochastic models also tackle the atomic scale breakdown of passivity leading to pit initiation as a purely stochastic process [294]. Even fewer models try to combine the elements of stochastic and deterministic models [290, 291, 295], for example by combining stochastic pit initiation with deterministic pit propagation [290]. The vast majority of such models with atomic resolution rely on empirical parameters primarily due to the lack of observable experimental data at this scale [187, 296], but this gap is being filled by newer experiments and literature [296–298]. Finally, dedicated models for the breakdown of passive films under specific condition (such as mechanical or electrochemical loading) also exist for applications like stress-corrosion cracking, but rely largely on empirical parameters [299, 300].

6.3.3 Combined growth and breakdown models

The Point Defect Model (PDM) of Macdonald *et al.* is a deterministic analytical framework for describing the growth, breakdown and general protectiveness of passive films [182, 301]. This model incorporates the effect of unit processes involved in film growth (surface oxidation, sulfidation and ionic diffusion) but also accounts for surface defect formation and defect dynamics associated with film dissolution. Relying only on independently measurable physical properties of the passive film (such as diffusivity etc.)

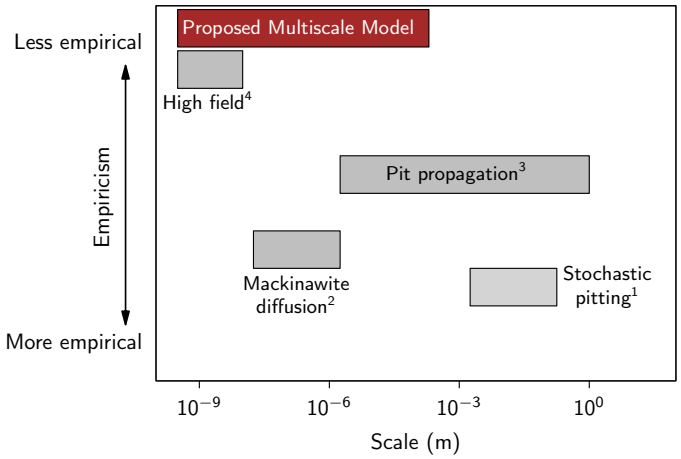

Figure 6-1: Phase space of existing passive film models

the model can make prediction about the general growth rate of the passive film as well as localized damage to the passive film.

6.4 Formulation of the Multiscale Passive Film Model

The previous section highlights the challenges involved in modeling multiphase highly defective passive films that are sensitive to changes in global variables like electrolyte chemistry and system temperature etc. These challenges are well understood [284] and the case of a realistic passive film represents a classic example of some unit processes with sub-nm resolution as well as modeling of mesoscale microstructure of chemical and electrical potentials on length scales of 100s of nanometer or even microns.

The primary difficulty in the formulation and implementation of such a passive film model is being able to simulate atomic length scale and nanosecond time scale unit processes at the metal-film and film-environment interfaces and also model macroscopic mass transport and sulfur chemical potential dependent evolution of a multiphase microstructure (both of which occur over macroscopic length scales and across time scales of several days or months). To reconcile the need for modeling a macroscopic (i.e. micron-scale) multiphase film with the need for simulating atomic scale process occurring at the surface of the passive film, we adopt a two-scale strategy, as espoused by Elliot *et al.* [302], where the microstructure and the bulk behavior and properties of the passive film are described by a mesoscale phase-field model, whereas atomic-scale behavior at the interfaces between the passive-film and the environment or between the passive-film and the metal are described by two dimensional kinetic Monte Carlo models that have appropriate resolution to tackle such details.

Figure 6-2 shows a schematic of the unit processes considered in the study to be responsible for the growth and breakdown of the FeS_x passive film. The unit processes considered here are a large subset of processes identified by the point defect theory [182, 301] and are common to passive films even outside the sour corrosion system. Specifically, film growth is modeled as a collective outcome of surface sulfidation and bulk diffusion. Localized film degradation, likewise, is modeled as occurring due to the formation of surface vacancies and subsequent vacancy dynamics due to film dissolution. In addition, we also consider localized film degradation due to hydrogen-induced

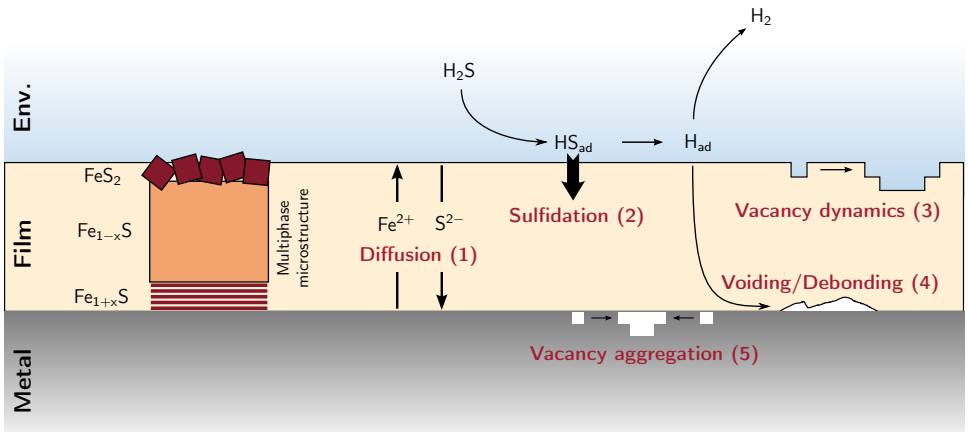

Figure 6-2: Schematic of the unit processes considered in the model of the multiphase film. Processes (1) Ionic diffusion and (2) Sulfidation contribute to film growth and processes (3) Surface vacancy dynamics, (4) hydrogen-induced debonding and (5) vacancy agglomeration lead to initiation of localized film degradation and pitting and are modeled using separate kinetic Monte Carlo models each.

void formation and film debonding at the metal-film interface as well as localized degradation due to vacancy formation and aggregation at the metal-film interface.

In the next section, we provide a brief primer to the phase field method as well as the numerical implementation of a model used to simulate iron and sulfur diffusion, evolution of the sulfur chemical potential profile and nucleation and growth of different iron sulfides. In subsequent sections, we describe, in general, the kinetic Monte Carlo simulation method and then describe three individual models that are used to simulate the processes of vacancy dynamics during film dissolution (Process 3 in Figure 6-2), H_2 formation and film debonding (Process 4 in Figure 6-2), and vacancy-agglomeration and void formation (Process 5 in Figure 6-2).

6.4.1 Phase field modeling

In order to model the time evolution of the compositionally and structurally inhomogeneous microstructure of the sour passive film, we use the free energy based diffuse interface phase field method, because such energy-based modeling is an appropriate methodology to describe the microstructure evolution in a physically consistent way. The phase-field approach [303–305] has been emerged as a powerful computational methodology for modeling the microstructure evolution of materials at the mesoscale and has already been used to investigate non equilibrium phenomena such as solute segregation/depletion [306] and grain growth [307, 308] among others. To interpret the multiscale model, we implement appropriate coupling between the kMC and PF model systems. This is a difficult, but critical part of any model [309].

The fundamental idea behind the phase field model is the use of so-called phase field variables, which vary continuously in space, and which describe the phase fractions of each material phase being modeled. Interfaces between phases are described by smooth but highly localized changes of this variable between fixed values of the phase field variable in the bulk phases (i.e. between 0 and 1). In this method, the free energy of the system is expressed only as a function of the individual phase field variable and their gradients and is obtained by coarse graining the realistic free-energy by integrating over atomic-scale details like atomic vibrations and individual defects. The time evolution of the phase field variables and therefore of the film microstructure is governed by the Langevin equation of motion and this approach is attractive because it avoids the

Field variable	Symbol	Description	Range of values
Metal phase field	ϕ_{met}	Phase fraction of metal at a grid point	[0,1]
Mackinawite phase field	ϕ_{mkw}	Phase fraction of mackinawite at a grid point	[0,1]
Pyrrhotite phase field	ϕ_{pht}	Phase fraction of pyrrhotite at a grid point	[0,1]
Pyrite phase field	ϕ_{pyr}	Phase fraction of pyrite at a grid point	[0,1]
Environment phase field	ϕ_{env}	Phase fraction of mackinawite at a grid point	[0,1]
Sulfur chemical potential	μ_S	Chemical potential of sulfur in different phases	$[\mu_S^{min}, \mu_S^{max}]$
Hydrogen concentration	$[H^+]$	Proton concentration in the electrolyte	$[10^{-14}, 10^0]$
Orientation	Θ	Orientation of the [100] direction of the pyrite crystal relative to the simulation cell	$[-\frac{\pi}{4}, \frac{\pi}{4}]$
Electrical potential	ψ	Electrical potential in the double layer	$[\psi_{met}, 0]$
Voids	ρ_V	Extent of voiding at the each grid point	[0,1]

Table 6.1: Field variables in the phase field simulation of the MPFM

mathematically difficult problem of tracking the position and orientation of the interface as all interfacial terms can simply be written as a function of the gradual of phase field variables.

While such a coarse graining of system free energy is very attractive for modeling mesoscale system properties, a rigorous connection between the microscopic and mesoscopic descriptions of free energy is possible only for the simplest physical systems. For more realistic systems, we are forced to use approximate expressions of free energy that are usually polynomial functions of experimental variables like pressure, temperature, electrical potential, chemical potential etc. In the current model, the free energy functional is a function of the five phase field variable, each representing a phase fraction of iron sulfide phases present in the lattice point, ϕ_{met}, ϕ_{mkw}, ϕ_{pht}, ϕ_{pyr}, ϕ_{env} as well as chemical potential of sulfur μ_S, the spatial orientation of the iron sulfide grains Θ, and the temperature, T. Table 6.1 lists the exhaustive set of field variables defined at each grid point with the phase field simulation system along with a brief description and the allowed range of values the variable can take.

The dynamics of these phase fields are described by dissipative Langevin equations using one of two time-dependent Ginzburg Landau models based on whether the field variable is conserved or non-conserved.

Evolution of non-conserved field variables

The evolution of a continuous non-conserved field variable, ϕ_i under Langevin dynam-

ics proceeds through the Allen-Cahn equation

$$\frac{\partial \phi_i}{\partial t} = -M_\phi \frac{\delta \mathscr{F}}{\delta \phi_i}$$

which defines the rate of evolution of a phase field variable $\phi_i \in [\phi_{met}, \phi_{env}]$ in response to the thermodynamic driving force $\frac{\delta F}{\delta \phi_i}$. The proportionality factor between the driving force and the response is $-M_\phi$, where M_ϕ is a strictly positive value that is called the field mobility that defines the kinetics of the evolution of the phase i.

Evolution of conserved field variables

The equation of motion governing the evolution of a conserved field variable (like the concentration of sulfur or hydrogen, in the case of sour corrosion) is the Cahn-Hilliard equation, whose dynamics must satisfy the conservation equation

$$\frac{d}{dt} \int dr\ \phi(r) = 0$$

Dissipative dynamics under this condition gives us the expression

$$\frac{\partial \phi}{\partial t} = \nabla \cdot \left(D \nabla \frac{\delta \mathscr{F}}{\delta \phi} \right)$$

which is identical to the Fick's second law of diffusion, with the term $\frac{\delta \mathscr{F}}{\delta \phi}$ representing the chemical potential of the field variable, ϕ. In the MPFM, this method is applied to the field variables, μ_S and $[H^+]$ that are conserved and undergo diffusive relaxation.

Evolution of other field variables – Electric potential

In order to understand the impact of surface electrical potential and the double layer electric field on the surface sulfidation reaction (Chapter 2), the MPFM includes a module that solves the Poisson Boltzmann equation in the aqueous region of the simulation cell at each time step to extract the distribution of the electrical potential in the double layer region (i.e. the field variable ψ).

$$\nabla^2 \psi = -\frac{\rho_q}{\epsilon\ \epsilon_0}\ ;\ \rho_q = \left[H^+\right] |e| \exp\left(-\frac{\psi\ e}{k_B T} \right)$$

The model accepts as input the corrosion potential of the metal as well as the average pH of the electrolyte, since the model assumes that the electrode potential is screened only by the H^+ or OH^- counter ions in the electrolyte. Figure 6-3 shows a two-dimensional map of the distribution of electric potentials in the electrochemical double layer formed on a rough metallic surfaces at different pH values.

Evolution of other field variables – Electric potential

In order to investigate the nucleation and growth of individual pyrite crystals (as seen in film microstructure images) and to understand the impact of boundaries between pyrite crystals, we introduce a new field variable, Θ, that describes the orientation of the [100] direction of the pyrite crystal with the z-axis of the simulation cell. Using Θ, we can define the orientation-dependent surface energies using $\sigma = \sigma(\Theta)$ to construct pyrite's characteristic four-fold symmetric surface energy. The evolution of this non-conserved field variable is done using the Allen-Cahn equation similar to the case for phase field variables.

$$\frac{\partial \Theta}{\partial t} = -M_\Theta \frac{\partial \mathscr{F}}{\partial \Theta} = \nabla \cdot (D_\Theta \nabla \Theta)$$

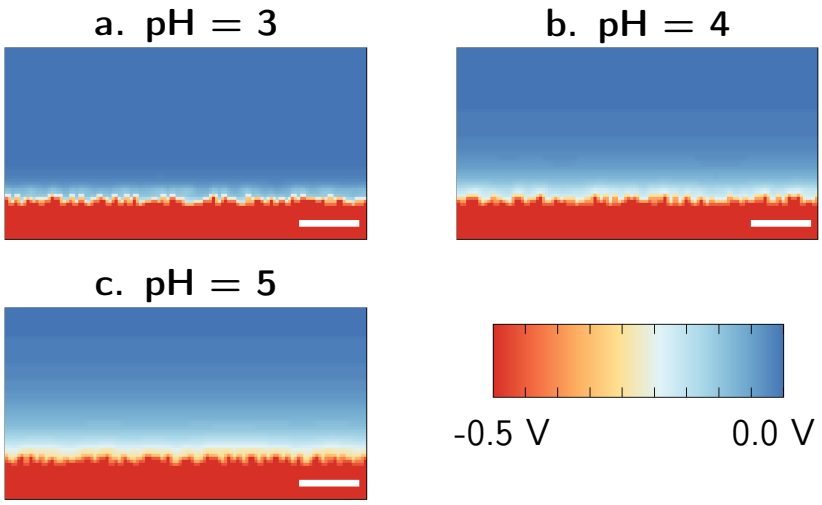

Figure 6-3: Distribution of electrical potential given by the Poisson-Boltzmann equation in conditions of (a) pH = 3, (b) pH = 4 and (c) pH = 5. The white scale bars in each figure correspond to a length of 100 nm. The metal is held at -0.5 V SHE, close to the corrosion potential in sour corrosion.

where the effective diffusivity parameter is defined using the expression

$$D_{\Theta} = \frac{1}{|\nabla \Theta|}\left(M_{min} + (M_{max} - M_{min})\,\phi_{pyr}\right)$$

such that each isolated pyrite crystal has a unique and constant value of Θ.

6.4.2 Phase field – Numerical Implementation

One of the primary assumptions of the phase field model is the choice of the free energy functional, i.e. the mathematical form of the free energy as a function of the phase field (ϕ_i, μ_S, η) and global variables (T). The expression for the free energy of the point inside the simulation cell in the phase field method is

$$\begin{aligned}\mathscr{F}(\boldsymbol{\phi}, \boldsymbol{\Theta}, \boldsymbol{T}) \quad = \quad & \sum_{i<j}^{N,N} \sigma_{ij}\left(\phi_i \nabla\phi_j - \phi_j \nabla\phi_i\right)^2 + H_{ij}\phi_i^2\phi_j^2 + \\ & \left(\left(\phi_i^3 + \phi_i^2\phi_j - \phi_j^2\phi_i - \phi_j^3\right) \times \left(w_i - w_j\right)\right) + \\ & \delta_{i,pyr}\ \delta_{j,pyr}\ \phi_i\ s\ |\nabla\Theta|\end{aligned}$$

where w_i represents the free energy of the phase i, which are effectively inputs to the phase field model. For the purpose of the phase-field calculations, the free energy of the metal is taken to be zero and the other values are scaled accordingly. Additionally, sulfur is assumed to exist as a dilute solution in both the metal and the environment, therefore the chemical potential of sulfur in these phases (in J mol^{-1}) is given by $\mu_{S,environment} = RT\ln[S]$. The relative free energies of the different material phases used in the MPFM are listed in Table 6.2.

In order to solve the Allen Cahn equation for the evolution of non-conserved phase-

Phase	Free energy (J/mole)
Metal	$w_{\text{met}}(T,\mu_S) = 0$
Mackinawite	$w_{\text{mkw}}(T,\mu_S) = 9.96\times10^{-7}\mu_S^2 + 20.53\ T - 65060$
Pyrrhotite	$w_{\text{pht}}(T,\mu_S) = 9.96\times10^{-7}\mu_S^2 + 20.53\ T - 72050$
Pyrite	$w_{\text{pyr}}(T,\mu_S) = 9.96\times10^{-10}\mu_S^2 + 50.36\ T - 98710$
Environment	$w_{\text{env}}(T,\mu_S) = \mu_S$

Table 6.2: Free energies of material phases used in the multiscale passive film model

fractions, we recognize that the above equation can be rewritten in pair-wise terms such as

$$\mathscr{F}(\phi) = \sum_{i<j}^{N,N} \mathscr{F}_{ij}$$

Since the sum of the phase fractions is a conserved quantity, the Allen-Cahn evolution equation can be rewritten as

$$\frac{\partial \phi_i}{\partial t} = \sum_{i\neq j}^{N} -M_{ij}\left(\frac{\partial \mathscr{F}_{ij}}{\partial \phi_i} - \frac{\partial \mathscr{F}_{ij}}{\partial \phi_j}\right)$$

With the condition that $M_{ij} = M_{ji}$

Plugging this back into the original Allen Cahn equation, we get

$$\begin{aligned}\frac{\partial \phi_i}{\partial t} &= \sum_{i\neq j}^{N} -M_{ij}\Big[-\sigma_{ij}\ \left(\phi_i\nabla^2\phi_j - \phi_j\nabla^2\phi_i\right) + 2H_{ij}\phi_i\phi_j\left(\phi_i-\phi_j\right) + 2\left(w_i - w_j\right)\left(\phi_i+\phi_j\right)^2\Big] + \\ &\quad \delta_{i,pyr}\ \delta_{j,pyr}\phi_i s|\nabla\Theta|\end{aligned}$$

Similarly, the Cahn-Hilliard equation for conserved fields, ϕ, is simply

$$\frac{\partial \phi}{\partial t} = D\nabla^2\frac{\delta \mathscr{F}}{\delta \phi}$$

The primary input to the Cahn-Hilliard equation are the ionic diffusivities of different phases (Table 6.3) as well as the sulfidation rates on the surface of different phases benchmarked to experimental film growth rates (Table 6.4).

In order to numerically solve these equations, we first discretize them by writing $\phi_i = \phi_i(x,y,z)$ where x, y, and z denote the positions of the grid point. The Laplacians in both the Allen-Cahn and Cahn-Hilliard equations are discretized using the finite difference method on a 27-point stencil, which is appropriate for three-dimensional Cartesian grids. This discretization will yield a set of $x\times y\times z$ linear equations for the Cahn-Hilliard evolution of sulfur concentration field and $x \times y \times z$ non linear Allen-Cahn equations for each phase field variable.

All equations used in the phase field model are solved numerically using the Portable Extensible Toolkit for Scientific Computation (PETSc) library of solvers [320, 321], developed and maintained by Argonne National Laboratories. We cast the phase-field system into a three-dimensional $x \times y \times z$ Cartesian grid distributed array, with 10 variables (as shown in Table 6.1) at each grid point. The discretized Allen-Cahn and

Diffusivity	Description	Value (m^2/s)	Source
D_{Fe}^{Fe}	Self diffusivity of BCC Fe	$7.87 \times 10^{-7} \exp\left(-\frac{57.9\ kJ}{RT}\right)$	[310]
D_{S}^{Fe}	Diffusivity of sulfur in BCC Fe	$1.78 \exp\left(-\frac{205\ kJ}{RT}\right)$	[311]
D_{Fe}^{mkw}	Diffusivity of iron in mackinawite	$3.37 \times 10^{-16} \exp\left(-\frac{15.5\ kJ}{RT}\right)$	[312]
D_{Fe}^{pht}	Diffusivity of iron in pyrrhotite	$10^{\left(-\frac{7056}{T}-2.679\right)}$	[127]
D_{S}^{pyr}	Diffusivity of sulfur in pyrite	$1.75 \times 10^{-14} \exp\left(-\frac{132.1kJ}{RT}\right)$	[313]
D_{Fe}^{pyr}	Diffusivity of iron in pyrite	$2.5 \times 10^{-16} \exp\left(-\frac{41.8\ kJ}{RT}\right)$	[314]
D_{S}^{env}	Diffusivity of sulfur in environment	1.73×10^{-9}	[315]
D_{Fe}^{env}	Diffusivity of iron in environment	7.19×10^{-9}	[316]

Table 6.3: Ionic diffusivity of phases in the multiscale passive film model

Material	Environment	Sulfidation rate (in nm/s)	Source
Iron	Gas	$10^{0.00473T-5.645+0.4\frac{\mu_S+63.5\ kJ}{RT}}$	[317]
Mackinawite	Gas	$0.01372 + 0.04356 \exp\left(\frac{\mu_S}{RT}\right)$	[11]
Pyrrhotite	Gas	$\exp\left(-\frac{11766}{T} - 0.6478\right) \times\ 10^9$	[129]
Pyrite	Gas	$7.45 \times 10^8 \times \exp\left(-\frac{98400}{RT}\right)$	[318]
Iron	Liquid	$0.0666 \times \left(1 + \frac{\mu_S+63562}{RT}\right)$	[288]
Mackinawite	Liquid	$0.1332 \times \left(1 + 2\ \frac{\mu_S+63562}{RT}\right)$	[287]
Pyrrhotite	Liquid	2.416	[11]
Pyrite	Liquid	0.003543	[319]

Table 6.4: Sulfidation rates on the surface of different material phases in the multiscale passive film model

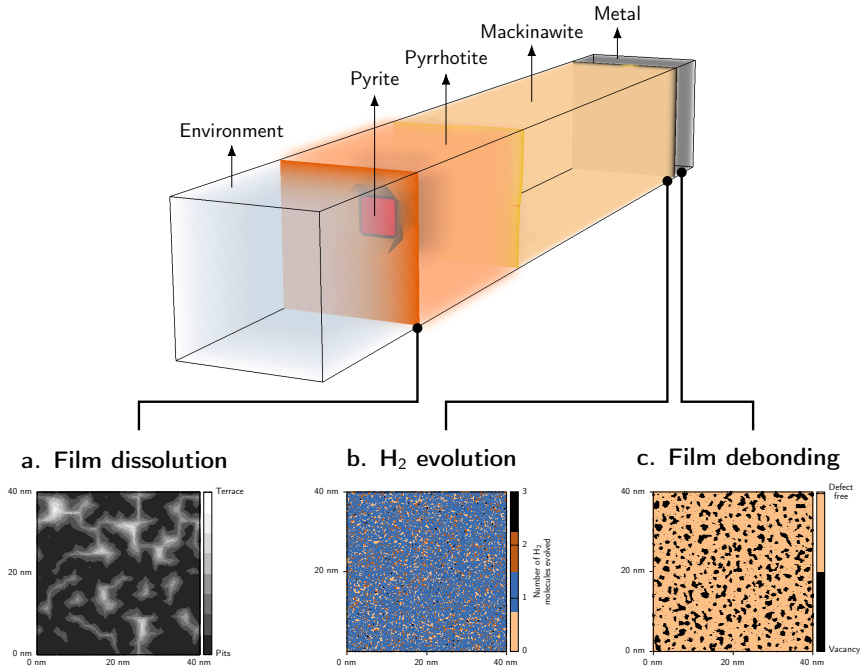

Figure 6-4: A representative output of an MPFM simulation on a 40 nm × 40 nm × 320 nm unit cell showing the evolution of a multiphase FeS_x film between the metal (gray) and sulfidizing environment (light-blue) indicating the formation of layered microstructure comprising of mackinawite (light orange), pyrrhotite (dark orange) and pyrite phases (pink). Inset (a) shows the representative output of the kinetic Monte Carlo model at the film-environment interface dealing with the film dissolution process and vacancy dynamics. The color map shows the topography of the film surface indicating the different terrace (light) and pit (dark) regions. Inset (b) shows the output from the kMC model of H_2 evolution in the mackinawite phase indicating the atomic-scale spatial distribution of H_2 evolution events in the passive film. Inset (c) shows the distribution of vacancy agglomeration (black) at the metal-film interface, which leads to debonding of the passive film.

Cahn-Hilliard equations are then solved using the linear KSP solver framework or the SNES non-linear solver framework. The KSP module of linear equation solvers uses a combination of a preconditioner and Krylov subspace iterative methods to solve linear equations. While PETSc provides a wide variety of both preconditioners and Krylov subspace methods, we use the Block-Jacobi preconditioner in combination with the conjugate-gradient based iterative solver to solve the discretized linear equations for the time-evolution of the sulfur chemical potential and the hydrogen concentration. The SNES module of non-linear solvers provides a robust set of Newton-type, Quasi-Newton and multigrid methods. To calculate the time-evolution of the phase and orientation fields within the MPFM, we construct both the discretized non-linear equations as well as the $(10 \times x \times y \times z)^2$-element Jacobian matrix and solve them using the Non-linear Generalized Minimum Residual method.

6.4.3 Kinetic Monte Carlo calculations

In addition to the phase field description of the 'bulk' behavior of the passive film, we also model localized degradation processes at near-atomic resolutions at the interfaces between the passive film and the surrounding metal and environment regions using three distinct two-dimensional on-lattice kMC models. A brief description of each model along with the simulated degradation process is listed below.

kMC Model	Location in the simulation cell	Model description
Film dissolution	Interface between film and environment	Model local film dissolution and vacancy dynamics leading to nanopit initiation
Vacancy agglomeration	Metal side of the film-metal interface	Agglomeration of vacancies at the metal-film interface leading to debonding at the interface
H_2 blister formation	Film side of the film-metal interface	Association of H_2 molecules leading to blistering at the metal film interface leading to delamination

Table 6.5: Description of kMC models implemented in the MPFM

Below, we describe the general features and formulation of the on-lattice kMC models along with a description of parameters and methods specific to each kMC model. In the former discussion, we will focus on on-lattice models. The interested reader is further referred to the literature by Fichthorn *et al.* [322], Lukkien *et al.* [323], and Voter [324] for a rigorous foundation and further discussion of the different kMC methods

kMC methods achieve long-timescale simulations at atomic-level resolutions primarily by integrating out short-timescale degrees of freedom such as atomic and molecular vibrations and relaxations, that are explicitly modeled in time-constrained molecular dynamics and DFT calculations. By focusing only on 'rare' events such as vacancy formation and vacancy/adatom migration, we can model longer timescales while still retaining atomic level resolution in space. In this infrequent-event paradigm, dynamics are characterized by occasional transitions from one state to another, with long periods of relative inactivity (molecular vibration/relaxation) between the transitions. For each possible transition pathway to another state, there is a rate constant that characterizes the possibility, per unit time, for that transition, and an energy barrier that characterizes the difficulty of achieving the transition.

A master equation is a first-order differential equation describing the time-evolution of the probability that a system occupies each one of a discrete set of states. The probability of an infrequent-event system at a particular state σ and time t is given by [322]

$$\frac{dP(\sigma,t)}{dt} = \Sigma_{\sigma'}\left(W\left(\sigma' \rightarrow \sigma\right)P\left(\sigma',t\right) - W\left(\sigma \rightarrow \sigma'\right)P\left(\sigma,t\right)\right)$$

where σ and σ' are successive states of the system, $P(\sigma,t)$ is the probability that the system is in state σ at time t and $W(\sigma' \rightarrow \sigma)$ is the transition rate between the two states σ' and σ. At steady state, the time derivative of the above equation is zero and the sum of all transitions into a particular state σ equals the sum of all transitions out of the state, corresponding to detailed balance. In this framework, the transitions between states is a memory-less process, i.e. the next state of the system only depends on the current state and not on the ones before (this is the 'Markov property'). Therefore, the time-evolution of the system can be described as a Markov chain with the defined transition rates, W. While an exact modeling of this master equation and of each configuration along the Markov chain is not feasible for any but the smallest systems sizes, kinetic Monte Carlo simulations offer an attractive option for stochastic modeling.

On-lattice kMC is widely used to simulate thermally activated microscopic processes in which the rates of events are governed by energy barriers. Since the jump over the

energy barrier occurs by thermal activation, the probability of exceeding the energy barrier simply follows a Boltzmann distribution [325] and the jump rate is the product of this probability and a constant

$$W_{\sigma\to\sigma'} = \nu_0 \exp\left(-\frac{E^a_{\sigma\to\sigma'}}{k_B T}\right)$$

where $E^a_{\sigma\to\sigma'}$ is the energy barrier associated with event, and ν_0 is the frequency an attempt is made to exceed the barrier. In solids, the attempt frequency is simply the vibration frequency of atoms in the energy basin for each configuration. Once all of the transition rates out of the current state i are computed, the probability for the system at the current state is given by the first-order decay process

$$\frac{dP_{curr}}{dt} = -P_{curr} \cdot W_{tot}$$

where P_{curr} is the probability that the system is in its current state and $W_{tot} = \Sigma_{\sigma'} W_{\sigma\to\sigma'}$ is the total transition rate out of state σ.

Based on this description, the algorithm to perform on-lattice kMC simulations is implemented using the following n-fold-way algorithm or as rejection-free kMC, in which the computation complexity is O(N).

1. Initialize the system distributing particles in the system and zero the time, $t = 0$.

2. Form the list of all possible events (pathways) and compute the transition rate, W_i,for each event.

3. Calculate the cumulative rates, $W_{sum} = \sum_i W_i$, for all $i = 1, 2, \ldots, N$. Where N is the total number of possible events.

4. Generate a uniformly distributed random number $u \in [0, 1]$

5. Select a single event, i, such that $\sum_1^{i-1} W_k < u \cdot W_{sum} < \sum_1^i W_k$

6. Implement the event, i, and move the system into the new state and update all events and probabilities.

7. Generate another uniformly distributed random number $u_2 \in [0, 1]$

8. Advance the system clock by $\Delta t = -\frac{\ln u_2}{W_{sum}}$

9. Return to Step 1

All kMC calculations in the phase field model are performed using the open source kinetic Monte Carlo package, SPPARKS [326] developed and maintained by Sandia National Laboratories and distributed under the GNU Public License. The program implements an efficient binary tree search implementation of the rejection-free on-lattice kinetic Monte Carlo algorithm with a modular architecture, which is useful to construct kMC simulations composed of custom unit processes. For implementation in the passive film model, three new kinetic Monte Carlo model, as described in the last section were coded as separate 'apps' within the SPPARKS framework and called from the parent phase field model code.

Material	Dissolution rate (in nm/s)	Source
BCC iron	$0.257\ [OH^-]^{0.6}\exp\left(\frac{82012\ (V+0.45)}{RT}\right)$	[327]
Mackinawite	0.015	[174]
Pyrrhotite	$289.15 \times 10^{-1.46\ pH} \times \exp\left(-\frac{65.9\ kJ}{RT}\right)$	[328]
Pyrite	0.00017244	[329]

Table 6.6: General dissolution rates for each material phase in the passive film model with data taken from literature

6.4.4 Individual kMC models

Surface dissolution model

In this model we take inspiration from our work on the surface of pyrite to simulate three processes at the film-environment interface: Vacancy formation, vacancy annihilation and vacancy diffusion. Similar to our work in Chapter 4, the vacancy formation energies and the vacancy migration barriers were dependent on the number of broken bonds and the vacancy formation energies were further benchmarked to the dissolution rate.

Coupling between the mesoscale system and the kMC model occurs during the setup of the kMC calculation where the local film dissolution rates (and the corresponding vacancy formation energies are derived from the local phase fractions, temperature and pH of the each grid point at the interface and are benchmarked to dissolution rates of different phases obtained from field data, as shown in the Table 6.6.

After the kMC calculation, which results in inhomogeneous dissolution, the resulting profile of the partially-dissolved film is imposed on the phase field model. In addition, the local pH, which is affected by the inhomogeneous dissolution (due to the hydrolysis reaction shown below), is also coupled back into the mesoscale phase-field model.

$$Fe^{2+} + H_2O \rightarrow FeOH^+ + H^+$$

Vacancy agglomeration

Another probable method of local degradation is the agglomeration of vacancies at the metal-film interface. We model this as a simple kMC model containing one unit process – vacancy migration between surface lattice sites.

The initial coupling between the mesoscale PF and kMC models happens during model setup, when the initial vacancy concentration at the interface is determined from the relative rates of film growth and the local diffusivity of iron in metallic iron. Specifically, the interfacial vacancy concentration is the value required to ensure a flux of metal atoms to the surface to sustain the observed film growth rate. Mathematically, this is equal to

$$\rho_{Fe}\ D_{Fe}^{Fe}\frac{C_{\mathrm{v}}^{\mathrm{int}}}{10\ \mathrm{nm}} = \rho_{\mathrm{mkw}}\ k_{\mathrm{film}}$$

where $\rho_{Fe}$is the density of atoms in BCC Fe, $D_{Fe}^{Fe}$is the self diffusivity of BCC Fe, $C_{\mathrm{v}}^{\mathrm{int}}$ is the interfacial vacancy concentration, $\rho_{\mathrm{mkw}}$is the density of Fe atoms in mackinawite

and k_{film} is the growth rate of the passive film.

After the kMC simulation, the formation of any vacancy agglomerations are coupled back to the phase field model as void/delaminations by setting the value of local diffusivity in that region to be zero.

H_2 blister formation

In order to estimate the impact of local H_2 formation and delamination of the mackinawite passive film from the metal surface, we model the dynamics of interstitial H defects at the mackinawite-metal interface.

The processes modeled in this model include migration of H and H_2 interstitials and association of two neighboring atomic interstitials to form a H_2 molecule and, to maintain detailed balance, dissociation of H_2 molecules to form two atomic H interstitials.

Initial coupling between the phase field and kMC models occurs during the setup of the kMC model, where the initial concentration of the atomic H interstitials is defined by the sulfidation rate of the film according to the chemical reaction below.

$$Fe + H_2S \rightleftharpoons FeS_{\text{x}} + 2H_{\text{int}}$$

During the kMC calculation, we use the relation between gas pressure and yield strength of the mackinawite layer as described in [330] and references therein to identify if agglomerated H_2 molecules lead to blister formation and delamination. This hydrogen evolution kMC model provides a mechanistic input to the phase field model that is lacking in other phase field models of materials damage in corrosion conditions [331]

6.5 Results

The composition of the passive film has long been derived from Pourbaix diagrams [332] even though they strictly apply only to equilibrium conditions and cannot be applied to a dynamic system like a growing passive film, whose stability depends upon their rate of formation and destruction [333]. But the purely thermodynamic analysis found in Pourbaix and phase diagrams cannot predict quantities like the thickness of the passive film (which can range from nm to microns [296]) or its stability, which depends on a host of environmental factors [296, 334, 335].

Therefore the passive film models must be capable of modeling film growth in different regimes dominated by the kinetics of different unit processes and also be capable of representing relative film stability as a function of not only of the thermodynamic stability but also of the kinetics of growth and dissolution of phases. In the next section, we demonstrate these two capabilities by constructing kinetic stability diagrams demonstrating different regimes of film growth and composition of films at different times.

6.5.1 Film growth regimes

One basic test of the multiscale passive film model is the reproduction of observed kinetics of film growth in an anhydrous environment, as described by other analytical film growth models (Section 6.3). Specifically, in anhydrous environments, film growth is dominated by one of two unit processes, sulfidation or diffusion. Figure 6-5 shows the thickness of a single phase (mackinawite) FeS film as a function of time in the film

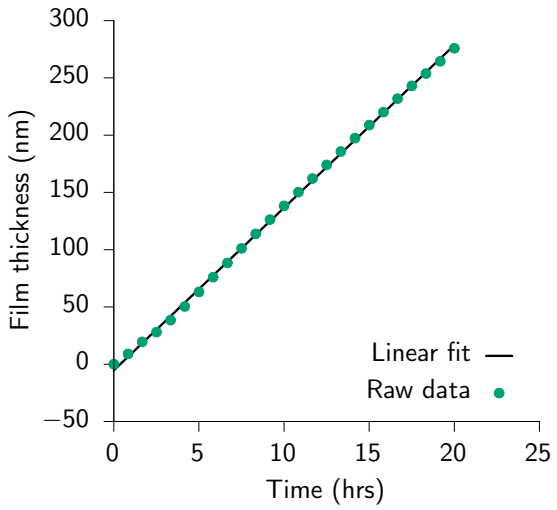

Figure 6-5: Growth profile of a mackinawite film under sulfidation-limited conditions shows the expected linear growth kinetics

growth regime where surface sulfidation is the rat-limiting unit process. Since film growth is limited by the constant rate of sulfidation, it is independent of time and film thickness. Therefore, the thickness of the passive film as a function of time in this regime is characterized by a constant slope giving rise to a linear growth profile described by the equation $L = k_S t$.

Figure 6-6 shows the thickness of a growing single phase (mackinawite) film as a function of time in a film growth regime where ionic diffusion through the passive film in the rate limiting unit process. In this regime, the flux of atoms through the film decreases with increasing film thickness (and increasing time) because the driving force for diffusion (i.e. the concentration gradient across the film, $\frac{\partial C}{\partial x}$ decreases with increasing film thickness. Therefore, the thickness of the passive film as a function of time in this regime is characterized by a quadratic rate expression given by $L = \sqrt{k_p t}$.

In the intermediate mixed regime where the diffusion flux of Fe and S atoms is approximately equal to the sulfidation rate, the growth profile of a single phase FeS film demonstrate a transition between two growth regimes (Figure 6-7). At early times, when film thickness is small, diffusion flux is much larger than the sulfidation rate and the film growth demonstrates sulfidation-limited linear growth kinetics. At later times and higher film thicknesses, diffusion becomes much slower and rate-limiting. Therefore, film thickness in this mixed regime follows the functional form of the Deal-Grove model [278].

While such an analytical expression for the growth of the single-phase film are long known, the growth-profiles of multiphase films is less well investigated and their modeling is usually performed numerically, rather than analytically. Figure 6-8 shows the growth of a multiphase (mackinawite and pyrrhotite) film as a function of time indicating the initial formation of a thin mackinawite film and the subsequent nucleation and the growth of an external, more sulfur-rich pyrrhotite film. The relative magnitudes of the ionic diffusivities of the different phases in relation to the sulfidation is also apparent from the linear growth profile of the mackinawite phase and the parabolic growth profile of the pyrrhotite film.

In order to model the growth in aqueous conditions, it is necessary to model the film dissolution unit process in addition to the sulfidation- and diffusion-limited film growth

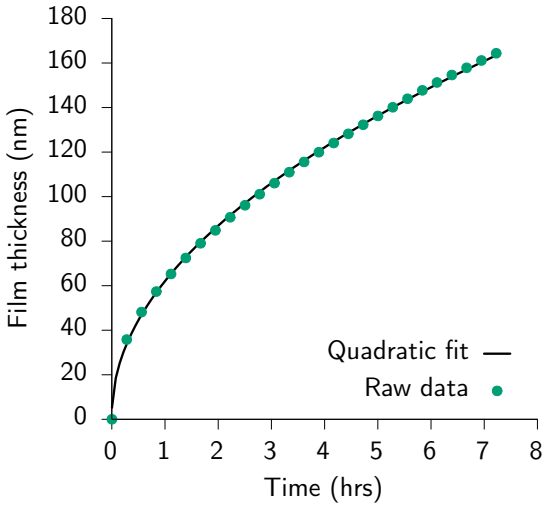

Figure 6-6: Growth profile of a mackinawite film under sulfidation-limited conditions shows the expected linear growth kinetics

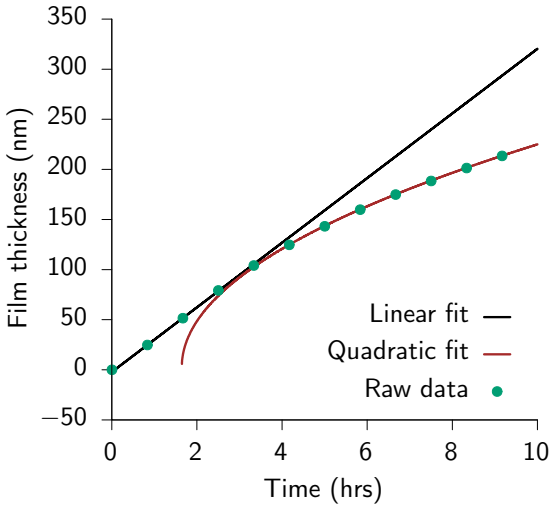

Figure 6-7: Growth profile of a mackinawite film undergoing a transition from sulfidation-limited conditions to diffusion-limited conditions shows the initially linear and subsequent parabolic growth kinetics

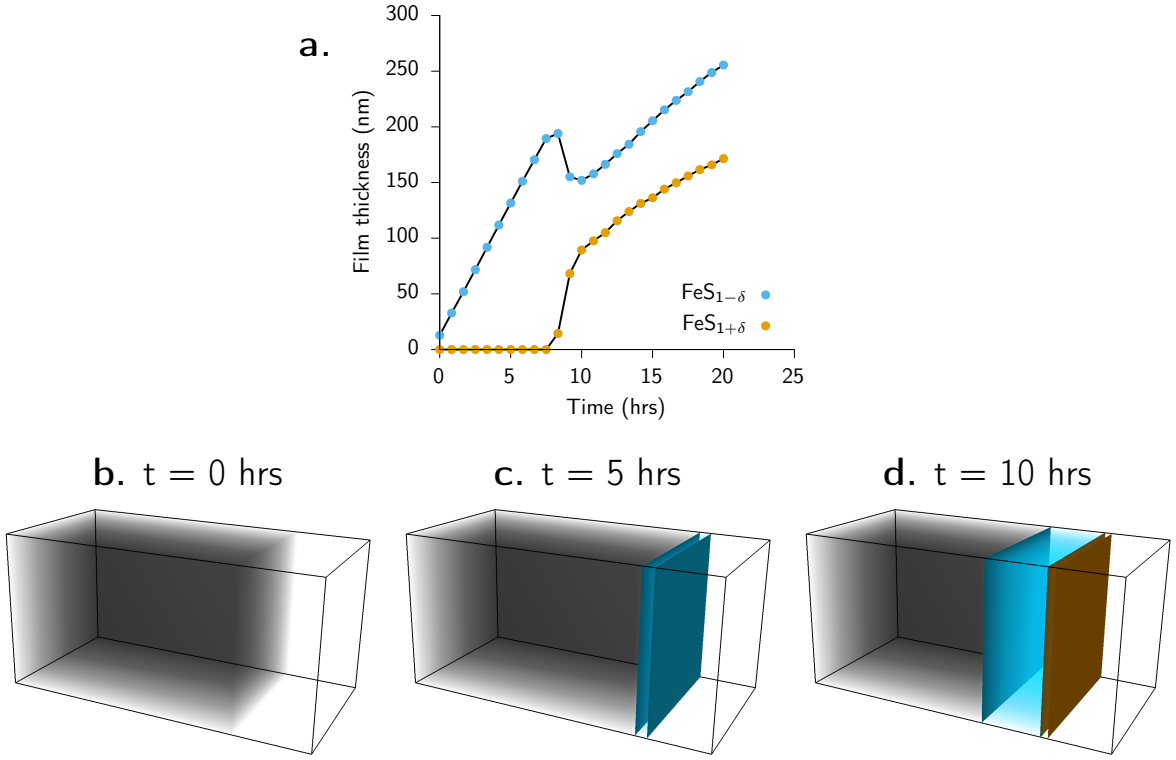

Figure 6-8: (a)Relative thicknesses of the two phases (mackinawite and pyrrhotite) in a passive film formed under moderate anhydrous sulfidizing environments. The onset of formation of each phase, as well as the growth profiles are determined by the relative thermodynamic and kinetic stability and diffusivities of each phase. (b,c) At early times, passive film growth occurs by surface-sulfidation-limited growth of the mackinawite phase (blue) between the metal (gray) and the environment (white). (d) With continued sulfidation, the sulfur overpotential at the mackinawite-environment interface becomes large enough to nucleate the pyrrhotite phase (yellow), whose subsequent diffusion-limited growth leads to a bilayer multiphase microstructure of the passive film with the Fe-rich mackinawite phase closer to the the metal and the S-rich pyrrhotite phase in contact with the sulfidizing environment.

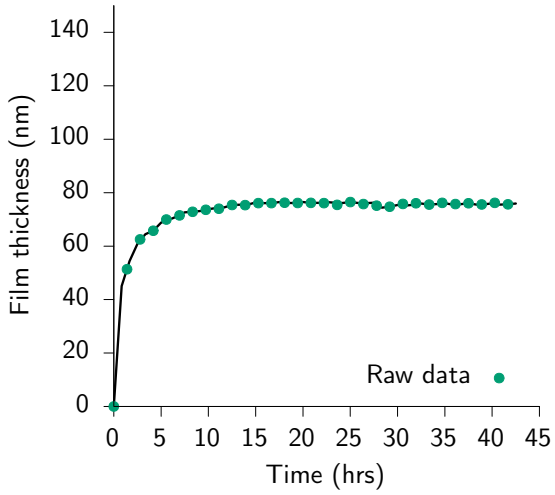

Figure 6-9: The growth of a mackinawite film under aqueous conditions reaches steady state thickness when the diffusion-limited growth rate of the film becomes equal to the dissolution rate in the given environment

processes. Figure 6-9 shows the growth profile of a single phase (mackinawite) passive film in aqueous environments. At short times, film growth is dominated by the diffusion of ions through the thin film, which occurs much faster than the relatively slow dissolution. The balance of these two processes leads to a net growth of the mackinawite passive film. Once the film reaches a critical thickness, the rate of diffusion becomes equal to the rate of film dissolution and the balance of these relative rates if film formation and degradation leads to a dynamically stable film of constant thickness.

Having quantified the kinetics of film growth and degradation, one of the most useful results of this modeling framework is in identifying the composition of the passive film under non-equilibrium conditions. Figure 6-10 shows the component phases present in the passive film for a range of sulfur chemical potentials (ranging from a H_2S partial pressure of 10^{-8} atm to 10^{2} atm) and at intermediate temperatures (300K to 600K) at different times after exposure of the pure Fe metal to the sulfidizing aqueous environment. In addition to showing film compositions at different times as a function of environmental conditions, the diagram also provides information about the environmental conditions most suitable for the nucleation and growth of iron sulfide phases. As Figure 6-10 shows, mackinawite nucleation occurs initially in the low temperature, intermediate μ_S regime, while pyrrhotite nucleation occurs initially in the high-temperature, intermediate μ_S and pyrite nucleation prefers the low-temperature high μ_S region. Such kinetic stability diagrams have been proposed as useful improvements over Pourbaix diagrams [333] and have previously been derived for sulfide and oxide scales [336]

6.5.2 Film degradation

Localized degradation is characterized by relatively gradual initiation of pitting and localized damage followed by significantly faster growth of existing pits. Therefore, models of local film degradation must account for atomistic details of the pit initiation process. In the passive film model, this atomic resolution is provided by three kinetic Monte Carlo models, each describing a single mechanism of localized film degradation. In the section below, we describe results from each model along with an indication of the environmental conditions under which each model is dominant.

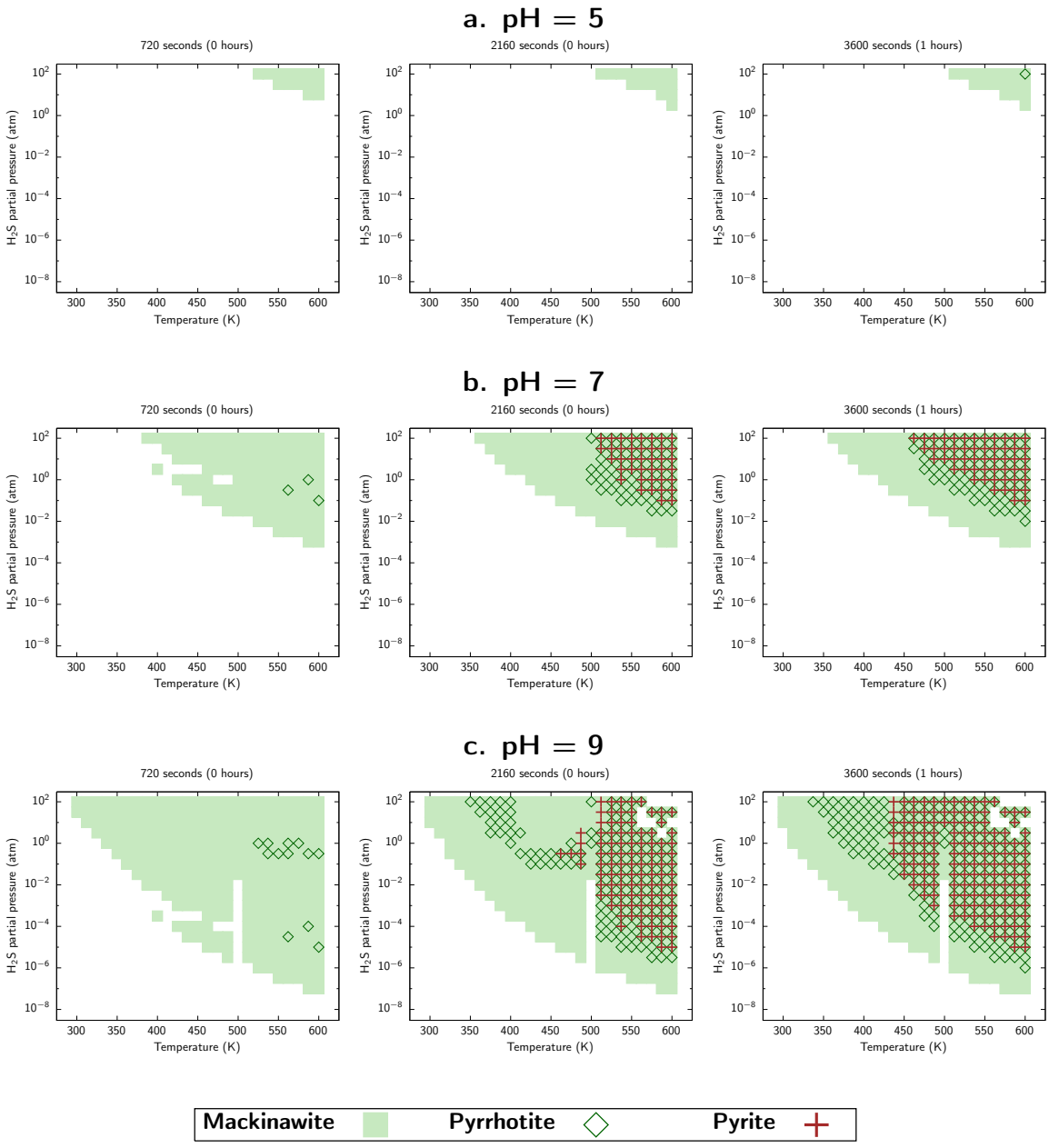

Figure 6-10: Phase stability diagram for an iron surface in contact with a sulfidizing environment at 0 hours (Left), and 1 hours (Right) as a function of temperature and the partial pressure of H_2S at pH values of (a) 5, (b) 7 and (c) 9 respectively showing the formation of mackinawite (light green), pyrrhotite (dark green) and pyrite phases (red) on steel surfaces.

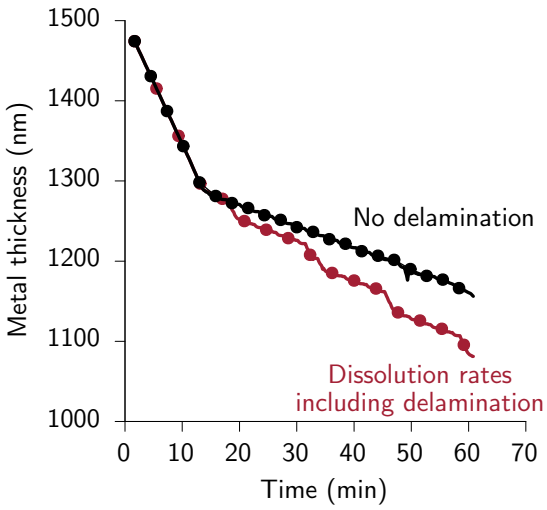

Figure 6-11: H_2 induced delamination leads to metastable pitting resulting in a greater effective corrosion rate, as indicated by the faster metal loss rate.

H_2-induced debonding

In this mechanism, agglomeration of H_2 molecules near deformation is the crystal lattice leads to the formation of H_2 blisters, which act as voids preventing ionic diffusion through the film. This disturbs the dynamic equilibrium established by a balance of film growth and film dissolution. In the absence of film growth due to lack of diffusion, film dissolution locally reduces the film thickness leading to pit formation. Figure 6-11 shows the difference between one-dimensional growth of a single-phase (mackinawite) film when this mechanism is operative and when it isn't. When hydrogen-induced debonding exists, the film undergoes a series of growth and breakdown cycles, culminated each time by a rapid metal loss as the underlying metal is exposed to the environment. This is a representation of the situation in metastable pitting and leads to a greater effective corrosion rate.

The mechanism of film degradation is most observable in environmental conditions where a high H_2 evolution rate (corresponding to a greater metal loss) is coupled with very low film thickness (as a consequence of fast film dissolution and/or slow film growth). These conditions can be found in conditions of intermediate-high temperatures (450K to 600K) and at intermediate sulfur concentrations (H_2S partial pressures in the range of 10^{-4} to 10^{-2} atm). The dark region in Figure 6-12 falls within this definition and represents the environmental conditions where H_2 evolution on defect-free mackinawite is responsible for local degradation. As shown in Chapter 5 section 5.6.2, the presence of crystal defects increases the number of evolved H_2 molecules 8-fold. This is reflected in Figure 6-12 , by an expanded region (light green) responsible for H_2 induced delamination. This region represents the environmental conditions where H_2 evolution in defective mackinawite (0.8% Fe vacancy) is responsible for local degradation of the passive film.

Vacancy-agglomeration-induced pit initiation

This mechanism of localized film degradation occurs due to void formation at the metal-film interface due to condensation of vacancies in the metal region. To understand the reason for the presence of vacancies in the metal, it is important understand the mech-

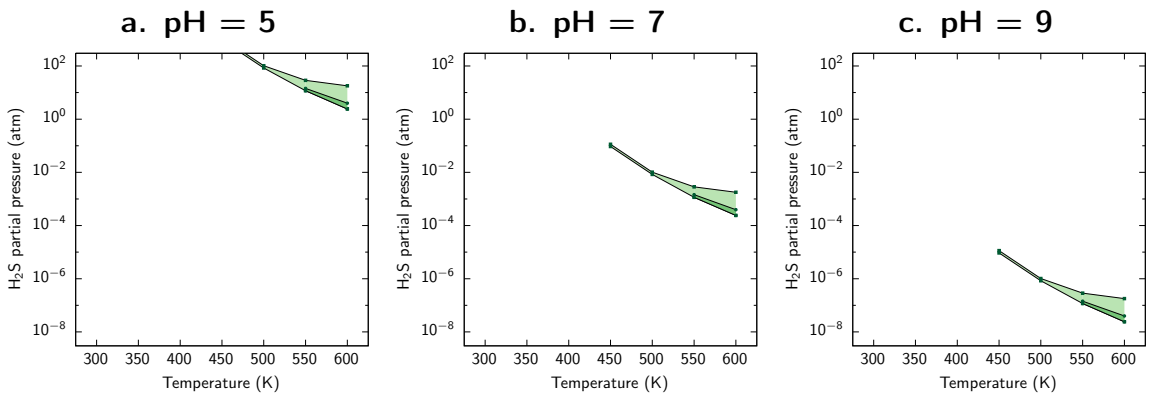

Figure 6-12: (Dark green) region where hydrogen evolution in interlaminar regions of defect-free mackinawite leads to film breakdown and (light green) regions where hydrogen evolution in interlaminar regions of defective (0.8% Fe vacancy) mackinawite leads to localized passive film breakdown as a function of electrolyte pH

anism of film formation at the metal-film interface. Film formation proceeds by sulfidation of the metal surface. At the atomic scale, this process involves the hopping of an Fe atom at the surface of the metal into the lattice position of the FeS_x crystal structure in the passive film, leaving behind two electrons on the metal (the oxidation/sulfidation process) along with a vacancy at the Fe site. Such vacancies at the surface are subsequently annihilated by the flux of Fe atoms from the bulk of the metal phase which is driven by the gradient of vacancy concentration from the surface of the steel to the bulk. For large values of diffusivity of Fe metal (or equivalently, low rates of film growth), the flux of Fe atoms is sufficient to annihilate the interfacial vacancies generated by film growth. But at lower diffusivities, there is a significantly higher concentration of interfacial vacancies, which, through agglomeration can lead to the formation of voids. As shown in the previous section, such voids can locally disturb the dynamic equilibrium between film growth and film dissolution leading to put initiation.

Figure 6-13 shows the environmental conditions where vacancy-agglomeration-induced debonding and pit initiation leads to local degradation of the film. Comparing this figure to the kinetic stability diagrams in Figure 6-10, it is easily noticed that this region corresponds to conditions of rapid growth, which is indicated by the early appearance of the mackinawite phase in the passive film. Finally, we also notice that at higher temperatures, due to the higher diffusivity of atoms in bulk iron, the vacancy-agglomeration-induced voiding mechanism is not operative.

Finally, the data from the kinetic stability diagram (Figure 6-10) and the degradation maps (Figures 6-12 and 6-13) can be combined to identify environmental conditions where iron sulfide passive film is stable against localized degradation. Figure 6-14 shows an example of such a film stability map at different pH conditions. The gray regions indicate environmental conditions (P_{H_2S} and T) where the formation of a FeS_x passive film is thermodynamically prohibited. Further the regions highlighted in in green and blue respectively correspond to environmental conditions where the failure of the FeS_x film occurs by H_2 blistering and vacancy-agglomeration-induced debonding. Therefore, only the regions indicated in white correspond to the existence of a stable passive film. As acidic pH values close to 5, the formation of a stable passive film is unfeasible in nearly all environmental conditions considered, primarily due to the low values of sulfur chemical potential, μ_S. Similarly, at near neutral pH values close to 7,

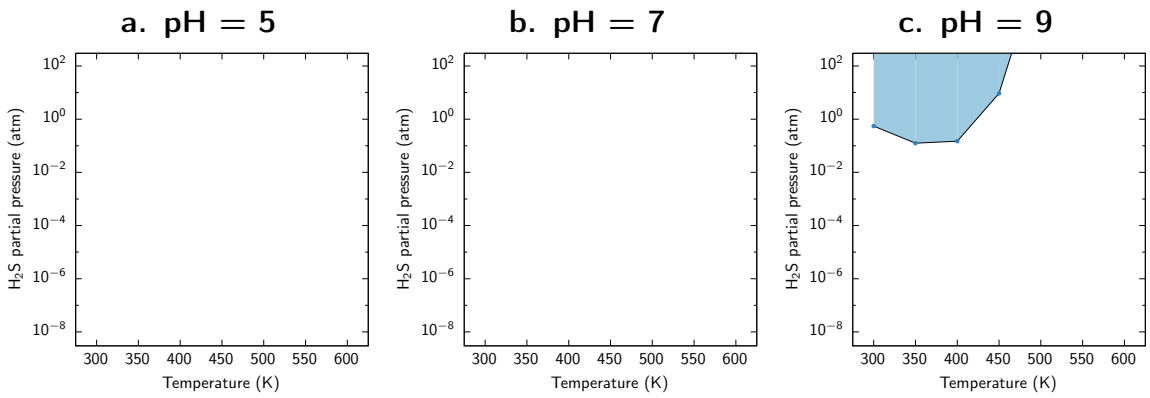

Figure 6-13: Region where rapid film growth rates leads to vacancy formation and voiding on the metal surface and subsequent debonding and film degradation is highlighted in blue. In acidic (pH = 5) and neutral (pH = 7) conditions, pit initiation mechanism is not a dominant degradation mechanism in the range of H2S partial pressures considered, but becomes an important mechanism of degradation in the low temperature - high partial pressure regime at basic pH of 9

stable passive films can be expected to occur at intermediate temperatures and relatively high H_2S concentrations. At basic pH = 9, vacancy agglomeration induced degradation mechanism plays an important role in limiting the formation of a stable passive film to regions of high temperature and high values of P_{H_2S}.

6.5.3 Kinetic parameter effects

Another common mechanism for local film degradation is pit initiation due to agglomeration of dissolution-induced vacancies on the surface of the passive film (in contact with the environment) followed by pit growth due to the evolution of an aggressive chemical environment in the nascent pit due to hydrolysis. This behavior is governed, at the atomic scale, by the values of surface vacancy agglomeration energies and diffusivity of surface vacancies. Coupling between atomic and meso-scale properties and behavior allows us to get useful mechanistic insights into the growth and breakdown of passive films. More specifically, we can use the modeling framework to identify the impact of atomic scale material and kinetic properties on the morphology and protectivity of the passive film. Such an exercise is useful in two ways. First, it provides a more detailed characterization of film passivity at a given environmental condition by quantifying useful parameters such as the relative rates of general and localized corrosion as well as qualities like concentration and growth of pitting sites. This represents a useful improvement over existing models, where film passivity is quantified using just an effective rate of metal loss. Second, and perhaps more importantly, this type of analysis helps identify the relative importance of different atomic properties towards film passivity and is therefore invaluable in the materials design process for more corrosion-resistant coatings and films.

Figures 6-15, 6-16 and 6-17 show the dependence of morphology of the FeS_x film on atomic properties such as ionic diffusivity, vacancy formation energy and vacancy agglomeration energy. In the context of sour corrosion, the primary motivation of such calculations is the exploration of the vast phase-space of material and kinetic properties to identify regions that correspond to films which are stable against localized corrosion and pitting. In the subsections below, we provide a summary of the trends in propensity

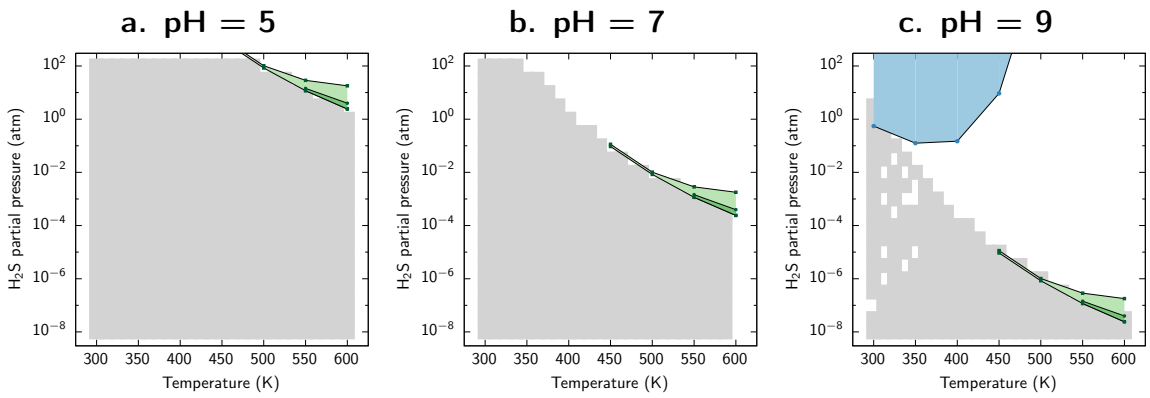

Figure 6-14: A combined overlay of the the kinetic stability diagrams and maps of different regimes of degradation allows us to identify environmental conditions the lead to the formation of stable, protective passive films. In the figure above, the gray regions highlight environmental conditions where formation of iron sulfide phases is thermodynamically prohibited and the green and blue regions respectively denote environments where the iron sulfide passive film undergoed localized degradation due to hydrogen blistering or vacancy-agglomeration and debonding. The remaining white regions, therefore, indicate the extent of environmental conditions where the iron sulfide passive film is both thermodynamically stable, and unaffected by localized corrosion due the these two mechanisms.

toward pitting and localized corrosion for each atomic property and conclude with a broad identification of properties that lead to the formation of uniform and protective passive films resistant against localized degradation.

6.5.4 Ionic diffusivity

Pit formation in FeS_x is preceded by the dissolution-induced formation of individual surface vacancies and their subsequent reorganization to form agglomeration, which serve as sites for pit initiation (See Section 4.4), The further growth of pits from these sites is determined by the evolution of local electrochemistry (μ_S, pH, T and ψ) around the pit sites.

Therefore, the morphology of the film depends greatly on the ionic diffusivity, which controls the kinetics of vacancy dynamics on the surface of the film and the size of the resulting vacancy agglomeration. In Figure 6-15, we plot the calculated morphologies of the passive film simulated at two representative ionic diffusivity values of D_0 and $0.1D_0$ respectively. At higher diffusivity values, the highly mobile surface vacancies distribute themselves more uniformly throughout the surface results in the formation of smaller vacancy agglomerations scattered throughout the surface. These smaller agglomerations serve as sites for initiation of metastable pits which are highly prone to repassivation leading to a more uniform film.

On the other hand, in systems of lower diffusivity, the relatively less mobile surface vacancies tend to get trapped in local minima in the potential energy landscape, which correspond to vacancy agglomerations. As a result, the surface morphology in this system is described by fewer, but larger vacancy agglomerations, which can serve as sites for nucleation of stable, and deep pits leading to a highly pitted and non-protective films.

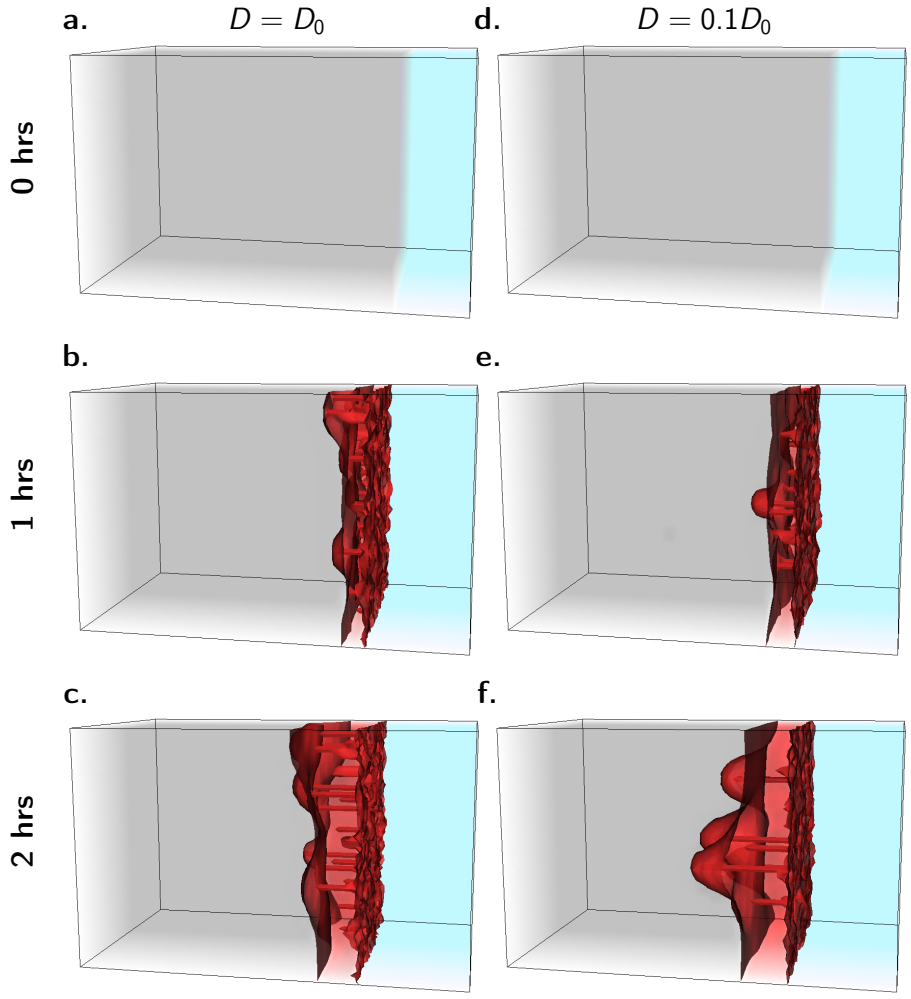

Figure 6-15: Morphology of the film surface as a function of ionic diffusivity of films. The isosurfaces of the film phase fraction shows that lower effective film diffusivities lead to fewer, deeper pits as film damage is localized.

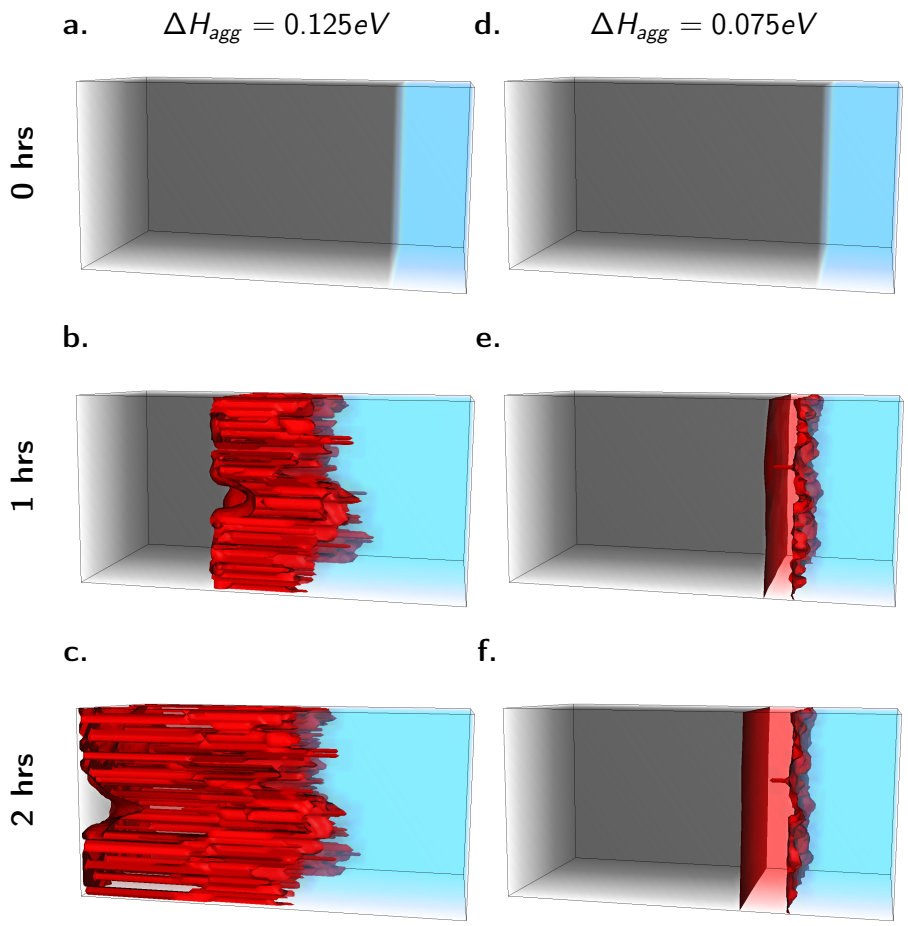

Figure 6-16: Morphology of the film surface as a function of energy of agglomeration of surface vacancies. The isosurfaces of the film phase fraction shows that a greater vacancy agglomeration energy, which leads to a greater concentration of pit initiation sites, results in a more heavily pitted film, with several deep and stable pits. In contrast, a relatively lower agglomeration energy results in the formation of fewer pit initiation and growth events and lead to a more uniform passive film, whose protectivity depends only on the general corrosion rate.

6.5.5 Vacancy agglomeration

Another important atomic parameter that controls vacancy dynamics on the film surface is the energy of agglomeration of surface vacancies. The vacancy agglomeration energy, ΔH_{agg}, is defined as the potential energy difference between two isolated and adjacent vacancies, and defines the propensity for surface vacancies to agglomerate to form pit initiation sites. A greater, or more positive value for ΔH_{agg} indicates that isolated vacancies are more unstable and there exists a significant driving force for the formation of vacancy agglomerations. A smaller value of ΔH_{agg} indicates that there is no significant reduction in energy due to the formation of vacancy agglomerations and therefore the formation of isolated vacancies (which are entropically stabilized) is more likely. Figure 6-16 shows the simulated morphologies calculated at relatively lower and higher ΔH_{agg} values of 0.075 eV and 0.125 eV respectively.

A greater value for the agglomeration energy implies a passive film surface dominated by large stable vacancy agglomerations and consequently a heavily-pitted and nomi-

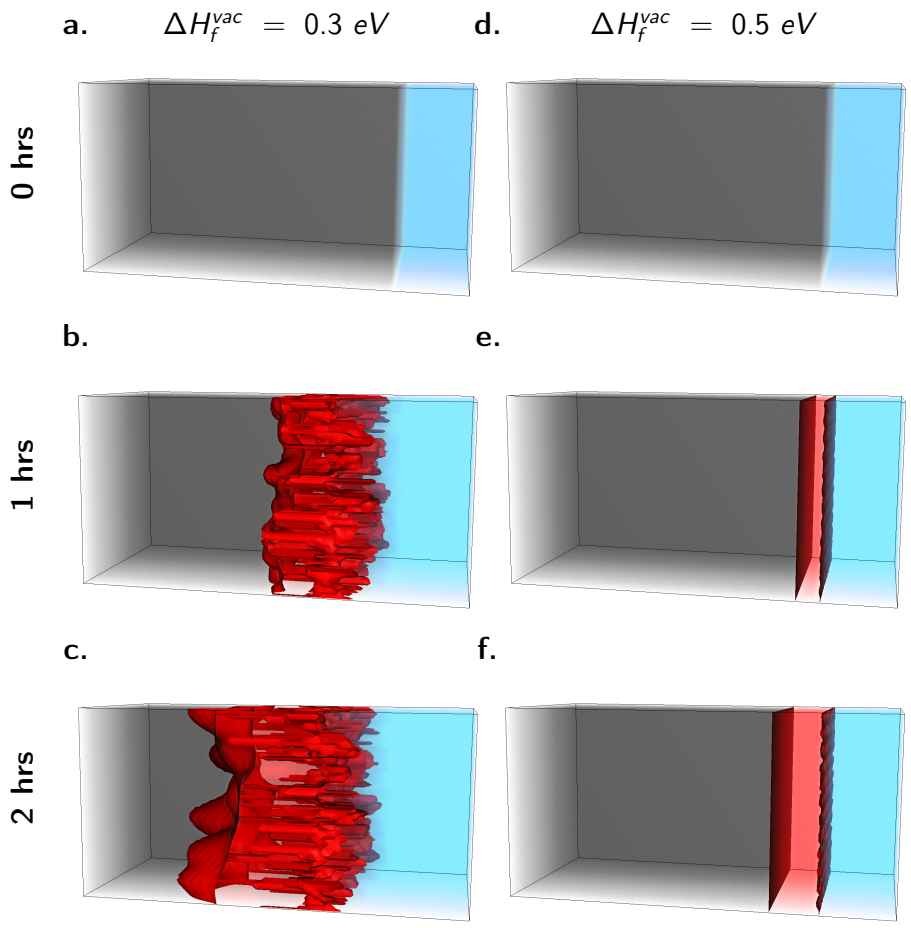

Figure 6-17: Morphology of the film surface as a function of formation energy of surface vacancies. A lower defect formation energy of 0.3 eV implies a greater concentration of surface vacancies and, therefore, a greater concentration of pit initiation sites, which leads to a more heavily pitted surface and also a greater effective rate of film dissolution. A greater defect formation energy of 0.5, on the other hand, leads to a more uniform, less defective film surface with a lower effective rate of dissolution.

nally unprotective passive film. A further consequence of this non-passive film is the greater rate of metal loss and a higher corrosion current in the system. In contrast, a lower value of ΔH_{agg} results in a more homogeneous distribution of surface vacancies and fewer, if any, pit initiation events quickly followed by repassivation.

6.5.6 Vacancy formation energy

The formation energy of vacancies on the surface of the passive film, ΔH_f^{vac}, also plays an important role in modifying the protectivity of the film. The value of ΔH_f^{vac} determines the concentration of surface vacancies, which, in turn, determines the probability of formation of vacancy agglomerates and pit initiation. Figure 6-17 shows that a relatively lower vacancy formation energy of 0.3 eV leads to a mechanically degraded film with few deep pits, while a relatively larger value of the vacancy formation energy (of 0.5 eV)leads to a more uniform film resistant to pitting. Another important consequence of the greater ΔH_f^{vac} is the lower rate of film dissolution and therefore a correspondingly lower rate of metal loss and general corrosion.

6.5.7 Electrolyte pH

Another important experimental parameter that has a significant influence on the final morphology of the passive film is the pH of the electrochemical solution. The pH affects the passivity of the film in two distinct ways:

1. The pH of the solution affects the local dissolution rate of the passive film and therefore the concentration of vacancies on the surface of the passive film, which act as precursors for pit initiation

2. The pH of the solution also affects the evolution of the profile of H^+ concentration within the pits, and therefore also affects the rate of autocatalytic pit growth aided by hydrolysis within the pits

Figure 6-18 shows morphology of iron sulfide passive films formed under a constant sulfur chemical potential (i.e. at a constant driving force for film formation) at three different values of pH in the environment. At identical sulfur chemical potential, the rate of film formation, and the initial morphology of the three films are identical. At later times, morphology is dominated by formation of pit initiation sites on the surface of the passive film and the subsequent growth of existing pits due to hydrolysis and evolution of pH gradient inside the pits. Acidic pH values (pH $= 5$) imply a greater rate of film dissolution and a greater concentration of surface vacancies and vacancy agglomerations in the surface of the film, as evident from the greater number of metastable pits observed at time $t = 0.1$ hrs. Hydrolysis acts a source of H^+ ions and causes local acidification of the electrolyte in the pits. The evolution of the pH profile in the pit is governed by the relative rate of hydrolysis and the rate of diffusion of H^+ ions from the pit to the bulk of the electrolyte. At higher electrolyte pH values, the rate of outward diffusion of H^+ ions is suppressed due to the shallower concentration gradient, leading to extensive acidification of the pits, leading to rapid growth of stable pits (Figure 6-18c). In contrast, environments at basic pH values develop steeper H^+ gradients, and a greater rate of outward diffusion of H^+ ions to counteract hydrolysis-induced pit acidification, leading to more effective repassivation and the formation of a less-pitted passive film (Figure 6-18i).

Summarizing these trends in the passivity of the corrosion film with variation in material properties, we find that the region of the material phase space defined by high ionic diffusivities and high defect formation energies and low agglomeration energies is an attractive region to explore, though material screening or design schemes, in order to identify ionic film structures and chemistries stable against pitting corrosion in sour environments.

6.6 Outcome and Future Work

In this chapter, we describe the formulation and implementation of a multiscale, coupled phase-field and kinetic Monte Carlo model of the iron sulfide passive film that bridges atomistic resolution of events at the interface to mesoscale properties of the bulk of the passive layer in an effort to understand the impact of atomic processes on the overall passivity and protectiveness of the corrosion film. Below, we summarize the capabilities of this new model and important outcomes of applying it to iron sulfide passive films. Finally, we conclude with some suggestions on the extending this framework to other chemistries and for more predictive modeling.

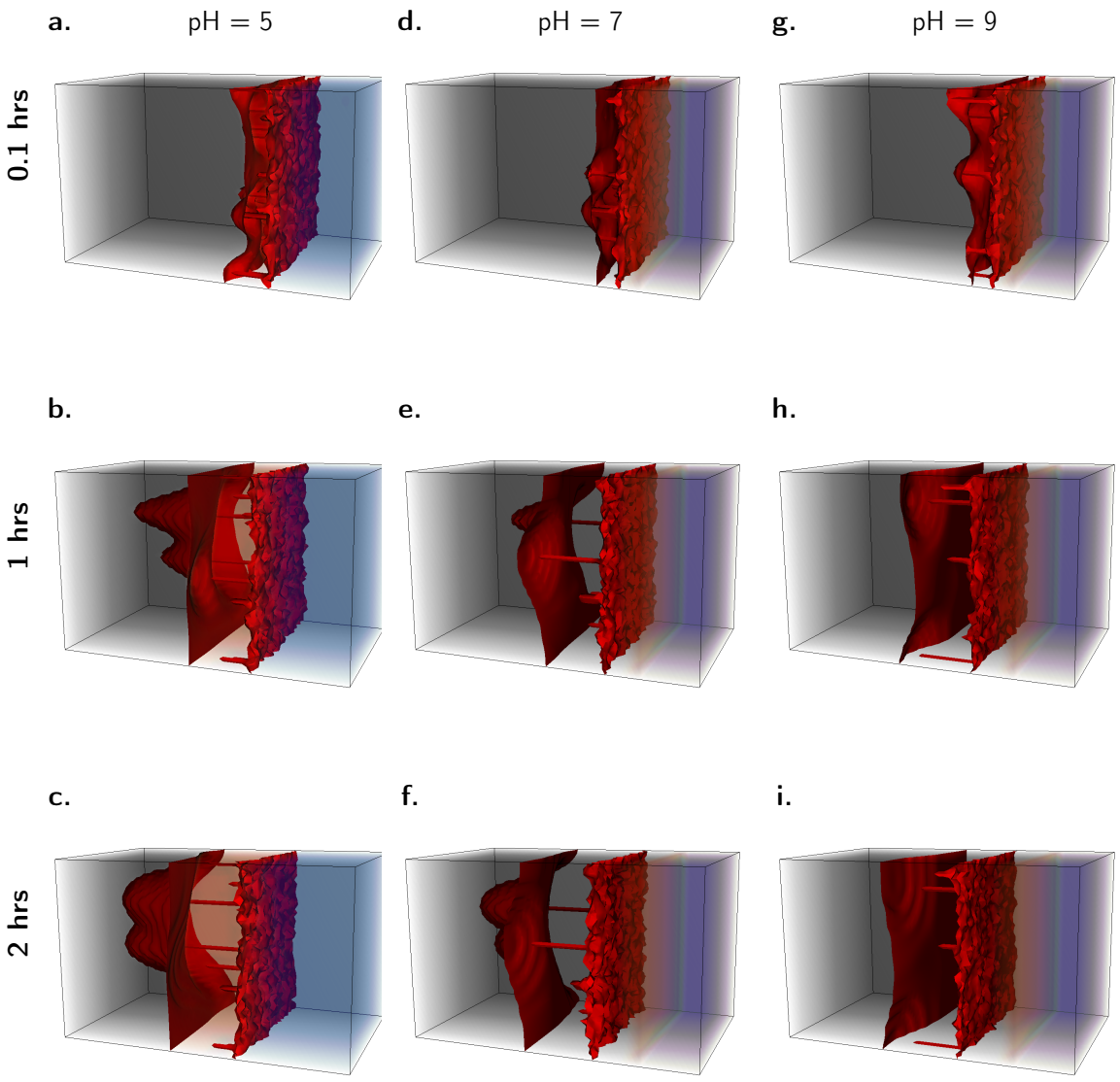

Figure 6-18: Morphology of the film surface as a function of formation energy of surface vacancies. A lower defect formation energy of 0.3 eV implies a greater concentration of surface vacancies and, therefore, a greater concentration of pit initiation sites, which leads to a more heavily pitted surface and also a greater effective rate of film dissolution. A greater defect formation energy of 0.5, on the other hand, leads to a more uniform, less defective film surface with a lower effective rate of dissolution.

6.6.1 Outcomes

The multiscale model is consistent with existing analytical models in describing growth profiles of passive layers in different anhydrous and aqueous environments and under different growth regimes and can also be used to describe the growth of multiphase films. This accuracy allows us to plot kinetic stability diagrams that can describe the environmental conditions required for rapid nucleation and growth of different iron sulfide phases and can also identify stability regimes for different phases that are not predicted by Pourbaix diagrams.

Coupling atomic-scale H_2 formation and blistering in kMC to void formation in the phase-field simulation was used to identify environmental conditions (high temperatures, low sulfidation rates) where local film degradation by H_2-induced delamination occurs. Increased H_2 evolution due to the presence of iron vacancies in the mackinawite crystal is reflected in a larger phase-space where H_2-induced delamination is detrimental. Similarly, film debonding due to agglomeration of metal vacancies was found to be dominant at low temperature and high sulfidation regimes, where film growth rates are rapid.

Finally, we also demonstrate the impact of atomic parameters like ionic diffusivity, vacancy formation energy and agglomeration energy on the morphology and protectiveness of the film. Lower surface diffusivities lead to fewer, but deeper, pits on the surface of mackinawite films corresponding to a less protective film.

6.6.2 Future Work

The model is currently benchmarked to thermodynamic and kinetic data (relative stabilities, sulfidation rates and diffusivities), which are currently hard-coded into the model. Extension to other potentially interesting chemistries (like early stage oxidation of Zr) would require coupling the model to existing thermodynamic databases like CALPHAD [337], or frameworks like the Materials Project [338] that can calculate thermodynamic data for material phases on the fly. Further, the subset of unit processes considered in the model can be expanded to include factors like chemical and stress-induced crack initiation to simulate important processes like stress-corrosion cracking.

In its current state, the model still includes empirical kinetic parameters benchmarked to field data. To address this, the model can further be coupled to reactive molecular dynamics simulations both to bridge the length-scale between atomic and phase-field methods and also to provide non-empirical rate and kinetic metrics for processes like sulfidation.

Chapter 7

Conclusions

This thesis explored the bulk and surface defect structures, electronic states as well as transport and mechanical properties of the three most important iron sulfide phases in the sour corrosion reaction system – mackinawite, pyrrhotite and pyrite. A primary goal of this thesis, as stated in Chapter 1, is to understand the mechanisms behind the growth and breakdown of the FeS_x passive film through a study of individual unit processes, the factors that affect them as well as their collective behavior and to supplement this mechanistic picture through a quantification of the reaction kinetics in an effort to model the passivity of the corrosion layer from the 'bottom up'. In the section below, we summarize our results from Chapter 2 through Chapter 6 and list the primary scientific contributions of the thesis.

7.1 Thesis Contributions

7.1.1 Surface reactivity of pyrite

- After identifying a suitable Hubbard parameter (U-J = 1.6 eV for Fe 3d) to accurately represent the electronic structure of the pyrite crystal, we demonstrate that the stable (100) surface of pyrite has a significantly lower band gap of 0.5 eV compared to the bulk value of 0.85 eV, due to the presence of surface states at the edge of the valence and conduction bands. Further, the presence of surface defects (mainly Fe and S vacancies) introduces discrete defect states in the already reduced band gap making for more facile charge transfer and reactant activation. This is evident in the calculated activation barriers for the dissociation of H_2S molecules, which is 0.85 eV on a defect-free surface but is barrier-less on a surface with S vacancy. These calculation identify the thermodynamic basis for the high surface activity of the nominally passive FeS_2 (100) surface and also suggest a potential explanation for the poor performance (particularly low open circuit potential) of pyrite-based photovoltaic devices.
- Within the DFT framework, most reactivity metrics are calculated in the limit of zero surface coverage of reactant molecules. In contrast, in this thesis, we calculated H_2S adsorption energy as a function of surface coverage to identify that interactions between neighboring adsorbate H_2S molecules can affect the adsorption energy by as much as 0.55 eV, with a correspondingly large impact on the surface activity towards H_2S dissociation. Further, we identify that the change in the surface electronic structure due to H_2S adsorption is the main reason for the

variation in adsorption energies of subsequent H_2S molecules. Other factors such as the Coulombic repulsion between adsorbates as well as steric repulsion are quantifiably minor components of the overall inter-adsorbate interactions. These calculations provide evidence against the use of zero-coverage adsorption energies to make determinations about the reactivity of ionic surfaces in screening schemes for heterogeneous catalysts. It also estimates the corrections required to approximate more realistic adsorption energies for the case of compact, uncharged reactants like H_2S.

- We find that the reactivity of the charged pyrite surface can be adequately described by the *d*-band theory of transition metal reactivity because the primary effect of charging the surface (or equivalently, varying the surface potential) is to alter the position of the Fermi level within the electronic structure of the crystal. Other effects of surface charging such as the formation of an intense electric field in the double layer region and the polarization response of the solvent water molecules play only a minor role and do not significantly affect the absorption energy and dissociation barriers and can therefore be ignored in any first-order approximation of the reactivity of the charged surface.

7.1.2 Ionic diffusion

- The growth of thicker FeS_x films is limited by the rate of diffusion through the pyrrhotite phase. Here, we show, through combined kinetic Monte Carlo simulations and magnetokinetic experiments that the diffusion of Fe^{2+} ions through the pyrrhotite phase is independent of the vacancy arrangements and multiple ordered polytypes in the pyrrhotite phase and occur with a constant migration barrier of 1.2 eV. In a related calculation, we show that ionic migration through the anti-ferromagnetic pyrrhotite phase is more difficult ($E_a^{migr} = 1.6$ eV) than migration through ferromagnetic pyrrhotite ($E_a^{migr} = 0.8$ eV) in the first demonstration of the impact of local magnetic structure on diffusivity of ionic crystals. This provides the basis for explaining recent radiotracer experiments and provides useful input to higher-scale models for sour passive films and also suggests important implications for cation diffusion in other ionic crystals like NiO and MgO.

7.1.3 Pit initiation mechanisms

- We identified a mechanism for the nucleation of nano-pit sites that serve as initiation sites for metastable pitting. Surface vacancies formed due to film dissolution undergo diffusion and association within experimental timescales (of approximately a few hours) to form a nano-pitted surface morphology with several initiation sites for subsequent pitting. This mechanism can explain the unusual non-Arrhenius behavior of the defect concentration on the FeS_2 surface and the kinetics of vacancy dynamics can be used to estimate the protective lifetime of stable sour passive films.
- We also identify that H_2 evolution (from atomic H) is thermodynamically favorable in the interlaminar region of the cathodically polarized mackinawite phase, particularly in mackinawite crystals containing a small fraction ($< 1\%$) of Fe vacancies, which evolves H_2 molecules at a rate 7 times higher than the defect-free crystal. These H_2 molecules cause embrittlement of the mackinawite crystal leading to local blistering and debonding of the mackinawite film from the metal surface, exposing the underlying metal to further corrosion and pit initiation.

These interstitial dynamics provide theoretical proof of H_2 embrittlement of layered crystals and also suggests novel synthesis routes for H_2-induced exfoliation of layered crystals to produce two dimensional monolayers

7.1.4 Multiscale modeling

- The passive film is an intrinsically multiscale system with processes occurring across a wide range of length and time scales. To model this complex system, we developed a new multiscale framework consisting of kinetic Monte Carlo and phase-field models to tackle processes occurring at the atomic and mesoscale length scales respectively. Predicated on the ubiquitous point defect model, this model incorporates unit processes common to most passive film systems and can be used to identify different regimes of film growth in gaseous and aqueous environments and can also be used to identify the kinetics of metal loss and film growth to estimate film passivity. The coupling between length scales and the importance of understanding unit processes is most useful when we use the model to identify environmental conditions where local degradation mechanisms are operative and also the impact of atomic parameters like surface diffusivity and vacancy formation energy and agglomeration energy on the overall propensity to pit initiation and growth. This level of detail provides the information required for better-informed design of more resilient passive films.

7.2 Perspectives and Future Work

The majority of the work in this thesis is devoted to testing the hypothesis that with sufficiently detailed understanding of the mechanism and kinetics of a set of fundamental unit processes, we can model complex emergent behavior that define the passivity of a corrosion film. Towards this end, we have been partially successful both in being able to probe and quantify, in isolation, the kinetics and mechanisms of a few important unit processes and also to demonstrate a proof of concept modeling framework that integrates information from multiple length scales for a 'bottom-up' model of the passive film. Having already discussed some initial results from the model, we provide here some comments on the future directions in which this work can be extended and offer some perspective on the potential of such endeavors.

The point defect model provides a nearly universal framework describing the complex behavior arising from the dynamics of point defects (vacancies, interstitials etc.). However, to a significantly large extent, corrosion scenarios in real life (including stress-corrosion cracking and erosion-corrosion) are driven by mechanisms like stress and fluid flow that are not point-defect based. Therefore, the first useful extension to the existing model is to identify or construct theoretical pictures of the passive film that accounts for non-point-defect-based unit processes. Concomitantly, newer computational models to quantify the rates of these larger-scale complex unit processes must also be identified or formulated.

Second, the current multiscale framework is informed, in large part, by ab initio calculations and, where required, also benchmarked to field data for unit processes that cannot be easily simulated within the DFT framework. Looking forward, for a more predictive model, these empirical parameters must be replaced by computational data from existing databases like CALPHAD or the Materials Project or, if such data is unavailable, be generated on-the-fly using reliable techniques like reactive force-field molecular dynamics.

The study of material degradation in aggressive environments is a nearly 300-year old enterprise and the modeling of passive film behavior is a relatively recent addition in our quest towards corrosion mitigation. The mechanistic integration of component unit processes into a descriptive multiscale framework is a novel and incredibly useful extension with the potential to be applicable to other electrochemical ionic systems beyond corrosion films and this thesis represents the first few steps in this extremely fruitful direction and it is exciting to consider the scientific challenges that these studies entail.

Appendix A

Identification of the optimal $U-J$ value

Iron sulfides are a diverse group of compounds of varying stoichiometries, abundant in the Earth's crust. They are known to play an important role in the biogeochemical sulfur cycle and anoxic high-temperature corrosion processes encountered in the petrochemical industry[5]. Recently, iron disulfide, pyrite (FeS_2) has been in the spotlight for potential photovoltaic [339], battery cathode[340] and thermoelectric [341] applications. Despite this wide-ranging interest, important questions about the mechanism of pyrite oxidation and transport properties in defective pyrite (with intrinsic defects or with impurities) have not been answered fully. An aim of the present study is to contribute to the understanding of the reactivity of FeS_x phases in extreme environments that characterize corrosion processes [5, 52].

Ab initio atomistic modeling techniques, validated by suitable experiments, can advance our theoretical understanding of these processes at the electronic and atomic level. However, well-established techniques like density functional theory (DFT) face major challenges in accurately representing the electronic and crystal structure of the different iron sulfide phases. This drawback is chiefly attributed to non-local functionals like the generalized gradient approximation (GGA), which do not reproduce the localized nature of the Fe $3d$ states[342]. Since GGA causes an unphysical delocalization of these electrons, it leads to significant errors in the calculated electronic properties of the material, i.e., underestimation of the band gap. This error is demonstrated in ab initio studies with GGA that predict that pyrite is a gap-less conductor[343], while it has been experimentally observed to have a band gap in the range of 0.85-0.95 eV using different experimental techniques such as photoconductivity[41], optical absorption [39] and x-ray absorption spectroscopy [43] measurements. Hybrid functionals such as the Becke, 3-parameter, Lee-Yang-Parr functional (B3LYP), which contain fractional non-local or Hartree-Fock exchange are good at reproducing the experimentally observed band gap in many classes of materials, but overestimate FeS_2 band gaps by as much as 100% [344]. Furthermore, hybrid functionals are computationally expensive and are not viable for performing large-scale calculations in a practical time frame. In this work, we parameterize and incorporate Hubbard U corrections to DFT (the DFT+U method), which considers on-site Coulomb interactions to model intra-atomic electronic correlations. This method has been used successfully to predict the correct electronic ground states of several transition metal oxides for which the non-hybrid DFT-GGA has failed [345, 346]. The DFT+U method has also been applied to a narrow range of $3d$ transition metal sulfides to reproduce their crystal and electronic structure [59, 342]. Prior work has demonstrated that a single correction parameter (i.e., a single value of U) can

describe the electronic structure of a transition metal in different oxidation states[347]. This makes the DFT+U method ideally suited to model the behavior of transition metal compounds in the context of corrosion, where the oxidation state of the metal ion may change due to the environmental conditions and phase transformations.

Real sour corrosion films are multiphase systems and to be able to model reactions in such systems, methods must be developed that can best describe the physical properties of multiple iron sulfide phases, which are of relevance to corrosion, simultaneously within the same simulation cell. This capability is required to study complex processes like phase transformations and the role of phase boundaries which are important to consider in the context of corrosion. In this article we parameterize the DFT+U method, through the $U-J$ parameter, to best represent multiple iron sulfide phases. In this respect, we chose troilite (FeS), MnP-type FeS and pyrite (FeS_2) as model phases for $U-J$ parameterization because they are the most commonly encountered phases in iron sulfide corrosion systems and they are the phases with which we expect to do most of our calculations in the future. Further, we chose to use unit cell volume, bulk modulus and band gap as the properties for $U-J$ optimization as representations of the structural, mechanical and electronic properties of the phases. These properties determine important parameters, for example defect concentrations, fracture strength, ease of surface charge transfer, which govern the corrosion reactivity of surface films. While the parameterized $U-J$ value may not model any one property of any one phase with complete accuracy, our objective is to identify one that is the best compromise at representing all the three phases and all the three properties as accurately as possible. It will be seen in the results section that this approach actually enabled us to characterize the selected iron sulfide phases with very good accuracy.

We adopt the DFT+U method developed by Dudarev *et al.*, where the strength of the on-site Coulomb correction is given by the difference between the Coulomb (U) and exchange terms (J) [80]. Since the correction depends only on the value of $U-J$ in this scheme, the value of J was fixed to be 0 eV and optimization was done only on the U parameter. The optimization of the U parameter was performed on three FeS_x phases of relevance to anoxic corrosion, troilite, MnP-type FeS and pyrite (crystal structures are depicted in figure 1). To our knowledge, this is the first study to attempt concurrent Hubbard U parameterization for multiple iron sulfide phases4. This is important because the ultimate aim of the current study is to analyze and quantify the corrosion behavior of different iron sulfide phases. This entails comparison between the calculated corrosion-related properties of different iron sulfide phases. A meaningful comparison of calculated properties across different phases can be made only if DFT calculations are performed using identical simulation parameters such as energy cutoffs and $U-J$ values for all phases.

Catalytic and corrosion activity is controlled by an interplay between the material's electronic structure, transport and mechanical properties, which are represented in this study using the band gap, the unit cell volume and the bulk modulus of each phase, respectively. To optimize the U parameter, the calculated values of the three physical properties of each phase at different values of $U-J$ are compared to the experimentally determined value. The optimum value of the U parameter is one which minimizes the difference between the calculated and the experimental property values for all the phases.

A.1 Results

To identify the optimum U parameter, the physical properties discussed above (section 2.1) were calculated for U values from 0 eV (pure GGA) to $U = 3.5$ eV in steps of

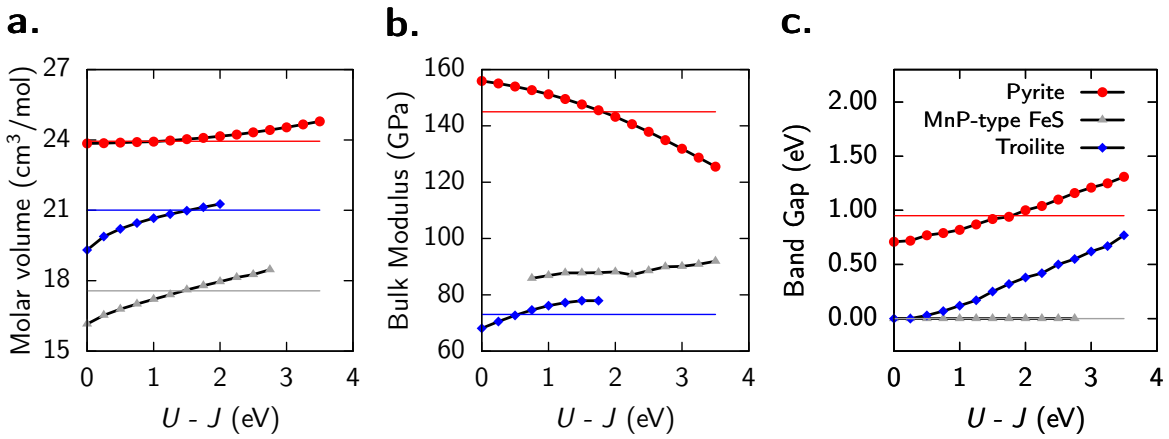

Figure A-1: Variation of (a) molar volume, (b) bulk modulus and (c) bulk band gap of FeS_x phases as a function of the $U-J$ value. Dashed lines indicate the experimentally determined values for each parameter in the corresponding phase. In (c), the experimental band gaps for the troilite and MnP-type FeS phases are represented by a single dashed line at 0 eV

0.25 eV. As Figure A-1 demonstrates, this variation of U results in a dramatic change in certain properties as the troilite pyrite band gap, while other properties as the pyrite cell volume and MnP-type FeS band gap remain almost unchanged. This is consistent with the fact that non-hybrid and uncorrected DFT calculations on pyrite have shown good agreement with experiments for structural parameters, but not for electronic parameters [343]. Because the MnP-type FeS band gap (that is 0 eV) is insensitive to the $U-J$ values explored, we disregard this property during our calculation of the optimum $U-J$ parameter. The calculation of bulk elastic modulus for MnP-type FeS is particularly problematic for ab initio methods, and the two previous attempts to calculate the bulk modulus using DFT resulted in values of 76.8 GPa [348] and 73.1 GPa [349], both very different from the experimentally determined values of 44 GPa [350] and 35 GPa [351]. We suspect that temperature-dependent magnetic spin transitions [352], which are not reproduced with DFT calculations at 0 K contribute to discrepancies between experiments and DFT calculations on this property. Additionally, Ono *et al.* [349] suggested that the experimental value may be in error due to the particular difficulty in calculating the bulk modulus of a phase with a very narrow stability field (3 to 7 GPa).

The troilite crystal structure is not stable at $U-J$ values exceeding 2 eV. At higher values, the crystal structure reverts back into the more symmetric NiAs crystal structure on which the troilite crystal structure is based. While it is possible to constrain the crystal to remain in the troilite crystal structure, such calculations will not be compatible with calculations done on other phases. Therefore, data points for $U > 2$ eV are excluded from Figure A-1. Experimentally, it is known that the compressibility of troilite increases with pressure[351]. Therefore, its bulk modulus increases with increasing unit cell volume or equivalently, the $U-J$ parameter. This trend is only followed in the region $U-J \leq 2$ eV for which data points are presented.

The errors in the calculated properties (as a percentage of the experimentally determined value) were weighted equally and summed up, and the optimum U parameter is chosen as the one that yields the minimum average error. The net total of errors from these properties for all three phases is minimized when $U-J = 1.6$ eV (Figure A-2). This is the Hubbard correlation correction that best describes the FeS_x phases considered here. The average error at $U-J = 1.6$ eV is comprised chiefly of error in the bulk modulus of MnP-type FeS (12.5% out of 16.5%). The average error in the remaining properties is less than 4%. This value for the $U-J$ parameter for FeS_x phases also

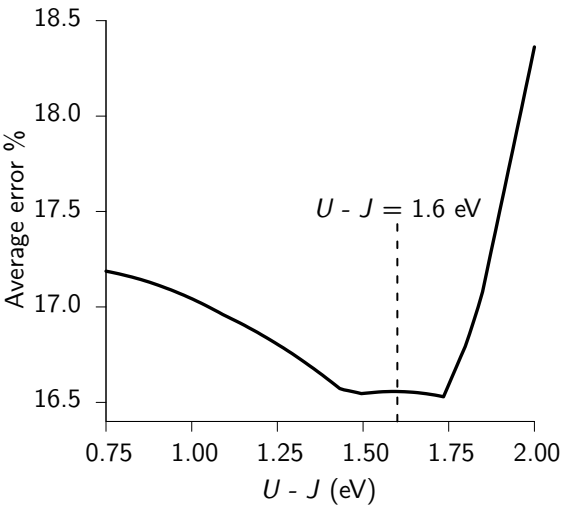

Figure A-2: Optimal value of $U-J$ that minimizes total errors for all the properties of the three FeS_x phases. Note that most of the average error stems from error in the bulk modulus of MnP-type FeS (12.5%) as discussed in the text. The average error in the remaining properties is less than 4% for $U-J=1.6$ eV.

agrees with previously determined values for $Fe_xMn_{1-x}S_2$ ($U=3$ eV, $J=1$ eV) [353] and troilite and NiAs-type FeS phases ($U-J=1$ eV)[342].

Appendix B

Hydrogen evolution on the mackinawite surface

An important factor to consider in the proposed mechanism of hydrogen-induced embrittlement of mackinawite is the relative rates of hydrogen evolution in the interlaminar bulk regions and the exposed surface of mackinawite crystals. If the hydrogen evolution reaction proceeds very rapidly on the surface of the mackinawite crystal, then the number of atomic hydrogen interstitials in the bulk of the mackinawite is likely to be low and the hydrogen-induced delamination mechanism would become inoperative. To investigate this possibility, we quantify the kinetics of the unit steps involved in hydrogen evolution on the mackinawite surface using DFT, NEB and kMC as described in Section 5.6.2. These steps are identical to those investigated in bulk mackinawite crystal with two significant differences:

1. Diffusion of adsorbed hydrogen atoms cannot proceed through the (relatively facile) inter-layer hopping mechanism. Instead, diffusion occurs through (the energetically expensive) direct hopping between adjacent surface sulfur atoms.
2. The adsorption ($H^+ + e^- \longrightarrow H_{ad}$) and desorption ($H_{ad} \longrightarrow H^+ + e^-$) of hydrogen on the mackinawite surface is modeled explicitly. This is in contrast to the case of bulk mackinawite, where a thermodynamically consistent concentration of atomic hydrogen interstitials is assumed to exist.

The *ab initio* energy barriers used as inputs for the kMC model are described in Figure B-1. While the hydrogen diffusion barriers can be calculated directly using the NEB method, the adsorption and desorption barriers are difficult to quantify because of the difficulty in accurately characterizing the solvated proton within the DFT framework. Since the adsorption and desorption processes are simply the Volmer discharge reaction occurring in the forward and reverse direction respectively, we adopt the barriers found for the Volmer reaction on MoS_2 to represent these processes. In this context, we make two further assumptions in deriving the free energy landscape for the hydrogen evolution reaction on the mackinawite surface.

1. The barriers for the Volmer reaction on the FeS surface are assumed to be equal to those on the MoS_2 surface.
2. The rate limiting reaction for hydrogen evolution on the metallic mackinawite (001) surface is assumed to be the Tafel reaction ($2\,H_{ad} \longrightarrow H_2$) and not the Heyrovsky reaction ($H_{ad} + H^+ + e^- \longrightarrow H_2$)

The results of the kMC calculation of hydrogen evolution on both the vacancy-free bulk

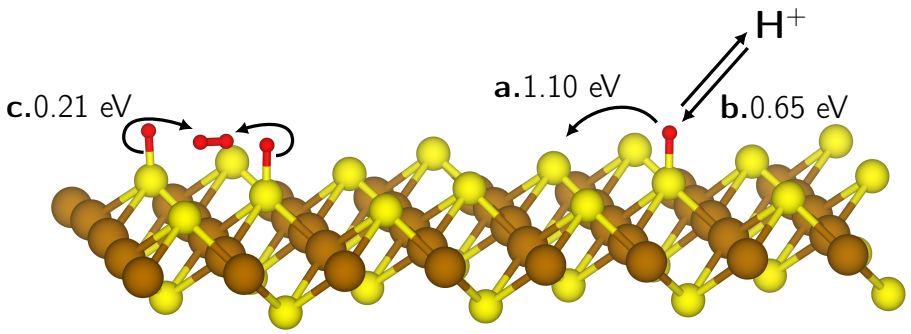

Figure B-1: Unit steps involved in hydrogen evolution on the mackinawite surface. The kinetic Monte Carlo model accounts for processes such as hydrogen adatom diffusion (a), hydrogen adsorption and desorption (b) and hydrogen association to form H_2 molecules (c).

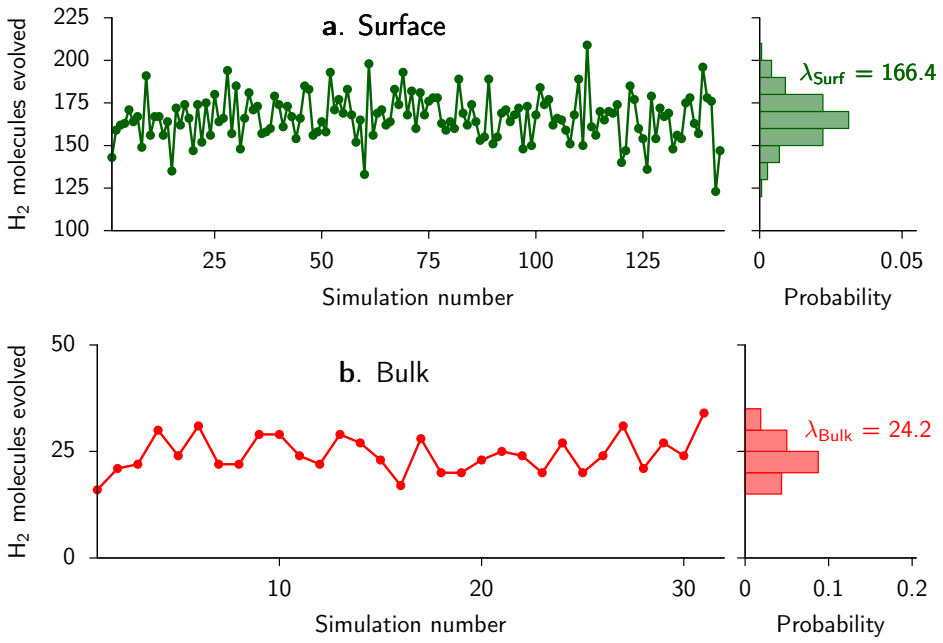

Figure B-2: Hydrogen evolution from the (a) (001) surface of mackinawite is comparable in magnitude to that from the (b) mackinawite bulk. The simulations are performed by holding each simulation system at a constant potential of -0.7 V SHE. The number of calculations done on the bulk supercells is smaller than those done on surface cells, owing to the fact that bulk calculations take significantly longer due to the existence of several low-barrier diffusion unit processes.

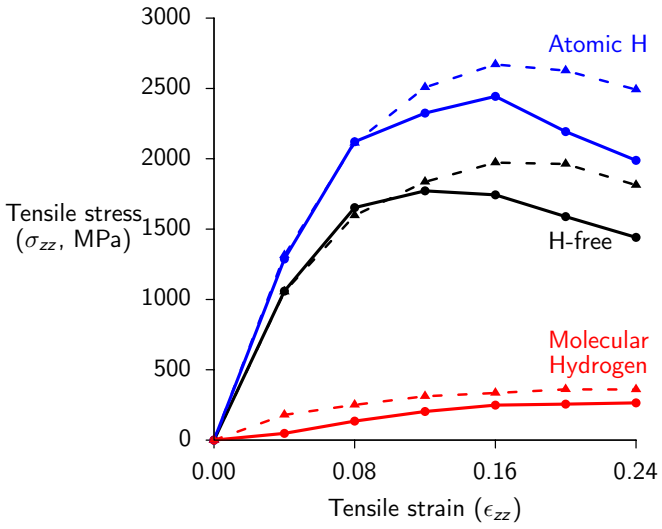

Figure B-3: The tensile stress-strain curve for mackinawite crystals containing different configurations of hydrogen interstitials computed using the DFT-D2 (solid/circles) and optB86b (dashed/triangles) correlation functionals shows that the qualitative behavior of the interstitial configurations is consistent between the two different functional types.

and vacancy-free (001) surface held at -0.7 V SHE are shown in Figure B-2, which indicates that the rate of hydrogen evolution in the bulk mackinawite crystal is slower, but comparable to (i.e. within an order of magnitude of) the rate of hydrogen evolution on the mackinawite (001) surface. These relative rates show that hydrogen evolution in bulk mackinawite crystals is important in the overall cathodic hydrogen evolution reaction and provides support for the mechanism of hydrogen-induced delamination of mackinawite crystals.

B.1 Comparison of functionals for calculating van der Waals forces

In Figure B-3, we compare the tensile stress-strain diagrams computed for mackinawite crystals containing both types of hydrogen interstitials (at 50% concentration) as well as hydrogen-free mackinawite crystals using both the DFT-D2 functional as well as the optB86b functional. The primary difference between these two non-local correlation functionals is that the semi-empirical DFT-D2 functional contains fitting parameters (named C_6 and R_0) that can be freely varied. The optB86b does not contain any analogous empirically variable parameters. The figure demonstrates that while the DFT-D2 functional systematically underestimates van der Waals binding energies, the trends between the different interstitial types are remarkably similar between the two different functionals.

Bibliography

1. Faraday, M. *Experimental researches in electricity* (Dover Publications, New York, 1965).
2. Frankenthal, R. P., Kruger, J. & Society., E. *Passivity of metals : proceedings of the fourth International Symposium on Passivity* xviii, 1077 p. (Electrochemical Society, Princeton, N.J., 1978).
3. Koch, G. H. *Corrosion cost and preventive strategies in the United States* (U.S. Dept. of Transportation, McLean, Va., 2002).
4. Smith, S. N. & Joosten, M. W. *Corrosion of Carbon Steel by H_2S in CO_2 Containing Oilfield Environments* in *Corrosion 2006* (NACE International, San Diego, CA, 2006).
5. Rickard, D. & Luther, G. W. Chemistry of Iron Sulfides. *Chemical Reviews* **107,** 514–562 (2007).
6. Shoesmith, D. W., Bailey, M. G. & Ikeda, B. Electrochemical formation of mackinawite in alkaline sulphide solutions. *Electrochimica Acta* **23,** 1329–1339 (1978).
7. Sun, W. & Nešić, S. A Mechanistic Model of Uniform Hydrogen Sulfide/Carbon Dioxide Corrosion of Mild Steel. *Corrosion* **65,** 291–307 (2009).
8. Shoesmith, D. W., Taylor, P., Bailey, M. G. & Ikeda, B. Electrochemical behaviour of iron in alkaline sulphide solutions. *Electrochimica Acta* **23,** 903–916 (1978).
9. Nešić, S., Li, H., Huang, J. & Sormaz, D. *An Open Source Mechanistic Model For CO_2/H_2S Corrosion Of Carbon Steel* in *Corrosion 2009* (NACE International, Houston, Texas, 2009).
10. Kvarekval, J., Nyborg, R. & Choi, H. *Formation of Multilayer Iron Sulfide Films During High Temperature CO_2/H_2S Corrosion of Carbon Steel* in *Corrosion 2003* (NACE International, San Diego, CA, 2003).
11. Ramanarayanan, T. & Smith, S. Corrosion of Iron in Gaseous Environments and in Gas-Saturated Aqueous Environments. *Corrosion* **46,** 66–74 (1990).
12. Smith, S. N., Brown, B. & Sun, W. *Corrosion at Higher H_2S Concentrations and Moderate Temperatures* in *NACE International Corrosion Conference Series* **11081** (NACE International, Houston, TX, 2011), 1–18.
13. Vedage, H., Ramanarayanan, T. A., Mumford, J. D. & Smith, S. N. Electrochemical Growth Of Iron Sulfide Films In H_2S-Saturated Chloride Media. *Corrosion* **49,** 114–121 (1993).
14. Popper, K. R. Pyrite and the origin of life, journal = Nature, year = 1990, volume = 344, pages = 387–387, number = 6265, date = MAR 29 1990,
15. Marcus, P. *Corrosion mechanisms in theory and practice* 3rd. *Corrosion technology* **26,** xii, 929 p. (CRC Press, Boca Raton, 2012).
16. Sabatier, P. Hydrogenation and dehydrogenation for catalysis. *Berichte Der Deutschen Chemischen Gesellschaft* **44,** 1984–2001 (1911).
17. Bronsted, J. Acid and basic catalysis. *Chemical Reviews* **5,** 231–338 (1928).
18. Evans, M. & Polanyi, M. Inertia and driving force of chemical reactions. *Transactions of the Faraday Society* **34,** 0011–0023 (1938).
19. Nørskov, J. *et al.* Universality in heterogeneous catalysis. *Journal of Catalysis* **209,** 275–278 (2002).

20. Nørskov, J. K., Bligaard, T., Rossmeisl, J. & Christensen, C. H. Towards the computational design of solid catalysts. *Nature Chemistry* **1,** 37–46 (2009).

21. Greeley, J., Jaramillo, T. F., Bonde, J., Chorkendorff, I. B. & Norskov, J. K. Computational high-throughput screening of electrocatalytic materials for hydrogen evolution. *Nature Materials* **5,** 909–913 (2006).

22. Feibelman, P. J. & Hamann, D. R. Electronic Structure of a "Poisoned" Transition-Metal Surface. *Physical Review Letters* **52,** 61–64 (1984).

23. Harris, J. & Andersson, S. H_2S Dissociation at Metal Surfaces. *Physical Review Letters* **55,** 1583 (1985).

24. Yang, W. T. & Parr, R. G. Hardness, Softness, and the Fukui Function in the Electronic Theory of Metals and Catalysis. *Proceedings of the National Academy of Sciences of the United States of America* **82,** 6723–6726 (1985).

25. De Leeuw, N. H., Parker, S. C., Sithole, H. M. & Ngoepe, P. E. Modeling the Surface Structure and Reactivity of Pyrite: Introducing a Potential Model for FeS_2. *The Journal of Physical Chemistry B* **104,** 7969–7976 (2000).

26. Hammer, B. & Nørskov, J. K. Why gold is the noblest of all the metals. *Nature* **376,** 238–240 (1995).

27. Schnur, S. & Groß, A. Strain and coordination effects in the adsorption properties of early transition metals: A density-functional theory study. *Physical Review B* **81,** 033402 (2010).

28. Abild Pedersen, F., Greeley, J. & Nørskov, J. Understanding the Effect of Steps, Strain, Poisons, and Alloying: Methane Activation on Ni Surfaces. *Catalysis Letters* **105,** 9–13 (2005).

29. Vegge, T., Hedegaard Jensen, L. S., Bonde, J., Munter, T. R. & Nørskov, J. K. Trends in hydride formation energies for magnesium-3d transition metal alloys. *Journal of Alloys and Compounds* **386,** 1–7 (2005).

30. Fernández, E. M. *et al.* Scaling Relationships for Adsorption Energies on Transition Metal Oxide, Sulfide, and Nitride Surfaces. *Angewandte Chemie International Edition* **47,** 4683–4686 (2008).

31. Jung, J., Shin, H. J., Kim, Y. & Kawai, M. Ligand Field Effect at Oxiide-Metal Interface on the Chemical Reactivity of Ultrathin Oxide Film Surface. *Journal of the American Chemical Society* **134,** 10554–10561 (2012).

32. Gómez Balderas, R., Oviedo Roa, R., Martínez Magadán, J. M., Amador, C. & Dixon, D. A. A comparative DFT study of the catalytic activity of the 3d transition metal sulphides surfaces. *Surface Science* **518,** 163–173 (2002).

33. Bronold, M., Tomm, Y. & Jaegermann, W. Surface-States on Cubic d-Band Semiconductor Pyrite (FeS_2). *Surface Science* **314,** L931–L936 (1994).

34. Krishnamoorthy, A., Herbert, F. W., Yip, S., Van Vliet, K. J. & Yildiz, B. Electronic states of intrinsic surface and bulk vacancies in FeS_2. *Journal of Physics-Condensed Matter* **25,** 045004 (2013).

35. Yu, L. P. *et al.* Iron Chalcogenide Photovoltaic Absorbers. *Advanced Energy Materials* **1,** 748–753 (2011).

36. Jiang, D. E. & Carter, E. A. Effects of Alloying on the Chemistry of CO and H_2S on Fe Surfaces. *The Journal of Physical Chemistry B* **109,** 20469–20478 (2005).

37. Heine, V. Theory of Surface States. *Physical Review* **138,** 1689–& (1965).

38. Kronik, L. & Shapira, Y. Surface photovoltage spectroscopy of semiconductor structures: at the crossroads of physics, chemistry and electrical engineering. *Surface and Interface Analysis* **31,** 954–965 (2001).

39. Bi, Y., Yuan, Y., Exstrom, C. L., Darveau, S. A. & Huang, J. Air Stable, Photosensitive, Phase Pure Iron Pyrite Nanocrystal Thin Films for Photovoltaic Application. *Nano Letters* **11,** 4953–4957 (2011).

40. Yang, T. *et al.* Optical-absorption Study of Synthetic Pyrite FeS_2 Single-crystals. *Journal of Applied Physics* **77,** 1710–1714 (1995).

41. Ho, C. H., Huang, Y. S. & Tiong, K. K. Characterization of near band-edge properties of synthetic p-FeS_2 iron pyrite from electrical and photoconductivity measurements. *Journal of Alloys and Compounds* **422,** 321–327 (2006).

42. Tsay, M.-Y., Huang, Y.-S. & Chen, Y.-F. Photoconduction of synthetic pyrite FeS_2 single crystals. *Journal of Applied Physics* **74,** 2786–2789 (1993).

43. Wadia, C. *et al.* Surfactant-Assisted Hydrothermal Synthesis of Single phase Pyrite FeS_2 Nanocrystals. *Chemistry of Materials* **21,** 2568–2570 (2009).

44. Sun, R., Chan, M. K. Y., Kang, S. & Ceder, G. Intrinsic stoichiometry and oxygen-induced p-type conductivity of pyrite FeS_2. *Physical Review B* **84,** 035212 (2011).

45. Hu, J., Zhang, Y., Law, M. & Wu, R. First-principles studies of the electronic properties of native and substitutional anionic defects in bulk iron pyrite. *Physical Review B* **85,** 085203 (2012).

46. Matsunaga, K., Tanaka, T., Yamamoto, T. & Ikuhara, Y. First-principles calculations of intrinsic defects in Al_2O_3. *Physical Review B* **68,** 085110 (2003).

47. Fiechter, S. Defect formation energies and homogeneity ranges of rock salt-, pyrite-, chalcopyrite- and molybdenite-type compound semiconductors. *Solar Energy Materials and Solar Cells* **83,** 459–477 (2004).

48. Ellmer, K. & Höpfner, C. On the stoichiometry of the semiconductor pyrite (FeS_2). *Philosophical Magazine A* **75,** 1129–1151 (1997).

49. Van Vechten, J. A. Simple Theoretical Estimates of the Schottky Constants and Virtual-Enthalpies of Single Vacancy Formation in Zinc-Blende and Wurtzite Type Semiconductors. *Journal of the Electrochemical Society* **122,** 419–422 (1975).

50. Birkholz, M., Fiechter, S., Hartmann, A. & Tributsch, H. Sulfur deficiency in iron pyrite (FeS_{2-x}) and its consequences for band-structure models. *Physical Review B* **43,** 11926 (1991).

51. Hammer, B. & Nørskov, J. K. Electronic factors determining the reactivity of metal surfaces. *Surface Science* **343,** 211–220 (1995).

52. Murphy, R. & Strongin, D. R. Surface reactivity of pyrite and related sulfides. *Surface Science Reports* **64,** 1–45 (2009).

53. Guevremont, J. M., Elsetinow, A. R., Strongin, D. R., Bebie, J. & Schoonen, M. A. A. Structure sensitivity of pyrite oxidation: Comparison of the (100) and (111) planes. *American Mineralogist* **83,** 1353–1356 (1998).

54. Sacchi, M., Galbraith, M. C. E. & Jenkins, S. J. The interaction of iron pyrite with oxygen, nitrogen and nitrogen oxides: a first-principles study. *Physical Chemistry Chemical Physics* **14,** 3627–3633 (2012).

55. Qiu, G., Xiao, Q., Hu, Y., Qin, W. & Wang, D. Theoretical study of the surface energy and electronic structure of pyrite FeS_2(100) using a total-energy pseudopotential method, CASTEP. *Journal of Colloid and Interface Science* **270,** 127–132 (2004).

56. Eggleston, C. M., Ehrhardt, J. J. & Stumm, W. Surface structural controls on pyrite oxidation kinetics: An XPS-UPS, STM, and modeling study. *American Mineralogist* **81,** 1036–1056 (1996).

57. Rosso, K. M., Becker, U. & Hochella, M. F. Atomically resolved electronic structure of pyrite (100) surfaces: An experimental and theoretical investigation with implications for reactivity. *American Mineralogist* **84,** 1535–1548 (1999).

58. Nair, N. N., Schreiner, E. & Marx, D. Glycine at the Pyrite-Water Interface: The Role of Surface Defects. *Journal of the American Chemical Society* **128,** 13815–13826 (2006).

59. Sun, R., Chan, M. K. Y. & Ceder, G. First-principles electronic structure and relative stability of pyrite and marcasite: Implications for photovoltaic performance. *Physical Review B* **83,** 235311 (2011).

60. Fiechter, S. *et al.* The Microstructure and Stoichiometry of Pyrite FeS_{2-x}. *Journal of Materials Research* **7,** 1829–1838 (1992).

61. Feng, Z., El Gabaly, F., Ye, X., Shen, Z. & Chueh, W. Fast vacancy-mediated oxygen ion incorporation across the ceria-gas electrochemical interface. *Nature Communications* **5** (2014).

62. Lindan, P. & Zhang, C. Exothermic water dissociation on the rutile TiO_2(110) surface. *Physical Review B* **72,** 075439 (2005).

63. Diemant, T., Rauscher, H., Bansmann, J. & Behm, R. J. Coadsorption of hydrogen and CO on well-defined $PT_{35}Ru_{65}$/Ru(0001) surface alloys - site specificity vs. adsorbate-adsorbate interactions. *Phys Chem Chem Phys* **12,** 9801–10 (2010).

64. Miller, S. D., Inoğlu, N. & Kitchin, J. R. Configurational correlations in the coverage dependent adsorption energies of oxygen atoms on late transition metal FCC(111) surfaces. *J Chem Phys* **134,** 104709 (2011).

65. Aldao, C., Guidoni, S., Xu, G., Nakayama, K. & Weaver, J. Monte Carlo modeling of Si(100) roughening due to adsorbate-adsorbate repulsion. *Surface Science* **551,** 143–149 (2004).

66. Grabow, L. C., Hvolbaek, B. & Norskov, J. K. Understanding Trends in Catalytic Activity: The Effect of Adsorbate-Adsorbate Interactions for CO Oxidation Over Transition Metals. *Topics in Catalysis* **53,** 298–310 (2010).

67. Qi, L. & Li, J. Adsorbate interactions on surface lead to a flattened Sabatier volcano plot in reduction of oxygen. *Journal of Catalysis* **295,** 59–69 (2012).

68. Kitchin, J. Correlations in coverage-dependent atomic adsorption energies on Pd(111). *Physical Review B* **79,** 205412 (2009).

69. Lerch, D., Wieckhorst, O., Hammer, L., Heinz, K. & Muller, S. Adsorbate cluster expansion for an arbitrary number of inequivalent sites. *Physical Review B* **78,** 121405 (2008).

70. Guo, X. *et al.* DFT study of coverage-depended adsorption of NH3 on TiO_2-B (100) surface. *Physical Chemistry Chemical Physics* **14,** 16618–16625 (2012).

71. Wang, T. *et al.* Coverage-Dependent CO Adsorption and Dissociation Mechanisms on Iron Surfaces from DFT Computations. *Acs Catalysis* **4,** 1991–2005 (2014).

72. Sanchez, J., Ducastelle, F. & Gratias, D. Generalized cluster description of multicomponent systems. *Physica A: Statistical Mechanics and its Applications* **128,** 334–350 (1984).

73. Wu, C., Schmidt, D., Wolverton, C. & Schneider, W. Accurate coverage-dependence incorporated into first-principles kinetic models: Catalytic NO oxidation on Pt (111). *Journal of Catalysis* **286,** 88–94 (2012).

74. Xiang, H., Kan, E., Wei, S., Gong, X. & Whangbo, M. Thermodynamically stable single-side hydrogenated graphene. *Physical Review B* **82,** 165425 (2010).

75. Kohn, W. & Sham, L. J. Self-Consistent Equations Including Exchange and Correlation Effects. *Physical Review* **140,** A1133 (1965).

76. Kresse, G. & Furthmüller, J. Efficiency of ab-initio total energy calculations for metals and semiconductors using a plane-wave basis set. *Computational Materials Science* **6,** 15–50 (1996).

77. Kresse, G. & Furthmüller, J. Efficient iterative schemes for *ab initio* total-energy calculations using a plane-wave basis set. *Physical Review B* **54,** 11169 (1996).

78. Perdew, J. P., Burke, K. & Ernzerhof, M. Generalized Gradient Approximation Made Simple. *Physical Review Letters* **77,** 3865 (1996).

79. Blöchl, P. E. Projector augmented-wave method. *Physical Review B* **50,** 17953 (1994).

80. Dudarev, S. L., Botton, G. A., Savrasov, S. Y., Humphreys, C. J. & Sutton, A. P. Electron-energy-loss spectra and the structural stability of nickel oxide: An LSDA+U study. *Physical Review B* **57,** 1505 (1998).

81. Van de Walle, A. & Ceder, G. Automating first-principles phase diagram calculations. *Journal of Phase Equilibria* **23,** 348–359 (2002).

82. Van de Walle, A., Asta, M. & Ceder, G. The Alloy Theoretic Automated Toolkit: A user guide. *Calphad-Computer Coupling of Phase Diagrams and Thermochemistry* **26,** 539–553 (2002).

83. Monkhorst, H. J. & Pack, J. D. Special points for Brillouin-zone integrations. *Physical Review B* **13,** 5188 (1976).

84. FORTRAN TPD. *The source code for the FORTRAN program used to perform TPD simulations is available at https://github.mit.edu/aravindk/h2s-fes2-tpd . Some scripts for visualization of the TPD spectrum are also provided.*

85. Dumesic, J. A. *The Microkinetics of Heterogeneous Catalysis* xii, 315 p. (American Chemical Society, Washington, D.C., 1993).

86. Guevremont, J. M., Strongin, D. R. & Schoonen, M. A. A. Thermal chemistry of H_2S and H_2O on the (100) plane of pyrite: Unique reactivity of defect sites. *American Mineralogist* **83,** 1246–1255 (1998).

87. Momma, K. & Izumi, F. VESTA: a three-dimensional visualization system for electronic and structural analysis. *Journal of Applied Crystallography* **41,** 653–658 (2008).

88. Stirling, A., Bernasconi, M. & Parrinello, M. Ab initio simulation of water interaction with the (100) surface of pyrite. *The Journal of Chemical Physics* **118,** 8917–8926 (2003).

89. Mantina, M., Chamberlin, A., Valero, R., Cramer, C. & Truhlar, D. Consistent van der Waals Radii for the Whole Main Group. *Journal of Physical Chemistry a* **113,** 5806–5812 (2009).

90. Juwono, T., Abou Hamad, I., Rikvold, P. & Wang, S. Parameter estimation by Density Functional Theory for a lattice-gas model of Br and Cl chemisorption on Ag (100). *Journal of Electroanalytical Chemistry* **662,** 130–136 (2011).

91. Todorova, M., Reuter, K. & Scheffler, M. Density-functional theory study of the initial oxygen incorporation in Pd(111). *Physical Review B* **71,** 195403 (2005).

92. Zeng, Z., Da Silva, J. & Li, W. Density functional theory and *ab initio* molecular dynamics study of NO adsorption on Pd(111) and Pt(111) surfaces. *Physical Review B* **81,** 085408 (2010).

93. Xie, R., Chen, D., Wang, X., He, T. & Liu, F. Adsorbate-induced surface stress of chloride monolayer on Au(111) electrode. *Journal of Physical Chemistry B* **106,** 12948–12956 (2002).

94. Tang, W., Sanville, E. & Henkelman, G. Grid-based Bader analysis algorithm without lattice bias. *J Phys Condens Matter* **21,** 084204 (2009).

95. Mavrikakis, M., Hammer, B. & Norskov, J. K. Effect of strain on the reactivity of metal surfaces. *Physical Review Letters* **81,** 2819–2822 (1998).

96. Gsell, M., Jakob, P. & Menzel, D. Effect of substrate strain on adsorption. *Science* **280,** 717–720 (1998).

97. Kushima, A., Yip, S. & Yildiz, B. Competing strain effects in reactivity of $LaCoO_3$ with oxygen. *Physical Review B* **82,** 115435 (2010).

98. Osterloh, F. & Parkinson, B. Recent developments in solar water-splitting photocatalysis. *MRS Bulletin* **36,** 17–22 (2011).

99. Li, Y. *et al.* MoS_2 Nanoparticles Grown on Graphene: An Advanced Catalyst for the Hydrogen Evolution Reaction. *Journal of the American Chemical Society* **133,** 7296–7299 (2011).

100. Chhowalla, M. *et al.* The chemistry of two-dimensional layered transition metal dichalcogenide nanosheets. *Nature Chemistry* **5,** 263–275 (2013).

101. Skulason, E. *et al.* Density functional theory calculations for the hydrogen evolution reaction in an electrochemical double layer on the Pt(111) electrode. *Physical Chemistry Chemical Physics* **9,** 3241–3250 (2007).

102. Norskov, J. *et al.* Origin of the overpotential for oxygen reduction at a fuel-cell cathode. *Journal of Physical Chemistry B* **108,** 17886–17892 (2004).

103. Karlberg, G. *et al.* Cyclic voltammograms for H on Pt(111) and Pt(100) from first principles. *Physical Review Letters* **99,** 126101 (2007).

104. Carrasco, J., Hodgson, A. & Michaelides, A. A molecular perspective of water at metal interfaces. *Nat Mater* **11,** 667–674 (2012).

105. Santos, E., Quaino, P. & Schmickler, W. Theory of electrocatalysis: hydrogen evolution and more. *Physical Chemistry Chemical Physics* **14,** 11224–11233 (2012).

106. Stancheva, M., Diawara, B., Lebreau, F. & Bojinov, M. Multi-Scale Modeling of the Initial Stages of Anodic Oxidation of Titanium. *Journal of the Electrochemical Society* **161,** E3188–E3195 (2014).

107. Ren, J. & Meng, S. Atomic structure and bonding of water overlayer on Cu(110): The borderline for intact and dissociative adsorption. *Journal of the American Chemical Society* **128,** 9282–9283 (2006).

108. Langenbach, E., Spitzer, A. & Luth, H. The Adsorption of Water on Pt(111) Studied by IR-reflection and UV-photoemission Spectroscopy. *Surface Science* **147,** 179–190 (1984).

109. Taylor, C., Wasileski, S., Filhol, J. & Neurock, M. First principles reaction modeling of the electrochemical interface: Consideration and calculation of a tunable surface potential from atomic and electronic structure. *Physical Review B* **73** (2006).

110. Trasatti, S. Structure of the metal/electrolyte solution interface: new data for theory. *Electrochimica Acta* **36,** 1657–1658 (1991).

111. Plimpton, S. Fast Parallel Algorithms for Short-Range Molecular Dynamics. *Journal of Computational Physics* **117,** 1–19 (1995).

112. Jorgensen, W. L., Chandrasekhar, J., Madura, J. D., Impey, R. W. & Klein, M. L. Comparison of Simple Potential Functions for Simulating Liquid Water. *Journal of Chemical Physics* **79,** 926–935 (1983).

113. Philpott, M. R., Goliney, I. Y. & Lin, T. T. Molecular dynamics simulation of water in a contact with an iron pyrite FeS_2 surface. *Journal of Chemical Physics* **120,** 1943–1950 (2004).

114. Grimme, S. Semiempirical GGA-type density functional constructed with a long-range dispersion correction. *Journal of Computational Chemistry* **27,** 1787–1799 (2006).

115. Zope, B., Hibbitts, D., Neurock, M. & Davis, R. Reactivity of the Gold/Water Interface During Selective Oxidation Catalysis. *Science* **330,** 74–78 (2010).

116. Stirling, A., Rozgonyi, T., Krack, M. & Bernasconi, M. Pyrite in contact with supercritical water: the desolation of steam. *Physical Chemistry Chemical Physics* **17,** 17375–17379 (2015).

117. Letchworth Weaver, K. & Arias, T. Joint density functional theory of the electrode-electrolyte interface: Application to fixed electrode potentials, interfacial capacitances, and potentials of zero charge. *Physical Review B* **86** (2012).

118. Bonnet, N., Dabo, I. & Marzari, N. Chemisorbed Molecules under Potential Bias: Detailed Insights from First-Principles Vibrational Spectroscopies. *Electrochimica Acta* **121,** 210–214 (2014).

119. Nihonyanagi, S. *et al.* Potential-dependent structure of the interfacial water on the gold electrode. *Surface Science* **573,** 11–16 (2004).

120. Noguchi, H., Okada, T. & Uosaki, K. Molecular structure at electrode/electrolyte solution interfaces related to electrocatalysis. *Faraday Discussions* **140,** 125–137 (2008).

121. Fryt, E. M., Smeltzer, W. W. & Kirkaldy, J. S. Chemical Diffusion and Point-Defect Properties of Iron Sulfide (Fe1-Delta-S) at Temperatures 600-Degrees-1000-Degrees-C. *Journal of the Electrochemical Society* **126,** 673–683 (1979).

122. Belton, G. R., Worrell, W. L. & of Pennsylvania., U. *Heterogeneous kinetics at elevated temperatures; proceedings* viii, 532 p. (Plenum Press, New York, 1970).

123. Sterten, A. Nonstoichiometry and diffusivities in iron monosulphide at elevated temperatures. *Corrosion Science* **14,** 377–390 (1974).

124. Hobbins, R. R. *The self-diffusion of iron in single crystals of ferrous sulfide and magnetically saturated iron* PhD thesis (University of Delaware, Delaware, 1969).

125. Condit, R. H., Hobbins, R. R. & Birchenall, C. E. Self-diffusion of iron and sulfur in ferrous sulfide. *Oxidation of Metals* **8,** 409–455 (1974).

126. Herbert, F., Krishnamoorthy, A., Yildiz, B. & Van Vliet, K. Diffusion-limited kinetics of the antiferromagnetic to ferrimagnetic λ-transition in $Fe_{1-x}S$. *Applied Physics Letters* **106** (2015).

127. Herbert, F., Krishnamoorthy, A., Rands, L., Van Vliet, K. & Yildiz, B. Magnetic diffusion anomaly at the Néel temperature of pyrrhotite, $Fe_{1-x}S$. *Physical Chemistry Chemical Physics* **17,** 11036–11041 (2015).

128. Marusak, L. A. & Mulay, L. N. Polytypism in the Cation-Deficient Iron Sulfide, Fe_9S_{10}, and the Magneto-Kinetics of the Diffusion Process at Temperatures About the Anti-Ferromagnetic to Ferrimagnetic (λ) Phase-Transition. *Physical Review B* **21,** 238–244 (1980).

129. Herbert, F. W. *Mechanisms Governing the Growth, Reactivity and Stability of Iron Sulfides* PhD thesis (Massachusetts Institute of Technology, Cambridge, MA, 2015), 140.

130. Barnes, H. L. *Geochemistry of hydrothermal ore deposits* 3rd, xx, 972 p. (John Wiley & Sons, New York, 1997).

131. Nakazawa, H. & Morimoto, N. Phase relations and superstructures of pyrrhotite, $Fe_{1-x}S$. *Materials Research Bulletin* **6,** 345–357 (1971).

132. Elliot, A. D. Structure of pyrrhotite 5C (Fe_9S_{10}). *Acta Crystallographica Section B* **66,** 271–279 (2010).

133. De Villiers, J. P. R., Liles, D. C. & Becker, M. The crystal structure of a naturally occurring 5C pyrrhotite from Sudbury, its chemistry, and vacancy distribution. *American Mineralogist* **94,** 1405–1410 (2009).

134. Francis, C. A. & Craig, J. R. Pyrrhotite; the nA (or 2A, 3C) superstructure reviewed. *American Mineralogist* **61,** 21–25 (1976).

135. Nakazawa, H., Morimoto, N. & Watanabe, E. in *Electron Microscopy in Mineralogy* (ed Wenk, H. R.) 304–309 (Springer Berlin Heidelberg, 1976).

136. Hagemann, I. S., Huang, Q., Gao, X. P. A., Ramirez, A. P. & Cava, R. J. Geometric Magnetic Frustration in $Ba_2Sn_2Ga_3ZnCr_7O_{22}$: A Two-Dimensional Spinel Based Kagomé Lattice. *Physical Review Letters* **86,** 894–897 (2001).

137. Powell, A., Vaqueiro, P., Knight, K., Chapon, L. & Sanchez, R. Structure and magnetism in synthetic pyrrhotite Fe_7S_8: A powder neutron-diffraction study. *Physical Review B* **70** (2004).

138. Yue, G. H. *et al.* Finite-size effect on magnetic properties in iron sulfide nanowire arrays. *Nanotechnology* **19** (2008).

139. Tokonami, M., Nishiguc.K & Morimoto, N. Crystal Structure of a Monoclinic Pyrrhotite (Fe_7S_8). *American Mineralogist* **57,** 1066–& (1972).

140. Kruse, O. Mossbauer and X-Ray Study of the Effects of Vacancy Concentration in Synthetic Hexagonal Pyrrhotites. *American Mineralogist* **75,** 755–763 (1990).

141. Wang, H. & Salveson, I. A review on the mineral chemistry of the non-stoichiometric iron sulphide, $Fe_{1-x}S$ ($0 \leq x \leq 0.125$): polymorphs, phase relations and transitions, electronic and magnetic structures. *Phase Transitions* **78,** 547–567 (2005).

142. De Villiers, J. P. R. & Liles, D. C. The crystal-structure and vacancy distribution in 6C pyrrhotite. *American Mineralogist* **95,** 148–152 (2010).

143. Townsend, M., Webster, A., Horwood, J. & Rouxbuisson, H. Ferrimagnetic Transition in $Fe_{0.9}S$ - Magnetic, Thermodynamic and Kinetic Aspects. *Journal of Physics and Chemistry of Solids* **40,** 183–189 (1979).

144. Waldner, P. & Pelton, A. Thermodynamic modeling of the Fe-S system. *Journal of Phase Equilibria and Diffusion* **26,** 23–38 (2005).

145. Jesche, A. *et al.* Giant magnetic anisotropy and tunnelling of the magnetization in $Li_2(Li_{1-x}Fe_x)N$. *Nature Communications* **5** (2014).

146. Loving, M. *Understanding the magnetostructural transformation in FeRh thin films* PhD thesis (Northeastern University, Boston (Mass.) : Northeastern University, 2013).

147. Metzler, R. & Klafter, J. The random walk's guide to anomalous diffusion: a fractional dynamics approach. *Physics Reports* **339,** 1–77 (2000).

148. Kakalios, J., Street, R. A. & Jackson, W. B. Stretched-exponential relaxation arising from dispersive diffusion of hydrogen in amorphous silicon. *Physical Review Letters* **59,** 1037–1040 (1987).

149. Ding, H., Razumovskiy, V. & Asta, M. Self diffusion anomaly in ferromagnetic metals: A density-functional-theory investigation of magnetically ordered and disordered Fe and Co. *Acta Materialia* **70,** 130–136 (2014).

150. Wen, H., Ma, P. & Woo, C. Spin-lattice dynamics study of vacancy formation and migration in ferromagnetic BCC iron. *Journal of Nuclear Materials* **440,** 428–434 (2013).

151. Sandberg, N., Chang, Z., Messina, L., Olsson, P. & Korzhavyi, P. Modeling of the magnetic free energy of self-diffusion in BCC Fe. *Physical Review B* **92,** 184102 (2015).

152. Mayeshiba, T. & Morgan, D. Strain effects on oxygen migration in perovskites. *Physical Chemistry Chemical Physics* **17,** 2715–2721 (2015).

153. Krukau, A., Vydrov, O., Izmaylov, A. & Scuseria, G. Influence of the exchange screening parameter on the performance of screened hybrid functionals. *Journal of Chemical Physics* **125** (2006).

154. Archer, T. *et al.* Exchange interactions and magnetic phases of transition metal oxides: Benchmarking advanced *ab initio* methods. *Physical Review B* **84** (2011).

155. Franchini, C., Podloucky, R., Paier, J., Marsman, M. & Kresse, G. Ground-state properties of multivalent manganese oxides: Density functional and hybrid density functional calculations. *Physical Review B* **75** (2007).

156. Akamatsu, H. *et al.* Antiferromagnetic superexchange via 3d states of titanium in $EuTiO_3$ as seen from hybrid Hartree-Fock density functional calculations. *Physical Review B* **83,** 214421 (2011).

157. El Mellouhi, F., Brothers, E., Lucero, M., Bulik, I. & Scuseria, G. Structural phase transitions of the metal oxide perovskites $SrTiO_3$, $LaAlO_3$, and $LaTiO_3$ studied with a screened hybrid functional. *Physical Review B* **87** (2013).

158. Henkelman, G., Uberuaga, B. P. & Jónsson, H. A climbing image nudged elastic band method for finding saddle points and minimum energy paths. *The Journal of Chemical Physics* **113,** 9901–9904 (2000).

159. Fleet, M. E. Crystal Structure of a Pyrrhotite (Fe_7S_8). *Acta Crystallographica Section B-Structural Crystallography and Crystal Chemistry* **B 27,** 1864–& (1971).

160. Dekkers, M. J. Magnetic Properties of Natural Pyrrhotite. Part I: Behavior of Initial Susceptibility and Saturation-magnetization-related Rock-magnetic Parameters in a Grain-size Dependent Framework. *Physics of the Earth and Planetary Interiors* **52,** 376–393 (1988).

161. Letard, I., Sainctavit, P. & Deudon, C. XMCD at Fe L-2,L-3 edges, Fe and S K edges on Fe_7S_8. *Physics and Chemistry of Minerals* **34,** 113–120 (2007).

162. Fillion, G., Mattei, J. l., Rochette, P. & Wolfers, P. Neutron Study of 4C Pyrrhotite. *Journal of Magnetism and Magnetic Materials* **104,** 1985–1986 (1992).

163. Murch, G. E., Rolls, J. M. & Bruin, H. J. D. Diffusion in Non-Stoichiometric Solids - A Monte-carlo Analysis for Pyrrhotite. *Philosophical Magazine* **29,** 337–348 (1974).

164. Goodenough, J. B. An Interpretation of the Magnetic Properties of the Perovskite-type Mixed Crystals $La_{1-x}Sr_xCoO_{3-\lambda}$. *Journal of Physics and Chemistry of Solids* **6,** 287–297 (1958).

165. Kanamori, J. Superexchange Interaction and Symmetry Properties of Electron Orbitals. *Journal of Physics and Chemistry of Solids* **10,** 87–98 (1959).

166. Lyubutin, I. *et al.* High-temperature redistribution of cation vacancies and irreversible magnetic transitions in the $Fe_{1-x}S$ nanodisks observed by the Mössbauer spectroscopy and magnetic measurements. *Journal of Nanoparticle Research* **13.** J Nanopart Res, 5507–5517 (2011).

167. Hutchings, M. T. & Samuelsen, E. J. Measurement of Spin-Wave Dispersion in NiO by Inelastic Neutron Scattering and Its Relation to Magnetic Properties. *Physical Review B* **6,** 3447–& (1972).

168. Pask, J., Singh, D., Mazin, I., Hellberg, C. & Kortus, J. Structural, electronic, and magnetic properties of MnO. *Physical Review B* **64** (2001).

169. Herbert, F., Krishnamoorthy, A., Ma, W., Van Vliet, K. & Yildiz, B. Dynamics of point defect formation, clustering and pit initiation on the pyrite surface. *Electrochimica Acta* **127,** 416–426 (2014).

170. Zheng, S. J. *et al.* Identification of $MnCr_2O_4$ nano-octahedron in catalysing pitting corrosion of austenitic stainless steels. *Acta Materialia* **58,** 5070–5085 (2010).

171. McCafferty, E. Sequence of steps in the pitting of aluminum by chloride ions. *Corrosion Science* **45,** 1421–1438 (2003).

172. Punckt, C. *et al.* Sudden onset of pitting corrosion on stainless steel as a critical phenomenon. *Science* **305,** 1133–1136 (2004).

173. Frankel, G. S. Pitting corrosion of metals - A review of the critical factors. *Journal of the Electrochemical Society* **145,** 2186–2198 (1998).

174. Smith, L. & Craig, B. *Corrosion Mechanisms and Material Performance in Environments Containing Hydrogen Sulfide and Elemental Sulfur* in *SACNUC Workshop: Sulphur-Assisted Corrosion in Nuclear Waste Disposal Systems* (Studiecentrum voor Kernenergie, Brussels, 2008).

175. Bargeron, C. B. & Givens, R. B. Localized Corrosion of Aluminum: Blister Formation as a Precursor of Pitting. *Journal of The Electrochemical Society* **124,** 1845–1848 (1977).

176. Lillard, R. S., Wang, G. F. & Baskes, M. I. The role of metallic bonding in the crystallographic pitting of magnesium. *Journal of the Electrochemical Society* **153,** B358–B364 (2006).

177. Sun, W., Nesic, S., Young, D. & Woollam, R. C. Equilibrium Expressions Related to the Solubility of the Sour Corrosion Product Mackinawite. *Industrial & Engineering Chemistry Research* **47,** 1738–1742 (2008).

178. Valor, A., Caleyo, F., Alfonso, L., Velzquez, J. C. & Hallen, J. M. Markov Chain Models for the Stochastic Modeling of Pitting Corrosion. *Mathematical Problems in Engineering* **2013,** 13 (2013).

179. Williams, D. E., Westcott, C. & Fleischmann, M. Stochastic Models of Pitting Corrosion of Stainless Steels: I . Modeling of the Initiation and Growth of Pits at Constant Potential. *Journal of The Electrochemical Society* **132,** 1796–1804 (1985).

180. Seyeux, A., Maurice, V. & Marcus, P. Breakdown Kinetics at Nanostructure Defects of Passive Films. *Electrochemical and Solid-State Letters* **12,** C25–C27 (2009).

181. Maurice, V., Klein, L., Strehblow, H. & Marcus, P. In situ STM study of the surface structure, dissolution, and early stages of electrochemical oxidation of the Ag(111) electrode. *Journal of Physical Chemistry C* **111,** 16351–16361 (2007).

182. Macdonald, D. The Point Defect Model for the Passive State. *Journal of the Electrochemical Society* **139,** 3434–3449 (1992).

183. Zhang, Y. N., Hu, J., Law, M. & Wu, R. Q. Effect of surface stoichiometry on the band gap of the pyrite FeS_2(100) surface. *Physical Review B* **85,** 085314 (2012).

184. Jasperse, J. R. & Doherty, P. E. Nucleation of surface pits by the condensation of vacancies. *Philosophical Magazine* **9,** 635–644 (1964).

185. Zhang, Z., Pan, J. S., Zhang, J. & Tok, E. S. Kinetics of Ge diffusion, desorption and pit formation dynamics during annealing of $Si_{0.8}Ge_{0.2}$/Si(001) virtual substrates. *Physical Chemistry Chemical Physics* **12,** 7171–7183 (2010).

186. Massoud, T. *et al.* Local Electronic Properties of the Passive Film on Nickel Studied by Scanning Tunneling Spectroscopy. *Journal of the Electrochemical Society* **159,** C351–C356 (2012).

187. Marcus, P., Maurice, V. & Strehblow, H. Localized corrosion (pitting): A model of passivity breakdown including the role of the oxide layer nanostructure. *Corrosion Science* **50,** 2698–2704 (2008).

188. Zhou, H., Fu, J. & Silver, R. Time-resolved kinetic Monte-Carlo simulation study on Si (111) etching. *Journal of Physical Chemistry C* **111,** 3566–3574 (2007).

189. Hu, J., Zhang, Y., Law, M. & Wu, R. Increasing the Band Gap of Iron Pyrite by Alloying with Oxygen. *Journal of the American Chemical Society* (2012).

190. Chaturvedi, S., Katz, R., Guevremont, J., Schoonen, M. & Strongin, D. XPS and LEED study of a single-crystal surface of pyrite. *American Mineralogist* **81,** 261–264 (1996).

191. Rosso, K. M., Becker, U. & Hochella, M. F. Surface defects and self-diffusion on pyrite 100: An ultra-high vacuum scanning tunneling microscopy and theoretical modeling study. *American Mineralogist* **85,** 1428–1436 (2000).

192. Fan, F. & Bard, A. Scanning Tunneling Microscopy and Tunneling Spectroscopy of n-type Iron Pyrite (N-FeS_2) Single-crystals. *Journal of Physical Chemistry* **95,** 1969–1976 (1991).

193. Liao, L. *et al.* Efficient solar water-splitting using a nanocrystalline CoO photocatalyst. *Nat Nano* **9,** 69–73 (2014).

194. Kalos, M. H. & Whitlock, P. A. *Monte Carlo methods* (J. Wiley & Sons, New York, 1986).

195. Li, L. A. & Zhou, G. W. 3D KMC simulations of crater growth during the reduction of oxide nanoislands on metal surfaces. *Surface Science* **605,** 54–61 (2011).

196. Russo, G., Sander, L. M. & Smereka, P. Quasicontinuum Monte Carlo: A method for surface growth simulations. *Physical Review B* **69** (2004).

197. Hebert, K. R., Albu, S. P., Paramasivam, I. & Schmuki, P. Morphological instability leading to formation of porous anodic oxide films. *Nature Materials* **11,** 162–166 (2012).

198. Zhou, Y. *et al.* Atomic-scale decoration for improving the pitting corrosion resistance of austenitic stainless steels. *Scientific Reports* **4** (2014).

199. Andersson, K. *et al.* Experimental and theoretical characterization of the structure of defects at the pyrite FeS_2(100) surface. *Physical Review B* **70** (2004).

200. Mitsui, T., Rose, M., Fomin, E., Ogletree, D. & Salmeron, M. Dissociative hydrogen adsorption on palladium requires aggregates of three or more vacancies. *Nature* **422,** 705–707 (2003).

201. Ren, C. Q., Liu, D. X., Bai, Z. Q. & Li, T. H. Corrosion behavior of oil tube steel in simulant solution with hydrogen sulfide and carbon dioxide. *Materials Chemistry and Physics* **93,** 305–309 (2005).

202. Shoesmith, D. W., Taylor, P., Bailey, M. G. & Owen, D. G. Formation of Ferrous Monosulfide polymorphs during the corrosion of iron by aqueous hydrogen sulfide at 21 °C. *Journal of the Electrochemical Society* **127,** 1007–1015 (1980).

203. Davoodi, A., Pakshir, M., Babaiee, M. & Ebrahimi, G. R. A comparative H_2S corrosion study of 304L and 316L stainless steels in acidic media. *Corrosion Science* **53,** 399–408 (2011).

204. Sosa, E., Cabrera Sierra, R., García, I., Oropeza, M. T. & González, I. The role of different surface damages in corrosion process in alkaline sour media. *Corrosion Science* **44,** 1515–1528 (2002).

205. Wikjord, A. G., Rummery, T. E., Doern, F. E. & Owen, D. G. Corrosion and Deposition during the Exposure of Carbon-Steel to Hydrogen Sulfide-Water Solutions. *Corrosion Science* **20,** 651–671 (1980).

206. Azevedo, C. R. F. Failure analysis of a crude oil pipeline. *Engineering Failure Analysis* **14,** 978–994 (2007).

207. Schoonen, M. A. A. & Barnes, H. L. Reactions forming pyrite and marcasite from solution: II. Via FeS precursors below 100 °C. *Geochimica et Cosmochimica Acta* **55,** 1505–1514 (1991).

208. Tewari, P. H., Bailey, M. G. & Campbell, A. B. Erosion-Corrosion of Carbon-Steel in Aqueous H_2S Solutions up to 120 °C and 1.6 MPa Pressure. *Corrosion Science* **19,** 573–& (1979).

209. Kucher, L. O. & Vasilenko, I. I. Mechanism of Interaction of Hydrogen-Sulfide with the Surface of Iron in Hydrogen Sulfide-Bearing Media. *Soviet Materials Science* **24,** 497–499 (1988).

210. Abelev, E., Sellberg, J., Ramanarayanan, T. & Bernasek, S. Effect of H_2S on Fe corrosion in CO_2-saturated brine. *Journal of Materials Science* **44,** 6167–6181 (2009).

211. Dong, X. M., Tian, Q. C. & Zhang, Q. A. Corrosion behaviour of oil well casing steel in H_2S saturated NACE solution. *Corrosion Engineering Science and Technology* **45,** 181–184 (2010).

212. Mullet, M., Boursiquot, S., Abdelmoula, M., Génin, J.-M. & Ehrhardt, J.-J. Surface chemistry and structural properties of mackinawite prepared by reaction of sulfide ions with metallic iron. *Geochimica et Cosmochimica Acta* **66,** 829–836 (2002).

213. Devey, A. J., Grau Crespo, R. & de Leeuw, N. H. Combined density functional theory and interatomic potential study of the bulk and surface structures and properties of the iron sulfide mackinawite (FeS). *Journal of Physical Chemistry C* **112,** 10960–10967 (2008).

214. Ehm, L. *et al.* Structural changes in nanocrystalline mackinawite (FeS) at high pressure. *Journal of Applied Crystallography* **42,** 15–21 (2009).

215. Ohfuji, H. & Rickard, D. High resolution transmission electron microscopic study of synthetic nanocrystalline mackinawite. *Earth and Planetary Science Letters* **241,** 227–233 (2006).

216. Jeong, H. Y., Lee, J. H. & Hayes, K. F. Characterization of synthetic nanocrystalline mackinawite: Crystal structure, particle size, and specific surface area. *Geochimica et Cosmochimica Acta* **72,** 493–505 (2008).

217. Wolthers, M., Van der Gaast, S. J. & Rickard, D. The structure of disordered mackinawite. *American Mineralogist* **88,** 2007–2015 (2003).

218. Liu, Z. *et al.* Interlayer shear strength of single crystalline graphite. *Acta Mechanica Sinica* **28,** 978–982 (2012).

219. Rickard, D. *et al.* Composition of nanoparticulate mackinawite, tetragonal iron(II) monosulfide. *Chemical Geology* **235,** 286–298 (2006).

220. Burrard Lucas, M. *et al.* Enhancement of the superconducting transition temperature of FeSe by intercalation of a molecular spacer layer. *Nat Mater* **12,** 15–19 (2013).

221. Lennie, A. R. *et al.* Transformation of mackinawite to greigite: An in situ X-ray powder diffraction and transmission electron microscope study. *American Mineralogist* **82,** 302–309 (1997).

222. Brgoch, J. & Miller, G. J. Validation of Interstitial Iron and Consequences of Nonstoichiometry in Mackinawite ($Fe_{1+x}S$). *Journal of Physical Chemistry A* **116,** 2234–2243 (2012).

223. Kwon, K. D. *et al.* Magnetic ordering in tetragonal FeS: Evidence for strong itinerant spin fluctuations. *Physical Review B* **83,** 064402 (2011).

224. Lukowski, M. *et al.* Enhanced Hydrogen Evolution Catalysis from Chemically Exfoliated Metallic MoS_2 Nanosheets. *Journal of the American Chemical Society* **135,** 10274–10277 (2013).

225. Patchkovskii, S. *et al.* Graphene nanostructures as tunable storage media for molecular hydrogen. *Proceedings of the National Academy of Sciences of the United States of America* **102,** 10439–10444 (2005).

226. Naguib, M. *et al.* Two-Dimensional Nanocrystals Produced by Exfoliation of Ti_3AlC_2. *Advanced Materials* **23,** 4248–4253 (2011).

227. Jiang, D. & Carter, E. First principles assessment of ideal fracture energies of materials with mobile impurities: implications for hydrogen embrittlement of metals. *Acta Materialia* **52,** 4801–4807 (2004).

228. Zahler, J., Morral, A., Griggs, M., Atwater, H. & Chabal, Y. Role of hydrogen in hydrogen-induced layer exfoliation of germanium. *Physical Review B* **75** (2007).

229. Rashkeev, S. N., Sohlberg, K. W., Zhuo, S. & Pantelides, S. T. Hydrogen-Induced Initiation of Corrosion in Aluminum. *The Journal of Physical Chemistry C* **111,** 7175–7178 (2007).

230. Youssef, M. & Yildiz, B. Hydrogen defects in tetragonal ZrO_2 studied using density functional theory. *Physical Chemistry Chemical Physics* **16,** 1354–1365 (2014).

231. Rak, Z., Mahanti, S., Mandal, K. & Fernelius, N. Defect-induced rigidity enhancement in layered semiconductors. *Solid State Communications* **150,** 1200–1203 (2010).

232. Compton, O. C. *et al.* Tuning the Mechanical Properties of Graphene Oxide Paper and Its Associated Polymer Nanocomposites by Controlling Cooperative Intersheet Hydrogen Bonding. *Acs Nano* **6,** 2008–2019 (2012).

233. Yoon, G. *et al.* Factors Affecting the Exfoliation of Graphite Intercalation Compounds for Graphene Synthesis. *Chemistry of Materials* **27,** 2067–2073 (2015).

234. Qi, Y., Guo, H., Hector, L. & Timmons, A. Threefold Increase in the Young's Modulus of Graphite Negative Electrode during Lithium Intercalation. *Journal of the Electrochemical Society* **157,** A558–A566 (2010).

235. Peelaers, H. & Van de Walle, C. Elastic Constants and Pressure-Induced Effects in MoS_2. *Journal of Physical Chemistry C* **118,** 12073–12076 (2014).

236. Klimes, J., Bowler, D. & Michaelides, A. Van der Waals density functionals applied to solids. *Physical Review B* **83** (2011).

237. Denholme, S. *et al.* Pressure-dependent magnetization and magnetoresistivity studies on tetragonal FeS (mackinawite): revealing its intrinsic metallic character. *Science and Technology of Advanced Materials* **15** (2014).

238. Ziambaras, E., Kleis, J., Schroder, E. & Hyldgaard, P. Potassium intercalation in graphite: A van der Waals density-functional study. *Physical Review B* **76** (2007).

239. Bjorkman, T., Gulans, A., Krasheninnikov, A. & Nieminen, R. van der Waals Bonding in Layered Compounds from Advanced Density-Functional First-Principles Calculations. *Physical Review Letters* **108** (2012).

240. Hajgato, B. *et al.* Out-of-plane shear and out-of plane Young's modulus of double-layer graphene. *Chemical Physics Letters* **564,** 37–40 (2013).

241. Arellano, J., Molina, L., Rubio, A. & Alonso, J. Density functional study of adsorption of molecular hydrogen on graphene layers. *Journal of Chemical Physics* **112,** 8114–8119 (2000).

242. Tang, D. *et al.* Nanomechanical cleavage of Molybdenum disulphide atomic layers. *Nature Communications* **5** (2014).

243. Liang, T., Sawyer, W., Perry, S., Sinnott, S. & Phillpot, S. First-principles determination of static potential energy surfaces for atomic friction in MoS_2 and MoO_3. *Physical Review B* **77** (2008).

244. Wood, G. C. & Stringer, J. The adhesion of growing oxide scales to the substrate. *Journal De Physique Iv* **3,** 65–74 (1993).

245. Shi, Y., Li, H. & Li, L. Recent advances in controlled synthesis of two-dimensional transition metal dichalcogenides via vapour deposition techniques. *Chemical Society Reviews* **44,** 2744–2756 (2015).

246. Munoz Santiburcio, D., Wittekindt, C. & Marx, D. Nanoconfinement effects on hydrated excess protons in layered materials. *Nature Communications* **4** (2013).

247. Xing, C. *et al.* In situ growth of FeS microsheet networks with enhanced electrochemical performance for lithium-ion batteries. *Journal of Materials Chemistry A* **3,** 8742–8749 (2015).

248. White, L., Bhartia, R., Stucky, G., Kanik, I. & Russell, M. Mackinawite and greigite in ancient alkaline hydrothermal chimneys: Identifying potential key catalysts for emergent life. *Earth and Planetary Science Letters* **430,** 105–114 (2015).

249. Kaniyoor, A., Baby, T. & Ramaprabhu, S. Graphene synthesis via hydrogen induced low temperature exfoliation of graphite oxide. *Journal of Materials Chemistry* **20,** 8467–8469 (2010).

250. Zhang, Y. *et al.* Understanding dopant and defect effect on H_2S sensing performances of graphene: A first-principles study. *Computational Materials Science* **69,** 222–228 (2013).

251. Borisova, D., Antonov, V. & Proykova, A. Hydrogen sulfide adsorption on a defective graphene. *International Journal of Quantum Chemistry* **113,** 786–791 (2013).

252. Sun, Y., Gao, S., Lei, F. & Xie, Y. Atomically-thin two-dimensional sheets for understanding active sites in catalysis. *Chemical Society Reviews* **44,** 623–636 (2015).

253. Skulason, E. *et al.* Modeling the Electrochemical Hydrogen Oxidation and Evolution Reactions on the Basis of Density Functional Theory Calculations. *Journal of Physical Chemistry C* **114,** 18182–18197 (2010).

254. Gao, M. *et al.* An efficient Molybdenum disulfide/cobalt diselenide hybrid catalyst for electrochemical hydrogen generation. *Nature Communications* **6** (2015).

255. Liu, D., Guo, Y., Fang, L. & Robertson, J. Sulfur vacancies in monolayer MoS_2 and its electrical contacts. *Applied Physics Letters* **103** (2013).

256. Le, D., Rawal, T. & Rahman, T. Single-Layer MoS_2 with Sulfur Vacancies: Structure and Catalytic Application. *Journal of Physical Chemistry C* **118,** 5346–5351 (2014).

257. Kwon, K., Refson, K. & Sposito, G. Transition metal incorporation into mackinawite (tetragonal FeS). *American Mineralogist* **100,** 1509–1517 (2015).

258. Berner, R. A. Iron Sulfides Formed from Aqueous Solution at Low Temperatures and Atmospheric Pressure. *Journal of Geology* **72,** 293–306 (1964).

259. Sweeney, R. E. & Kaplan, I. R. Pyrite Framboid Formation - Laboratory Synthesis and Marine Sediments. *Economic Geology* **68,** 618–634 (1973).

260. Bi, W. *et al.* Spatial Location Engineering of Oxygen Vacancies for Optimized Photocatalytic H_2 Evolution Activity. *Small* **10,** 2820–2825 (2014).

261. Liang, Q., Li, Z., Huang, Z.-H., Kang, F. & Yang, Q.-H. Holey Graphitic Carbon Nitride Nanosheets with Carbon Vacancies for Highly Improved Photocatalytic Hydrogen Production. *Advanced Functional Materials* **25,** 6885–6892 (2015).

262. Niu, P., Liu, G. & Cheng, H. Nitrogen Vacancy-Promoted Photocatalytic Activity of Graphitic Carbon Nitride. *Journal of Physical Chemistry C* **116,** 11013–11018 (2012).

263. Lu, X. *et al.* Redox cycles promoting photocatalytic hydrogen evolution of CeO_2 nanorods. *Journal of Materials Chemistry* **21,** 5569–5572 (2011).

264. Tsai, C., Chan, K., Abild Pedersen, F. & Norskov, J. Active edge sites in $MoSe_2$ and WSe_2 catalysts for the hydrogen evolution reaction: a density functional study. *Physical Chemistry Chemical Physics* **16,** 13156–13164 (2014).

265. Rodriguez, J., Hanson, J., Frenkel, A., Kim, J. & Perez, M. Experimental and theoretical studies on the reaction of H_2 with NiO: Role of O vacancies and mechanism for oxide reduction. *Journal of the American Chemical Society* **124,** 346–354 (2002).

266. Karunadasa, H. *et al.* A Molecular MoS_2 Edge Site Mimic for Catalytic Hydrogen Generation. *Science* **335,** 698–702 (2012).

267. Hinnemann, B. *et al.* Biomimetic Hydrogen Evolution: MoS_2 Nanoparticles as Catalyst for Hydrogen Evolution. *Journal of the American Chemical Society* **127,** 5308–5309 (2005).

268. Voiry, D. *et al.* Conducting MoS_2 Nanosheets as Catalysts for Hydrogen Evolution Reaction. *Nano Letters* **13,** 6222–6227 (2013).

269. Nørskov, J. *et al.* Trends in the exchange current for hydrogen evolution. *Journal of the Electrochemical Society* **152,** J23–J26 (2005).

270. Xie, J. *et al.* Controllable Disorder Engineering in Oxygen-Incorporated MoS_2 Ultrathin Nanosheets for Efficient Hydrogen Evolution. *Journal of the American Chemical Society* **135,** 17881–17888 (2013).

271. Zhuang, Z. *et al.* Nickel supported on nitrogen-doped carbon nanotubes as hydrogen oxidation reaction catalyst in alkaline electrolyte. *Nature Communications* **7** (2016).

272. Li, H. *et al.* Activating and optimizing MoS_2 basal planes for hydrogen evolution through the formation of strained sulphur vacancies. *Nature Materials* **15,** 48–+ (2016).

273. Verwey, E. Electrolytic conduction of a solid insulator at high fields - The formation of the anodic oxide film on aluminium. *Physica* **2,** 1059–1063 (1935).

274. Cabrera, N. & Mott, N. F. Theory of the Oxidation of Metals. *Reports on Progress in Physics* **12,** 163–184 (1948).

275. Fehlner, F. P. & Mott, N. F. Low-temperature oxidation. *Oxidation of Metals* **2.** Oxid Met, 59–99 (1970).

276. Wagner, C. & Schottky, W. Theory of controlled mixed phases. *Zeitschrift Fur Physikalische Chemie-Abteilung B-Chemie Der Elementarprozesse Aufbau Der Materie* **11,** 163–210 (1930).

277. Danielewski, M., Mrowec, S. & Stoklosa, A. Sulfidation of iron at high temperatures and diffusion kinetics in ferrous sulfide. *Oxidation of Metals* **17,** 77–97 (1982).

278. Deal, B. & Grove, A. General Relationship for Thermal Oxidation of Silicon. *Journal of Applied Physics* **36,** 3770 (1965).

279. Chee, S. W. *et al.* Studying localized corrosion using liquid cell transmission electron microscopy. *Chem Commun (Camb)* **51,** 168–71 (2015).

280. Guo, J. *et al.* Real-space imaging of interfacial water with submolecular resolution. *Nature Materials* **13,** 184–189 (2014).

281. Wang, M. & Hebert, K. Metal and oxygen ion transport during ionic conduction in amorphous anodic oxide films. *Journal of the Electrochemical Society* **146,** 3741–3749 (1999).

282. Hendy, S., Laycock, N. & Ryan, M. Atomistic modeling of cation transport in the passive film on iron and implications for models of growth kinetics. *Journal of the Electrochemical Society* **152,** B271–B276 (2005).

283. Maurice, V. & Marcus, P. Passive films at the nanoscale. *Electrochimica Acta* **84,** 129–138 (2012).

284. Gunasegaram, D., Venkatraman, M. & Cole, I. Towards multiscale modelling of localised corrosion. *International Materials Reviews* **59,** 84–114 (2014).

285. Jakab, M., Little, D. & Scully, J. Experimental and modeling studies of the oxygen reduction reaction on AA2024-T3. *Journal of the Electrochemical Society* **152,** B311–B320 (2005).

286. Chen, Z., Cui, F. & Kelly, R. Calculations of the cathodic current delivery capacity and stability of crevice corrosion under atmospheric environments. *Journal of the Electrochemical Society* **155,** C360–C368 (2008).

287. Sun, W. & Nesic, S. *A Mechanistic Model of H_2S Corrosion of Mild Steel* in *Corrosion 2007* (NACE International, Houston, Texas, 2007).

288. Sun, W., Nešić, S. & Papavinasam, S. *Kinetics of Iron Sulfide and Mixed Iron Sulfide/Carbonate Scale Precipitation in CO_2/H_2S Corrosion* in *Corrosion 2006* (NACE International, Houston, Texas, 2006).

289. Malki, B. & Baroux, B. Computer simulation of the corrosion pit growth. *Corrosion Science* **47,** 171–182 (2005).

290. Laycock, N., Noh, J., White, S. & Krouse, D. Computer simulation of pitting potential measurements. *Corrosion Science* **47,** 3140–3177 (2005).

291. Turnbull, A., McCartney, L. & Zhou, S. A model to predict the evolution of pitting corrosion and the pit-to-crack transition incorporating statistically distributed input parameters. *Corrosion Science* **48,** 2084–2105 (2006).

292. Lei, L., Xiaogang, L., Chaofang, D., Kui, X. & Lin, L. Cellular automata modeling on pitting current transients. *Electrochemistry Communications* **11,** 1826 –1829. ISSN: 1388-2481 (2009).

293. Zhu, Z., Sand, K. & Teevens, P. *A numerical study of under-deposit pitting corrosion in sour petroleum pipelines* in *NACE Northern Area Western Conference 2010* (NACE International, Calgary, AB (Canada); NACE International, Houston, TX (United States); Cimarron Engineering Ltd., Calgary, AB (Canada), Canada, 2010), 1–22.

294. Reigada, R., Sagues, F. & Costa, J. A Monte-Carlo Simulation of Localized Corrosion. *Journal of Chemical Physics* **101,** 2329–2337 (1994).

295. Engelhardt, G. & Macdonald, D. Unification of the deterministic and statistical approaches for predicting localized corrosion damage. I. Theoretical foundation. *Corrosion Science* **46,** 2755–2780 (2004).

296. Kempf, D., Vignal, V., Martin, N. & Virtanen, S. Relationships between strain, microstructure and oxide growth at the nano- and microscale. *Surface and Interface Analysis* **40,** 43–50 (2008).

297. Williams, D., Kilburn, M., Cliff, J. & Waterhouse, G. Composition changes around sulphide inclusions in stainless steels, and implications for the initiation of pitting corrosion. *Corrosion Science* **52,** 3702–3716 (2010).

298. Renner, F. *et al.* Initial corrosion observed on the atomic scale. *Nature* **439,** 707–710 (2006).

299. Tan, H. in *Comprehensive Structural Integrity* (ed Karihaloo, I. M. O. R.) 413–451 (Pergamon, Oxford, 2003).

300. Franco, A. & Gerard, M. Multiscale model of carbon corrosion in a PEFC: Coupling with electrocatalysis and impact on performance degradation. *Journal of the Electrochemical Society* **155,** B367–B384 (2008).

301. Macdonald, D. D. Passivity - the key to our metals-based civilization. *Pure and Applied Chemistry* **71,** 951–978 (1999).

302. Elliott, J. Novel approaches to multiscale modelling in materials science. *International Materials Reviews* **56,** 207–225 (2011).

303. Boettinger, W., Warren, J., Beckermann, C. & Karma, A. Phase-field simulation of solidification. *Annual Review of Materials Research* **32,** 163–194 (2002).

304. Granasy, L. *et al.* Phase field theory of crystal nucleation and polycrystalline growth: A review. *Journal of Materials Research* **21,** 309–319 (2006).

305. Steinbach, I. Phase-field models in materials science. *Modelling and Simulation in Materials Science and Engineering* **17** (2009).

306. Heo, T., Bhattacharyya, S. & Chen, L. A phase field study of strain energy effects on solute-grain boundary interactions. *Acta Materialia* **59,** 7800–7815 (2011).

307. Yang, L.-Q. C., Wei, Chen, L. & Yang, W. Computer simulation of the domain dynamics of a quenched system with a large number of nonconserved order parameters: The grain-growth kinetics. *Physical Review B* **50,** 15752–15756 (1994).

308. Kim, S., Kim, D., Kim, W. & Park, Y. Computer simulations of two-dimensional and three-dimensional ideal grain growth. *Physical Review E* **74** (2006).

309. De Pablo, J. & Curtin, W. Multiscale modeling in advanced materials research: Challenges, novel methods, and emerging applications. *MRS Bulletin* **32,** 905–911 (2007).

310. Mendelev, M. I. & Mishin, Y. Molecular dynamics study of self-diffusion in BCC Fe. *Physical Review B* **80,** 144111 (14 2009).

311. Fillastre, C., Barbouth, N. & Oudar, J. Diffusion of sulphur in iron-chromium alloys. *Scripta Metallurgica* **16,** 537 –540. ISSN: 0036-9748 (1982).

312. Amri, J., Kvarekvål, J. & Malki, B. *Simulation Of Solid-State Growth Of Iron Sulfides In Sour Corrosion Conditions* in *NACExpo 2011* (NACE International, Houston, Texas, 2011).

313. Watson, E. B., Cherniak, D. J. & Frank, E. A. Retention of biosignatures and mass-independent fractionations in pyrite: Self-diffusion of sulfur. *Geochimica et Cosmochimica Acta* **73,** 4792–4802 (2009).

314. Chen, J. & Harvey, W. Cation self-diffusion in chalcopyrite and pyrite. *Metallurgical and Materials Transactions B* **6,** 331–339 (1975).

315. Tamimi, A., Edward B. Rinker & Orville C. Sandall. Diffusion Coefficients for Hydrogen Sulfide, Carbon Dioxide, and Nitrous Oxide in Water over the Temperature Range 293-368 K. *Journal of Chemical & Engineering Data* **39,** 330–332 (1994).

316. Jacob H. Dane. *Methods of Soil Analysis. Part 4. Physical Methods (Soil Science Society of America Book Series, Vol. 5)* ISBN: 9780891188414 (Soil Science Society of America, Jan. 2002).

317. John, R. C. *et al.* Assessing corrosion in oil refining and petrochemical processing. en. *Materials Research* **7,** 163–173. ISSN: 1516-1439 (Mar. 2004).

318. Padilla, R., Olivares, E., Ruiz, M. C. & Sohn, H. Y. Kinetics of the sulfidation of chalcopyrite with gaseous sulfur. *Metallurgical and Materials Transactions B* **34,** 61–68. ISSN: 1543-1916 (2003).

319. Harmandas, N. G., Fernandez, E. N. & Koutsoukos, P. G. Crystal growth of pyrite in aqueous solutions. Inhibition by organophosphorus compounds. *Langmuir* **14,** 1250–1255 (1998).

320. Balay, S., Gropp, W. D., McInnes, L. C. & Smith, B. F. *Efficient Management of Parallelism in Object Oriented Numerical Software Libraries* in *Modern Software Tools in Scientific Computing* (eds Arge, E., Bruaset, A. M. & Langtangen, H. P.) (Birkhäuser Press, 1997), 163–202.

321. Balay, S. *et al. PETSc Users Manual* tech. rep. ANL-95/11 - Revision 3.5 (2014).

322. Fichthorn, K. & Weinberg, W. Theoretical foundations of dynamical Monte Carlo simulations. *Journal of Chemical Physics* **95,** 1090–1096 (1991).

323. Lukkien, J., Segers, J., Hilbers, P., Gelten, R. & Jansen, A. Efficient Monte Carlo methods for the simulation of catalytic surface reactions. *Physical Review E* **58,** 2598–2610 (1998).

324. Voter, A. F. in (eds Sickafus, K. E., Kotomin, E. A. & Uberuaga, B. P.) 1–23 (Springer Netherlands, Dordrecht, 2007). ISBN: 978-1-4020-5295-8.

325. Kang, H. & Weinberg, W. Dynamic Monte Carlo Simulations of Surface-Rate Processes. *Accounts of Chemical Research* **25,** 253–259 (1992).

326. Plimpton, S. *et al. Crossing the Mesoscale No-Man's Land via Parallel Kinetic Monte Carlo* tech. rep. SAND2009-6226 (2009).

327. Chin, R. J. & Nobe, K. Electrodissolution Kinetics of Iron in Chloride Solutions: III . Acidic Solutions. *Journal of The Electrochemical Society* **119,** 1457–1461 (1972).

328. Chiriţă, P. & Rimstidt, J. D. Pyrrhotite dissolution in acidic media. *Applied Geochemistry* **41,** 1 –10. ISSN: 0883-2927 (2014).

329. Asta, M. P., Cama, J., Soler, J., Arvidson, R. S. & Lüttge, A. Interferometric study of pyrite surface reactivity in acidic conditions. *American Mineralogist* **93,** 508–519. ISSN: 0003-004X (2008).

330. Xie, D. G. *et al.* In situ study of the initiation of hydrogen bubbles at the aluminium metal/oxide interface. *Nature Materials* (2015).

331. Fried, E., da Silva, J. Milton N., Duda, F. P. & Souza, A. C. *Phase-field Model For the Corrosion And Cracking of Metals In Aqueous Environments* in *Twenty-first International Offshore and Polar Engineering Conference* (International Society of Offshore and Polar Engineers, Maui, Hawaii, 2011), 19–24.

332. Roberge, P. R. *Corrosion engineering : principles and practice* xiv, 754 p. (McGraw-Hill, New York, 2008).

333. Macdonald, D. D. Kinetic Stability Diagrams. *ECS Transactions* **3,** 403–418 (2007).

334. Cole, I., Muster, T., Furman, S., Wright, N. & Bradbury, A. Products formed during the interaction of seawater droplets with zinc surfaces: I. Results from 1-and 2.5-day exposures. *Journal of the Electrochemical Society* **155,** C244–C255 (2008).

335. Sziraki, L., Cziraki, A., Gerocs, I., Vertesy, Z. & Kiss, L. A kinetic model of the spontaneous passivation and corrosion of zinc in near neutral Na_2SO_4 solutions. *Electrochimica Acta* **43,** 175–186 (1998).

336. Wen, Y., Chen, L. & Hawk, J. Phase-field modeling of corrosion kinetics under dual-oxidants. *Modelling and Simulation in Materials Science and Engineering* **20** (2012).

337. Kaufman, L. & Bernstein, H. *Computer calculation of phase diagrams with special reference to refractory metals Refractory materials* **4,** xi, 334 p. (Academic Press, New York, 1970).

338. Jain, A. *et al.* Commentary: The Materials Project: A materials genome approach to accelerating materials innovation. *Apl Materials* **1** (2013).

339. Ennaoui, A. *et al.* Iron disulfide for solar energy conversion. *Solar Energy Materials and Solar Cells* **29,** 289–370 (1993).

340. Strauss, E., Golodnitsky, D. & Peled, E. Study of phase changes during 500 full cycles of Li/composite polymer electrolyte/FeS_2 battery. *Electrochimica Acta* **45,** 1519–1525 (2000).

341. Kato, K., Okamoto, Y., Morimoto, J. & Miyakawa, T. The thermoelectric properties of FeS_2. *Journal of Materials Science Letters* **16,** 914–916 (1997).

342. Rohrbach, A., Hafner, J. & Kresse, G. Electronic correlation effects in transition-metal sulfides. *Journal of Physics-Condensed Matter* **15,** 979–996 (2003).

343. Muscat, J., Hung, A., Russo, S. & Yarovsky, I. First-principles studies of the structural and electronic properties of pyrite FeS_2. *Physical Review B* **65,** 054107 (2002).

344. Muscat, J., Wander, A. & Harrison, N. M. On the prediction of band gaps from hybrid functional theory. *Chemical Physics Letters* **342,** 397–401 (2001).

345. Anisimov, V. I., Kuiper, P. & Nordgren, J. First-principles calculation of NiO valence spectra in the impurity-Anderson-model approximation. *Physical Review B* **50,** 8257 (1994).

346. Nekrasov, I. A., Streltsov, S. V., Korotin, M. A. & Anisimov, V. I. Influence of rare-earth ion radii on the low-spin to intermediate-spin state transition in lanthanide cobaltite perovskites: $LaCoO_3$ versus $HoCoO_3$. *Physical Review B* **68,** 235113 (2003).

347. Wang, L., Maxisch, T. & Ceder, G. Oxidation energies of transition metal oxides within the GGA+U framework. *Physical Review B* **73,** 195107 (2006).

348. Martin, P., Price, G. D. & Vocadlo, L. An *ab initio* study of the relative stabilities and equations of state of FeS polymorphs. *Mineral Mag* **65,** 181–191 (2001).

349. Ono, S. *et al.* High-pressure phase transformations of FeS: Novel phases at conditions of planetary cores. *Earth and Planetary Science Letters* **272,** 481–487 (2008).

350. Kusaba, K., Syono, Y., Kikegawa, T. & Shimomura, O. Structure of FeS under high pressure. *Journal of Physics and Chemistry of Solids* **58,** 241–246 (1997).

351. King, J. H. E. & Prewitt, C. T. High-pressure and high-temperature polymorphism of iron sulfide (FeS). *Acta Crystallographica Section B* **38,** 1877–1887 (1982).

352. Kruse, O. Spin flip and troilite-MnP structure transition in FeS as studied by Mössbauer spectroscopy. *Journal of Physics and Chemistry of Solids* **54,** 1593–1597 (1993).

353. Persson, K., Ceder, G. & Morgan, D. Spin transitions in the $Fe_xMn_{1-x}S_2$ system. *Physical Review B* **73,** 115201 (2006).